Numerical Modeling of Air Cushion Vehicle Flexible Seals

Robert E. Cole

Dissertation submitted to the Faculty of the Virginia Polytechnic Institute and State University in partial fulfillment of the requirements for the degree of

Doctor of Philosophy

in

Aerospace Engineering

Wayne L. Neu, Chair

Eric G. Paterson

Kevin G. Wang

Richard W. Smith

4 May 2018

Blacksburg, Virginia

Keywords: fluid-structure interaction, computational fluid dynamics, hydrodynamic resistance, air cushion vehicles

Numerical Modeling of Air Cushion Vehicle Flexible Seals

Robert E. Cole

ABSTRACT

Air cushion vehicle flexible seals operate in a complex and chaotic environment dominated by fluid-structure interaction. An efficient means to explore interdependencies between various governing parameters that affect performance is through high fidelity numerical simulation. As previous numerical efforts have employed separate iterative partitioned solvers, or have implemented simplified physics, the approaches have been complex, computationally expensive, or of limited utility. This research effort performs numerical simulations to verify and validate the commercial multi-physics tool STAR-CCM+ as a stand-alone partitioned approach for fluid-structure interaction problems with or without a free surface.

A dimensional analysis is first conducted to identify potential non-dimensional forms of parameters related to seal resistance. Then, an implicit, Reynolds-averaged Navier-Stokes finite volume fluid solver is coupled to an implicit, nonlinear finite element structural solver to successfully replicate benchmark results for an elastic beam in unsteady laminar flow. To validate the implementation as a seal parameter exploratory tool, a planer bow seal model is developed and results are obtained for various cushion pressures and inflow speeds. Previous numerical and experimental results for deflection and resistance are compared, showing good agreement. An uncertainty analysis for inflow velocity reveals an inversely proportional resistance dependency.

Using Abaqus/Explicit, methodologies are also developed for a two-way, loosely coupled explicit approach to large deformation fluid-structure interaction problems, with and without a free surface. Following numerous verification and validation problems, Abaqus is ultimately abandoned due to the inability to converge the fluid pressure field and achieve steady state.

This work is a stepping stone for future researchers having interests in ACV seal design and other large deformation, fluid-structure interaction problems. By modeling all necessary physics within a verified and validated stand-alone approach, a designer's ability to comprehensively investigate seal geometries and interactions has never been more promising.

Numerical Modeling of Air Cushion Vehicle Flexible Seals

Robert E. Cole

GENERAL AUDIENCE ABSTRACT

Air cushion vehicles are specialized marine craft that utilize flexible seals to enable improved performance and fully amphibious operation. An efficient means to explore interdependencies between various seal design parameters that affect performance is through computer modeling of the fluid-structure interaction between the seal and the sea. This research effort performs numerical simulations to verify and validate the commercial multi-physics tool STAR-CCM+ as a single computer program for fluid-structure interaction problems occurring on the water surface.

A dimensional analysis is first conducted to identify parameters related to seal resistance. Then, a fluid model is coupled to a structural model to successfully replicate benchmark results for a flexible beam in an oscillating fluid flow. To validate the implementation as a seal parameter exploratory tool, a model of an ACV bow seal is developed and results are obtained for various operational conditions and inflow speeds. Previous numerical and experimental results for seal deflection and seal resistance are compared, showing good agreement. This work is a stepping stone for future researchers having interests in ACV seal design and other large deformation, fluid-structure interaction problems. By modeling all necessary physics within a verified and validated stand-alone computer program, a designer's ability to comprehensively investigate seal geometries and interactions has never been more promising.

Acknowledgements

This research was conducted at the Naval Surface Warfare Center Panama City Division (NSWCPCD) with primary funding provided by the DoD Science, Mathematics, and Research for Transformation (SMART) Scholarship for Service Program. Without the support of SMART, continuation of my graduate studies would not have been possible. A sincere thank-you is extended to my management for permitting me to deviate from my regular duties and pursue this research interest. I trust the results will be valuable for future tasking at NSWCPCD, and for the US Navy as a whole.

I sincerely thank my advisor Dr. Wayne Neu for graciously accepting me as his student. His significant experience and insight proved very valuable throughout this process, especially when the progress was slow. I also thank my remaining committee members Dr. Eric Paterson, Dr. Kevin Wang, and Dr. Rick Smith. The committee's genuine concern for my academic success is evident, and I am challenged daily to be a student worthy of their advisement. Special thanks are offered to Rick, who has been a friend and mentor at NSWCPCD for many years. His constant encouragement and willingness to share knowledge has contributed greatly to this research and my career in general.

The list of those who have helped me along the way in my academic pursuits is numerous. Academic support has been provided by: Dr. Leigh McCue, Dr. Andrew Bloxom, Dr. Andrew Wiggins, Dr. Larry Doctors, and Dr. Steve Zalek. Computing support has been provided by Mr. Steve Edwards, the staff at Virginia Tech's Advanced Research Computing Office, and the staff at the DoD-High Performance Computing Modernization Office. Management support at

NSWCPCD has been provided by Mr. Ivan Lugo, Mrs. Laura Thompson, Mr. Bob Teer, Mr. Dave Vickers, and Dr. Frank Crosby through the In-house Laboratory, Independent Research (ILIR) program.

Most importantly, I would like to acknowledge the support of my family and friends; especially my wife Page and children Brayton and Catherine. Your understanding and love remain steadfast, no matter the pursuit, and my motivation is often found in the desire to make you proud! To my parents Rob and Pat Cole, many thanks for offering a quiet back-bedroom and plenty of espresso to facilitate the work. To my sister Dr. Steph Jehl and her family: a little sibling rivalry is healthy, right?

Contents

List of Figures

List of Tables

List of Abbreviations

ACV – Air cushion vehicle

ALE – Arbitrary Lagrangian-Eulerian

ALT – Air Lubrication Technology

ARL – Army Research Laboratory

CEL – Coupled Eulerian Lagrangian

CFD – Computational fluid dynamics

CSM – Computational structural mechanics

EAG – Equivalent air gap

EF21 – Expeditionary Force 21

EOS – Equation of state

EVF – Eulerian volume fraction

FEM – Finite element method

FSI – Fluid-structure interaction

GCI – Grid convergence index

LCAC – Landing Craft Air Cushion

MCDP – Marine Corps Doctrinal publication

MCTF – Marine Corp Total Force

MR – Mooney-Rivlin

NACA – National Advisory Committee for Aeronautics

ONR – Office of Naval Research

OOA – Observed order of accuracy

PC – Probabilistic collocation

SES – Surface effect ship

T-Craft – Transformable craft

VOF – Volume of Fluid

V&V – Verification and Validation

WIG – Wing-In-Ground

Chapter 1

Introduction

The purpose of this research is to evaluate and apply commercial fluid-structure interaction computational tools toward the problem of air cushion vehicle (ACV) hydrodynamic seal resistance. An ACV seal is a flexible hull structure that interfaces with the supporting surface and captures a cushion of air beneath a marine surface craft. The seal environment is highly dynamic and difficult to characterize, with multiple scaling relationships in play. Thus, seal design at present remains an iterative, evolutionary process based upon subscale testing and simplistic theoretical models. This requires that designs are established early in a craft's development program at great expense, with minimal opportunity for modification concurrent to final craft design. With recent advancements in computational methods for fluid-structure interactions (FSI), the development and employ of seal design tools can supplement the traditional design approach and consequently be relevant at all stages of craft development.

While recent experimental research has focused on the problem of seal resistance (Wiggins, 2014, Doctors et al., 2014, Zalek and Doctors, 2010), concurrent computational approaches have utilized physical and algorithmic simplifications for both the fluid and structural models. For example, some researchers have studied interactions between the bow and stern seals with attention to effects on resistance, but at the expense of using rigid seals and/or linearized potential flow fluid models (Kramer, 2013). Others have explored the problem with idealized membrane seals using explicit

methods and loose coupling (Challa, 2015). Even smoothed particle hydrodynamic approaches have been explored (Yang, 2011, Gilbert, 2015). In the most detailed computational effort to date, where more accurate physical models for the seal, fluid, and interaction are employed, separate partitioned solvers were required at high complexity and computational cost (Bloxom, 2014). Thus, there remains much to learn regarding how seal materials are chosen, how their geometries can be beneficially arranged, and what scaling laws are suitable. This work seeks to take the next step in computational approaches to the problem of ACV seal resistance. It develops modeling approaches that accurately represent the physics of the seal-fluid interaction within a single integrated computational desktop, thus enabling more efficient predictions of resistance for these craft.

1.1 Research scope and objective

The primary contribution of this research is the verification and validation of a commercial multi-physics program for FSI problems with or without a free surface. A further contribution is the application of the tool toward the simulation of ACV seals, establishing its basis as a seal resistance exploratory tool. Thus, this work is a clear stepping stone for future researchers having interests in ACV seal design.

A secondary contribution of this work is the successes and failures of the two-way, loose coupling explicit approach implemented within Abaqus/Explicit for both fluid dynamic and FSI simulations. Techniques for achieving stable free surfaces for channel flow are developed, and methods are demonstrated for reducing the instability of the compressible flow equations at low sound speeds.

As it is generally understood that one-off research codes typically remain with the originating programmer or within a specialized research group, this avenue is deliberately avoided. Development of novel computational tools or algorithms is not the focus of this work. The goal is to validate a commercial tool and demonstrate its ability to handle both the fluid and structural domains in high fidelity within a common user interface.

The computational work is performed using both STAR-CCM+ (12.04.011 and 12.06.010) and Abaqus/Explicit (6.13). Following extensive evaluation, Abaqus is ultimately abandoned and STAR-CCM+ is used exclusively for both the structural and fluid computational domains. To verify and validate the approach, two model problems are thoroughly investigated using a tightly-coupled, partitioned approach for fluid-structure coupling. The first is an elastic beam FSI simulation based upon a benchmark problem proposed by Turek and Hron (2006). The second is a planer bow seal simulation using empirical and numerical results from Zalek and Doctors (2010) and Bloxom (2014).

As a means to explore the computational results, a dimensional analysis is used to develop scaling relationships between the seal resistance force and various governing parameters. It is these relationships that are valuable to future seal development efforts. Because of the large range and variety of design variables applicable to this problem, a comprehensive investigation by means of an empirical approach is prohibitive. Utilizing parameters identified in the dimensional analysis allows for an efficient investigation of the problem.

1.2 Organization

The organization of this work is as follows. *Introduction* (Chapter 1) provides the research scope, objectives, and motivation for the work. It briefly reviews the ACV mission, its principles of operation, and the applicability of modeling and simulation. A review of the most recent and relevant ACV seal studies follows, which establishes the foundational precedent for this work. *Dimensional analysis* (Chapter 2) identifies key physical variables that should be considered when exploring the problem of ACV seal resistance. A derivation of dimensionless parameters is provided, which serves to identify scaling interdependencies. *Computational approach* (Chapter 3) reviews the numerical physics models employed, including the finite element method, finite volume method, and fluid-structure interaction. A discussion of verification, validation, and uncertainty is provided. *Results* (Chapter 4) provides details of the verification and validation for both the elastic beam FSI simulations and planer bow seal simulations. Descriptions of the model development and computational parameters are provided for each, along with thorough discussions of the results. *Abaqus/Explicit* (Chapter 5) covers verification and validation of an explicit approach to large deformation fluid-structure interaction modeling. This section is included for completeness and may be read independently as a stand-alone portion of the work. *Conclusion* (Chapter 6) summarizes the research findings and offers suggestions for future work.

1.3 Motivation and background

In this section, motivation for the topic and its implications for amphibious naval operations in a larger context is provided. Following is an overview of ACV resistance, skirt systems, and skirt materials to acclimate the reader to this niche area of naval architecture.

1.3.1 The ACV mission

A principal mission area of the United States naval forces is the amphibious movement of equipment from the sea to the shore in support of the Marine Corp Total Force (MCTF). The operational and doctrinal foundations for conducting this mission can be found within Marine Corp Doctrinal Publication 1-0 (MCDP 1-0) (MCDP 2011), which establishes the concepts of Operational Maneuver from the Sea, Ship to Objective Maneuver, Seabasing, and Marine Corps Operating Concepts. In March 2014 the Commandant of the United States Marine Corp, General James E. Amos, released an aspirational vision for the MCTF entitled "Expeditionary Force 21" (EF21) (EF21, 2014) to build upon doctrinal foundations established within MCDP 1-0. EF21 establishes a roadmap for developing the future force and provides a concise "shopping list" for future-force capabilities for amphibious operations. From EF21, "Mindful of limitations on resources, we need to develop a viable combination of connectors, landing craft, amphibious vehicles, and boats, as well as the ships… that":

- *Are deployable, employable and sustainable given the power projection means available.*
- *In coordination with the Navy, employ low-signature landing craft and boats with increased range and speed, as well as the ability to penetrate an unimproved coastline.*
- *Provide the means to conduct surface maneuver from amphibious ships beyond 65 nm offshore.*
- *Provide the capability to maneuver through the complex terrain of the littorals.*
- *Provide maneuver options to extend operations within constraints of fuel resupply resources.*

From the above list, it is clear that future amphibious craft must identify and capitalize on technologies that increase agility, reduce fuel consumption, and enhance capability in adverse seas; all while maintaining fully amphibious operation. Self-deployment may be of benefit, but EF21 permits a degree of husbandry by a supporting force. "Complex terrain of the littorals" infers there

is a need for navigation through the sea-to-shore transition, including dangerous shoals, shallow reefs, or breaking waves.

"Maneuver" is a focus area identified within EF21 as key to conducting the MCTF mission in littoral environments. Achieving Maneuver capability requires operation in permissive, uncertain, or even hostile environments where forces may be at risk (EF21, 2014). Further, the proliferation of coastal defenses cruise missiles (CDCM) and increased sophistication of anti-access/area denial (A2/AD) systems has increased the standoff distance required for combatants and support forces. As a result, EF21 lays out considerations deemed important for future amphibious operations (EF21, 2014):

- *An integrated A2/AD threat with CDCMs necessitates standoff range greater than previously considered.*
- *The proliferation of CDCMs and sophisticated target acquisition and guidance systems requires standoff from beyond 65nm until the threat is mitigated.*
- *Once the CDCM threat is reduced, standoff can also be reduced. If a CDCM threat remains standoff can be reduced to a sea echelon area 30 nm to 50 nm to provide standoff from area denial threats, adequate CDCM acquisition, and protection by DDG/CGs. As mentioned above this is always a careful calculation of risk by the involved commanders.*
- *Once landing sites are controlled, amphibious ships may close to facilitate speed of build-up ashore. When a CDCM threat is completely neutralized, an amphibious ship can reduce the standoff distance when provided appropriate escorts to mitigate any residual risk. The discharge point for Amphibious Assault Vehicles and other surface connectors may be closer to shore, but generally will remain beyond 12 nm.*
- *Vehicles, boats, and landing craft require the endurance and speed to operate from 65 nm independently or in combination with other connectors.*

From the above, it is clear that ranges for initial debarkation will exceed 65 nm but may be reduced to between 30 nm to 50 nm as conditions warrant. They will generally not be less than 12 nm. For this reason, overall vehicle range and the ability to return for reconstitution and subsequent missions will be of prime importance in future force concepts.

A separate but related work conducted by the US Marine Corp. Amphibious Capabilities Working Group is titled "*Naval Amphibious Capability in the 21st Century*" (2012). Similar to EF21, this strategic plan "assesses the challenges and opportunities for amphibious operations within the context of 21st century naval and joint warfighting." Prime among these challenges are hybrid and non-state actors, A2/AD technology, large scale political instability, and increased complexities, among others. All point to increased maritime capabilities for improved maneuver in littoral regions and increased standoff distances.

The report also provides an assessment of both existing and conceptual surface connectors and how they may be used together in various war-game scenarios to land a complete Marine Expeditionary Brigade or the larger composite Marine Expeditionary Force. While the details of such simulations are not the focus of this work, the results demonstrated the unique role of each connector and the comparative advantages of each (Figure 1). Two conclusions that are especially compelling include availability of the Mobile Landing Platform (MLP) in future operations, and the use of self-deployable surface connectors capable of long-range open ocean transits (Report of the Amphibious Capabilities Working Group, 2012). Each of these reinforces the need for technologies that directly increase performance (speed, range, seakeeping) of the surface connector.

Figure 1. Current naval surface connectors (Naval Amph. Cap., 2012)

Historically, the key technologies and platform solutions that have enabled the above capabilities and fully amphibious operation have been employed via the ACV. And while certainly the technical community must pursue alternative platforms and means to meet all EF21 objectives, a current clear path to evolve the future force is through the continued development of ACV technologies via understanding of the underlying physics involved in their operation.

ACVs are a unique subset of advanced marine vehicles in the category of air cushion supported vessels. Others in this family include Surface Effect Ships (SES), Wing-In-Ground (WIG), and any hull utilizing Air Lubrication Technology (ALT) (Faltinsen, 2004, Mantle, 1980). While all rely on compressed air to reduce the hull wetted surface area and corresponding frictional drag component, only the SES and ACV craft are aerostatic and utilize flexible rubber seals to capture the compressed air while at low speeds or stationary. ALT concepts must rely on forward speed to achieve aerodynamic support during operation. Pressurized air for an SES/ACV is provided by one or more lift fans, which allows more diverse operational advantages when compared to other air support vessels (Palanikolau, 2001). The SES differs from the ACV in that individual flexible seals run athwartships between two catamaran hulls, whereas the ACV employs a seal around the entire perimeter of the hull. This peripheral "skirt" provides fully amphibious capability, but at

reduced stability and increased complexity and cost. Further, a fully amphibious craft typically must rely solely upon air propulsion and the designers must consider carefully the footprint and noise associated with such systems (Faltinson, 2005). Mantle's work expands upon the above and provides a thorough explanation of the differing features within the class of air cushion supported vessels (Mantle, 1980, Palanikolau, 2001).

Prominent ACVs employed by modern navies and commercial ventures include: Landing Craft Air Cushion (LCAC/LCAC 100 class) and C-7 (United States); Pelikan, Puma, Pomornik, and Sibir (Russia); Tiger 16, SAH 2000, G2000, 4000 TD, ABS M-10, and Dash 400 (UK); Turk IV MkI/II and LSF-2 (S. Korea); PH11 and Colibrie (Netherlands); T2000 (Finland). Noteworthy SESs developed by modern navies and commercial ventures include: SES-200A (United States); Westmarin 4000, UT904, Oksoy, and Skjold (Norway); Dong Yang and TSL-A70 (Japan); Smyge (Sweden); and Pacscat (UK). While not all encompassing, this list conveys the diverse employment of these craft, indicating a universal recognition of their utility for commercial, naval, and humanitarian assistance/disaster relief (HADR) missions. A more thorough historical review of ACV development can be found in work by Lavis (2011).

1.3.2 Air cushion vehicle drag

The sources of ACV resistance are similar to those of other high performance marine vehicles and include aerodynamic drag, momentum drag, wave-making drag, and wetting drag (Mantle, 1980). The summation of these comprises the total craft drag shown in Figure 2. Aerodynamic drag is the force resulting from relative velocity of air over the structure. Momentum drag is the force resulting from accelerating the air mass used to pressurize the cushion up to the relative craft velocity. Wave-making drag is the force required to displace the supporting surface beneath the

craft providing buoyancy. Wetting drag is the viscous forces resulting from contact between the supporting surface (typically water) and the flexible seal.

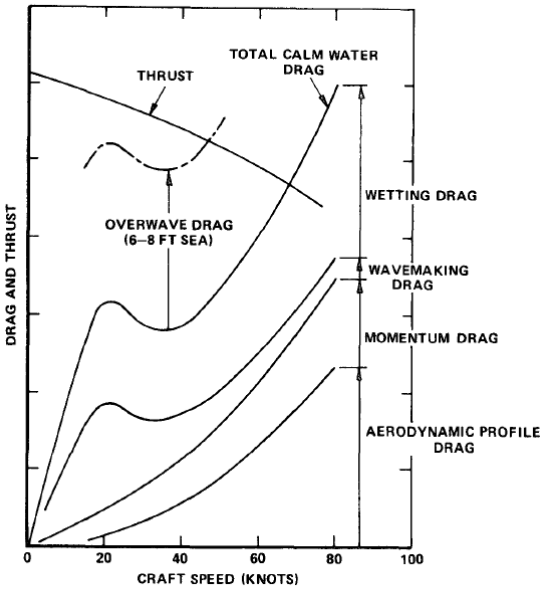

Figure 2. ACV drag contributions (Mantle, 1980)

The primary difference between ACVs and other high performance marine vehicles is the source of the drag contributions, and how the drag contributions vary as a function of speed. For an ACV, the wave-making drag decreases with speed as the dynamic lift of the cushion overcomes the displacement lift of the cushion. This is referred to as primary "hump" and is shown at approximately 20 kts in this example (Froude number, F_n ~= 0.4). At lower speeds, a secondary, larger "hump" also exists theoretically when the length of the wave generated by the bow seal approaches the craft length, causing impinging waves upon the stern seal. However, Doctors (1972) has shown sufficient craft acceleration prevents development of this drag spike. Although obvious, it is interesting to consider that a fully amphibious ACV generates no wave-making drag

when over land or ice. With sufficient air gap, its performance is limited only by the balance of thrust upon the aerodynamic and momentum resistances.

Momentum drag is another unique source of resistance. It is the cost of accelerating stagnant ambient air up to the craft velocity. For an ACV (and somewhat for an SES), it is much larger when compared to other turbine powered naval craft, as lift fans ingest significant quantities of air to develop a properly pressurized cushion.

Also different for an ACV, the wetting drag results from contact between the skirt and the supporting surface. Increased cushion flow can increase the equivalent air gap (EAG), which is the average clearance between the skirt and water. This reduces the wetting area, and thus the drag, but at the cost of both increased power consumption of the lift system and increased momentum drag. One can observe that optimizing ACV performance is a challenging balancing act of interdependent parameters.

Of all the drag contributors, wetting drag is the least understood. Since the skirt is a constantly deforming flexible structure with varying contact area, one cannot rely on traditional viscous scaling approaches using subscale tow tank data. For this reason, full scale data is typically used to correlate resistance coefficients obtained in subscale model testing. However, as wetting drag makes up a large portion of the total craft drag (Mantle, 1980, Doctors and McKesson, 2006), it also represents a large opportunity for optimization.

1.3.3 ACV skirt systems

The use of air lubrication and support for various craft can be traced to work as early as 1716 (Lavis, 2011) with key advancements in flexible seals in 1908 by Porter, 1922 by Breguet, and

1942 by Cristadoro. Finally in the mid-1950s, this technology became economically viable with utilization of the peripheral jet based on work by Cockerell and development of the SR.N1 (Yun and Bliault, 2000). Subsequent improvements to air distribution and containment via the skirt configuration have been made, culminating in the modern bag-and-finger skirt system (Figure 3).

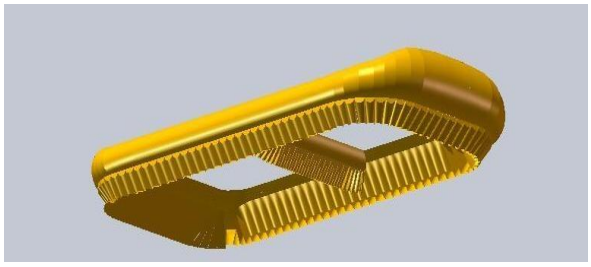

Figure 3. Bag and finger skirt system (Cole, 2010)

Moving forward it is important to make the distinction between the SES and ACV as their seal systems are concerned. While it has evolved over time, the state of the practice for ACV seal design is to employ individual "fingers" around the perimeter of the peripheral bag in order to conform to the supporting surface and minimize leakage of the cushion (Yun and Bliault, 2000). This is especially useful for ACVs overland and in the littorals. Figure 4 shows the flow path within an ACV skirt. Pressurized air from within the hull enters the periphery bag and distributes to the fingers through advantageously arranged feed holes. Air exiting the finger maintains the supporting cushion and escapes through the developed air gap.

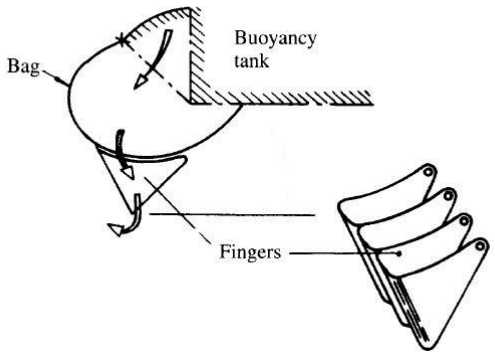

Figure 4. Bag and finger skirt flow path (Yun and Bliault, 2000)

An SES on the other hand, does not need this overland capability and functions without a peripheral bag. The seal can attach directly to the wet deck between the side hulls. For this reason, a designer can consider either individual fingers or a single planer seal along the bow, depending on craft size and environmental suitability. Modern large SES concepts such as the Norwegian Skjold class have specified finger seals to maintain conformity to varying incoming flow (Figure 5). Similarly, the T-Craft concept (Figure 6) uses a combination of fixed and deployable bag and finger seals to enable the various operational modes and fully amphibious capability.

Figure 5. Skjold class SES (Torgeir Haugaard/FRM)

Figure 6. Textron T-Craft concept (Skolnick and Wilson, 2011)

1.3.4 ACV skirt materials and elasticity

A material's modulus of elasticity is a critical characteristic that defines how deformation is related to stress. A linear elastic material exhibits a modulus that can be approximated by a linear relationship between stress and strain, whereas a nonlinear elastic material exhibits a modulus that varies with the strain or strain rate. In the literature, the modulus of elasticity is referred to equally as elastic modulus, tensile modulus, or Young's modulus.

ACV seals are typically fabricated using layers of natural or synthetic rubber vulcanized over a synthetic base cloth (Yun and Bliault, 2000, Wiggins, 2014). The rubber is typically a natural blend, neoprene, or nitrile (NBR or buna-n). It provides the environmental abrasion and tearing resistance and is a primary factor in the component's fatigue life. The base cloth typically consists of a bi-directional weave using nylon, polyester, or other synthetic fiber. It provides the primary tensile strain resistance. Wiggins (2014) found that due to the relatively high base cloth strength, seals can generally be considered inextensible and the effective tensile response is dominated by properties of the reinforcement. Further, he showed the bending rigidity of the fabric is dominated by the elastic modulus of the coating. As the material behavior of the rubber coating and base

cloth differ widely, their combination creates a unique composite structure that must be modeled accurately. As such, simplified approaches to seal design which have considered the structure as simply an inflated membrane without flexural rigidity may not be appropriate. Because of their composite construction, the material's rigidity is important for establishing stability in the absence of secondary, transverse inflation stresses.

The base cloth is linear elastic under tension and provides little flexural stiffness in the application range (Wiggins, 2014). It is generally anisotropic and may exhibit vastly different properties depending on the load orientation as a result of the weave and calendaring processes. For a typical industry plain weave, the "warp" direction fibers are stationary and pre-tensioned, while the "weft" ("fill" in North America) is drawn across using an over-under pattern. The weft fibers are not drawn as tight and typically do not lay as flat as the warp fibers, and thus the weft stiffness is generally lower than the warp.

The rubber coating however, is nonlinear elastic in nature and considered isotropic and incompressible. Due to its nonlinear stress response, it is typically characterized using a battery of laboratory tests relating its stress state to its strain energy potential. With these results, a hyperelastic material model can be fit to describe the modulus response. Numerous forms of strain energy potential models have been developed for nonlinear elastic materials and the accuracy of each varies according to the material data available and the strain regime of interest (Brieu, 2007, Dassault Systemes, 2013).

1.3.6 Modeling and simulation

Modeling and simulation (M&S) is the numerical characterization and investigation of a physical system or process to provide a basis for technical or strategic decisions. M&S "reduces the time,

resources, and risks of the acquisition process and increases the quality of the systems being acquired" (DoD 5000.1). Validated simulations are often useful to identify uncertainty, mitigate risk, and have been shown to decrease overall program costs if employed early in the design phase (Hillegas et al., 2001).

While it is always the goal of a naval designer to increase performance capability for equivalent cost, it is made evident within the context of EF21 that the attributes of speed, performance, endurance, etc., will be especially important factors within the designer's trade-space for future surface connectors. Further, the ability to predict these factors with sufficient accuracy within given time constraints will add dimensionality to the trade-space for future design programs. Through the advancement and validation of design tools, no longer will reliance on expensive and time-consuming experimentation dictate the pace of a design's evolution. Further, designers will also no longer be slave to the state-of-practice but may be empowered to develop state-of-the-art solutions simultaneous to final design.

With this vision, an advanced naval vehicle M&S development program was initiated by the Office of Naval Research (ONR) in 2006 as a means to engage the academic community in this pursuit. Part of the larger Transformable Craft (T-Craft) Innovative Naval Prototype program, the T-Craft Tools program awarded research grants to build the M&S knowledgebase in support of T-Craft prototype designs. The T-Craft itself was envisioned as self-deployable ocean-going SES with capability for shallow water and potentially fully-amphibious operations through the use of deployable side seals. It would provide lift capacities 4 to 6 times higher than existing surface connectors; all while offering good sea keeping and efficient operation (Skolnick and Wilson, 2011). With numerous unique and ambitious design attributes, T-Craft was a prime candidate for

research efforts across a broad range of marine disciplines, including: composite construction, fluid-structure interaction, resistance and performance prediction for multi-hull ships, littoral hydrodynamics such as shallow water wave effects, surface piercing propellers, hull form analysis/optimization, flexible seal design, waterjet design and analysis, control and optimization of motions, etc. (T-Craft Tool Development, 2012).

Generally, employed seal systems for ACVs are design evolutions based upon scaled model testing and empirical data. To alter this paradigm, several M&S efforts funded through the T-Craft Tools program focused on the prediction of drag for flexible seals. Specifically, Yang (2011) and Bloxom (2014) focused on numerical simulations of the fluid-structure interaction between the bow seal and oncoming flow. Wiggins (2014) and Zalek and Doctors (2010) undertook a large scale experimental approach to develop a SES/ACV bow seal post-buckling model and dataset useful for numerical validation. Doctors (2012) and Doctors et al. (2014) presented theoretical seal models and compared a total hydrodynamic resistance model to various experimental results. These efforts and other related work are reviewed in more detail below.

1.4 Review of prior work

In this section, recent applicable experimental and numerical studies of SES/ACV seal drag and fluid-structure interaction (FSI) are reviewed. The experimental work provides foundational datasets useful for numerical validation, while the numerical approaches are vastly different and reveal various strengths, weakness, and opportunities for future modeling efforts.

1.4.1 Hydroelastic response of surface effect ship bow seal

Funded as part of the T-Craft Tools program, Wiggins (2014) and Zalek and Doctors (2010) undertook a large scale experimental approach to develop a SES/ACV bow seal post-buckling model and dataset useful for numerical validation. Test platforms were developed and tested first at the University of Michigan and following at the William B. Morgan Large Cavitation Channel (LCC). A planer bow seal and two different five-finger bow seals were instrumented to capture resistance and deflection data at various inflation pressures and immersions. As part of the LCC effort, Doctors (2012) and Doctors et al. (2014) developed theoretical seal resistance models (flat, parabolic, cubic) for comparison with the experimental results. One set of comparisons is shown in Figure 7. Good agreement between the cubic seal theory is achieved at low Froude numbers, but not at higher ones. This indicates important physics at higher speeds may not be properly captured in the theoretical model. Further, the large deviations at the highest Froude number reveals the difficulty in experimentally collecting meaningful data at some conditions.

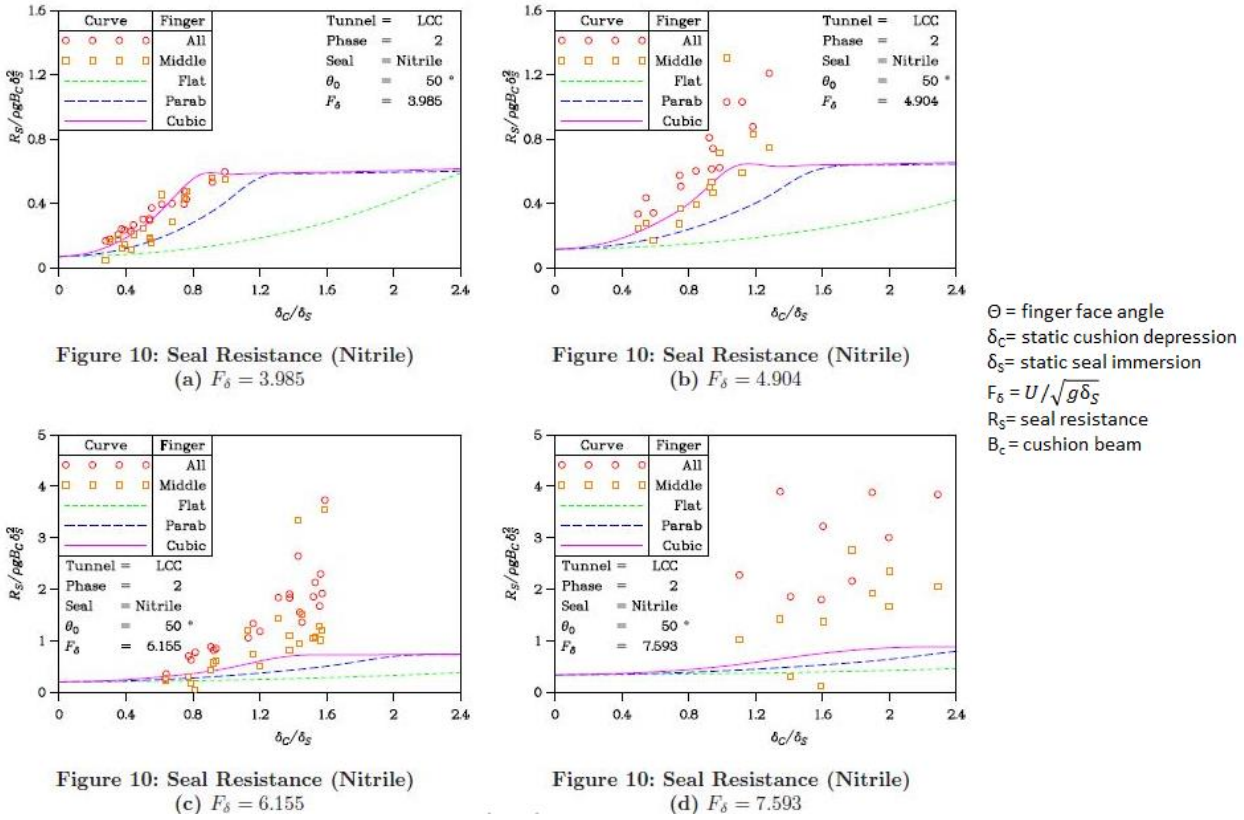

Figure 7. Resistance versus seal immersion ratio (Doctors et al., 2014)

A complimentary part of the testing effort was to conduct a formal scaling study in order to extrapolate the results for larger bow seals such as the one posed for T-Craft. Wiggins (2014) found significant difficulty in capturing the relevant physics, primarily due to cushion compliance and seal construction techniques. For instance, if the subscale seal is properly scaled for mass, it would be unrealistically fragile for the testing environment. Yet, a sufficiently robust seal led to a bending stiffness that exceeded the scaled stiffness by an order of the scale ratio, λ. Some realistic combinations of seal parameters simply cannot be practically achieved at subscale. More discussion on the difficulty of seal scaling is provided below in the *Dimensional analysis* section.

1.4.2 Smoothed particle simulations of the FSI surface effect ship bow seal

As part of the T-Craft tool program, Yang (2011) focused on numerical simulations of a similar problem and was thus able to utilize recent the experimental work of Zalek and Doctors (2010) for validation. Yang loosely-coupled novel Smoothed Particle Hydrodynamics (SPH) and FEM codes and used them to model a two-dimensional deformable seal interacting with a free stream flow and free surface. The fluids were simulated using SPH, whereas large-deformation FEM was used for the seal. SPH is a meshless Lagrangian fluid simulation method where the state of the system is represented by a set of particles. The particles carry all of the computational information and move according to the governing conservation equations. The power of the SPH method is that it does not require mesh connectivity between the particles and is thus naturally adaptive, bridging the gap between continuum and discrete particle approaches (Liu and Liu, 2003, Monaghan, 2005). It is therefore well-suited for large deformation problems that would pose difficulty for grid-based approaches. Further, by representing a continuum as a set of individual particles, multiple fluid types such as air and water can easily be introduced into the computational domain (Monaghan, 2005).

For simulation of the air cushion using SPH, Yang used both a specified pressure approach, where a prescribed cushion pressure is applied directly to the seal, and an air-particle approach, where both air and water are simulated simultaneously (Figure 8). In general, the results for both approaches were good at low speeds but deviated largely from Zalek's results (2010) at higher speeds. Yang suggests the specified pressure approach is better suited when only the bow seal is of interest, acknowledging the wave profile within the cushion would not be correct. He suggests

use of the air-particle approach for full configuration ACV simulations where trim and seal leakage is a concern.

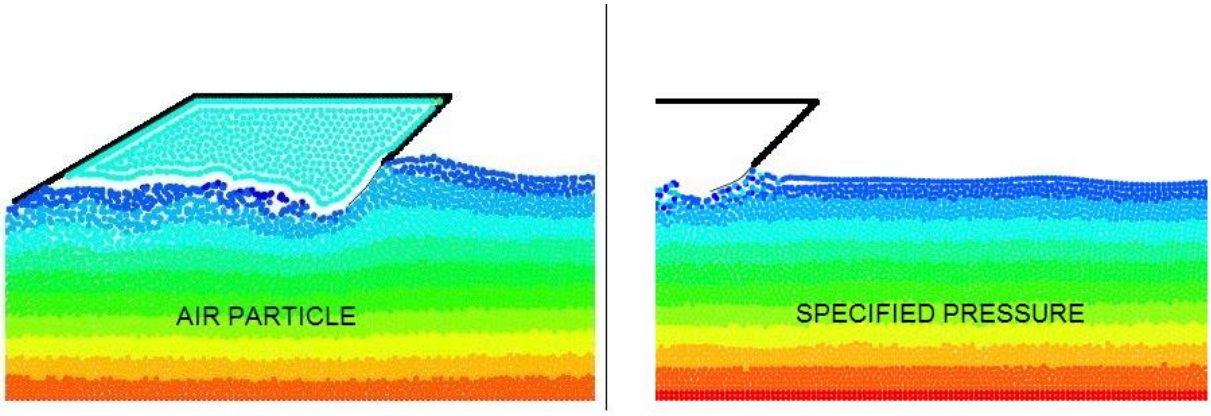

Figure 8. Air particle model versus specified pressure model (Yang, 2011)

Without further development, the immediate results of this work have limited applicability to real ACV seal systems due to the obvious simplifications of the seal and domain. Computationally, the biggest drawbacks to the approach taken by Yang were the novel aspects of the SPH and FEM code. Suggested future work is the use of more computationally efficient (possibly commercial) software. Additional drawbacks were those inherent to the SPH method itself, such as the particle approximations to the governing conservation equations (Liu and Liu, 2003). Also, as the spatial derivatives of the physical quantities are obtained using gradients of a smoothing function applied over the "smoothing length," *h*, the form of the smoothing kernel and values for *h* are tuned to fit specific problems.

Another common issue in SPH approaches is boundary treatments. As particles move near a domain boundary, inaccuracies can result if the smoothing length exceeds the proximity to the boundary. While a number of techniques have been proposed to solve this issue (Liu and Liu, 2003, Monaghan, 2005, Colagrossi and Landrini, 2003, Dalrymple and Knio, 2001), these "edge

effects" remain and introduce error. Boundary effects also occur at contact surfaces internal to the domain and remain a current research focus (Gilbert, 2015). As a consequence of the above, rigorous verification and validation for SPH solutions is difficult and the current state of SPH technology for free surface problems remains immature (Kiara, 2010), especially as offered within commercial code.

As a natural continuation of Yang's work, Gilbert (2015) also looked at the planer bow seal problem but extended it to three dimensions (Figure 9). A novel SPH code and an open-source FEM code (Code Aster) provided a partitioned, coupled approach to solving the FSI problem. Based on the recommendations of Yang, Gilbert also chose the specified pressure approach to model the cushion for simplicity. A primary contribution of this work was the use of a Graphics Processing Unit (GPU) to speed the solution of the fluid domain. Although his results were three-dimensional, this effort only considered short term dynamics of a planer seal and did not converge the simulation into a steady state condition where resistance could be obtained.

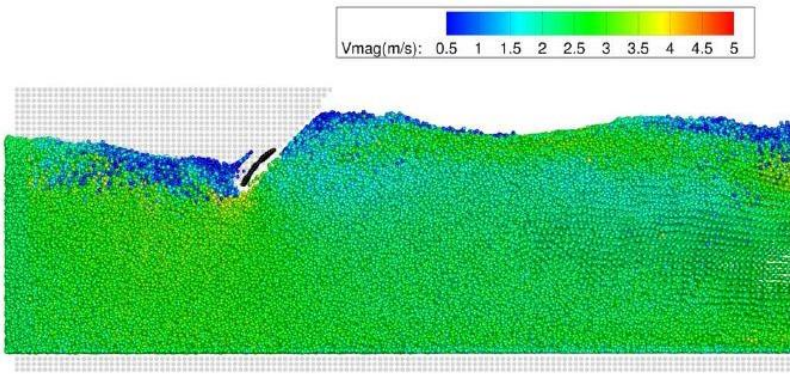

Figure 9. Smoothed particle hydrodynamics bow seal model (Gilbert, 2015)

1.4.3 Numerical simulation of a planer surface effect ship bow seal

Also part of the T-Craft tool program, Bloxom (2014) undertook a more conventional continuum mechanics approach to solve the planer bow seal FSI problem. Using a strongly coupled, partitioned algorithm, the commercial software STAR CCM+ solved the fluid domain and the commercial software Abaqus solved the structural domain. Both codes utilized implicit mesh-based approaches. While continuum mesh-based approaches are more established and generally more accurate than meshless approaches for hydrodynamics problems (Liu and Liu, 2003), they require special techniques to accommodate large structural deformation. The implicit nature means the separate governing equations for the fluid and structural components must be solved simultaneously in order to advance temporally. Because of this, sufficiently refined implicit models come with very large computational costs.

Bloxom developed a more accurate representation of the planer bow seal model by conducting additional seal material studies and including more craft details. The cushion was enveloped by a rigid body wet deck and side hulls (Figure 10) and the pressure was maintained using a momentum source term and lift fan model. With a combination of mesh motion, re-meshing, and restarting, Bloxom achieved good qualitative comparisons to Zalek's and Doctors' work (2010). He measured the displacement of the 3D planer seal along the centerline and found that 20 s of simulated time was required to acquire a steady planer shape. Resistance and deformation analyses were conducted using an average of the final 5 s of the simulation.

Due to the large run times and extreme deformation of the seal, a macro script was required to automate the repetitive processes of re-meshing and re-starting. This is one of the major drawbacks of a mesh-based approach to large deformation problems; the mesh must follow the control volume

for both the fluid and structure. When deformation of the mesh reaches a distortion limit, the simulation must halt and the domain must be re-meshed to resume. Toward the end of Bloxom's research effort, he was able to incorporate STAR-CCM+'s mesh morphing algorithm to eliminate the need for re-meshing. This advancement is critical to efficient implicit solutions and will be discussed further below.

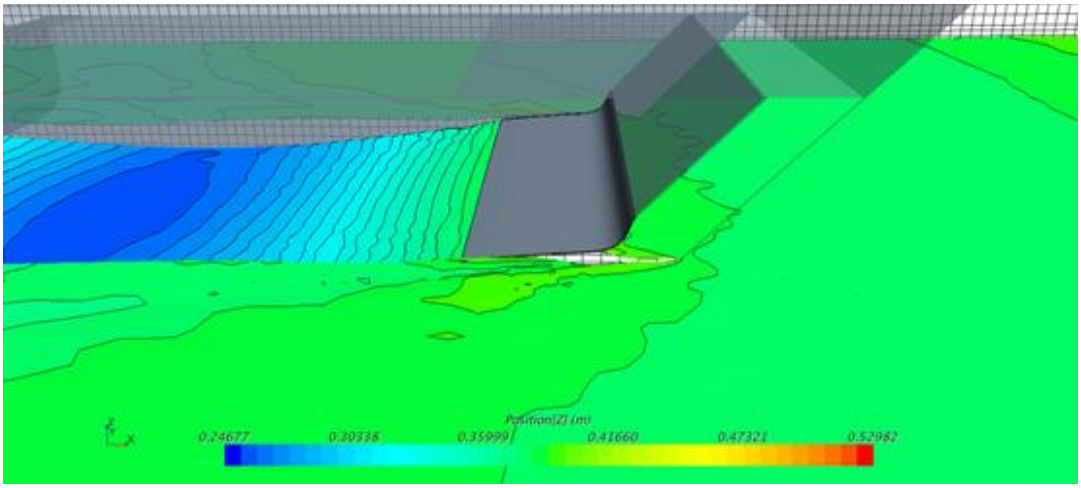

Figure 10. Planer seal simulation (Bloxom, 2014)

1.4.4 Simulation of a surface effect ship bow seal finger using ALE approach

Recognizing the difficulty of large deformation FSI simulations, Challa (2015) used an Arbitrary Lagrangian-Eulerian (ALE) technique offered by the explicit code LS-Dyna to (1) simulate a full SES model with rigid seals and (2) simulate a single flexible bow finger seal in a free surface. An experimental data set obtained from a 1/30th scale free-running SES model was used for validation. The scale model utilized a single bow finger constructed from nylon fabric as the forward seal. Based on observation of the seal underway, Challa concluded that motions of the finger were largely isolated to the finger face and a suitable numerical model could be constructed by fixing the finger face edges from motion. Further, he assumed stress through the material thickness was

negligible and the ratio of material thickness to curvature was small. This enabled the use of membrane elements for the seal which dramatically simplified the FSI interaction. The result was a loosely coupled one-way interaction.

With these assumptions, fingertip displacements provided by the numerical model appeared to compare well to observations of the free-running scale model. However, as the free running model's seal did not accurately represent the material properties of a full-scale SES seal, it is unclear if the membrane assumption and boundary conditions applied in the work could apply to a full-scale craft. Further, the computational domain used for the simulation (Figure 11) did not model inflation pressure upon the fluid free surface within the cushion. Pressure was explicitly prescribed as a constant follower load normal to the finger surface, and the simulation did not include hydrostatic back pressure at the exit boundary. Instead, only a rigid aft seal was placed in the flow to provide some resistance on the fluid exiting the cushion volume. An initial "water set-down" was achieved by specifying a pre-defined field within the fluid domain. With the specified inlet velocity of 0.7 m/s and depth of 1.5 m/s, the depth-based Froude number (F_δ) of 0.18 is subcritical. This indicates that downstream disturbances (and their inaccuracies) will propagate upstream. The simulation also had difficulty maintaining the hydrostatic backpressure aft of the stern seal. While the work is a good first approach to explicitly modeling the complex interactions of a cushion supported craft, there are opportunities for improvements in future work.

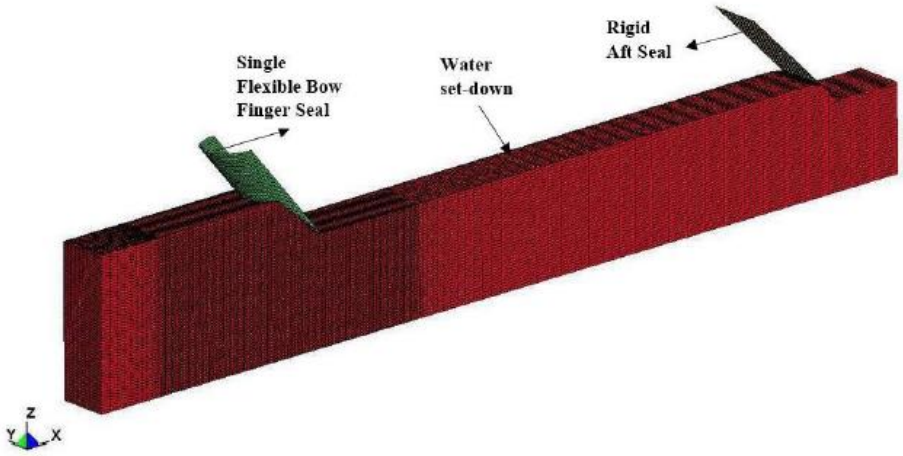

Figure 11. Bow finger simulation (Challa, 2015)

In summation, the achievements of these researchers point toward implicit, mesh-based methods as having the most potential for solving the complex FSI problem for ACV seals. Also, it is believed an explicit mesh-based approach may also find success if further attention is paid to the boundary conditions and material models.

Chapter 2

Dimensional analysis

Dimensional analysis is a powerful technique used to identify relationships between various parameters within a physical phenomenon that are unknown a priori. It is based on the assumption that governing equations are dimensionally homogenous and are inter-related by fundamental quantities of mechanics. Its power lies in the fact that the relationships can be revealed with only a partial understanding of the problem. The correctness of the analysis is based upon the initial choice of independent physical variables, requiring only a qualitative insight. Examples of dimensional analyses for various hydrodynamic problems are provided by Birkhoff (1955), Newman (1977) and Comstock (1983).

The numerous parameters that affect seal drag make an exhaustive computational or experimental investigation very difficult, if not impossible. For this reason, a dimensional analysis can be used to decrease the scope of the investigation and provide guidance for the final form of the governing physical relationships.

2.1 Key physical parameters

Based upon the above prior work, first-hand observation, and previous seal scaling studies conducted by others (Wiggins, 2014, Malakhoff and Davis, 1980), the following physical parameters are believed to affect seal resistance, R_S:

- Seal width, w (m). Much like the beam of a ship, the width of the inflated seals affects the area exposed to the flow, and thus contributes to the form drag.
- Seal height, h (m). The height of the seal is defined as the minimum distance from the mounting rail to the tip. In operation, the deflection of the overall seal is the result of a moment balance between the inflation forces and the resistance forces. At high cushion pressures, deflection of the seal structure above the free surface should be small, especially for low immersion depths. However, at low cushion pressures and relatively large immersion depths, a tall seal may deflect and alter the face angle seen by the flow. Changes in face angle result in changes in the profile which will alter form drag.
- Seal face angle, θ (radians). Much like a cylinder in flow, changes in the face angle changes the shape of the profile seen by the flow, which will alter form drag.
- Static immersion depth, δ_s (m). As the seal is lowered into the free surface, the area exposed to the flow is increased, resulting in a resistance increase.
- Cushion pressure, p_c (N/m^2). If the inflation pressure within the cushion is increased, the forces upon the inside of the seal opposing the flow are increased. The seal shape is more easily maintained and less likely to deform.
- Seal material flexural rigidity, D_f (N-m^2/m). Recall the seal is essentially an inflated cylinder without secondary stress transverse to the primary hoop stresses. The rigidity of the material helps to maintain the shape of the inflated structure in the absence of these secondary stresses. If the rigidity of the fabric is increased, the seal is less likely to deform, similar to increases in cushion pressure. Wiggins (2014) rationalized the rigidity of seal material to be a function of both the coating modulus E_C and total thickness t as $D_f \sim E_C t^3$.

Therefore, variations in those parameters are accounted for in the rigidity and thus are not explicitly listed as independent physical variables. (Note on the units: Flexural rigidity is typically expressed in units of Pa-m^4. However, for fabric it is defined on a per unit-length basis (1/m), and thus becomes Pa-m^4/m = N-m^4/m^2/m = Nm.

- Fluid velocity, U (m/s). From Newton's second law, the drag forces on a seal in a fluid result from the change in momentum of the fluid over time. Therefore, altering the fluid relative velocity will affect the change in momentum, and thus the drag.
- Fluid dynamic viscosity, μ (N-s/m^2). Shear stresses develop within a viscous flow when velocity gradients are present. It is this shear stress that changes the momentum of the flow. In a Newtonian fluid (such as water) the fluid viscosity is a proportional constant relating the velocity gradient to the shear stress. Therefore, changing the viscosity will affect the stresses and the resulting momentum change within the fluid.
- Fluid density, ρ (kg/m^3). Because fluid momentum is equal to the mass of the fluid times the velocity of the fluid, changes in the fluid density (mass per volume) will alter momentum.
- Acceleration due to gravity, g (m/s^2). The Earth's gravity field results in a body force acting upon both the fluid and seal. While it is not likely to be used as a variable for an earth-based system, as is the density and viscosity, it could prove useful in non-dimensional forms.

2.2 Dimensionless group derivation

We can then write a symbolic governing equation for seal resistance as Eq. 1. If we assume a proportional relationship in the form of a power law, we arrive at Eq. 2, where *a*, *b*, *c*, *d*, *e*, *f*, *h*, *k*, and *n* are unknown constants.

$$R_s = f\left(w, h, \theta, \delta_s, p_c, D_f, U, \mu, \rho, g\right) \tag{1}$$

$$R_s \propto w^a \cdot h^q \cdot \theta^b \cdot {\delta_s}^c \cdot {p_c}^d \cdot {D_f}^e \cdot U^f \cdot \mu^h \cdot \rho^k \cdot g^n \tag{2}$$

The chosen system of basic units for fundamental mechanics is mass, length, and time (*M*, *L*, *T*). Each independent variable is a derived quantity and can be formulated by a combination of the basic units. For example, as the units of the resistance force is N (kg-m/s^2), N would be replaced with *ML/T*^{2}. Also, as the face angle in radians is unit-less, it does not require decomposition into fundamental units. Replacing the derived quantities with basic units results in Eq. 3.

$$MLT^{-2} = (L)^a(L)^q(\theta)^b\ (L)^c\ (ML^{-1}T^{-2})^d\ (ML^2T^{-2})^e(LT^{-1})^f(ML^{-1}T^{-1})^h(ML^{-3})^k(LT^{-2})^n \tag{3}$$

Equating the exponents gives:

$$1 = d + e + h + k \ \rightarrow\ k = 1 - d - e - h$$

$$1 = a + q + c - d + 2e + f - h - 3k + n \ \rightarrow\ a = 1 - c + d - 2e - f + h + 3k - n - q$$

$$-2 = -2d - 2e - f - h - 2n \ \rightarrow\ f = 2 - 2n - h - 2e - 2d$$

Next, we combine *k* and *f* into *a* to obtain the following exponential relationships. They are substituted into Eq. 2 to arrive at Eq. 4. Rearranging and grouping each independent variable by their exponents provides non-dimensional expressions proportional to seal resistance in Eq. 5.

$$k = 1 - d - e - h$$

$$a = 2 - c - 3e + n - h - q$$

$$f = 2 - 2n - h - 2e - 2d$$

$$R_s = w^{2-c-3e+n-h-q} \cdot h^q \cdot \theta^b \cdot {\delta_s}^c \cdot {p_c}^d \cdot {D_f}^e \cdot U^{2-2n-h-2e-2d} \cdot \mu^h \cdot \rho^{1-d-e-h} \cdot g^n \quad (4)$$

$$R_s \propto \rho w^2 U^2 f\left[\left(\frac{h}{w}\right)^q (\theta)^b \left(\frac{\delta_s}{w}\right)^c \left(\frac{p_c}{\rho U^2}\right)^d \left(\frac{D_f}{\rho w^3 U^2}\right)^e \left(\frac{\mu}{w\rho U}\right)^h \left(\frac{wg}{U^2}\right)^n\right] \quad (5)$$

Although the unspecified exponents remain unknown and the form of the function *f* must be found empirically, the usefulness in this result is that if the non-dimensional ratios remain equal for differently sized, but geometrically similar seals, the value for the non-dimensional resistance (Eq. 6) should be the same. Observe this form is, in essence, an Euler number.

$$R_s/_{\rho w^2 U^2} \propto f\left[\frac{h}{w}, \theta, \frac{\delta_s}{w}, \frac{p_c}{\rho U^2}, \frac{D_f}{\rho w^3 U^2}, \frac{\mu}{w\rho U}, \frac{wg}{U^2}\right] \quad (6)$$

Examination of the non-dimensional ratios given by the analysis reveals several well-known groups, where *w* is the characteristic length.

Reynolds number: $Re = \frac{w\rho U}{\mu}$ It represents the ratio of inertial force to viscous force.

Froude number: $Fr^2 = \frac{U^2}{wg}$ It represents the ratio of inertial force to gravity force.

Euler number: $Eu = \frac{p_c}{\rho U^2}$ It represents the ratio of pressure force to inertial force.

The remaining groups are unique to the problem of seal resistance and originate from the choice of independent variables. It should be reiterated that due to restrictions of subscale testing, it is difficult to simultaneously achieve correct force ratios for all of the groups. Maintaining the

correct Froude number will lead to an inaccurate Reynolds number, and vice versa. Achieving dynamic similitude for subscale tests has always been difficult, but is even more so for ACV seals due to the multitude of physical interactions that must be accounted for, such as lift flow rate, cushion pressure, seal stiffness, etc. (Lavis, 1974).

Wiggins (2014) showed that scaling seal dynamics is especially problematic due to compliance of the air cushion and inertial forces of the seal. For instance, in order to maintain inertial similarity, the mass of a model seal must scale according to the length ratio as $m_F = m_M\lambda$, where λ is the scaling factor. In order to maintain bending similarity, the fabric rigidity must also be scaled using $D_{fF} = D_{fM}\lambda^4$, requiring significant reduction in the elastic modulus of the coating so that the non-dimensional rigidities are equal. Unfortunately, currently available fabrics cannot meet both mass and rigidity reduction requirements (Yun and Bliault, 2000) and subscale skirt models are typically overly stiff. Personal experience has shown that simply pre-washing the model fabric makes a noticeable reduction (improvement) in the rigidity, but not enough. Thus, favoritism must be shown toward the phenomena of interest. For the steady problem, the correct scaling of the fabric mass is not as important as the correct scaling of fabric rigidity.

Previous work by Doctors et al. (2014) arrived at different forms of the non-dimensional groups. For instance, as cushion pressure can be written as $p_c = \rho g \delta_c$, where δ_c is the static depression of the free surface due to cushion pressure, we can consider δ_c as an independent parameter in lieu of p_c. Additionally, if the characteristic length is chosen as the seal static immersion δ_s instead of width *w*, then the groups identified by the dimensional analysis will be those of Eq. 7.

$$\left.R_f\right/_{\rho {\delta_s}^2 U^2} \propto f\left[\frac{h}{\delta_s}, \theta, \frac{w}{\delta_s}, \frac{\delta_c}{\delta_s}, \frac{D_f}{\rho {\delta_s}^3 U^2}, \frac{\mu}{\rho \delta_s U}, \frac{g\delta_s}{U^2}\right] \tag{7}$$

Pending sufficient manipulation of fluid density, fluid viscosity, and even gravity, the experimentalist will always need to consider scaling distortions in model test results. In large-scale SES programs of the past, such as T-Craft, significant questions regarding suitability and resistance penalties of bow seals have been raised by the designers, and rightfully so. The scaled models of such craft are typically 1/18 or worse. This leads to severe distortion of the scaled results and extrapolations to such a scale are not made with complete confidence. Even large-scale experiments have not been able to do better than 1/6 scale. For example, the proposed T-Craft bow seal height was 6 m, whereas the "large scale" LCC test seal height was only 1 m. Conversely, a numerical model is not restricted to physical limitations and is free to explore the exact geometry of interest. For this reason, it is proposed that a numerical model is best suited to explore scaling relationships and the sources of ACV seal resistance.

Chapter 3

Computational approach

This section describes the computational approach for conducting a numerical simulation of flexible ACV seals in a free surface flow. With the advancement of computational toolsets that can be applied to FSI problems and the recent success of the related work mentioned above, it is logical to investigate seal resistance in this manner. Observing lessons learned and previous successes by other researchers (Bloxom, 2014, Yang, 2011), a documented and prevalent commercial tool is pursued here rather than devoting resources to write a novel and potentially computationally inefficient research code.

Due to the extreme nonlinearities and structural deformation anticipated, a dynamic explicit approach for solving the problem was initially pursued. The computational costs for solving nonlinear, large deformation problems implicitly are burdensome, as confirmed by Farhat et al. (2010) and Bloxom (2014) above. Based upon an industry survey and relevant literature review, Dassault Systemes's finite element software program Abaqus/Explicit was initially chosen as the exclusive toolset. Following numerous verification and validation efforts, Abaqus/Explicit's Coupled Eulerian Lagrangian (CEL) approach was used to facilitate a loosely-coupled, partitioned fluid-structure interaction between the seal and the fluid. Unfortunately, it was soon revealed the simulations produced a pressure field rife with noise, resulting in large variations of force acting on the seal. Significant numerical manipulations, including smoothing and filtering of the force

data could not provide the quality needed for a sensitive parametric resistance study. After significant work, it became evident that adequately resolved resistance data would not be obtainable due to the absence of low-Mach preconditioning upon the fluid equations and the loose coupling FSI method employed. Thus, Abaqus was abandoned. However, the author does not totally discount this approach for other large displacement FSI problems; especially for compressible cases over small timescales, or at low speeds where gravity dominates the fluid behavior. A further discussion of the research approach and results using Abaqus/Explicit CEL is set aside solely in Chapter 5.

Having recognized an implicit, tightly coupled FSI approach would be needed to study seal resistance, the decision was made to return to STAR-CCM+ as previously used by Bloxom (2014). As there is great appeal in handling both the fluid and structure in the same computational space, STAR-CCM+ was initially discounted for this effort due to the cost and complexity of co-simulating a separate solver for the structure. However, in mid-2015, STAR-CCM+ made available a linear elastic FEM structural solver capable of nonlinear geometry deformation. With this software advancement, a partitioned FSI simulation could now be conducted all within STAR-CCM+. This is a significant advantage, especially in a production type environment, where limited resources are available to develop the coupling algorithm. Additionally, only a single program and associated license is required. The following section includes a review of computational mechanics as it pertains to this work, fluid-structure interaction, and verification, validation, and uncertainty quantification methods.

3.1 Finite element method

As a subset of computational structural mechanics, the Finite Element Method (FEM) is a numerical technique for solving boundary and initial value problems based upon an assembly of idealized discrete elements. Its use for structural problems is founded in matrix methods and primarily aims to solve the displacements and stresses resulting from imposed boundary conditions such as loading, temperature, or other constraints. Its application is common across a broad range of industries and is suitable for simulation of numerous physical phenomena (Pzremieniecki, 1985).

In FEM, a structure's physical geometry is represented by arranging a number of discrete finite elements. The elements are connected by shared nodes located at each corner. Together, the elements form the "mesh", which can vary in density by increasing or decreasing the number of elements. Boundary conditions are applied to the applicable nodes, and equilibrium equations can be written for each node in the system. The nodal displacements can then be computed to provide stresses and strains for each finite element.

A simple example is provided below to illustrate two vastly different techniques for solving a FEM problem. Take the bar of length "*L*" under tension "*P*" in Figure 12. It is modeled using three elements of equal length; node 1 is located at the wall attachment and node 4 is located at the tip. Assuming small deformation and linear elastic material gives Eq. 8 and Eq. 9, where ε_j is the strain in the element, u^i are displacements of each node, E is the elastic modulus, i is the node number, j is the element designator, and σ is the stress in the bar. The stress is equal to the internal load I_j applied over area A, which results in Eq. 10.

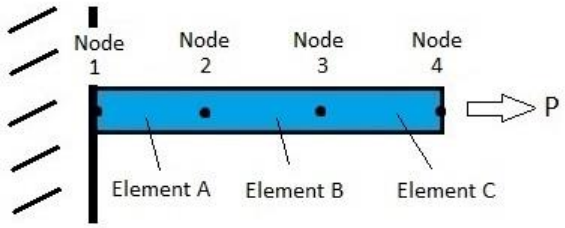

Figure 12. Tensioned bar

$$\varepsilon_j = \frac{u^{i+1} - u^i}{L/3} \tag{8}$$

$$\sigma_j = E\varepsilon_j \tag{9}$$

$$\frac{I_j}{A} = E\varepsilon_j \tag{10}$$

The internal loads I_j for each element are written by combining Eqs.8 and 10 as:

$$I_A = \frac{3EA}{L}(u^2 - u^1) \tag{11}$$

$$I_B = \frac{3EA}{L}(u^3 - u^2) \tag{12}$$

$$I_C = \frac{3EA}{L}(u^4 - u^3) \tag{13}$$

Equilibrium equations at each node are obtained by solving for the sum of forces, P_i, as:

$$node\ 1{:}\ P_1 + I_A = 0 \quad \rightarrow \quad P_1 + \frac{3EA}{L}(u^2 - u^1) = 0 \tag{14}$$

$$node\ 2{:}\ P_2 - I_A + I_B = 0 \quad \rightarrow \quad P_2 - \frac{3EA}{L}(u^2 - u^1) + \frac{3EA}{L}(u^3 - u^2) = 0 \tag{15}$$

$$node\ 3{:}\ P_3 - I_B + I_C = 0 \quad \rightarrow \quad P_3 - \frac{3EA}{L}(u^3 - u^2) + \frac{3EA}{L}(u^4 - u^3) = 0 \tag{16}$$

$$node\ 4{:}\ P_4 - I_C = 0 \quad \rightarrow \quad P_4 - \frac{3EA}{L}(u^4 - u^3) = 0 \tag{17}$$

In an implicit analysis, these form a system of equations that must be solved simultaneously, typically by matrix methods as in Eq. 18. Four equations are sufficient to solve the four unknowns: P_1, u^2, u^3, and u^4. The matrix within the bracket is referred to as the stiffness matrix, *K*, which is inverted to solve for the displacements using Eq. 19.

$$\begin{Bmatrix} P_1 \\ P_2 \\ P_3 \\ P_4 \end{Bmatrix} - \begin{bmatrix} \frac{3EA}{L} & -\frac{3EA}{L} & 0 & 0 \\ -\frac{3EA}{L} & \frac{6EA}{L} & -\frac{3EA}{L} & 0 \\ 0 & -\frac{3EA}{L} & \frac{6EA}{L} & -\frac{3EA}{L} \\ 0 & 0 & -\frac{3EA}{L} & \frac{3EA}{L} \end{bmatrix} \begin{Bmatrix} u^1 \\ u^2 \\ u^3 \\ u^4 \end{Bmatrix} = 0 \tag{18}$$

$$\{U\} = [K]^{-1}\{P\} \tag{19}$$

In an explicit analysis, a vastly different solution approach is taken. The displacements of the nodes are calculated based upon dynamic propagation of stress through the model from one node to the next. Therefore, a simultaneous system of equations is not required. Using the same example of the bar, the force *P* on node 4 results in acceleration for a given time increment (Eq. 20). The acceleration is integrated to a velocity, for which a strain rate in Element C can be computed (Eq. 21). Integrating the strain rate for that increment results in an incremental strain for Element C. The total strain for Element C is the sum of the initial strain and the incremental strain (Eq. 22). The total strain is then used to determine the element's stress, using an appropriate material model. Eq. 23 calculates the stress in Element C for an elastic material. In the first increment, only Element C is affected. Subsequent increments propagate the force (and stress) through the material and into Nodes 3, 2, and 1, etc. To ensure the integrations are stable in an explicit method, the element size and dilatational wave properties of the material are used to limit the time increment, as described in section 3.5.2

$$M_C \ddot{u}_4 = P \tag{20}$$

$$\frac{\int \ddot{u}_4 dt}{L/3} = \frac{3\ddot{u}_4}{L} = \dot{\varepsilon}_C \tag{21}$$

$$\varepsilon_0 + \int \dot{\varepsilon}_C \, dt = \varepsilon_C \tag{22}$$

$$\sigma_C = E\varepsilon_C \tag{23}$$

Regarding terminology, "iterations" are computations conducted for the same boundary conditions and temporal state in order to obtain a converged solution. A converged solution is one in which the residual error of the discretized equations is below a given threshold. An "increment" or "time step" is a given set of constant boundary conditions for a period of time. For instance, once the simulation has iterated the solution and obtained convergence for an increment, the time step is advanced and the process starts again. In a dynamic analysis within Abaqus, a series of increments together form a "step", which is the overall simulated time for which the analysis is conducted. Steps can be followed by subsequent steps to conduct a more complex analysis of the system (Dassault Systemes, 2013).

3.1.1 Element technology

The discrete elements in the Finite Element Method use various formulations to optimize the accuracy or computational efficiency for a simulated problem. The choice of element is dictated by the anticipated behavior of the representative structure (Pzremieniecki, 1985). While commercial FEM codes may employ many more element family types, four of the most common include: continuum elements, shell elements, beam elements, and rigid elements (Figure 13).

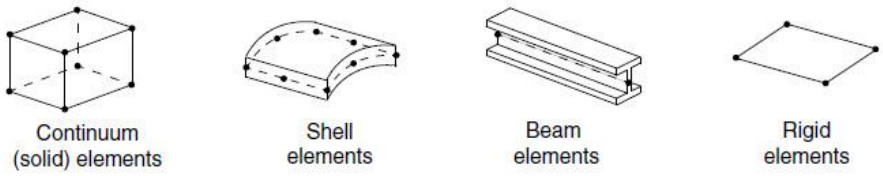

Figure 13. Common element family types (Dassault Systemes, 2013)

The continuum family type is the most versatile and commonly used element for stress/strain analysis and can represent the structure for almost any geometry and loading. They can be hexahedral, tetrahedral, or wedge-like in shape. The shell family type is employed to represent structures much smaller in thickness than the other dimensions, and where stress through the thickness is not important. These include pressure vessels or thin walled structures, fluid tanks, etc. The beam family type is used when the length of the geometry is much larger than the other two dimensions. Only the stress in the length direction is of importance and a section property must be assigned in order to dictate the elements behavior. The rigid family type is chosen to represent structure wherein stress and deformation is not important or of interest. These elements are positioned according to a single reference node, and all other "slave nodes" upon the element maintain their nodal positions relative to the reference node. Motion of all nodes is governed by the equations of motion for the body acting at the reference node.

The degrees of freedom (or variables) for an element are calculated only at each node as shown in Figure 14. To determine information about a variable at any other point within the element, interpolation is used based upon the values at the surrounding nodes. Interpolation using two nodes is linear in nature and considered first-order. Interpolation using three nodes is quadratic in nature and considered second-order. For example, values along the edge of an 8-node continuum element are interpolated using the values from the nodes at either corner upon the same edge. The

linear interpolation is provided in Eq. 24, where *x* is the nodal locations and *y* is the variable of interest.

$$y = y_0 + (y_1 - y_0)\frac{x-x_0}{x_1-x_0} \tag{24}$$

Values along the edge of a 20-node continuum element are interpolated using the values from the two corner nodes and the midpoint node located upon the same edge. The Lagrange interpolating polynomial used is provided in Eq. 25, where *x* represents the nodal locations and *y* is the variable of interest.

$$y = y_0\frac{(x-x_1)(x-x_2)}{(x_0-x_1)(x_0-x_2)} + y_1\frac{(x-x_0)(x-x_2)}{(x_1-x_0)(x_1-x_2)} + y_2\frac{(x-x_0)(x-x_1)}{(x_2-x_0)(x_2-x_1)} \tag{25}$$

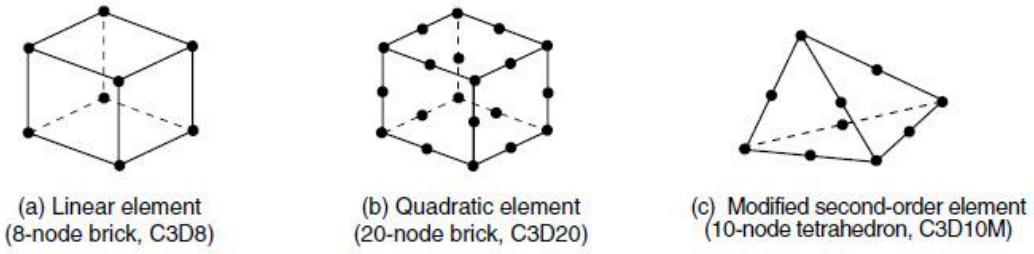

Figure 14. Various continuum elements (Dassault Systemes, 2013)

The stiffness that governs the response of each element is determined by integrating through the element's volume. The numerical technique of Gaussian quadrature is typically used, which can significantly affect the accuracy for a particular application, depending on the number of integration points used. A three-dimensional linear element uses two integration points in each direction, or $2 \cdot 2 \cdot 2 = 8$ integration points. A three-dimensional quadratic element uses three integration points in each direction, or $3 \cdot 3 \cdot 3 = 27$ integration points. Caution must be used with linear elements in simulations with large bending deformation, as this can result in "shear-

locking". As shown in Figure 15, linear elements only use two integration points along an edge, which cannot define a curve. As some shear stress is retained, this results in a significantly stiffer structure which cannot be compensated for using increased elements through the thickness. Conversely, the third integration point at the midpoint of each edge in a quadratic element allows for a more realistic bending deformation. This numerical nuance reinforces the importance of validating the element choice for modeling large deformation in bending.

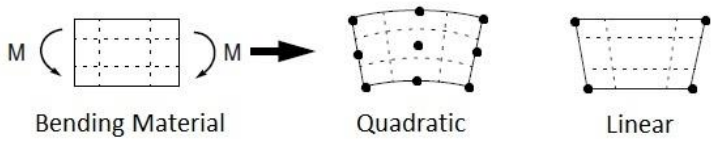

Figure 15. Shear locking in fully-integrated elements (Dassault Systemes, 2013)

Because a linear, fully–integrated element is prone to shear locking when subject to bending, a "reduced integration" option is available that removes one integration point from each direction. Thus, a three-dimensional linear element with "reduced integration" uses $1 \cdot 1 \cdot 1 = 1$ integration point at the centroid. A three-dimensional quadratic element with "reduced integration" uses $2 \cdot 2 \cdot 2 = 8$ integration points. The single integration point for a three-dimensional linear element means it cannot resist any bending moment on its own, as shown in Figure 16. This numerical "hour-glassing" results in an overly flexible structure, especially in coarse meshes. To combat this problem, Abaqus introduces a small amount of "hour-glass stiffness" to these elements and increased refinement is needed to obtain realistic results. If linear elements are utilized, using at least four linear elements through the thickness is recommended for any structures in bending so that at least two integration points are located on either side of the neutral axis. Quadratic, reduced-

integration elements are not prone to shear-locking, but are subject to hour-glassing in a very coarse mesh (Dassault Systemes, 2013).

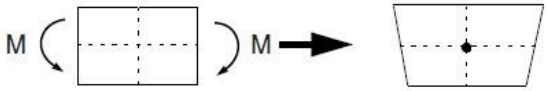

Figure 16. Reduced integration in linear elements (Dassault Systemes, 2013)

All element types are identified by a coded naming convention that describes their family, degrees of freedom, node count, formulation, and integration; in that order. Additional information about the mathematical character is sometimes denoted by a final character such as "R" or "H" for example, to denote a reduced integration or hybrid element. As there are slight variations of the convention and options for some family types, specific documentation for a commercial code should be referenced. Elements used within this study are:

C3D8 – continuum, three-dimensional, 8 nodes, full integration

C3D20R – continuum, three-dimensional, 20 nodes, reduced integration

S8R – shell, 8 nodes, reduced integration (the dimensional nature is inferred by the family type and thus omitted)

M3D4R – quadrilateral membrane, reduced integration, hourglass control, 4 nodes

3.1.2 Material and geometric nonlinearity

When constant loads imparted upon a structure result in small deformations and the structure consists of a linear elastic material, the assumption of linearity can be made to simplify the computation. While this is not a real occurrence in physical systems, it permits the FEM procedure to invert the stiffness matrix only once, and then vary the structure's response linearly according

to the applied load. It also allows application of subsequent loading via superposition by multiplying the inverted stiffness matrix with a new load vector.

Conversely, for a nonlinear system, the changes in stiffness as a result of displacement are significant and cannot be ignored. The response of the structure is not linearly related to the load, and superposition cannot be used for subsequent loadings. Both material properties and geometry deformation are sources of nonlinearity (Przemieniecki, 1985), and thus the linearity assumption is not valid for hyperelastic materials such as rubber, or for structures having large deformation. A nonlinear analysis procedure is required. For an FSI problem where the loads upon the structure may vary as a result of the deformation, boundary conditions become a third source of nonlinearity.

For example, in the case of a cantilevered beam bending under a vertical tip load, only shear and moments are considered in the beam for a linear analysis. In actuality, the load vector imparts additional axial tensions into the beam as the deflection increases and the geometry takes on a new shape and stiffness matrix. The initial stiffness matrix used at the beginning of the simulation is not valid for the current geometry and must be recomputed. This nonlinearity is a purely geometrical result, independent of the material properties. Assuming a linear modulus for the material does not change this fact. For this reason, a nonlinear implicit analysis is computationally expensive due to repeated construction and inversion of the stiffness matrix throughout the simulation. A nonlinear explicit analysis saves effort per increment in that the global stiffness matrix is not required. But while each increment is solved more quickly than for an implicit method, many more increments are required to simulate a given time due to the much smaller time step.

3.2 Finite volume method

Computational Fluid Dynamics (CFD) is the application of numerical techniques to solve equations governing fluid flow. It complements the more traditional approaches of theoretical and experimental analysis and approaches aero/hydrodynamic problems from a "new" third perspective (Anderson, 1995). Its use is widespread today and is commonly applied to problems in the fields of aerospace, naval architecture, hydraulics, pneumatics, manufacturing, heating/ventilation/air conditioning, construction, and more. Further, because it involves the simulation of fundamental physical behaviors found in nature, its application and uses appear endless.

When modeling a fluid in continuum mechanics, one can use either a finite control volume or an infinitesimal fluid element. The volume or element can move either with the surrounding flow or be fixed in space depending on perspective. Each approach will lead to different forms of the governing equations and lend themselves differently to numerical solution techniques. It is important to note that the equations developed from each of the four fluid models are equivalent in meaning. Manipulations of any of the integral equations can produce the partial differential forms and vice versa. While not detailed here, the steps to acquire the various forms are provided by Anderson (1995). Figure 17 depicts the four fluid models.

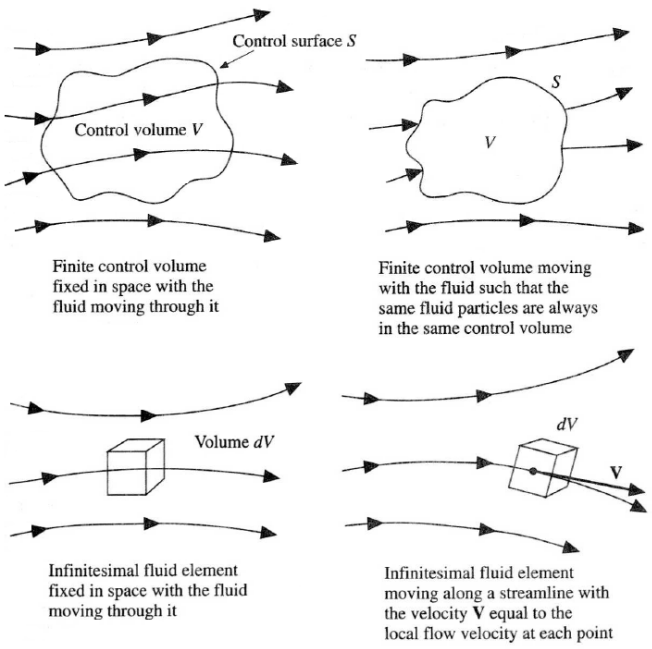

Figure 17. Continuum fluid models (Anderson, 1995)

The above fluid models provide the physical basis for the fluid flow governing equations; comprised of the continuity equation, momentum equations, and the energy equation. In most modern CFD texts, together they are referred to as the complete Navier-Stokes (NS) equations. However, because the five equations utilize six unknown variables (pressure, p, density, ρ, x-velocity, u, y-velocity, v, z-velocity, w, and internal energy, e), a final equation is needed to close the set. A thermodynamic equation of state, such as the ideal gas law for example, provides the final relationship between pressure, density, and temperature. The conservation equations for mass and momentum in integral form are shown in Eq. 26 and Eq. 27, where ρ is density, v is velocity, p is pressure, T is the viscous stress tensor, and f is the body force terms. Derivations originating from the above continuum fluid models can be found in Anderson (1995).

$$\frac{d}{dt}\int_V \rho \, dV + \oint_A \rho(\boldsymbol{v}) \cdot d\boldsymbol{a} = 0 \tag{26}$$

$$\frac{d}{dt}\int_V \rho\, \boldsymbol{v} dV + \oint_A \rho \boldsymbol{v} \otimes \boldsymbol{v} \cdot d\boldsymbol{a} = -\oint_A p\boldsymbol{I} \cdot d\boldsymbol{a} + \oint_A \boldsymbol{T} \cdot d\boldsymbol{a} + \oint_V \boldsymbol{f_b} d\boldsymbol{V} \quad (27)$$

Depending on the type of flow problem, useful assumptions can be made that simplify the NS equations:

1. If the flow is incompressible with constant viscosity, only the mass and momentum equations are coupled. The energy equation can be solved separately if desired using values provided by the coupled equations.
2. If the flow is steady, all time derivative terms reduce to zero.
3. If the problem is considered inviscid and isothermal, all viscous and thermal terms reduce to zero. This particular simplification results in the form known as the Euler equations.

With the fundamental fluid model established, the problem now becomes one of numerical approximation since few exact solutions to the NS equations have been found to date[1] (Anderson, 1995). The Finite Volume Method (FVM) is one technique within CFD to represent and evaluate the partial differential equations governing fluid flow. In this approach the domain of interest is discretized into a number of control volumes. The governing equations are then written as a summation of surface and volume integrals in the form of the general transport equation. It is composed of a transient term, convective flux, diffusive flux, and source term.

[1] Navier-Stokes Equation Millennium Problem Description, Clay Mathematics Institute, 10 Memorial Blvd. Suite 902, Providence, RI, USA

In STAR-CCM+, numerous schemes are offered to solve the discretized terms of the transport equations. In this work, the transient term is typically evaluated using a first-order scheme (Euler implicit) when steady state is sought and a second-order backwards differentiation scheme when a time-accurate unsteady solution is sought. For the convective flux term, second-order upwind is generally specified, except in cases where additional spatial dissipation afforded by the first-order upwind scheme is helpful. The diffusive term is approximated using a second order expression. Variable gradients at cell centers and cell faces are solved using the Hybrid Gauss-Least Squares Method with Venkatakrishnan flux limiters (Venkatakrishnan, 1994). Boundary conditions are then imposed upon internal and external faces to simulate enveloped objects, pressure loading, temperature, or other constraints. With the numerical basis established, a system of equations is then written and iteratively solved using a variety of point iterative methods. Additional descriptions of the numerical methodologies implemented within STAR-CCM+ are found in the documentation (Siemens, 2018).

3.2.1 Reynolds-averaged Navier-Stokes (RANS) equations

Previous work shows that friction forces upon seals are generally a small portion of the overall hydrodynamic drag for most combinations of cushion pressure and flow velocity (Bloxom, 2014). However, the influence of the shear stress upon seal surface does play a role in obtaining the correct deflection, especially when highly flexible materials are used. In order to more accurately model the flow, and thus the traction upon the seal, a RANS description of the flow equations is used.

For many hydrodynamic problems at practical scales, the flow regime is considered turbulent and characterized by unsteady perturbations of the flow quantities. To properly simulate friction forces upon wetted surfaces, this unsteadiness must be accounted for within the fluid equations.

However, as turbulent structures occur at much smaller scales and at higher frequencies than the physics of interest, the expense of a direct simulation can be prohibitive. One approach is to consider turbulent flow as a summation of mean and fluctuating velocities (Newman, 1977). In modern CFD, turbulent structures can be accounted for by this approach using the Reynolds-averaged Navier-Stokes (RANS) equations and a suitable turbulence model.

RANS equations are obtained by decomposing each solution variable within the NS equations into a mean component and fluctuating component, as in Eq. 28. The resulting form is simply the NS equations written in terms of the mean values (Eq. 29 and Eq. 30), along with an additional term, the Reynolds stress tensor $\boldsymbol{T_t}$ (Eq. 31), in the momentum equation.

$$\phi = \bar{\phi} + \phi' \tag{28}$$

$$\frac{d}{dt}\rho + \nabla \cdot (\rho \overline{\boldsymbol{v}}) = 0 \tag{29}$$

$$\frac{d}{dt}(\rho \overline{\boldsymbol{v}}) + \nabla \cdot (\rho \overline{\boldsymbol{v}} \otimes \overline{\boldsymbol{v}}) = -\nabla \cdot \bar{p}\,\mathbf{I} + \nabla \cdot (\boldsymbol{T} + \boldsymbol{T_t}) + \boldsymbol{f_b} \tag{30}$$

$$\boldsymbol{T_t} = -\rho \begin{pmatrix} \overline{u'u'} & \overline{u'v'} & \overline{u'w'} \\ \overline{u'v'} & \overline{v'v'} & \overline{v'w'} \\ \overline{u'w'} & \overline{v'w'} & \overline{w'w'} \end{pmatrix} \tag{31}$$

To close this new set of equations, the Boussinesq approximation of eddy viscosity (Eq. 32) is used as one method to estimate the Reynolds stress tensor. It is based upon the concept that the tensor can be derived from a relationship between a turbulent eddy viscosity parameter, μ_t, and the mean flow quantities. $\boldsymbol{S}$ is the mean strain rate tensor and $\boldsymbol{I}$ is the identity tensor.

$$\boldsymbol{T_t} = 2\mu_t \boldsymbol{S} - \frac{2}{3}(\mu_t \nabla \cdot \overline{\boldsymbol{v}})\boldsymbol{I} \tag{32}$$

The turbulent eddy viscosity parameter is then solved for by application of a suitable turbulence model. While numerous models are available in present day methods, the Standard Spalart-Allmaras (SSA) model (Spalart and Allmaras, 1992) is well-suited to unstructured grids and has found widespread use for this purpose in the aerospace industry (Siemens, 2018). It is not typically applied to buoyancy and free-shear flow problems. As large deformation of the seal results in high mesh motion and some amount of cell skewness, the advantage of SSA for an unstructured grid makes it a suitable choice. Further, previous work by Bloxom (2014) showed successful implementation of SSA for this purpose.

As accurate modeling of the fluid vorticity is important in turbulent flow, it is important to consider the treatment of the wall boundary layer. The boundary layer can be divided into the laminar sublayer (y^+ <= 5), buffer-layer (5 < y^+ <= 30), and the log-law layer (30 < y^+< 500), where y^+ is the non-dimensional wall distance and u^+ is the non-dimensional velocity (Popovac and Hanjalic, 2006). Each sublayer is characterized by a different relationship between u^+ and y^+. For RANS simulations in STAR-CCM+, an "all y^+" treatment can be specified to blend the various relationships as dictated by the mesh size adjacent to the wall. This is especially useful for FSI simulations where grid size may be limited and where mesh deformation is present near moving boundaries.

3.2.2 Equations of state and incompressibility

An equation of state (EOS) is a thermodynamic relation introduced to directly relate the fluid variables of pressure, density, and energy. When it is combined with the complete Navier-Stokes equations it closes the set governing the flow. There are various forms based upon the physics of

interest, and the most prevalent are constant density, polynomial density, ideal gas, and the empirically derived real gas.

For flow simulations in the speed regime of ACV seals, the particle velocity is much smaller than the speed of sound and the fluid can be assumed incompressible. Density is constant ($\rho = \rho_0$), its time derivative is zero, and the Mach number approaches zero. However, this simplification poses numerical difficulties for a coupled solution of the complete Navier Stokes equations due to the theoretically infinite speed of sound; the pressure cannot be explicitly stated (Anderson, 1995).

Techniques have since been developed to condition these equations to address this, and other various numerical problems. One method is the application of Artificial Compressibility by adding a time-derivative pre-conditioning term $\frac{1}{\beta^2}\frac{dp}{dt}$ to the continuity equation (Chorin, 1967, Turkel, 1996). But because a new, non-physical term is introduced in this approach, it is only applicable for the steady state solution when $\frac{dp}{dt} \to 0$. Also, artificial viscosity can be added to the continuity equation to provide additional damping and deal with even-odd decoupling that occurs with some numerical schemes (Jameson et al., 1981).

Despite the above approaches, the elliptic-parabolic behavior of the incompressible Navier-Stokes equations remains. One solution has been found through the development of pressure-based iterative algorithms such as "Semi-Implicit Method for Pressure Linked Equations" (SIMPLE) and "Pressure Implicit with Splitting of Operator" (PISO) (Patankar and Spalding, 1972, Patankar, 1980, Shyy et al., 1996). They use a predictor-corrector type approach to solve a pressure-correction equation constructed from the momentum and continuity equations. Updates to the pressure field provide corrections to the face mass flux and velocity terms in order to fulfill the

continuity equation. As the flow variables are sequentially solved one after the other, they are often referred to as "segregated solvers."

3.2.3 Free surface modeling

When simulating problems having free surface boundaries, interface tracking and interface capturing are two general classifications of methods employed. Interface tracking methods include Fast Marching (Sethian, 1994), Level Set (Osher and Sethian, 1988), and Line Segments (Nichols and Hirt, 1971). These utilize mathematical functions to define the shape and motion of a boundary surface. Alternatively, interface capturing methods such as Volume of Fluids (Hird and Nichols, 1981) deduce the boundary surface by the makeup of individual cell volume fractions. In many modern CFD codes, the Volume of Fluid (VOF) method has become a popular approach due to its ability to handle both large deformations of the free surface, as well as problems where multiple immiscible fluid species are present. Its premise is that individual fluid constituents within a volume combine to form a mixture, sharing pressure, velocity, and temperature properties.

VOF implementation within STAR-CCM+ is as follows. The volume fraction α_i (Eq. 33) provides the phase distribution for each cell, bounded between [0, 1]. The total fraction must sum to unity for any number of phases, N (Eq. 34). V is the cell volume and i represents the phase number. A mixture-based approach is used to calculate properties for cells of multiple phases according to Eqs. 35, 36, and 37, where ρ is the density, μ is the dynamic viscosity, and C_p is the specific heat. With the introduction of phase information, a volume fraction transport equation (Eq. 38) is needed to solve the distribution of volume fractions in the domain.

$$\alpha_i = {}^{V_i}/_{V} \tag{33}$$

$$\sum_i^N \alpha_i = 1 \tag{34}$$

$$\rho = \sum_i \rho_i \alpha_i \tag{35}$$

$$\mu = \sum_i \mu_i \alpha_i \tag{36}$$

$$C_p = \sum_i \frac{(C_p)_i \rho_i}{\rho} \alpha_i \tag{37}$$

$$\frac{d}{dt}\int_V \alpha_i dV + \oint_A \alpha_i(\boldsymbol{v}) \cdot d\boldsymbol{a} = \int_V S_{\alpha_i} dV \tag{38}$$

Typically, the volume fraction used to identify the interface between two phases is $\alpha_i = 0.5$. To construct a sharply defined surface representing this interface, various schemes are employed to reproduce the convective behavior of immiscible fluids. In transient simulations, STAR-CCM+ employs a blend of a First-Order Upwind (FOU) scheme and the High-Resolution Interface Capturing (HRIC) scheme (Muzaferija et al., 1999). This combination of HRIC and FOU provides sharpness when the local Courant number, *C*, is small, and stability when the local Courant number is high (at the expense of a smeared interface). Thus, it is important to solve the transport equation with sufficiently small timesteps to maintain a resolved interface. Using the normalized variable concept, the HRIC scheme calculates the center face value (ξ_C) and normalized face value (ξ_f). Blending of the schemes is accomplished by correcting the face value using Eq. 39. A user-defined upper Courant limit (C_u) and lower Courant limit (C_l) is compared to the local Courant number. When $C < C_l$, HRIC is used. When $C_l < C < C_u$, the schemes are blended via interpolation. When $C_u < C$, FOU is used. When the steady-state solution is sought, the Courant limits can be raised artificially high to force exclusive use of the HRIC scheme.

$$\xi_f^* = \begin{cases} \xi_f & , \ if\ C < C_l \\ \xi_C + (\xi_f - \xi_C)\frac{C_u - C}{C_u - C_l}, & if\ C_l \le C < C_u \\ \xi_C & , \ if\ C_u \le C \end{cases} \quad (39)$$

If the fluid interface is advancing normal to grid lines, the downwind nature of HRIC helps keep the interface well defined. Yet when the flow is parallel to the interface, distortion can occur. To smooth the interface, a further correction to the face value can be made by increasing the angle factor C_Θ, as shown in Eq. 40. Θ is the angle between the cell face surface vector and the interface normal vector. The final face volume fraction (α_f) obtained from the HRIC scheme is shown by Eq. 41, where *D* and *U* denote the downstream and upstream solutions.

$$\xi_f^{**} = \xi_f^*(\cos\theta)^{C_\theta} + \xi_C(1 - (\cos\theta)^{C_\theta}) \quad (40)$$

$$\alpha_f = \xi_f^{**}(\alpha_D - \alpha_U) + \alpha_U \quad (41)$$

3.2.4 Modeling space and mesh motion

Depending on the physics being simulated and the anticipated behavior of the objects within the computational domain, one may choose to discretize the structure or fluid in either an Eulerian or Lagrangian sense. In an Eulerian domain, the element nodes are fixed in space, and material is allowed to flow through. Thus, the material is not expressly tied to a specific element. As a result, Eulerian elements must be defined in terms of a volume fraction as they may be only partially filled with material. Conversely, they could be completely empty. For simplicity, the Eulerian domain is typically a structured Cartesian grid and must be constructed to encompass not only the Eulerian material boundaries, but also the anticipated region where the material may move. Caution must be taken when specifying the location and size of the Eulerian domain, as any

material (fluid or solid) that moves beyond the grid is lost. Appropriate boundary conditions are also important to either allow, or avoid, this occurrence as desired.

Another option for discretization is the Lagrangian domain. Here the nodes are fixed within the material and thus they translate in space according to element deformation resulting from the stress state. Lagrangian elements are completely filled with the material and the element boundaries locate the object boundaries. Solids and moderately deformable objects are typically meshed in a Lagrangian domain with careful attention to deformation of the elements. In the event the deformation becomes so extreme as to result in inaccuracies, the mesh may be re-generated and discretized with further refinement. However, these operations are typically non-conservative, computationally expensive, and may require user interaction. A material such as a fluid may be discretized in a Lagrangian domain only if deformations do not result in excessive element warping. For a fluid-structure interaction problem where the deformation of the Lagrangian structure does not approach the cell size of the adjacent Eulerian fluid, a fixed fluid mesh is well suited.

To accommodate larger deformations of the structure, mesh motion technology may be employed to avoid successive remeshing. Mesh vertices are precisely moved following each time step so that the flow field discretization accommodates the structural change. A common numerical approach for enabling mesh motion is multiquadric interpolation (Hardy, 1990). Select nodes located around the motion region boundaries are identified as displacement control vertices. At each time step, movement of the control vertices is determined according to Eq. 42, where d_i' is a vector of the displacement for each control vertex, λ_i is the expansion coefficient, and $f_{b,j}(r_{ij})$ is a radial basis function shown in Eq. 43. In order to ensure the motion region does not increase in

overall size, α is a vector that accommodates the constraint of Eq. 44. The magnitude of distance between two control vertices *i* and *j* is denoted as r_{ij}, and c_j is the basis constant. With these three equations solved, a cartesian displacement vector *d'(x)* is solved according to Eq. 45, where *r* is the magnitude of the distance between a non-control vertex, *x*, and a control vertex x_j. The remaining vertices located within the motion region are then translated according to this interpolated displacement vector.

$$\boldsymbol{d}_i' = \sum_{j=1}^{N} f_{b,j}\left(r_{ij}\right)\boldsymbol{\lambda}_j + \boldsymbol{\alpha} \tag{42}$$

$$f_{b,j}\left(r_{ij}\right) = \sqrt{r_{ij}^2 + c_j^2} \tag{43}$$

$$\sum_{j=1}^{N} \boldsymbol{\lambda}_j = 0 \tag{44}$$

$$\boldsymbol{d}'(x) = \sum_{j=1}^{N} f_{b,j}\,(r)\boldsymbol{\lambda}_j + \boldsymbol{\alpha} \tag{45}$$

To reduce the computational cost of this operation, control vertex thinning can be applied to reduce the number of vertices used for the displacement field interpolation. When an automatic thin-out algorithm is used, prior grid deformation is assessed and control vertices are reduced and/or selectively chosen to maximize the interpolation efficiency. Following movement of any mesh vertices, geometric conservation may be achieved by applying a grid flux correction to the convective flux term in the finite volume discretization to account for the volume change. In STAR-CCM+, mesh motion technology is utilized by activating the "Mesh Morpher" solver. The solver accelerates solution of the interpolated displacement vector by applying a preconditioned conjugate gradient method (Faul et al., 2005, Gumerov and Duraiswami, 2007) and a fast multipole method (Beatson et al., 2006) to the typical radial basis function approach above.

3.3 Fluid-structure interaction

For many aero/hydrodynamic problems, the forces and reactions of flow upon solid boundaries can be determined based upon the deformation of the fluid alone, regardless of any minute changes to the boundary geometry or motion (Antoci, 2007). The boundary or object is assumed stationary and non-deforming. Alternatively, a fluid-structure interaction problem describes a scenario wherein the fluid flow around an object is of sufficient effect to influence the behavior, motion, geometry, or other properties of the object to the point of conversely altering the flow itself. Or more simply, FSI occurs when the fluid affects the structure, and the structure affects the fluid. Examples of fluid changes are pressure, viscosity, velocity, or temperature, whereas examples of structural changes are stiffness, deformation, or temperature, etc.

In the context of a deformable skirt seal, the fluid pressure pushes against the flexible fabric, resulting in a shape change based upon the structural properties. The fluid then conforms to the new shape and the interaction continues until a quasi-steady state is reached for a given boundary condition. Assuming no other changes to the incoming flow field occur, the seal may remain in this state, or be subject to chaotic or periodic mode-switching as revealed by Wiggins (2014) and Malakoff and Davis (1981). Other more common examples of FSI include swaying skyscrapers and bridges, flying flags, sails, and inflated structures.

3.3.1 FSI terminology

With today's advancement in computing power, FSI problems are typically solved by coupling finite volume method (FVM) codes for the fluid with finite element method (FEM) codes for the structure. The nature of the problem and characteristics of interest dictate the form of the

mathematical representation and the type of coupled interaction. Assuming the fluid is modeled with the Navier-Stokes or Euler equations, either strong or weak FSI coupling can occur. Strong coupling results when the fluid and structure both undergo large deformations, whereas weak coupling results from small deformations in the fluid and structure (Rugonyi and Bathe, 2001).

Two solution approaches are primarily used for FSI problems: simultaneous (monotlithic, direct) or partitioned (iterative) (Hubner et al., 2004, Lohner, 2006). A simultaneous approach requires that the equations for both the fluid and structure are written together and solved as a single system of equations. Stability is usually ensured and the convergence can be accelerated. And while it uses a consistent time integration scheme and time step for the entire domain, it may be inefficient should one physical field require a much smaller step than the other (Hubner et al., 2004).

A partitioned approach treats the domains separately and thus requires that the fluid and structure equations are solved independent of each other at a given iteration within the time step. The domains are discretized separately and communicate by mapping their solutions across contacting surfaces. One advantage of these algorithms is the individual solvers can be chosen separately according to the intent of the analysis and the sophistication required. A solver can be exchanged, upgraded, or modified independently without affecting operation of the other solvers. This is especially useful when using a black-box commercial product where the user does not have access to the underlying source code (Vierendeels, 2006). It is generally accepted that partitioned approaches to FSI problems are typically the most efficient (Farhat et al., 2010).

Partitioned algorithms can be either loosely (explicitly) coupled or tightly (implicitly) coupled. A loosely coupled partitioned algorithm may be appropriate for FSI problems having both weak interactions and large deformation, as in the case of metallic yielding (Simulia, 2013). When

steady state solutions are sought, loose coupling may be appropriate once the structure has established equilibrium with the fluid. Its velocities approach zero and it imparts little motion upon the surrounding fluid.

Figure 18 provides an illustration of how STAR-CCM+ implements a loosely coupled (explicit) partitioned algorithm. Following initialization, the fluid solver develops the initial field variables and passes the pressure loading to the contacting structural surface. The structural solver updates the nodal displacements and the inner iteration (also known as sub-iteration) convergence criteria are evaluated. If the minimum iterations have not been achieved, or the residuals remain above the predetermined limit, the fluid solver recomputes the flow field. The important observation at this point in the algorithm is that the partitioned solvers do not continue to interact within this time step, and the structural displacements remain fixed. The fluid solver independently seeks its own convergence. Once the fluid solver convergence criteria are met, the Mesh Morpher solver updates the nodal positions within the fluid domain and the time step is advanced. This loop continues until the overall stopping criteria are met, which may include a maximum simulated time for unsteady problems, or a minimum displacement limit for steady state problems.

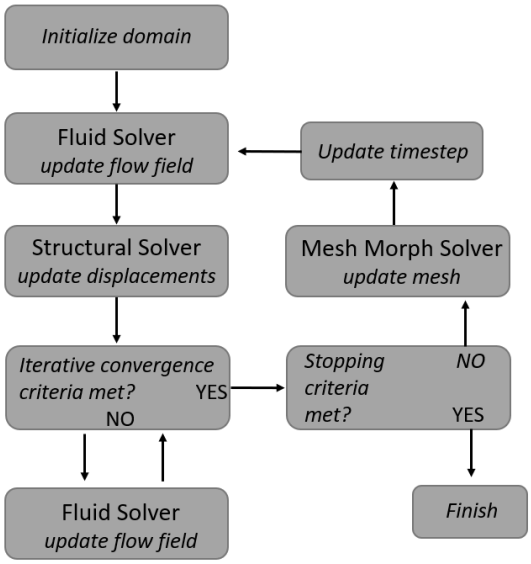

Figure 18. Loosely coupled partitioned algorithm in STAR-CCM+

For FSI problems with significant interactions or displacements, a tightly coupled partitioned algorithm is more appropriate (Causin et al., 2005, Le Tallec and Mouro, 2001). To create a tightly coupled partitioned algorithm, an additional iterative convergence loop between each partitioned solver is employed, providing better stability characteristics at the expense of additional numerical effort (Rugonyi and Bathe, 2001, Hubner et al., 2004, Causin et al., 2005).

STAR-CCM+ implements a tightly coupled (implicit) algorithm as illustrated in Figure 19. Following initialization, the fluid solver develops the initial field variables and maps the pressure loading to the contacting structural surface. The structural solver updates the nodal displacements and the inner iteration convergence criteria are evaluated. If the minimum iterations have not been achieved, or the residuals remain above the predetermined limit, the fluid solver and structural solver recompute their respective domains. The important observation at this point in the algorithm is that the structural displacements are updated at each inner iteration. They are not fixed as in the case of the loosely coupled scheme. In this way the fluid and structure iterate

together to find an equilibrium within the time step. Once the solvers meet the established iteration convergence criteria, the mesh morpher solver updates the nodal positions within the fluid domain and the time step is advanced. This loop continues until the outer iteration stopping criteria are met.

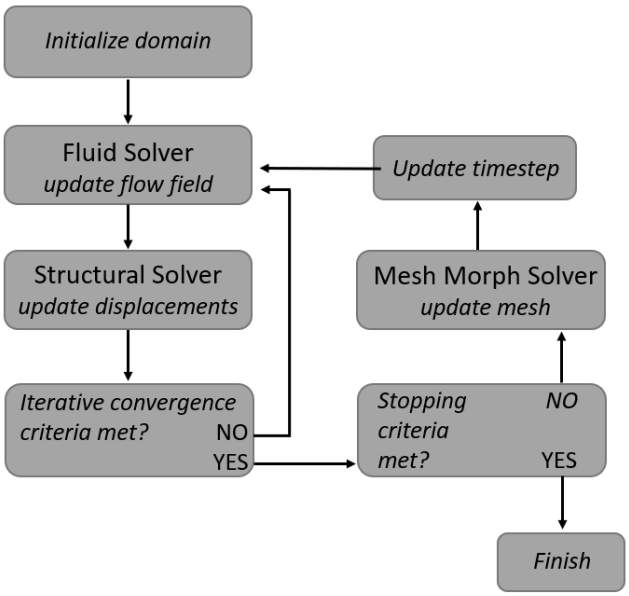

Figure 19. Tightly coupled partitioned algorithm in STAR-CCM+

In addition to the discussions above, solvers may employ either one-way or two-way coupling. In one-way coupling, forces from the fluid pressure are passed to the structure, but the reaction forces resulting from the structural strain are not passed back to the fluid. Weak interactions with loosely coupled schemes benefit from the efficiency of one-way coupling. However, one-way coupling is only appropriate when the structural response does little to affect the fluid. In two-way coupling, forces from both the fluid and structure are included in the interaction force balance. This is a necessity for strongly coupled problems and tightly coupled schemes. While STAR-CCM+ offers both one-way and two-way coupling, only two-way coupling is appropriate in this research. As it

is clear that the terminology surrounding fluid-structure interaction coupling can be confusing and the numerous algorithms are diverse (Collette and Sielski, 2016, Hou et al., 2012), a taxonomy for FSI coupling is shown in Figure 20. Of note is the inclusion of rigid body dynamics as a category of FSI. This class of problems assumes the structural domain is perfectly rigid, only requiring a one-way mapping of surface pressures to solve the equations of motion.

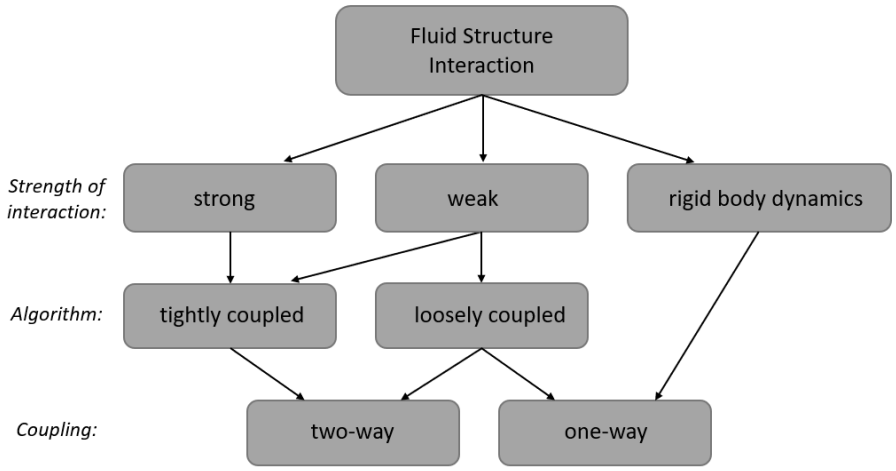

Figure 20. Fluid-structure interaction taxonomy

3.3.3 Nodal mapping

An important advantage when using a partitioned approach to solve FSI problems is the ability to model and discretize the fluid and structural domains separately. A nodal mapping algorithm is the key enabling technology required to accurately communicate information across a shared surface. Its purpose is to first identify which nodes across the separate physics domains are within the proximity tolerance for force exchange, and then to impose those forces proportionally based upon their relative positions. Various approaches to mapping allow data exchanges to occur node to surface, surface-to-surface, volume-to-surface, and even beam-to-surface. The majority of

schemes are based on interpolation theories, which are selected depending upon the source stencil (face, cell, or vertex). Regardless of scheme, it is helpful to match element sizes across domains so that interpolation errors are minimized. Further, specifying a conformal mapped mesh at an interface maximizes mesh continuity by matching the density and position of nodes. Mapping interpolations for FSI simulations in STAR-CCM+ are controlled by the interface boundary specification. It permits control of the proximity tolerance and angle for the nearest neighbor search (Siemens, 2018).

3.3.4 Added-mass instability

It is rightly asserted by Sheldon et al. (2014) that the primary challenge in solving FSI problems is not solving the fluid or solid governing equations but enforcing compatible conditions at the interface that ensure stability. In a FSI problem where the fluid and structural densities are comparable or when key physical dimensions are reached, the force exchange may be susceptible to destabilization by influence of the fluid mass upon the structural response (Causin et al., 2005, Forster, 2007). It has also been demonstrated that soft structures having low stiffness are prone to this non-convergence problem, regardless of the fluid/structure density ratio (Idelsohn et al., 2009). The phenomenon is commonly referred to as "added-mass effect" due to the analogy of inertia added to an accelerating body displacing fluid (Newman, 1977).

For partitioned solvers, strongly coupled algorithms are generally successful in mitigating added-mass effects if solution parameters are chosen to achieve an acceptable level of convergence (Idelsohn, 2009, Sheldon, 2014). While loosely coupled algorithms have been used successfully in aero-elasticity problems with low added-mass effects (Causin et al., 2005), numerous researchers (Burman and Fernandez, 2009, Rugonyi and Bathe, 2001, La Tallec and Mouro, 2001,

Causin et al., 2005) portend that loosely coupled algorithms are unstable for particular problems where added-mass effects are significant. This would apply to a FSI problem for an ACV seal in flow, as the fluid/structure density ratio is approximately one and the structure is extremely compliant. However, Farhat et al., (2005) have shown accurate results can be obtained for some loosely coupled FSI problems with strong added-mass effects if the flow is modeled as a compressible fluid. One conclusion drawn from the discussion above is that both the choice of coupling algorithm and sensitivity to added-mass effect is largely problem dependent.

3.5 Verification, validation, and uncertainty quantification

In this section, the definition and importance of verification and validation (V&V) is introduced, along with standards for reporting numerical V&V results. The topics of stability and numerical error are included as well, as they directly pertain to V&V assessments. Finally, an overview of uncertainty quantification is provided.

3.5.1 Verification and validation

Generally speaking, verification and validation (V&V) in modeling and simulation are processes that evaluate the "correctness" and "applicability" of a computer model with the goal of establishing its credibility. Due to the diversity within various organizations of the modeling and simulation community, numerous subtleties in the modern understanding of V&V have evolved (Oberkampf and Roy, 2010). From the Defense Modeling and Simulation Office, *verification* is considered the process of determining that a model implementation accurately represents the developer's conceptual description of the model. Similarly, *validation* is the process of determining the degree to which a model is an accurate representation of the real world from the

perspective of the intended uses of the model (DoD 5000.59, 1994). While there are numerous other forms of the definitions offered by AIAA, IEEE, ASME, CMMI, etc., the most simplistic might be: verification shows we solved the equations correctly, while validation shows we solved the correct equations. What remains obvious is that V&V is an important step in performing scientific or engineering simulations, especially for critical applications or where loss-of-life is a possibility.

As for a formal V&V of the work conducted using STAR-CCM+, verification of the structural solution is conducted in section 4.1.2. Bloxom's (2014) work is relied upon for verification of the fluid side of the problem. Validation of the coupled FSI solution is conducted in section 4.1.3. Should any gaps remain for the reader as to V&V of the specific fluid and structural solvers employed, they are directed to the extensive STAR-CCM+ V&V documentation (Siemens, 2018).

In section 5.2, a thorough V&V effort is conducted for the novel Abaqus/Explicit FSI modeling approach. First, a number of benchmark structural and fluid problems are conducted. Verification of the results is provided using analytic solutions to the governing equations. Validation of the fluid-structure interaction CEL capability is also conducted by comparing model results to published experimental and numerical data sets.

3.5.2 Stability and numerical error

In general, numerical stability in finite difference schemes is maintained when the total numerical errors are less than or equal to the numerical errors at the previous increment. Common sources of numerical error include truncation error, round-off error, and iterative convergence error (Oberkampf and Roy, 2010, Anderson, 1995).

Discretization error is the difference between the exact solution to the discrete equation approximation and the analytical solution to the partial differential equations being simulated. It results primarily from the difference approximations within the domain and at the boundaries and is usually the largest source of numerical error (Oberkampf and Roy, 2010). It is sometimes referred to as "truncation error" because finite Taylor series expansions are used to represent the derivatives within the governing equations. The expansions are truncated at some point and the contributions of those higher order terms are lost. It can be tracked two ways: locally and globally. The local truncation error is the error resulting from a single iteration, whereas the global truncation error is the summation of the local error over all iterations. If the local truncation error goes to zero when the mesh is refined, the discrete equation approximation is considered "consistent". If the global truncation error goes to zero when the mesh is refined, the discrete equation approximation is considered "convergent" (Oberkampf and Roy, 2010, Anderson, 1995). Thus, it is the goal of any numerical scheme for the solution to converge.

Round-off error is the accumulation of error due to repeated computations of finite arithmetic on digital computers (Oberkampf and Roy, 2010). The magnitude depends only on the number and type of arithmetic operations per increment and is unaffected by changes in mesh size. This makes explicit time-marching techniques with small time steps especially susceptible to this error over long simulations. A practical method for estimating the round-off error for a particular problem is to conduct the simulation using both single-precision and double-precision versions of a code. The difference in the solutions is the round-off error.

Lastly, iterative convergence error is introduced when an iterative method is used to solve an equation or system of equations when a direct algebraic solution does not exist. It is the difference

between the current solution and the exact, converged solution within an increment (Oberkampf and Roy, 2010). In an implicit method, the solver iterates the solution until the iterative convergence error is below some threshold, typically on the order of machine accuracy for steady problems. For long duration transient problems when steady state is of prime importance, the iterative convergence error is sometimes allowed to be higher at the cost of time accuracy, as it is typically too expensive to achieve machine accuracy at each time step. Iterative convergence error is typically not found in explicit time marching techniques.

The specific criteria for establishing numerical stability in an explicit method depend on the form of the governing equations and the specific difference approximations to those equations (Anderson, 1995). Because the coupled equations for an implicit technique are solved simultaneously, they are generally stable over large time increments. However, an explicit technique is conditionally stable based upon the truncation error of the finite difference approximation to the governing equations (Oberkampf and Roy, 2010, Anderson, 1995).

For example, consider an explicit marching technique used to simulate the first order wave equation given by Eq. 46. Largely following Anderson (1995), a difference equation can be written as Eq. 47 using a central scheme for the spatial derivative and a forward scheme for the time derivative. An alternate form of the time derivative is introduced via the Lax method in Eq. 48. The solution for the state variable at the next time step can then be found and is given in Eq. 49.

$$\frac{\partial u}{\partial t} + c\frac{\partial u}{\partial x} = 0 \tag{46}$$

$$\frac{u_i^{n+1} - u_i^n}{\Delta t} + c\frac{u_{i+1}^n - u_{i-1}^n}{2\Delta x} = 0 \tag{47}$$

$$\frac{u_i^{n+1} - {}^1\!/_2(u_{i+1}^n + u_{i-1}^n)}{\Delta t} + c\frac{u_{i+1}^n - u_{i-1}^n}{2\Delta x} = 0 \tag{48}$$

$$u_i^{n+1} = \frac{(u_{i+1}^n + u_{i-1}^n)}{2} - c\frac{\Delta t}{\Delta x}\frac{u_{i+1}^n - u_{i-1}^n}{2} \tag{49}$$

Understanding that the error also satisfies the difference equation, a von-Neumann stability analysis allows us to write: $error = \varepsilon_m(x,t) = e^{at}e^{ik_m x}$. The difference equation then becomes Eq. 50. Dividing by $e^{a(t)}e^{ik_m x}$ gives Eq. 51 and using the complex exponential identities of: $\cos(k_m \Delta x) = \frac{(e^{ik_m \Delta x} + e^{-ik_m \Delta x})}{2}$ and $\sin(k_m \Delta x) = \frac{(e^{ik_m \Delta x} - e^{-ik_m \Delta x})}{2i}$ gives Eq. 52.

$$e^{a(t+\Delta t)}e^{ik_m(x)} = \frac{(e^{a(t)}e^{ik_m(x+\Delta x)} + e^{a(t)}e^{ik_m(x-\Delta x)})}{2} - c\frac{\Delta t}{\Delta x}\frac{e^{a(t)}e^{ik_m(x+\Delta x)} - e^{a(t)}e^{ik_m(x-\Delta x)}}{2} \tag{50}$$

$$e^{a(\Delta t)} = \frac{(e^{ik_m(\Delta x)} + e^{ik_m(-\Delta x)})}{2} - c\frac{\Delta t}{\Delta x}\frac{e^{ik_m(\Delta x)} - e^{ik_m(-\Delta x)}}{2} \tag{51}$$

$$e^{a(\Delta t)} = \cos(k_m \Delta x) - c\frac{\Delta t}{\Delta x} i \sin(k_m \Delta x) \tag{52}$$

If stability requires the current numerical errors to be less than or equal to the numerical errors at the previous increment, then we can write Eq. 53 and equivalently, Eq. 54. We can then see that stability is maintained when $c\frac{\Delta t}{\Delta x} \leq 1$. This criterion limits the size of the time increment based upon the discretization size and material dilatational constant, *c*. It is commonly referred to as the Courant-Friedrichs-Lewy (CFL) condition. The Courant number is then defined as $C = c\frac{\Delta t}{\Delta x}$. It can be written for the *n*-dimensional case as Eq. 55, where *i* is the degree of freedom and u_x is velocity in the direction of discretization.

$$\left|\frac{\varepsilon_i^{n+1}}{\varepsilon_i^n}\right| = \left|\frac{e^{a(t+\Delta t)}e^{ik_m(x)}}{e^{a(t)}e^{ik_m(x)}}\right| = \left|e^{a(\Delta t)}\right| \leq 1 \tag{53}$$

$$\left|\cos(k_m \Delta x) - c\frac{\Delta t}{\Delta x} i \sin(k_m \Delta x)\right| \leq 1 \tag{54}$$

$$C = \Delta t \sum_{i=1}^{n} \frac{u_{x_i}}{\Delta x_i} \tag{55}$$

As shown above, the stability criteria for an explicit method results in very small time increments having relatively small computational costs per increment. The cost per increment for an implicit method is far greater than that of an explicit method, but orders of magnitude fewer increments are typically required (Dassault Systemes, 2013).

In order to verify numerical solutions are both consistent and convergent, standard approaches for reporting results have been established by the V&V community. Recall the truncation error is the difference between the governing differential equation and the discretized equation used in the numerical scheme. Thus, the formal order of accuracy, *p*, of an algorithm is the lowest order of the leading term in the truncation error. A common check for consistency and convergence of a numerical scheme is to compare the formal order of accuracy with the observed order of accuracy (OOA). The OOA is calculated using norms of the actual spatial error achieved, and thus encompasses all error sources within the algorithm (Roy, 2003). The OOA should approach the formal order if the solutions are in the range of asymptotic convergence (Roy, 2003). Thus, a comparison of the OOA with the formal order will reveal if other prevalent error sources exist.

First, calculations of the L_1, L_2, and L_∞ error norms are conducted for grid spacing, *k*, according to Eqs. 56, 57, and 58; where *f* is the numerical solution and *n* is summed over the number of points chosen for the calculation, *N*.

$$L_{1,k} = \sum_{n-1}^{N} \left| f_{k,n} - f_{exact,n} \right| \Big/ N \tag{56}$$

$$L_{2,k} = \sum_{n-1}^{N} \left(\left(\left| f_{k,n} - f_{exact,n} \right| \right)^2 \Big/ N \right)^{1/2} \tag{57}$$

$$L_{\infty,k} = max \left| f_{k,n} - f_{exact,n} \right| \tag{58}$$

Using these norms, the OOA ($\tilde{p}$) for a numerical algorithm can be calculated according to Eq. 59, where L is the chosen error norm and r is the grid refinement ratio defined in Eq. 60. The level of grid spacing relative to a set of solutions on multiple meshes is denoted by the base size h, with h = 1 for the finest mesh. In cases where a uniform mesh distribution cannot be obtained, such as when an unstructured mesh is employed, simply reducing the base size will not result in a perfectly proportioned increase in mesh nodes. Thus, it is possible to calculate an effective refinement ratio, r_{eff} (Eq. 61), where N_i is the total number of nodes used on the i-th grid and D is the dimensionality of the domain (Kwasniewski, 2013).

$$\tilde{p} = \frac{ln\left({}^{L_{k+1}}/_{L_k}\right)}{ln(r)} \tag{59}$$

$$r = {}^{h_{k+1}}/_{h_k} \tag{60}$$

$$r_{eff} = \left({}^{N_1}/_{N_2}\right)^{\frac{1}{D}} \tag{61}$$

The above approach requires that an exact, analytical solution is known. When this is not the case, an estimation of the exact solution ($\tilde{f}_{exact}$) can be derived using Richardson Extrapolation (RE) (Richardson, 1910). While a more thorough review is provided by Roache (1994), the end result is that two discrete solutions are used to estimate an exact solution according to Eq. 62. The power of RE is that the discretization error for any solution can be calculated regardless of the mesh density, assuming other numerical errors are small. Thus, highly refined and computationally expensive meshes can be avoided. However, RE does require sufficient refinement such that the solutions are in the asymptotic range of convergence. It also requires that refinement is conducted systematically and uniformly over the entire domain. It should be noted however that RE is not

applicable to problems where the boundary conditions evolve or the mesh deforms, such as in FSI problems.

$$\tilde{f}_{exact} = f_k + \frac{f_k - f_{k+1}}{r^p - 1} \tag{62}$$

To determine the OOA ($\tilde{p}$) of the scheme without knowledge of the exact solution, discrete solutions on three grid spacings are required according to Eq. 63. The grid refinement factor, *r*, must remain constant.

$$\tilde{p} = \frac{ln\left(\frac{f_{k+2} - f_{k+1}}{f_{k+1} - f_k}\right)}{ln(r)} \tag{63}$$

To provide a uniform means of reporting grid refinement studies, Roache (1994) introduced the Grid Convergence Index (GCI) shown in Eq. 64. Based upon the principle of RE, it converts the extrapolated error into an uncertainty using a factory of safety, F_s. Roache recommends $F_s = 1.25$ when the OOA matches the formal order and $F_s = 3$ when it does not.

$$GCI = \frac{F_s}{r^p - 1} |f_{k+1} - f_k| \tag{64}$$

With brief reviews of stability, numerical error, FEM, and CFD established above, a significant number of benchmark problems were conducted to verify Abaqus/Explicit's simulation of structural deformation, fluid flow, and FSI. The purpose is to not only confirm formal and observed orders of accuracy in order to predict errors, but also to achieve a general understanding of the code nuances and applicability to the physics of interest. The author has found this particularly important when utilizing a third-party or commercial product without access to source documents or code.

3.5.3 Uncertainty quantification

Numerous sources of uncertainty pervade numerical simulations of physical systems. Because small variations in operating conditions or parameters can result in large changes to the final result, it is important to consider their effect and quantify how they might propagate into the solution. For example, aero applications near the transonic regime may experience unexpected shock formation resulting from uncertain variation in the Mach number or angle of attack. Also, hydro applications operating near the onset of cavitation may experience unsteady shear loading or reduced resistance resulting from uncertain variation in the fluid density or velocity. As a topic closely related to V&V, uncertainty quantification (UQ) in CFD is a method to evaluate a computation's variability; the goal being to increase reliability and trustworthiness of the reported results.

A distinction should be drawn between "error" and "uncertainty." Error is a known deficiency in the modeling process, not due to a lack of knowledge (AIAA G-077, 2002). An acknowledged error is known to exist and can be estimated and reduced. Examples are the various computational errors described above or deliberate simplification of the physical model. An unacknowledged error is a coding or operator mistake. It involves the human element and can be minimized by a thorough verification effort. Conversely, uncertainty concerns the natural physical variations present or a potential modeling deficiency resulting from a lack of knowledge. The important difference between error and uncertainty is that error can be discovered and reduced based upon existing knowledge, whereas uncertainty cannot.

Oberkampf and Roy (2010) suggest two categories of uncertainty; epistemic and aleatory. Epistemic uncertainty is any deficiency in the modeling process that is due to a lack of knowledge.

These uncertainties can be reduced via additional study, experimentation, etc., and generally cannot be represented in a probabilistic manner. Examples of epistemic uncertainty in FSI simulations are improper choice for the interaction algorithm or incorrect specification of the slip condition upon a boundary.

Aleatory uncertainty is the inherent randomness in physical parameters or the environment that are manifest in the system being analyzed. They cannot be reduced by means of additional knowledge and are most appropriately described by probabilistic approaches. Examples of aleatory uncertainty in FSI simulations include the specification of material elastic properties, geometric variations in a manufactured part, or the freestream unsteadiness in aero/hydrodynamic flows.

With the importance and definition of UQ established, an efficient approach for its conduct must be identified. Due to the computationally intensive nature of unsteady CFD, and the fact that this present research utilizes commercial codes, the method should be "nonintrusive." Only approaches based upon a limited number of deterministic solutions are considered. In work by Loeven (2010), a wide range of test cases are performed to evaluate the efficiency of various UQ approaches as applied to CFD. He identifies the Probabilistic Collocation (PC) method (Tatang et al., 1997) as a simple and nonintrusive technique for aleatory uncertainty quantification.

The PC method is based upon polynomial chaos framework (Wiener, 1938) and requires that the uncertainty in any given parameter can be aptly characterized by probability density functions (Normal, Log Normal, Uniform, Weibull, etc.). As long as a parameter can be described statistically, the method can be expanded to account for simultaneous uncertainty among multiple parameters (Gautschi, 2005). The process is summarized as follows:

1. Define the probability distribution for the uncertain parameter(s).
2. Compute the collocation points and associated weighting factor for each parameter.
3. Run the computation at each collocation point to obtain a deterministic result.
4. Compute a mean and variance of the stochastic solution using Eq. 65 and Eq. 66.

As a simple example, the mean (μ) for a set of solutions can be calculated for a single uncertain parameter x by Eq. 65, where u_i is the deterministic solution at a collocation point i, ω_i is the probability weighting at the collocation point, and N_p is the number of collocation points. Similarly, the variance (σ^2) can be calculated using Eq. 66. This method is used to estimate the mean and variance for seal resistance in Section 4.2.8.

$$\mu = \sum_{i=1}^{N_p} u_i(x)\omega_i \tag{65}$$

$$\sigma^2 = \sum_{i=1}^{N_p} [(u_i(x) - \mu)^2]\, \omega_i \tag{66}$$

Chapter 4

Results

A significant step in this work is to verify and validate the STAR-CCM+ modeling approach for the ACV bow seal FSI problem. The approach is verified if the results are both computationally consistent and convergent. Further, the approach is validated if a favorable comparison can be made between the numerical results and a benchmark case or experimental dataset. In this section, two tightly-coupled FSI studies are conducted using STAR-CCM+ to verify, validate, and ultimately explore the problem of ACV seal resistance. The first study simulates the popular elastic beam FSI numerical benchmark set forth by Turek and Hron (2006). Exploration of spatial discretization, timestep, FSI under-relaxation, and inner iteration count is conducted to identify optimum parameters when using STAR-CCM+. The primary result is V&V of the approach for unsteady tightly-coupled FSI simulations having large added-mass instabilities.

The second study increases the problem complexity by simulating the planer bow seal described in section 1.4.1, as studied by Zalek and Doctors (2010), Bloxom (2014), and Wiggins (2014). The results compare favorably to those provided in previous work, validating STAR-CCM+ as a seal resistance exploratory tool.

4.1 Elastic beam fluid-structure interaction

The first problem explored is that of an incompressible Newtonian fluid interacting with an elastic solid in laminar channel flow. Turek and Hron (2006) first proposed this problem as a means to rigorously evaluate potential FSI coupling schemes and algorithms. It consists of a cylinder transverse to the flow with an elastic beam attached to the trailing edge. While the problem boundaries and conditions appear deceptively simple, the fluid solution is complex due to self-induced oscillations, vortex shedding, and added-mass effects. For this reason, this problem is referenced and utilized often within the FSI community (Breuer et al., 2012, Giannelis, 2015, Engels, 2015, Turek and Hron, 2011).

Nine variations of the problem are provided in the benchmark reference. CFD1, CFD2, and CFD3 are conducted with the elastic beam fixed so that only oscillations of the fluid are captured. CSM1, CSM2, and CSM3 remove the fluid and allow the structure to freely fall under the influence of gravity only. FSI1, FSI2, and FSI3 allow for full interaction between the fluid and structure. Due to the transient nature of this problem, time histories of the tip position, fluid oscillation frequencies, as well as lift and drag forces upon the submerged body are captured as the comparative benchmark data. The problem parameters are provided in Table 1 and Figure 21 for the cases CFD3 (Benchmark 1), CSM2 (Benchmark 2), and FSI3 (Benchmark 3).

Table 1. Elastic beam FSI benchmark parameters

Geometry	domain length	2.5	m
	domain height	0.41	m
	domain width	1	m
	cylinder radius	0.05	m
	cylinder center	0.2, 0.2	(*x*, *y*) m
	beam length	0.35	m
	beam thickness	0.02	m
	beam right corner position	0.6, 0.19	(*x*, *y*) m
Fluid properties (CFD3, FSI3)	density, ρ_f	1000	kg/m^3
	dynamic viscosity, μ_f	1	Pa-s
	characterisitic velocity, *U*	2	m/s
	Re number	200	
Solid properties (CSM2, FSI3)	density, ρ_s	1000	kg/m^3
	Poisson ratio, *v*	0.4	
	shear modulus, μ_s	2	kg/ms^2
	elastic modulus, *E*	5.6	MPa

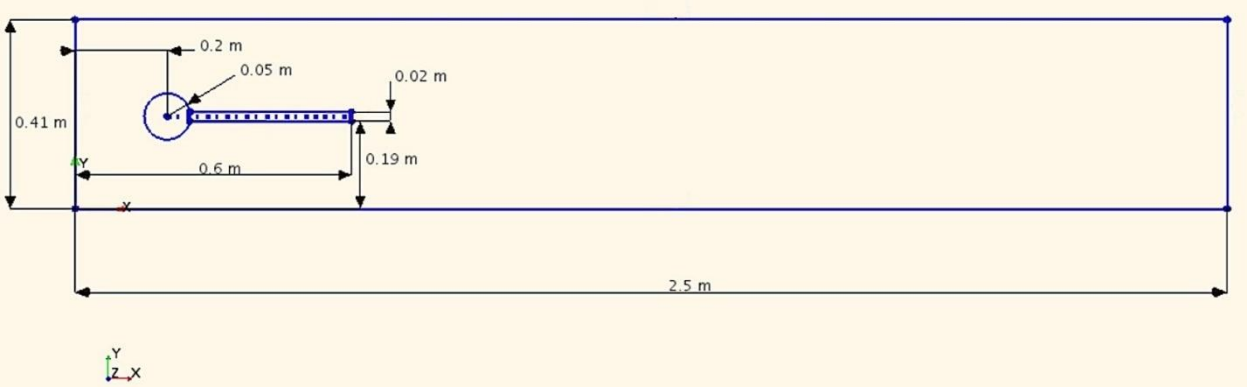

Figure 21. Elastic beam FSI benchmark dimensions

The problem setup using STAR-CCM+ (12.04.011) is as follows. As the fluid is considered incompressible and transient, an implicit, unsteady segregated solver is utilized having a second order upwind convection scheme. Under-relaxation factors for the velocity and pressure equations are set to 0.6 and 0.2, respectively. For boundary conditions, a no-slip condition is applied on the channel top and bottom walls and cylinder/beam surfaces. The sides of the channel (*Z*-normal)

are slip walls. A pressure outlet of P = 0 Pa is applied to the exit and the fluid speed and pressure are initialized at zero. A time-varying parabolic velocity inlet condition is applied pursuant to that of the benchmark problem by means of a user-defined field function within STAR-CCM+. It is given in Eq. 67 and 68. U is the characteristic velocity and u is the spatially and temporally varying inflow velocity.

$$u(0,y,t) = \begin{cases} u(0,y)\frac{1-\cos\left(\frac{\pi}{2}t\right)}{2} & if\ t < 2.0\ s \\ u(0,y) & otherwise \end{cases} \tag{67}$$

$$u(0,y) = 1.5U\frac{4.0}{0.1681}y(0.41-y) \tag{68}$$

The original benchmark problem is strictly two-dimensional and results are presented per unit depth. However, STAR-CCM+ requires three dimensions in order to utilize the fluid-structure coupling solver. Therefore, the baseline fluid mesh is developed using the Automatic Mesh functionality nested within the Directed Mesh approach. A volume distribution of a single, 1 m element is applied in the Z-direction to provide the third dimension. An unstructured triangle background mesh and two volumetric refinements establish the topology. The first refinement volume targets a surface size of 50% of the base size, and the second refinement volume targets a surface size of 25% of the base. The element length growth rate is limited to 1.1 to ensure smooth transitions between refinement areas. Simulations are conducted on three grid levels using base sizes of 0.020 m, 0.010 m, and 0.005 m in order to confirm grid independence as well as verify the observed order of accuracy (OOA). Figure 22 provides an example of the mesh topology for mesh level 1.

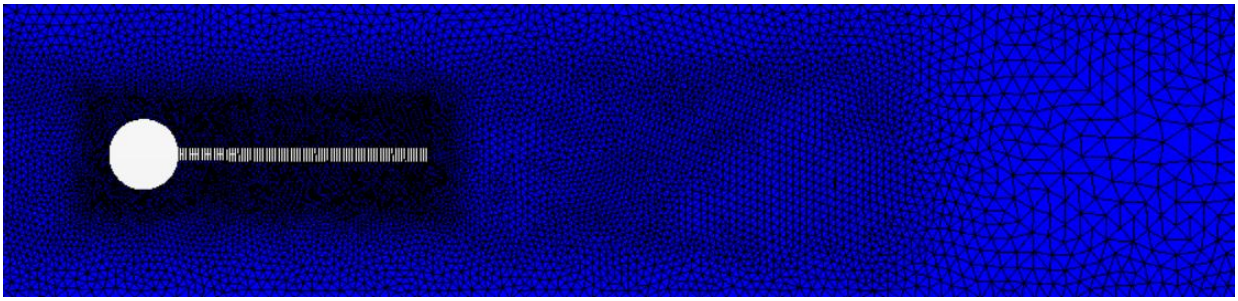

Figure 22. Volume refinements on mesh level 1

4.1.1 Benchmark 1: fluid

The first scenario benchmarks the fluid solution, utilizing the parameters for CFD3 and the geometry above. Second order temporal discretization is implemented and the time step is fixed at $\Delta t = 0.005$ s. CFL-based time step control is not applied. As initial simulations revealed elevated momentum residuals at this time step, additional iteration stopping criteria are established to ensure suitable convergence prior to progressing to the next time step. The normalized residual minimum is 1E-1 and the minimum inner iterations per time step are 50. Initially the solver had problems achieving these normalized residuals. Improvements to the convergence is found by reducing the width of the domain in the *Z*-direction, and thus improving the *X*/*Z* aspect ratio.

Due the problem's transient nature, a 10 s simulation is required to establish both fully developed flow and a steady fluid oscillation. Figure 23 plots lift versus time and reveals the initial instability and eventual steady oscillation by approximately 8.5 s. Figure 24 shows the velocity magnitude at the end of the simulation, revealing oscillation in the fluid downstream of the structure. The fixed trailing beam extends the recirculation region, increasing the characteristic length and stabilizing the flow.

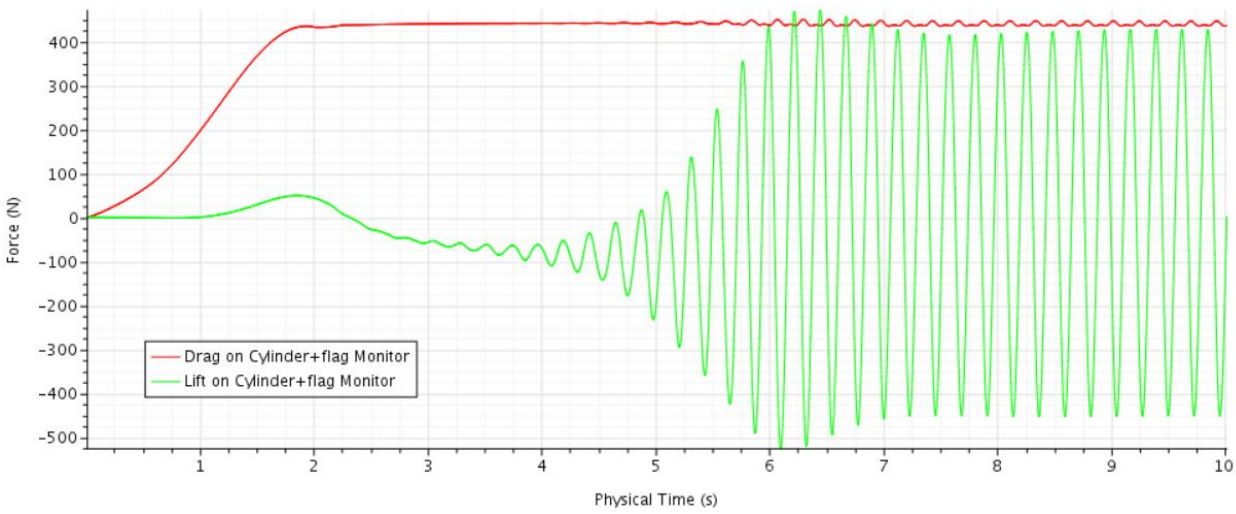

Figure 23. CFD3 benchmark lift versus time, 0 to 10 s, mesh level 1

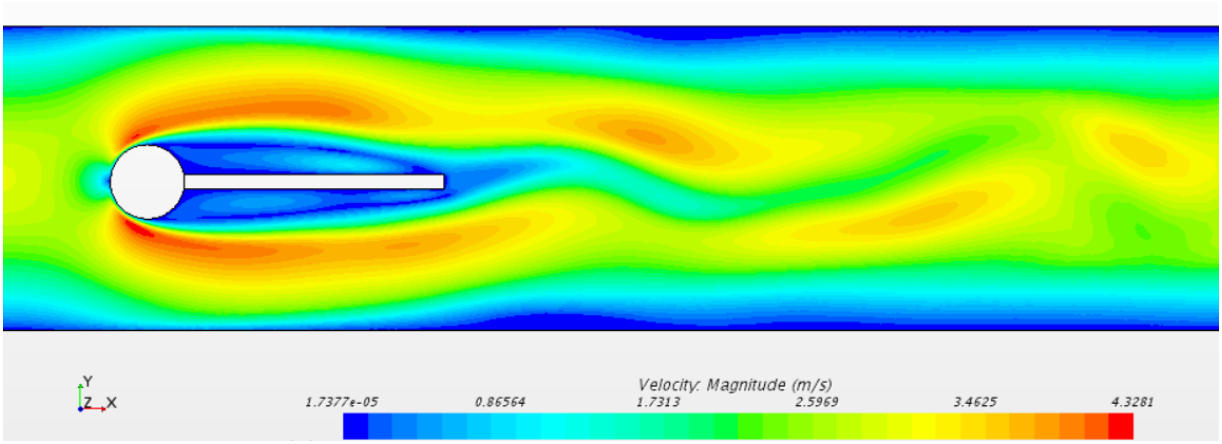

Figure 24. CFD3 benchmark velocity magnitude at t = 10 s

As the lift and drag results are time-dependent and subject to small perturbations, they are presented similar to the reference solution as: *mean* ± *amplitude* [*frequency*]. First, the averages of the extreme minimums (Min_{AVE}) and extreme maximums (Max_{AVE}) are calculated for the period of the final three oscillations. Then the *mean*, *amplitude*, and *frequency* are calculated according to Eq. 69, Eq. 70, and Eq. 71, respectively. The *frequency* calculation is also an average,

as it considers the total number of cycles (N_{cyc}) that occur between the time of the initial extreme maximum (t_{Max_init}) and final extreme maximum (t_{Max_final}).

$$mean = \frac{1}{2}(Max_{AVE} + Min_{AVE}) \tag{69}$$

$$amplitude = \frac{1}{2}(Max_{AVE} - Min_{AVE}) \tag{70}$$

$$frequency = \frac{N_{cyc}}{(t_{Max\_init} - t_{Max\_final})} \tag{71}$$

A summary of the lift and drag results for the simulation at each mesh level are tabulated in Table 2. The drag result at the finest mesh of 441.44 N ± 6.56 *N* [4.26 Hz] is a good match to the Turek and Hron (2006) reference solution of 439.45 N ± 5.6183 *N* [4.40 Hz]. The mean drag differs by only 0.45%, while the amplitude differs by 16.7% at the finest mesh level. The frequency differs by only 3.19% at the finest mesh level. Figure 25 plots drag versus time for the final oscillations at each mesh level. While the separate mesh levels result in different phases, it is noted that the drag curve exhibits both absolute and local extrema at twice the frequency of the lift curve (typical of bluff bodies).

Table 2. CFD3 benchmark results (Δt = 0.005 s)

Mesh Level	Base size (*m*)	Fluid elements	*r*	r_{eff}	Mean Drag (*N*, *Hz*)	Mean Lift (*N*)	OOA (Mean Drag)	f_{exact}
3	0.020	18214	-----	-----	458.37	-36.96	-----	-----
2	0.010	64170	2	1.8770	445.45	-10.83	-----	440.02
1	0.005	229630	2	1.8917	441.44	-2.13	1.84	439.76
				Present solution (mesh level 1):	441.44 ± 6.56[4.26]	−2.13 ± 462.80[4.26]		
Δt = 0.005 *s*				Reference solution:	439.45 ± 5.62[4.40]	−11.90 ± 437.81[4.40]		

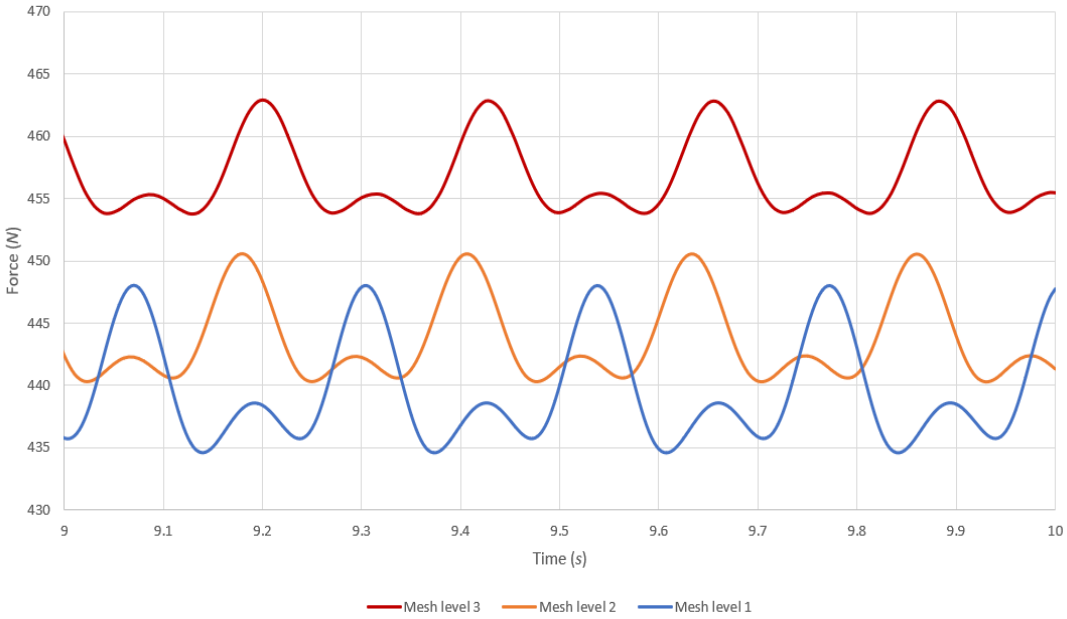

Figure 25. CFD3 benchmark drag versus time (Δt = 0.005 s)

Figure 26 plots lift versus time for the final oscillations at each mesh level. The lift result at the finest mesh of −2.13 N ± 462.80 *N* [4.26 Hz] varies more considerably from the reference solution of −11.90 N ± 437.81 *N* [4.40 Hz]. The mean lift has shifted to a more neutral value while the amplitude differs by 5.7% at the finest mesh level. The magnitude of these differences is not too concerning, especially when other researchers have shown similar deviations for this benchmark using other commercial software. For instance, Gianellis and Vio (2015) under-predicted the amplitudes of lift and drag for CFD3 by 3.3% and 13.3%, respectively, using ANSYS Fluent. The variation in this case was attributed to increasing mesh size downstream of the structure.

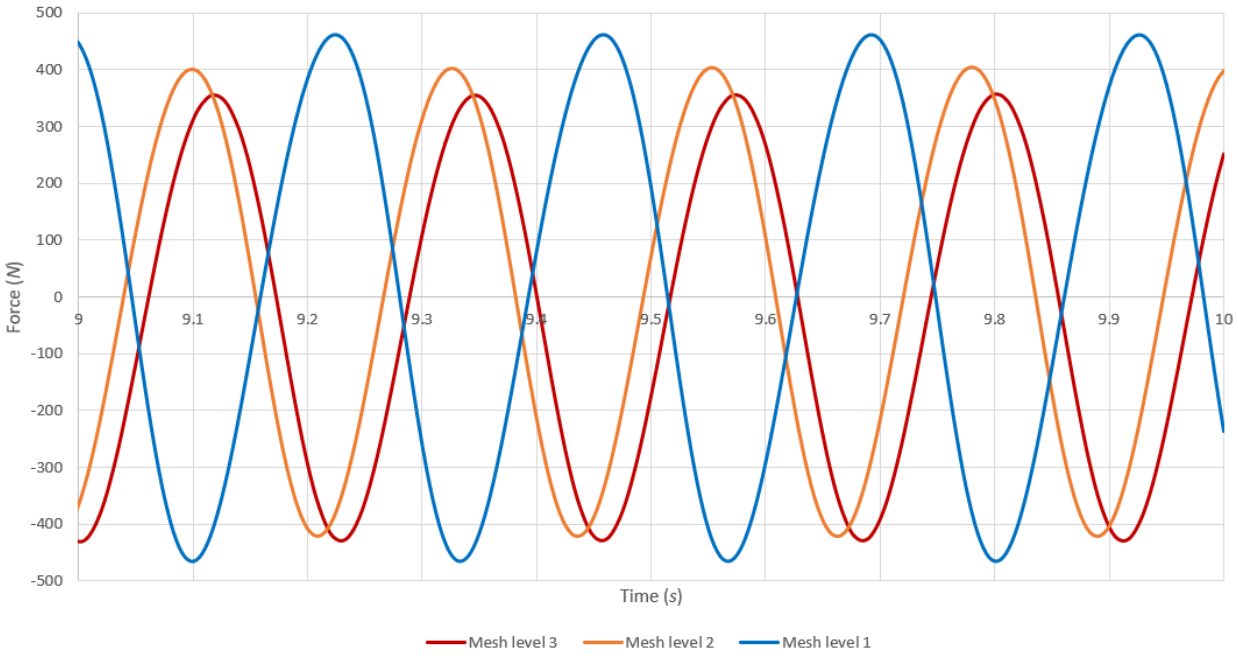

Figure 26. CFD3 benchmark lift versus time, t = 9 to 10 s (Δt = 0.005 s)

In Table 2, the effect of mesh spacing shows the present solutions converge toward the reference solutions with increased refinement. As the cell sizes resulting from the automated mesh are specified as a percentage of the base size, global refinements are uniformly implemented by simply halving the base size. The formal refinement ratio, r, is 2. However, the unstructured mesh results in slightly imperfect successive mesh refinements and thus it is useful to assess convergence using the effective refinement ratio (Eq. 61). The OOA based upon the mean drag value is calculated as 1.84 using Eq. 63, which confirms the formal accuracy as second order for the upwind convection scheme. Eq. 62 is used to estimate the mean drag exact solution as f_{exact} = 439.76 N, clearly showing agreement (0.07% error) with the reference solution of 439.45 N.

When simulating highly oscillatory transients, such as in cylinder vortex shedding, time step size plays an important role in result accuracy. In order to remain consistent with the reference solution,

the time step utilized for the above results is taken a priori from Turek and Hron (2006). Their work also confirms that shedding frequency is sensitive to temporal refinement, but less-so to spatial refinement. As an implicit convection scheme is implemented in STAR-CCM+, it is desirable to specify a time step that maximizes temporal accuracy so that the remaining errors in the solution are discretization, roundoff, and algorithmic in nature. In order to assess the effect of temporal refinement in the current STAR-CCM+ implementation, additional runs are conducted at a reduced timestep.

To determine the new time step size, a two-dimensional CFL analysis is conducted using Eq. 55 and the observed maximum velocities of $U_x = 4.10$ m/s and $U_y = 2.35$ m/s. Limiting $CFL \leq 1$ gives a time step of 1.55E-4 s for the finest mesh ($\Delta x \cong 0.001\ m$). Unfortunately, this timestep is costly for a 10 s of simulation at the finest mesh. As a compromise, a Strouhal analysis is conducted to determine if guidance based upon cylinder shedding is appropriate. Using the observed frequency, characteristic velocity, and cylinder diameter, the Strouhal number is *St* = 0.22. This is consistent with a long cylinder in uniform flow of Re = 200. Of course, the non-uniform inflow and constricting channel serves to increase the frequency, whereas the fixed trailing beam decreases frequency. These off-setting features do not appear to have a significantly altered the shedding frequency from that of an ideal cylinder. Therefore, the general practice of using a timestep of 1/100 of the fundamental period for cylinder shedding is chosen.

Table 3 provides CFD3 benchmark results using $\Delta t = {}^{1}/_{100}\left({}^{1}/_{4.3956\ s}\right) = 0.0022750\ s.$ These updated results show improvements in all regards, which reveals the importance of time step size in highly transient problems. On the finest mesh, the mean drag differs by only 0.42%, the drag amplitude differs by only 2.13%, and the drag frequency differs by 1.01%. Most improved

are results for lift. The mean lift differs by 2.52% and the lift amplitude differs by 3.61%. The OOA is calculated as 1.87 using the results on two meshes, per the procedure presented in section 3.5.2 The prediction of the exact solution, f_{exact}, differs from the benchmark result by only 0.034%.

Table 3. CFD3 benchmark results (Δt = 0.002275 s)

Mesh Level	Base size (m)	Fluid elements	r	r_{eff}	Mean Drag (N, Hz)	Mean Lift (N)	OOA (Mean Drag)	f_{exact}
2	0.010	64170	-----	-----	445.50	-10.63	-----	-----
1	0.005	229630	2	1.8917	441.28	-12.20	1.87	439.60
				Present solution (mesh level 1):	441.28 ± 5.74[4.44]	−12.20 ± 439.36[4.44]		
Δt = 0.0022750 s				Reference solution:	439.45 ± 5.62[4.40]	−11.90 ± 437.81[4.40]		

In summary, these CFD3 results show a successful implementation of the fluid solution for the benchmark problem. Both the spatial and temporal refinements yielded consistent improvements when compared to the benchmark drag result. The fluid solution is therefore considered verified based upon OOA and convergence. It is considered validated based upon the relative error to the benchmark results for drag and lift. Additional fluid benchmarks are not attempted here, as further verifications can be found in the extensive STAR-CCM+ Verification Suite (Siemens, 2018).

4.1.2 Benchmark 2: structure

The next benchmark focuses solely upon the structure using parameters of CSM2. With identical geometry to the previous problem, the elastic beam remains attached to the cylinder and is released to fall under the influence of the gravitational body force (-2 m/s^2). The surrounding fluid is removed from the simulation and there is no numerical material damping. The analysis is static, dynamics of the beam are not considered, and the steady state tip displacement is reported as the reference result (Figure 27).

CSM2 is implemented in STAR-CCM+ as follows. The solid stress solver is specified to use a 2nd order Newmark implicit integration scheme (Newmark parameter = 0.5) to minimize the numerical damping which would occur in the default 1st order Backward Euler scheme. Solid displacement motion is specified for the region, thus enabling nonlinear geometry via updates of the stiffness matrix at each iteration. The linear isotropic elastic material model provides the constitutive relations, with properties defined in Table 1 above.

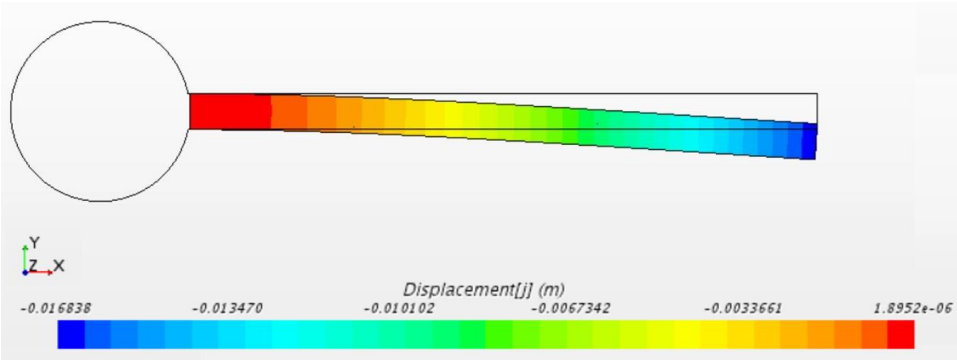

Figure 27. Example of CSM2 deflection

A directed mesh operation is used to uniformly discretize the beam, both through the thickness and along the length (Figure 28). As the simulation is quasi two-dimensional, only one element is specified in the width for all models. The mid-side vertex option is activated to achieve quadratic continuum elements, which enables increased accuracy in bending when only one element is used through the beam thickness. The coarsest mesh uses 1 element through the thickness and 20 elements along the length. Element counts are doubled in each dimension for successive meshes.

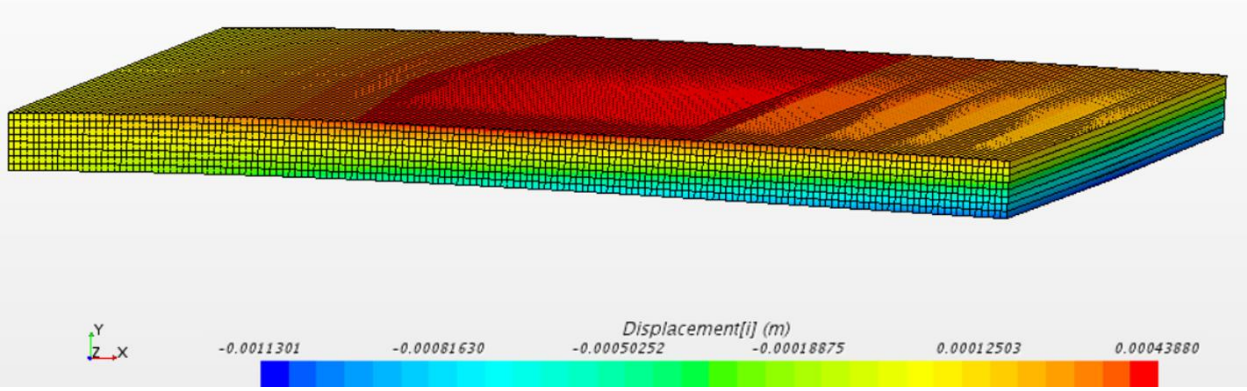

Figure 28. Elastic beam *x*-displacement on mesh level 3

The CSM2 benchmark result for the present STAR-CCM+ implementation is shown in Table 4. In general, increased refinement appears to converge both the *x*-displacement and *y*-displacement toward the reference solution. However, a 0.94% error remains even for the finest mesh, which is significantly discretized. An estimate of the exact solution for *y*-displacement based upon the convergence results is given by f_{exact} (-1.683E-2 m). This result is closer to that obtained by mesh level 1 (-1.681E-2 m) than the reference solution (-1.697E-2 m). f_{exact} differs from the benchmark by 0.8%.

At face value, the OOA appears to under-perform the advertised formal order of 2. However, it is quickly observed that the increased bending accuracy afforded by quadratic elements suppresses apparent improvements due to additional thickness discretization. For an interesting comparison on the effects of using the mid-side vertex option, and additional mesh level (l-b) is developed by reducing the thickness discretization to a single element while the length is maintained. The close match of mesh 1-b to f_{exact} reveals the relative insensitivity to thickness discretization for this problem when using quadratic elements.

Table 4. CSM2 benchmark results (quadratic elements)

Mesh Level	Nel length	Nel thickness	Total Nel	*r*	tip *X*-displacement (*m*)	tip *Y*-displacement (*m*)	OOA	f_{exact}
6	20	1	20	-----	-4.273E-04	-1.591E-02	-----	-----
5	40	2	80	2	-1.304E-04	-1.647E-02	1.488	-1.677E-02
4	80	4	320	2	-2.966E-04	-1.666E-02	1.190	-1.682E-02
3	160	8	1280	2	-3.794E-04	-1.675E-02	1.070	-1.683E-02
2	320	16	5120	2	-4.208E-04	-1.679E-02	1.137	-1.683E-02
1	640	32	20480	2	-4.815E-04	-1.681E-02	-----	-----
1b	640	1	640	-----	-4.598E-04	-1.677E-02		
				Reference solution :	-4.690E-04	-1.697E-02		

In order to more thoroughly document the OOA, solutions on mesh levels 1, 1b, 2, and 3 are repeated using strictly linear continuum elements. The results are shown in Table 5. As expected, the OOA is much improved, just below the formal order of 2. The estimate of the exact solution, f_{exact}, closely approximates both the finest mesh result (mesh 1), and the reference solution. As expected, a single linear element through the thickness (mesh 1b) results in an overly stiff response, underpredicting tip *y*-displacement by an order of magnitude.

Table 5. CSM2 benchmark results (linear elements)

Mesh Level	Nel length	Nel thickness	Total Nel	*r*	tip *X*-displacement (*m*)	tip *Y*-displacement (*m*)	OOA	f_{exact}
3	160	8	1280	-----	-5.224E-04	-1.646E-02	-----	-----
2	320	16	5120	2	-4.964E-04	-1.671E-02	1.716	-1.682E-02
1	640	32	20480	2	-4.803E-04	-1.679E-02	-----	-----
1b	640	1	640	-----	-1.444E-04	-9.424E-03		
				Reference solution :	-4.690E-04	-1.697E-02		

In summation, the solid stress solver is shown to perform adequately for further use in this benchmark study. Quadratic elements using the mid-side vertex option are slightly more accurate for highly refined meshes, but their use is more advantageous when one or two elements are used though the thickness. It is proposed to use a single quadratic element in the thickness for subsequent simulations. The solver is considered verified based upon convergence at a rate

approaching the formal order of accuracy. The solver is considered validated based upon tip displacements approaching the benchmark result.

4.1.3 Benchmark 3: fluid-structure interaction

The next scenario attempted is FSI3. The specified parameters result in both strong added-mass effects and large deflections, as the elastic material density provides $\rho_f/\rho_s = 1$, and the characteristic inflow provides Re = 200. Using the solvers, geometry, boundary conditions, and discretization described above, simulations are conducted to evaluate a matrix of run cases described in Table 6. This table explores variabilities in time step, spatial discretization, inner iterations, under-relaxation of the FSI solver, and FSI coupling method. The final column lists similar cases that vary in only one parameter, making them well suited for direct comparison.

Table 6. FSI3 benchmark run matrix

Case #	Time Step (s)	Fluid mesh edge length (m)	Inner Iterations	FSI under-relaxation	Coupling type	Comparative Cases
0	0.001	0.02	10	0.5	Explicit 2-way	-----
1	0.001	0.02	10	0.5	Implicit 2-way	2,3,4
2	0.001	0.01	10	0.5	Implicit 2-way	1,3,5
3	0.001	0.005	10	0.5	Implicit 2-way	1,2,6
4	0.0005	0.02	10	0.5	Implicit 2-way	1,5,6
5	0.0005	0.01	10	0.5	Implicit 2-way	2,4,6
6	0.0005	0.005	10	0.5	Implicit 2-way	3,4,5
7	0.0005	0.005	10	0.4	Implicit 2-way	6,8
8	0.0005	0.005	10	0.9	Implicit 2-way	6,7
9	0.0005	0.005	30	0.5	Implicit 2-way	6,10,11
10	0.0005	0.005	20	0.5	Implicit 2-way	6,9,11
11	0.0005	0.005	40	0.5	Implicit 2-way	6,9,10

In the reference work, solutions are provided for the benchmark 3 case (FSI3) using timesteps of 0.001 s and 0.005 s. As the highest frequency of interest was found to be oscillation of the lift force at 10.9 Hz, the largest timestep slightly misses the general criteria for 1/100 of the

fundamental period of interest: $^1/_{100}\,(^1/_{10.9\ Hz}) = 0.0009\ s \leq 0.001\ s.$ However, for consistency it is accepted as the baseline timestep for the cases herein.

As convergence of the fluid equations is concerned, it is typical to set a minimum limit to the residuals, such as 1E-7, in order to obtain consistent levels of iterative error across various simulations. This is especially important when comparative CPU time studies are performed. However, in this work, the desire is to explore the capability of the FSI solver when subjected to an explicit number of inner iterations, provided the fluid residuals have converged below some minimum level. This is because choice of the FSI displacement under-relaxation parameter has a large effect on the rate of FSI convergence. Generally, a smaller under-relaxation parameter slows convergence and increases stability, while a larger under-relaxation parameter speeds convergence (up to a point) and decreases stability. Further, the rate of convergence changes throughout the simulation due to the unsteadiness of the problem. Thus, the choice is made to explicitly hold the majority of simulations to 10 inner iterations per time step, except for cases 9, 10, and 11 which explore this factor as an independent variable.

Case 0: Explicit coupling

Case 0 simulates explicit (loose) coupling by setting the FSI displacement convergence tolerance = 1 for the fluid-structure coupling solver. In effect, the convergence tolerance is automatically met after only one iteration, thereby exhibiting loose coupling by definition. This case is specifically attempted to not only show the inappropriateness of loose coupling for large added-mass effect problems, but also to investigate whether the implicit fluid solver could be manipulated to maintain some level of stability and usefulness.

In general, the results show it is difficult to maintain fluid stability with only one FSI coupling per time step, as the simulation is unstable for the parameters specified in Table 6. The time step requires significant reduction from 0.001 s to *O*E-6 s on fluid mesh level 3 in order minimize displacement of the seal. A larger timestep allows the seal to displace beyond the ability of fluid solver to recover reasonable fluid values. This issue is most sensitive at the beam tip, where velocities quickly escalate. The mean and max CFL values at the reduced timestep are on the order of *O*E-6 and *O*E-7, respectively, which are incredibly small. This speaks to the inefficiency of the problem approach to simulate a transient event to a timescale of *O*E1 s. As this case demonstrates first-hand the issues with added-mass instability discussed by others (Causin et al., 2005, Le Tallec and Mouro, 2001), it is not given further consideration.

Cases 1 through 3: Effect of spatial discretization for Δt = 0.001 s

Cases 1 through 3 are conducted to investigate the effect of spatial discretization for three mesh levels at a timestep of Δt = 0.001 s. The results provided in Table 7 show mixed performance as the mesh is refined. At the finest mesh level, the mean drag only varies from the reference solution by 2.3%, however the frequency of oscillation is significantly lower. Also, the mean lift does not show monotonic convergence toward the reference solution and exhibits even larger errors in amplitude and frequency. As a cause for this departure, inspection of the fluid residuals achieved using 10 iterations per timestep reveals dramatic differences in convergence achieved between periods when the tip acceleration is small and when it is large; a clear indicator of added-mass instability. The solution is to add additional iterations to bring the residuals down.

Regarding the differences seen in the frequency result, it should be mentioned that the reference solution only uses one oscillation period to determine the periodic frequency. As the time histories

reveal small variations in the period throughout the simulation, the only means for an equivalent comparison is for the benchmark to specifically state the time for which the frequency measurement was made (which it does not). For this reason, the frequencies reported here are averages over three cycles, as defined previously in Eq.71 .

Table 7. Results for cases 1, 2, and 3; effect of spatial discretization, Δt = 0.001 s

Case	Mesh Level	Edge length (m)	Fluid elements	r	r_{eff}	Tip X-disp, m ($\times 10^{-3}$)	Tip Y-disp, m ($\times 10^{-3}$)	Mean Drag (N, Hz)	Mean Lift (N)
1	3	0.020	18214	-----	-----	-3.02 +/- 2.79[10.8]	1.12 +/- 35.45[5.2]	477.05 +/- 25.62[10.8]	-0.93 +/- 155.18[5.2]
2	2	0.010	64170	2	1.877	-3.88 +/- 3.48[10.0]	1.24 +/- 39.43[4.9]	468.02 +/- 31.22[10.0]	8.61 +/- 150.53[4.9]
3	1	0.005	229630	2	1.892	-5.17 +/- 4.72[7.0]	0.91 +/- 42.09[3.5]	446.86+/- 41.77[7.0]	0.84 +/- 186.28[3.5]
10 inner iterations									
Δt = 0.001 s, FSI underrelaxation = 0.5				Reference solution:		-2.69 +/- 2.53[10.9]	1.48 +/- 34.38[5.3]	457.3 +/- 22.66[10.9]	2.22 +/- 149.78[5.3]

Cases 4 through 6: Effect of spatial discretization for Δt =5E-4 s

Cases 4 through 6 are conducted to investigate the effect of spatial discretization for three mesh levels at a reduced timestep of Δt = 5E-4 s. The results provided in Table 8 shows improved convergence of the mean drag, but not the tip y-displacement, nor mean lift. On the finest mesh level, the mean drag error is 0.6%. Adding the drag amplitude to the drag mean for the finest mesh gives a maximum drag value of 498.45 N. The maximum drag value for the reference solution is 479.96 N, and thus the maximum error is 3.9%. The lift amplitude is over-predicted on all meshes, achieving the best error of 4.7% on the finest mesh. When compared to the previous cases at the larger timestep, the results show improvements in every category. Mean force values are in better agreement with the reference solutions, and the frequencies are approaching those reported as well. While it is obvious that a timestep reduction of 50% results in twice as many total iterations for an equivalent simulated time, an improvement to the results is only provided because the interaction timescale is smaller than the current temporal discretization.

Table 8. Results for cases 4, 5, and 6; effect of spatial discretization, Δt = 5E-4 s

Case	Mesh Level	Edge length (*m*)	Fluid elements	r	*r eff*	Tip X-disp, *m* ($x10^{-3}$)	Tip Y-disp, *m* ($x10^{-3}$)	Mean Drag (*N*, *Hz*)	Mean Lift (*N*)
4	3	0.020	18214	-----	-----	-2.98 +/- 2.75[10.2]	1.14 +/- 34.68[5.4]	477.87 +/- 26.4[10.2]	-1.67 +/- 160.52[5.4]
5	2	0.010	64170	2	1.8770	-3.12 +/- 2.95[10.4]	1.40 +/- 36.67[5.2]	465.60 +/- 29.6[10.4]	5.26 +/- 159.42[5.2]
6	1	0.005	229630	2	1.8917	-4.45 +/- 4.06[9.0]	1.18 +/- 41.7[4.5]	459.91 +/- 38.54[9.0]	8.45 +/- 156.85[4.5]
10 inner iterations									
Δt = 0.0005 *s*, FSI underrelaxation = 0.5 Reference solution:						-2.69 +/- 2.53[10.9]	1.48 +/- 34.38[5.3]	457.3 +/- 22.66[10.9]	2.22 +/- 149.78[5.3]

Cases 6, 7, and 8: Effect of FSI under-relaxation for Δt =5E-4 s

Cases 6, 7, and 8 are conducted at equal temporal and spatial discretization to investigate the effect of the FSI solver under-relaxation (*UR)* factor; 0.4, 0.5, and 0.9, respectively. *UR* factor stabilizes the interaction by reducing the structural displacements provided by the structural solver at each iteration. Low values of *UR* increase stability whereas high values reduce it. Values for *UR* below 0.4 were attempted, but convergence became a problem with inner iterations limited to 10. Attempts to run the problem without under-relaxation (*UR* = 1.0) failed quickly within the first several time steps. Table 9 shows that as the *UR* factor is increased, the mean drag and mean lift are improved, but only marginally. The oscillation frequency for all cases remains low, indicating elevated numerical damping at these case settings. As increased relaxation (decreases in *UR*) serves to stabilize the interaction at the cost of accuracy, it stands to reason that cases with higher levels of relaxation should be afforded more iterations. This is evident by comparing case 6 to case 10 below. Doubling the iterations from 10 to 20 for the same *UR* gave improvements in tip displacement, mean drag, mean lift, and frequency. The takeaway for this study is that an *UR* value of 0.5 up to 0.9 should prove adequate when inner iterations are limited and temporal accuracy is not required, as in the case when an unsteady approach is used to reach a steady state interaction.

Table 9. Results for cases 6, 7, and 8; effect of FSI under-relaxation, Δt = 5E-4 s

Case	Mesh Level	Edge length (m)	Fluid elements	FSI UR	Inner Iter.	Tip X-disp, m ($\times 10^{-3}$)	Tip Y-disp, m ($\times 10^{-3}$)	Mean Drag (N, Hz)	Mean Lift (N)
7	1	0.005	229630	0.4	10	-4.43 +/- 4.08[9.0]	1.17 +/- 41.75[4.5]	460.78 +/- 37.86[9.0]	8.97 +/- 158.13[4.5]
6	1	0.005	229630	0.5	10	-4.45 +/- 4.06[9.0]	1.18 +/- 41.7[4.5]	459.91 +/- 38.54[9.0]	8.45 +/- 156.85[4.5]
8	1	0.005	229630	0.9	10	-4.41 +/- 4.09[9.0]	1.12 +/- 41.58[4.5]	459.25 +/- 39.18[9.0]	7.88 +/- 159.79[4.5]
Δt = 0.0005 s					Reference solution:	-2.69 +/- 2.53[10.9]	1.48 +/- 34.38[5.3]	457.3 +/- 22.66[10.9]	2.22 +/- 149.78[5.3]

Cases 6, 9, 10, and 11: Effect of inner iterations for Δt =5E-4 s

The final cases of 9, 10, and 11 are conducted at equal temporal and spatial discretization to investigate the effect of inner iterations. The results in Table 10 generally show improvements in tip displacement, mean drag, and mean lift as the number of inner iterations increases. Percent errors in the mean drag are all 1% or less, while the best error achieved for mean lift is 4%. This is considered acceptable, as Sheldon et al. (2014) achieved drag errors between 2% to 4% in their partitioned solution of FSI2.

Table 10. Results for cases 6, 9, 10, and 11; effect of inner iterations, Δt = 5E-4 s

Case	Mesh Level	Edge length (m)	Fluid elements	FSI UR	Inner Iter.	Tip X-disp, m ($\times 10^{-3}$)	Tip Y-disp, m ($\times 10^{-3}$)	Mean Drag (N, Hz)	Mean Lift (N)
6	1	0.005	229630	0.5	10	-4.45 +/- 4.06[9.3]	1.18 +/- 41.7[5.3]	459.91 +/- 38.54[9.3]	8.45 +/- 156.85[5.3]
10	1	0.005	229630	0.5	20	-3.21 +/- 3.00[10.6]	1.36 +/- 36.46[5.3]	462.51 +/- 28.64[10.6]	2.37 +/- 160.36[5.3]
9	1	0.005	229630	0.5	30	-2.91 +/- 2.69[10.9]	1.42 +/- 34.94[5.5]	461.96 +/- 27.00[10.9]	2.13 +/- 163.37[5.5]
11	1	0.005	229630	0.5	40	-2.82 +/- 2.66[11.0]	1.43 +/-34.58[5.5]	461.07 +/- 28.00[11.0]	2.32 +/- 172.46[5.5]
Δt = 0.0005 s					Reference solution:	-2.69 +/- 2.53[10.9]	1.48 +/- 34.38[5.3]	457.3 +/- 22.66[10.9]	2.22 +/- 149.78[5.3]

However, as residuals are reduced with increased iterations, the influence of added-mass instability can be seen. Table 11 shows the percent error between the STAR-CCM+ results and the benchmark for tip y-displacement, drag, and lift. Observe that while the mean and amplitude of displacement improves consistently with increased iterations, the drag and lift forces are not as consistent. The percent error of lift amplitude increases with additional inner iterations. Figure 29 plots the tip y-displacement and lift versus time for case 11, where the added-mass instability

is greatest. Although the displacement of the seal is clearly stable, the added-mass effect upon the fluid solution results in a clear "beating" of the lift result. Sometimes referred to as "artificial added-mass effect", the "artificially" is demonstrated in that the beating is a numerical result only. No oscillation is observed in the displacement itself.

Table 11. Percent errors for cases 6, 9, 10, and 11

Case	Inner Iter.	Tip displacement, Y		Drag		Lift	
		mean	amplitude	mean	amplitude	mean	amplitude
6	10	20.27%	21.29%	0.57%	70.08%	280.63%	4.72%
10	20	8.11%	6.05%	1.14%	26.39%	6.76%	7.06%
9	30	4.05%	1.63%	1.02%	19.15%	4.05%	9.07%
11	40	3.38%	0.58%	0.82%	23.57%	4.50%	15.14%

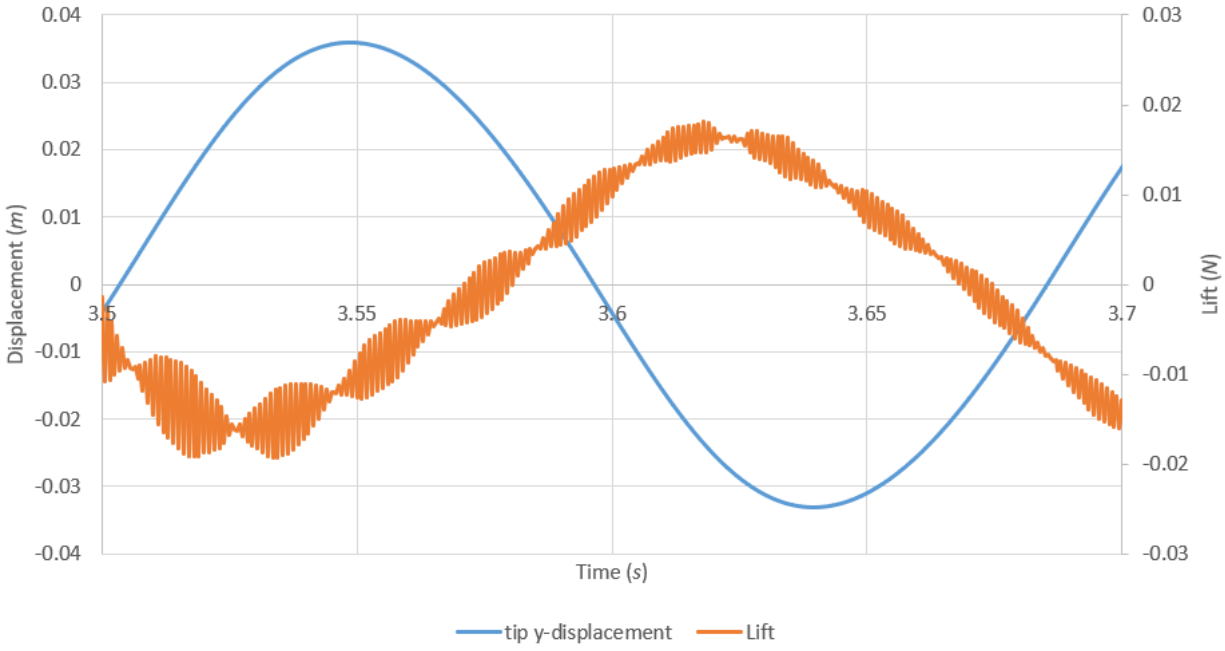

Figure 29. Case 11 results for tip *y*-displacement and lift versus time

The work above for benchmark 1, 2, and 3 clearly shows time-accurate results for unsteady FSI problems require judicious selection of the solver parameters, despite a finely resolved mesh. Timestep, FSI *UR*, and convergence are all important factors for unsteady periodic solutions when

added-mass instability is present. Concessions in levels of convergence and inner iterations can be acceptable when an efficient means to reach steady state is required. Finally, it is demonstrated that high limits on inner iterations can do more harm than good for problems where added mas effect is present. In summation, the work presented using STAR-CCM+ for benchmark 1, 2, and 3 verify the chosen solvers and validate their integrated use for tightly coupled, two-way FSI simulations.

4.2 Planer bow seal

This validation problem replicates the University of Michigan planer bow seal experiment as documented in work by Zalek and Doctors (2010). The problem motivation, description, and experimental results are summarized in Section 1.4.1. Additionally, further comparisons can be made based upon numerical work by Bloxom (2014), as summarized in Section 1.4.3.

As STAR-CCM+ is a modern commercial multi-physics simulation code, it offers a large variety of numerical approaches and physics models. Thus, the choice of solvers, models, and boundary conditions is not as straight-forward as the preceding numerical benchmark. A significant number of test cases and model explorations have been conducted to establish a robust simulation approach based upon the physics of interest. This section describes that approach and provides a comparison of the results to the prior experimental and numerical work.

4.2.1 Geometry and mesh

The computational domain developed is shown in Figure 30 and Figure 31. In general, the geometry parts that define the physical space of both the test platform and tow tank are established to be a near representation of the UM experiment. Particulars are given in Table 12. The

computational domain can be broken down into the static mesh fluid region, the morphing mesh fluid region, the seal structural region, and the fan region. The static mesh fluid region extends 11.5 m downstream of the inlet and 11.0 m upstream of the outlet. It surrounds the morphing mesh region and provides surfaces for various wall, inlet, and outlet boundaries. The morphing mesh fluid region is 3.5 m in length and surrounds the seal, conforming the mesh to the structural deformation. The fan region is 2 m long and interacts with the static mesh fluid region to provide the required cushion pressure.

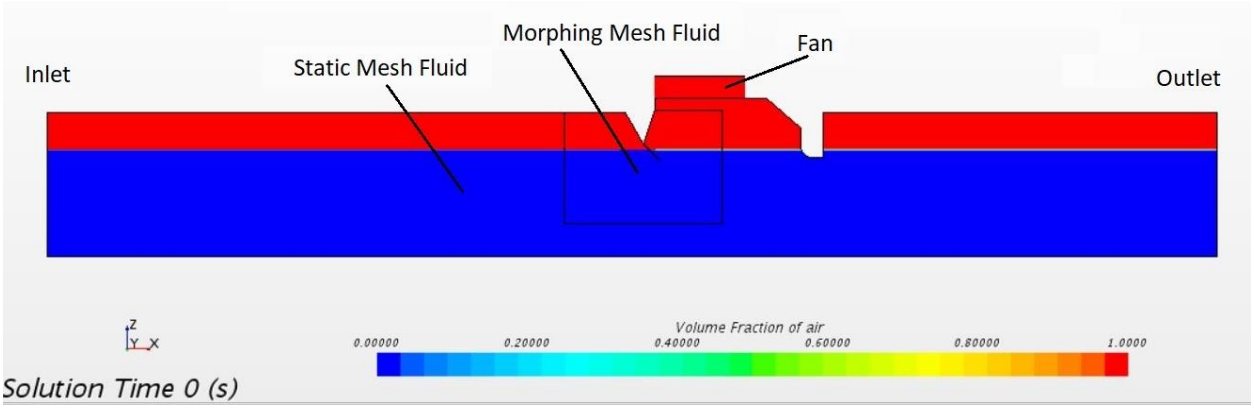

Figure 30. Bow seal domain (*t* = 0)

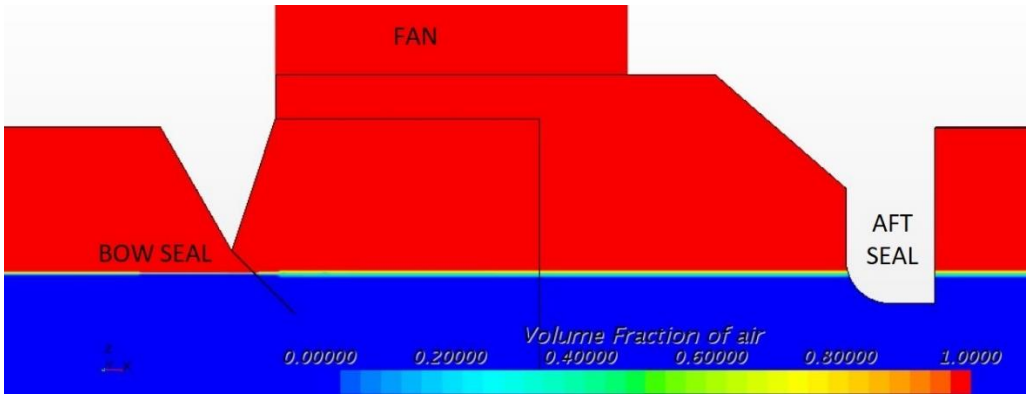

Figure 31. Bow seal domain detail (*t* = 0)

Table 12. Planer bow seal geometric particulars

Seal attachment position (x, z, *m*)	(13.500, 2.500)
Seal length (*m*)	0.507
Seal thickness (*mm*)	3.75
Domain length (*m*)	26.00
Domain height (*m*)	3.20
Cushion length (*m*)	3.50
Cushion height from attachment (*m*)	1.00
Morphing region length (*m*)	3.50
Rigid aft seal length (*m*)	0.50

While the beam of the platform used in the UM experiment was 1.524 m, a two-dimensional solution approach using single cell through the beam (*y*-direction) is used to minimize node count. Initially, a 1 m length was chosen for the beam to simplify scaling to the experimental values. However, it was soon observed that the *y*-momentum residuals were unstable. It is surmised that the spatial aspect ratios led to divergence of the VOF solver. The problem was solved by reducing the beam cell size to Δy = 0.01 m.

Various surface and volume meshing tools are provided by STAR-CCM+ to construct the baseline mesh. First, an automated meshing operation is established for the static and morphing fluid regions. A trimmed cell mesher establishes the basic mesh while a custom surface control refines the mesh as it approaches the seal front surface. Four volumetric control areas are included to selectively refine the mesh in various regions of interest. One refinement area covers the initial free surface and uses a cell height of approximately Δz = 0.008 m. Two refinement areas cover the area immediately upstream of the seal and use cell heights of approximately Δz = 0.008 m and 0.004 m. The final refinement area covers the entire free surface within the cushion and downstream and uses a cell height of Δz = 0.015 m. Figure 32 shows the results of these refinement specifications.

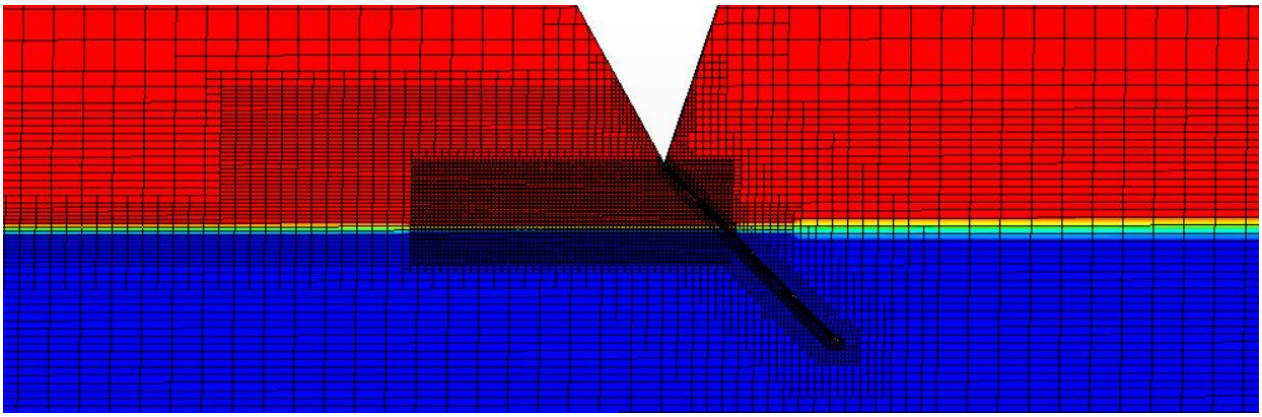

Figure 32. Mesh surrounding seal (t = 0)

In order to more closely resolve the boundary layer along the seal, a prism layer mesh is applied to its front surface (Figure 33). It is six layers deep with an overall thickness of 0.008 m and a constant growth ratio of 1.3. Surface mesh and volume mesh extruders discretize the domain upstream and downstream of the seal using 10 and 8 layers, respectively, and a constant growth ratio of 1.2. Finally, directed mesh operations are performed on the fan and seal in order to closely control the cell count and node spacing growth. The seal structure utilizes 100 cells along the length and is biased to where the cell edge length at the attachment is 10% of the cell edge length at the tip. The additional refinement at the location of greatest curvature increases accuracy of the solution. Two quadratic elements are used through the seal thickness.

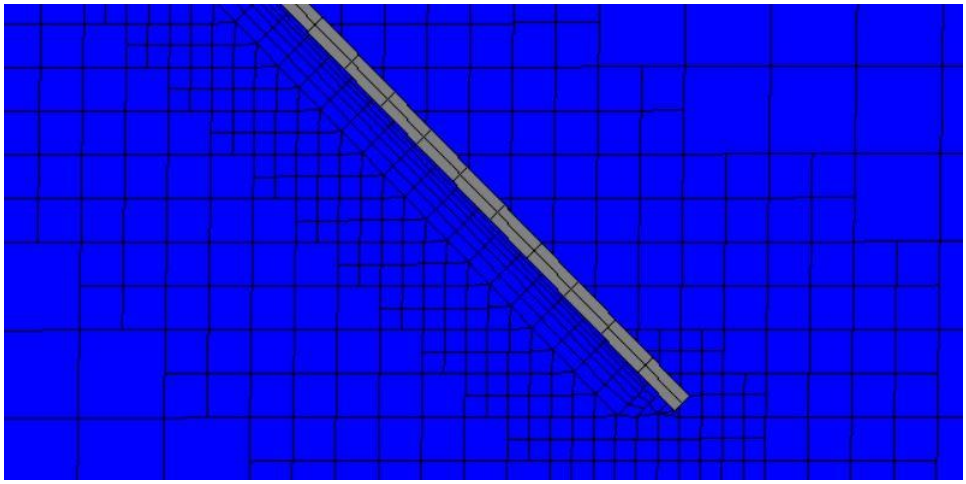

Figure 33. Prism layer mesh along seal front surface (*t* = 0)

4.2.2 Fluid physics models and solvers

In STAR-CCM+, compressible and incompressible forms of the fluid governing equations are available. For the bow seal problem, the velocities remain well below a Mach number of Ma = 0.3 and thermal transfer is not significant. Thus, the incompressible simplification is made for both the water and air, and the RANS equations are solved using the SIMPLE algorithm (Patankar and Spalding, 1972). The SSA turbulence model (under-relaxation = 0.75) is used with an initial turbulent viscosity ratio = 10, and the all-y^+ wall treatment is specified.

The Implicit Unsteady solver with first order temporal discretization is used to advance time in a transient analysis toward a steady state. While this study seeks to reach a stable interaction in order to evaluate the steady seal resistance, there are two significant restrictions which prevent the use of a steady time model. First, updates to the seal structural stiffness matrix must be made periodically in order for the structural solver to find a stable solution. If the seal displacement is too large for the given timestep the structural solver has significant difficulty bringing the interaction into equilibrium, regardless of the number of iterations. Second, the multiple fluid

species (air/water) require limitations on the CFL number in order to maintain resolution and stability of the mixing interface. Moderate CFL numbers (>1.0) result in diffusion and smearing of the free surface for this problem. Therefore, Convective CFL Time-Step Control is activated with a target mean CFL = 0.2 and a target max CFL = 0.5.

The VOF solver (under-relaxation = 0.5) is used to solve material species movement through the Eulerian mesh while the HRIC scheme tracks the surface interface between the water and air. To maintain resolution of the free surface ahead of the seal, the local Courant number limits of C_u and C_l are 1.0 and 0.5, respectively. The angle factor C_Θ is modified to 0.5, improving resolution of the surfaces moving parallel to the mesh. The flat-wave model option within the VOF solver is utilized to establish the initialized free surface height and inlet velocities. To damp sloshing of the free surface resulting from startup, a wave damping boundary option is applied to the inlet and outlet boundaries with damping lengths of 2.0 m.

The Mesh Morpher is activated in the morphing fluid region and the fluid nodes at the seal interface are free to move as dictated by motion of the seal nodes. A boundary plane constraint is applied to the sides of the morphing fluid region to allow nodal motion in the *X*-*Z* plane only. A control vertex thin-out factor of 1.0 is used to maximize the number of boundary vertices used in the displacement field interpolation. Similarly, for the seal, nodes along the fluid-structure interface are free to displace according to the stress field in the *X*-*Z* plane, but are constrained in the *Y*.

4.2.3 Fan physics models

In order to build gage pressure within the cushion, a fan momentum source region is added just above the cushion (Figure 31) and a contact interface is established between the regions to allow

free exchange. To control the source strength, a fan curve is prescribed for each of the pressure conditions simulated according to Table 13. The developed pressure is reduced with increased volumetric flowrate (m^3/s) to provide a stable cushion pressure through a large range of flows. To increase cushion stability, the flowrate magnitudes are tailored to accommodate momentary periods of venting when the free surface profile falls below the aft seal. Should the pressure fall too quickly, seal stability can be lost. This occurrence is more prevalent in the high cushion pressure cases where depression of the free surface is greatest.

Table 13. Cushion pressure fan curves

Pc = 252.4 Pa		**Pc = 475.5 Pa**	
Flowrate (m^3/s)	Pressure (Pa)	Flowrate (m^3/s)	Pressure (Pa)
0.001	252.4	0.001	475.5
0.01	252.4	0.01	475.5
0.02	200	0.05	475.5
0.05	100	0.1	100

Pc = 953.4 Pa		**Pc = 997.7 Pa**	
Flowrate (m^3/s)	Pressure (Pa)	Flowrate (m^3/s)	Pressure (Pa)
0.001	953.4	0.001	997.7
0.01	953.4	0.01	997.7
0.05	953.4	0.05	997.7
0.1	500	0.1	500

4.2.4 Seal physics model and solver

The implicit unsteady solid stress solver is activated and specified to use a 2^{nd} order Newmark temporal discretization (Newmark parameter = 0.5). Solid displacement motion is specified to enable nonlinear geometry via updates of the stiffness matrix at each iteration. To improve stability and reduce the influence of numerical noise in the structure, Rayleigh damping (Zienkiewicz, 1991) is activated with the mass coefficient α = 10 Hz and the stiffness coefficient

β = 0.86 s. As the steady state solution is sought, the choice of the damping coefficients is made to moderately over-damp the low frequencies of the structure.

A surface segment is created at the top edge of the seal and is spatially fixed. The edges are constrained in the *y*-direction and the remaining seal surfaces remain unconstrained. Point monitors are attached to the seal front surface to track displacements of these specific points (Figure 34).

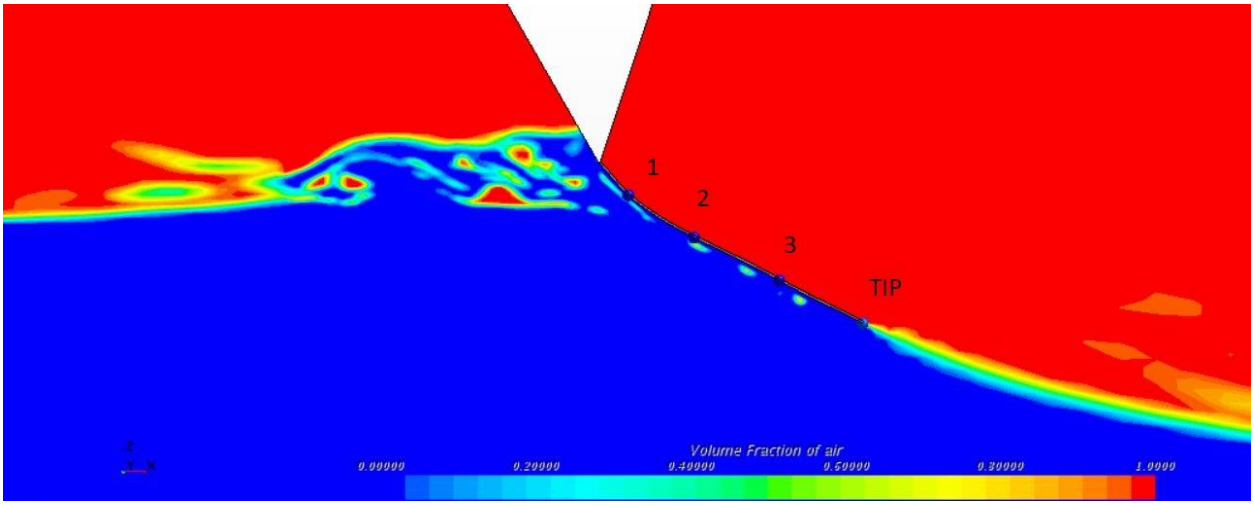

Figure 34. Seal point markers (*t* > 0)

4.2.5 Seal material properties

It has been presented that seal materials such as those tested in the UM bow seal experiment are more accurately modeled when a hyperelastic description is used for the flexural modulus of the rubber coating. However, as of the time of this work, only linear elastic material models are offered as part of the solid stress solver within STAR-CCM+. This adds to the difficulty of replicating the test results exactly. Further complicating the issue, it is not possible to employ a

multi-layer solid in combination with the partitioned FSI solver at this time. For this reason, the seal is modeled as a single isotropic, linear elastic material rather than the rubber coated fiber.

A multitude of linear elastic modulus estimates have been reported for various test seal materials. Zalek and Doctors (2010) reported a composite modulus for the UM experiment seal material (nitrile) of 16.7 MPa. In the appendices of the work by Wiggins (2014), an extensive material characterization was performed for the seal material used in the LCC tests, revealing the large range of material properties for ACV skirts. A synopsis of the values used for various works is shown in Table 14. Recognizing the weakness of assuming a linear elastic modulus for the rubber coating, Bloxom (2014) constructed a more accurate seal structural model by assigning different moduli to each of the three layers (rubber, fabric, rubber) instead of using a composite modulus. He also performed a cantilever bending test of a sample of seal material used in the experiment in order to tune coefficients for a hyperelastic Mooney-Rivlin model. The coefficients for the hyperelastic model are C10, C01, and D01. This model, and various others useful for characterizing nonlinear materials, are described in Appendix A.

Table 14. Seal material moduli

Source	Material	Tensile Modulus (MPa)		
Zalek and Doctors (2010)	laminate	16.7		
Wiggins (2014)	laminate (warp)	244.3		
	laminate (weft)	113.4		
	coating alone	4.5		
Bloxom (2014)		**C10**	**C01**	**D01**
	coating alone	1.30E+06	0	2.00E-08
	nylon base fabric	200		

To validate the choice of linear elastic modulus used in STAR-CCM+'s solid stress solver, a series of cantilever seal simulations is conducted similar to that performed by Bloxom in an attempt to

match his experimental data. The material sample is 0.35 m long, 0.00375 m thick, and is cantilevered at 45°. It is fixed in all degrees of freedom at the attachment and is allowed to deflect only due to its gravitational body force. The mesh is constructed using 100 C3D20 cells with a 10:1 bias toward the attachment. An implicit solver in Abaqus is used to efficiently reach steady state. Initially, runs for both one cell and two cells through the thickness were used, but a comparison of the deflections revealed no difference when using the quadratic elements.

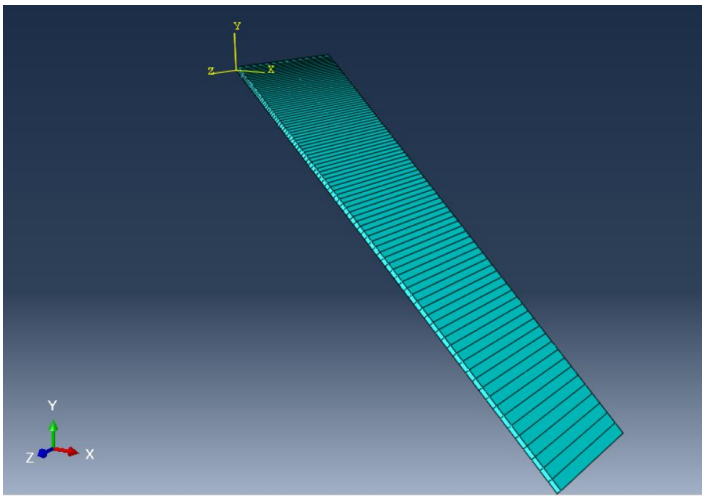

Figure 35. Meshed seal model

The seal deflections are compared to Bloxom's data in Figure 36. The moduli examined were 2.0, 2.5, 3.0, 3.5, 4.0, 4.5, and 8.5 MPa, yet only the results for 2.0, 4.0, and 4.5 MPa are shown for clarity. It is observed that the tip displacements vary greatly with small changes in modulus. However, the critical behavior that should be matched is both the general deflection beginning at the attachment where the bending moment is greatest, as well as the buckling curvature. As the modulus increases, the increased rigidity moves the buckling location farther from the attachment. 4.5 MPa is the value reported by Wiggins (2014) for the nitrile seal coating without base fabric

used in the LCC experiment. While this appears to be a close match from the figure, a slightly reduced modulus of 4.0 MPa matches the buckling location more closely.

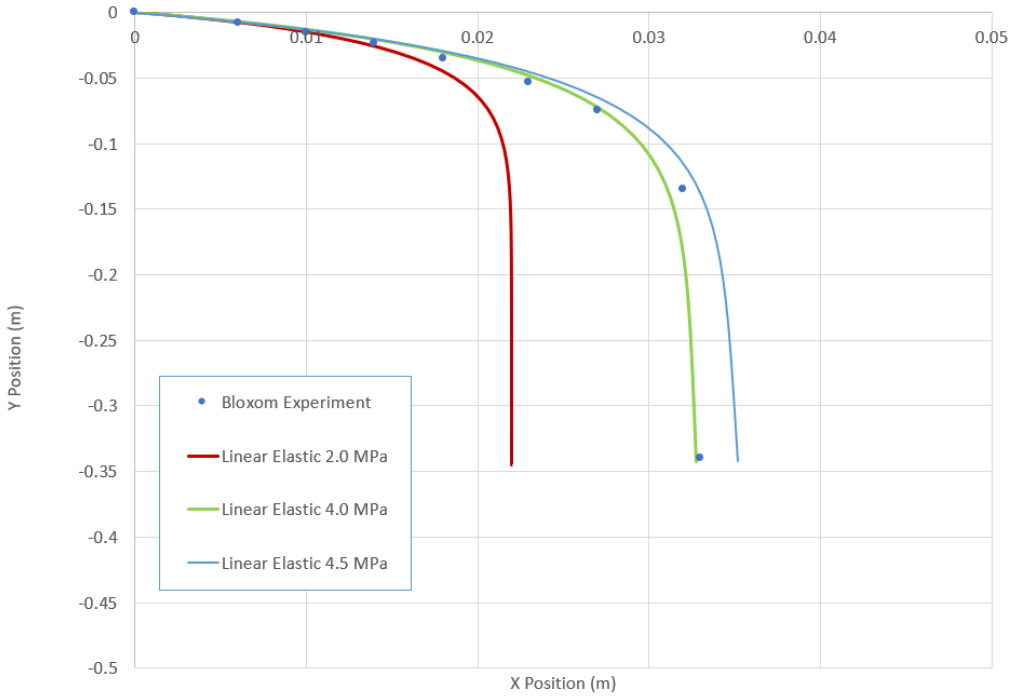

Figure 36. Seal deflection for various moduli

From the detailed view in Figure 37, the difficulty in matching a linear modulus to experiment results becomes more apparent. The 2.0 MPa results match the initial deflection more closely (Figure 37), but the reduced stiffness increases the rate of curvature and its peak location along the seal (Figure 36). From this data, 4.0 MPa is chosen as the isotropic elastic modulus used in the STAR-CCM+ solid stress solver. It generally replicates the rate of curvature and the bending location and does not deviate too greatly near the attachment. Later results will show that stability of the seal can lead to compromise in the choice of seal modulus, as the fluid conditions and inflation pressures dominate the deflection and resistance for the planer seal problem. Further properties utilized in the material model are: ρ_s = 1100 kg/m^3, and ν = 0.4.

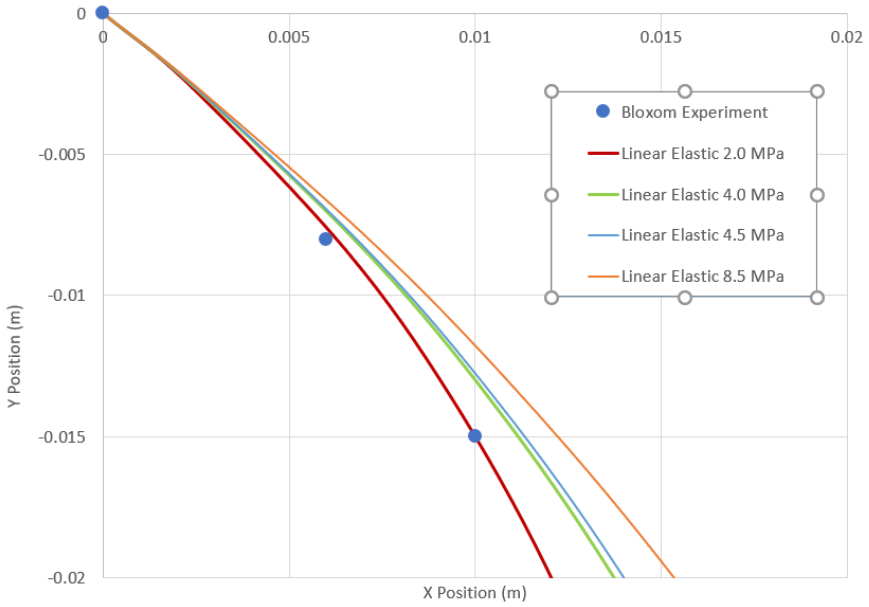

Figure 37. Seal deflection for various moduli (detail)

4.2.6 FSI coupling

To establish an FSI interaction between the seal region and the morphing fluid region, a mapped contact interface is specified between the seal surfaces and the morphing fluid surfaces in proximity to the seal. The fluid-structure coupling solver is activated with the two-way iterative coupling scheme specified. As the density of the bow seal and contacting fluid are very close, and given the fact both fluids are approximated as incompressible, achieving FSI stability can be a difficult prospect due to influence of the added-mass effect. Several techniques to increase stability in this regard are provided by STAR-CCM+ and are utilized herein. Within the fluid-structure coupling solver, the fluid load is specified to ramp linearly from 0% at T = 0 s to 100% at T = 0.25 s. This reduces the impulse to the seal and allows it to find its free running position in a more controlled manner. Loading the seal too quickly causes it to deflect too quickly and eventually part the free surface. The subsequent cushion venting and extreme mesh morphing

crashes the simulation. However, if the fluid load is imposed too slowly, the seal body force dominates the motion. The seal rotates downward in the absence of a restoring moment from the fluid which drastically alters the incoming flow field. A massive hydraulic jump forms in the cushion leading to a crash.

Because the FSI solver is iterative, it typically benefits from some amount of displacement under-relaxation. Investigations into this parameter revealed convergence is problematic without significant under-relaxation. A factor of 0.25 is found to be a good match for the time step and inner iteration limits used in this simulation. To further enhance stability of the interaction during startup, the pressure loads are clipped to ± 2000 Pa and the traction loads are clipped to 500 Pa. Evaluation of the maximum loads on the seal in the steady state condition reveal the clipping limits are set high enough to have no effect at the quasi-steady state when data is taken.

4.2.7 Boundary conditions, initial conditions, startup

The boundary conditions are as follows. At the inlet the STAR-CCM+ wave model is implemented which allows specification of the inlet velocities for the "heavy fluid" (water) and "light fluid" (air) independently. The advantage of this approach is that inflow of the air at the inlet can be activated or deactivated, allowing the simulation to replicate data obtained by either tow tank or water channel. The inflow velocity, *U*, is 2.43 m/s for water and 0 m/s for air. The heavy fluid height specified within the wave model is 2.37 m, providing a static seal immersion, δ_s, of 0.2286 m, necessary to match the experimental conditions for $F_\delta = {}^{U}/_{\sqrt{g\delta_s}} = 1.6$.

At the outlet, hydrostatic pressure developed by the water column is imposed. As part of the wave model the pressure outlet dynamically adjusts to accommodate changes in the free surface

elevation. Slip walls are implemented on all rigid surfaces within the domain, including the side walls. No-slip conditions are imposed on all surfaces of the deforming seal.

Obtaining a steady fluid-structure interaction given the relatively high inlet velocities and numerous physics is difficult. Observation of fluid residuals, mesh motion at each time step, and significant trial and error led to a standardized approach for the simulation startup, which is applied universally to each simulation. While slight alterations were found to work better for some conditions, the most reliable technique is as follows. The fluid is initialized throughout the domain at t = 0 s to the inlet free stream of 2.43 m/s. To reduce the impulse load on the seal, the solid stress solver, fluid-structure coupling solver, and mesh motion solver are frozen while time is allowed to advance to t = 10 s. This develops the free surface profile throughout the domain and allows the free surface oscillations to dissipate prior to releasing the seal. Without this stabilization period, a breaking wave that forms within the cushion (Figure 38) at the larger inflation pressures disturbs the seal beyond recovery. Beginning at t = 10 s, all frozen solvers are released and the fluid load on the seal is ramped up as described above. The simulation is allowed to run an additional 20 s until t = 30 s. To verify a steady state condition is reached, oscillations in both the seal position and fluid pressure ahead of the seal are checked to ensure they are stable and not increasing with time. Locations of the upstream fluid pressure monitor and the cushion pressure monitor are also shown in Figure 38.

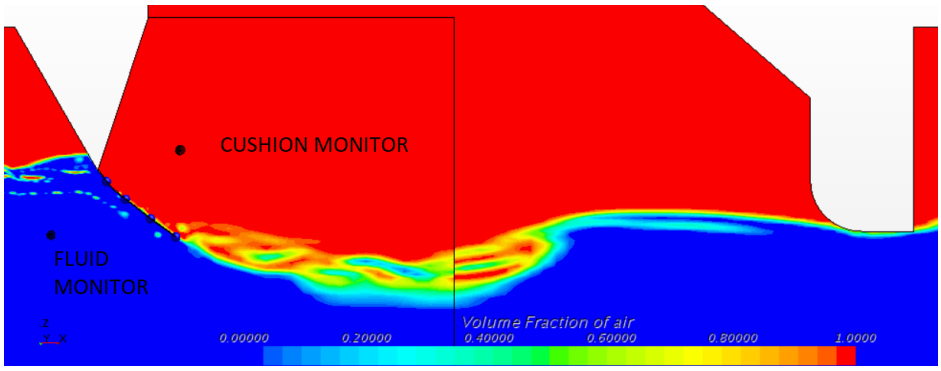

Figure 38. Formation of breaking wave within cushion

4.2.8 Planer bow seal results

Initial simulations are conducted for cushion gage pressures of 252, 475, 953, and 997 Pa. Inlet flow velocity is maintained at 2.43 m/s for all cases. These conditions were initially selected by Bloxom as a good representation of the UM experimental results. For each run, data is collected at 100 Hz and the final five seconds is averaged to obtain mean values for cushion pressure, seal deflection, and the forces acting on the seal front and back surfaces.

Cushion Pressure

The developed static pressure for the P_c = 997 Pa case is shown in Figure 39. A clear over-pressure is developed within the cushion and maintained by the flexible bow seal and rigid aft seal. Hydrostatic pressure through the fluid column is developed as intended. A plot of the pressures recorded by the cushion monitor for the various cases is shown in Figure 40. It reveals the calibrated fan curves and implementation of the fan momentum source do an excellent job of maintaining a stable cushion pressure in all cases.

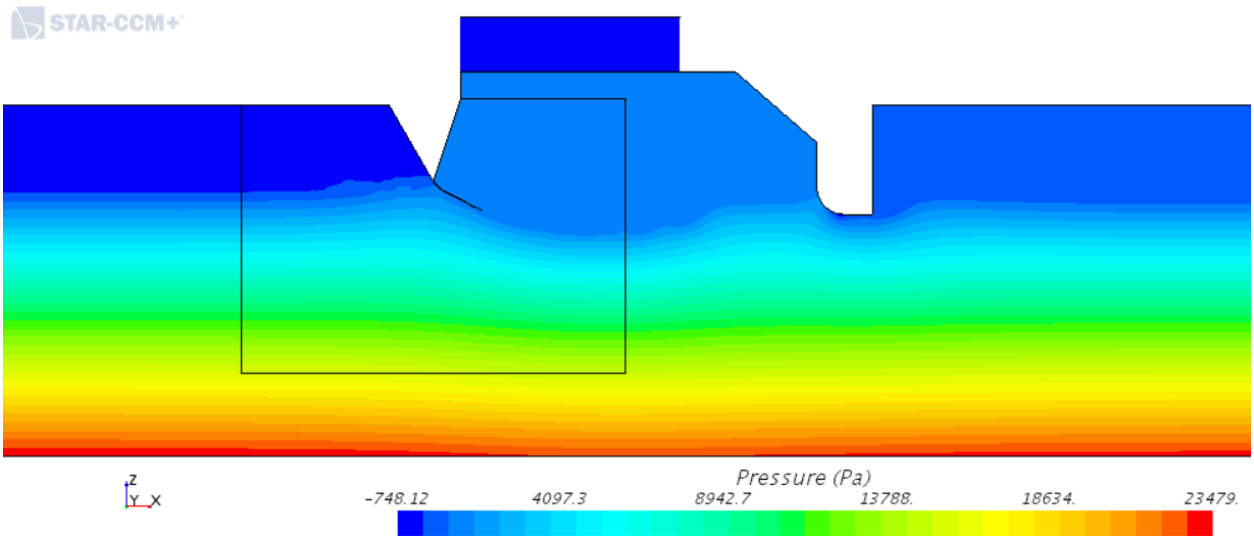

Figure 39. Planer seal domain pressure

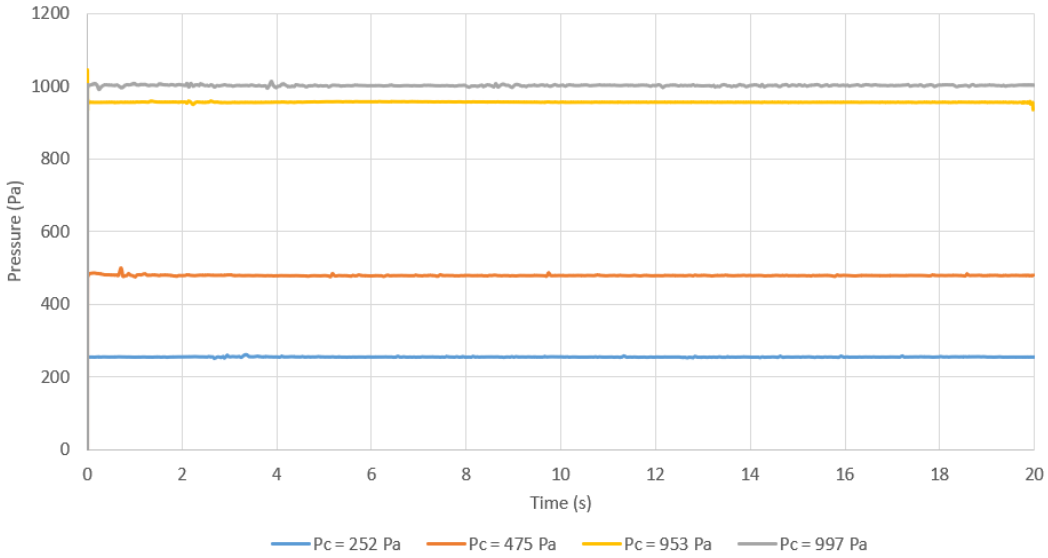

Figure 40. Sample cushion pressure monitor report

Seal Stability

Investigation into the choice of modulus for the seal reveals the onset of instability at higher cushion pressures of 953 Pa and 997 Pa for F_δ of 1.6. A sensitivity study to determine the

modulus limit is conducted by systematically reducing the modulus value and observing the oscillations of the seal. The simulation begins with P_c = 997 Pa and a stable seal modulus of 8 MPa. After achieving T = 18 s, the modulus is reduced and the simulation is restarted to achieve T = 30 s. Figure 41 plots the Z coordinate of the seal tip versus time for moduli of 4, 6, and 8 MPa. Table 15 provides the summary statistics for tip displacement from 18 s to 30 s. As the seal modulus reduces, the oscillation amplitudes and standard deviations are shown to increase. While these large oscillations do not entirely de-stabilize the seal, they do reduce the cell quality in the morphing region, as well as the quality of the deflection and resistance data. For this reason, 8 MPa is maintained as the seal modulus for the higher cushion pressures of P_c = 953 and 997 Pa.

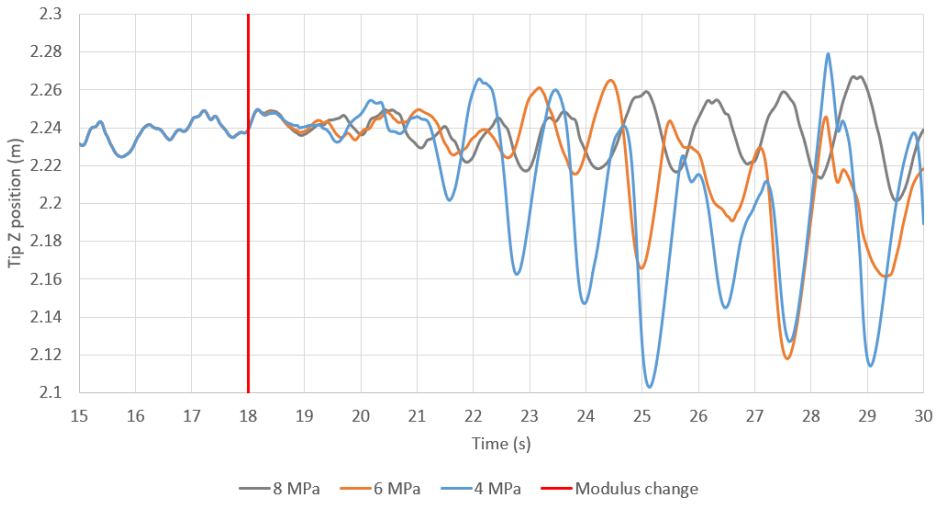

Figure 41. Tip *Z* position for various seal moduli, P_c = 997 Pa

Table 15. Summary statistics for tip *Z* position, various seal moduli, P_c = 997 Pa

Modulus (*MPa*)	4	6	8
Mean	2.2159	2.2246	2.2376
Standard Error	0.0010	0.0007	0.0003
Median	2.2340	2.2350	2.2388
Mode	2.2417	2.2455	2.2344
Standard Deviation	0.0387	0.0285	0.0123
Sample Variance	0.0015	0.0008	0.0002
Kurtosis	0.3052	2.4331	0.1349
Skewness	-1.1248	-1.6216	-0.3338
Range	0.1761	0.1473	0.0656
Minimum	2.1030	2.1179	2.2013
Maximum	2.2791	2.2651	2.2669

Seal Deflection

A comparison of the seal deflection for the various cushion pressures is shown in Figure 42 through Figure 45. For the current results (STAR-CCM+), each point represents the average position over the final five seconds of the transient simulation. The error bars show the extreme maximum and extreme minimum for each point over the same period. At the two lowest cushion pressures, the average positions are a good match to those reported by both Bloxom (2014) and Zalek and Doctors (2010). At the lowest pressure (Figure 42), there is a significantly larger range of motion in the seal.

In each of the two larger cushion pressure cases, the current results slightly under-predict the deflection seen in both the UM experiment and Bloxom's results. There are two hypotheses for the variation. First, it is a possibility that the sidewalls of the platform in the UM experiment slightly accelerate the flow at the seal edges where the position measurement was taken (as observed in Figure 2 of Zalek and Doctors, 2010), leading to additional deflection. This would explain Bloxom's slight underprediction of deflection as well. Second and most likely, the underprediction in deflection could result from the difference in the seal hyperelastic behavior

versus that of the linear elastic modulus used in the current work. The seal calibration conducted above reveals a reduced modulus of 2 MPa more closely replicates the largest bending moment near the attachment, but at the expense of deflection errors at lower bending moments. As a compromise, 4 MPa is used for the lowest two pressures, which is shown to provide a good agreement in deflection. For the two higher cushion pressures however, 8 MPa is used in order to maintain stability of the seal.

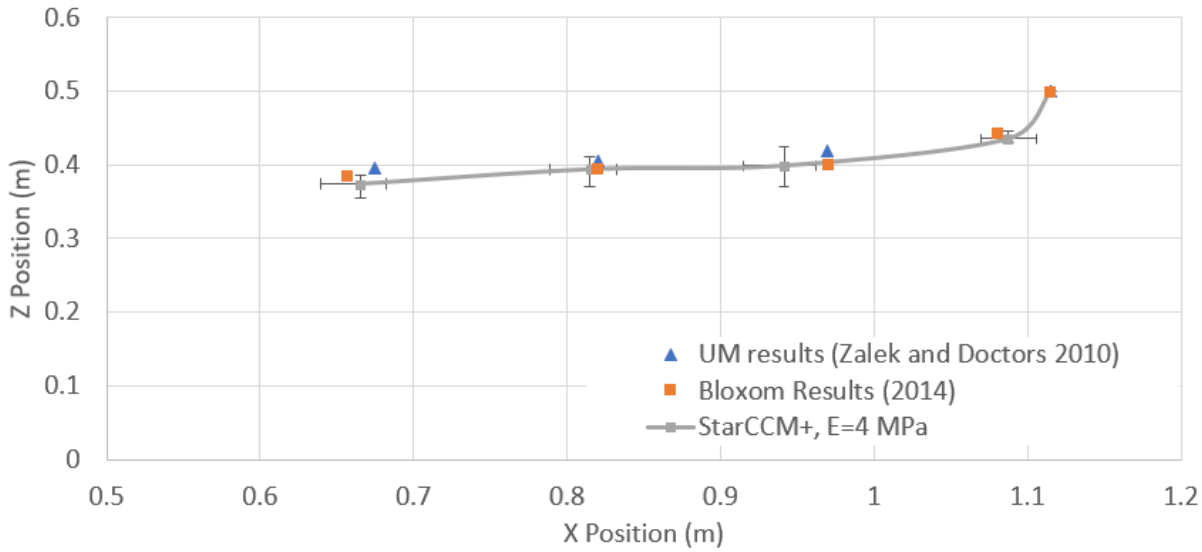

Figure 42. Seal deflection comparison, run 1051, P_c = 252 Pa

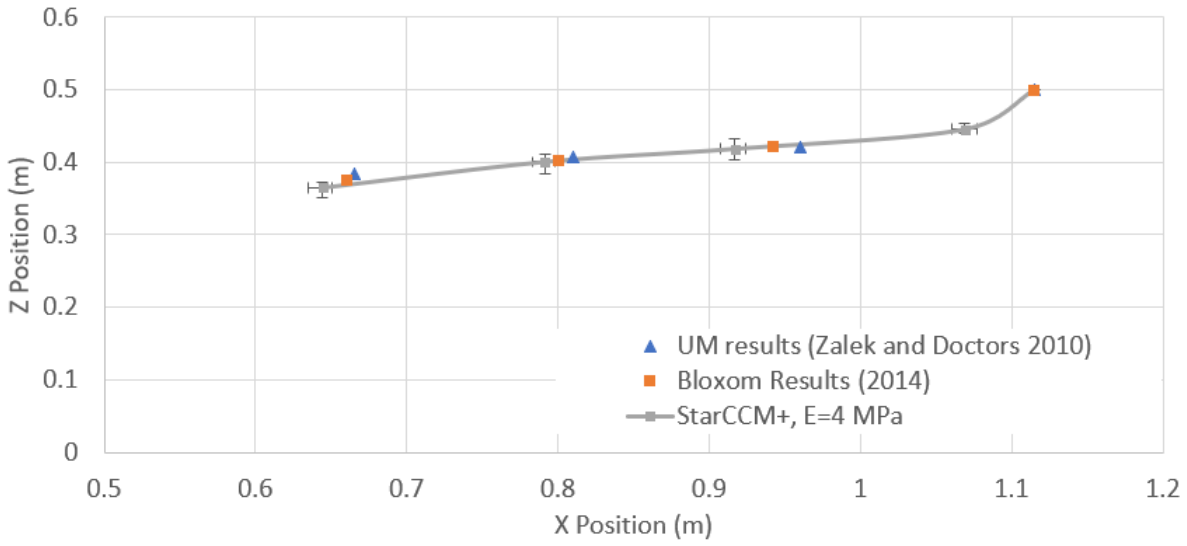

Figure 43. Seal deflection comparison, run 1058, P_c = 475 Pa

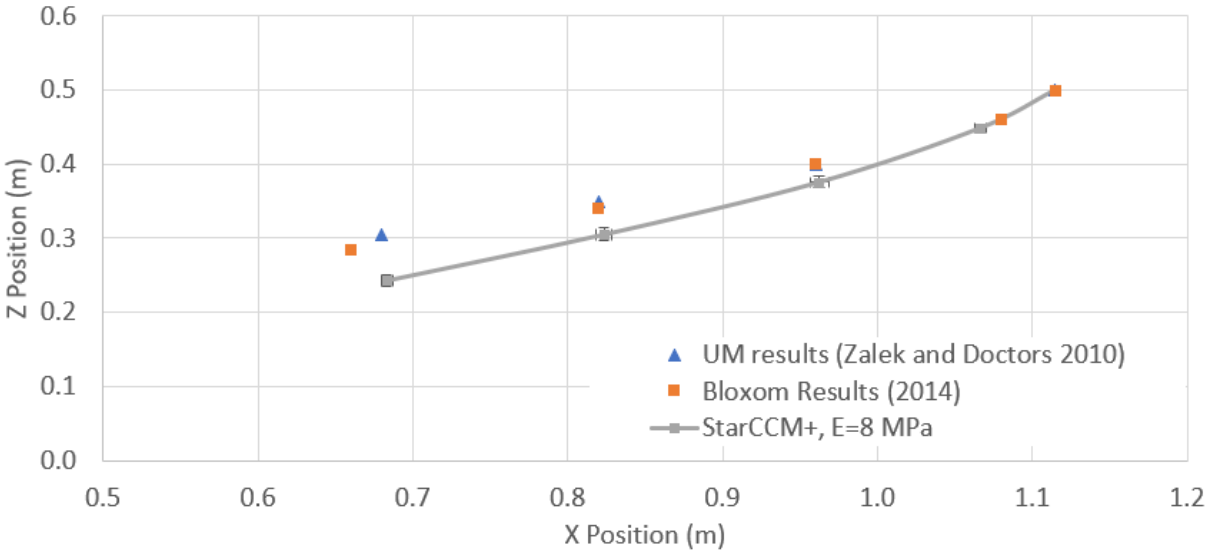

Figure 44. Seal deflection comparison, run 1114, P_c = 953 Pa

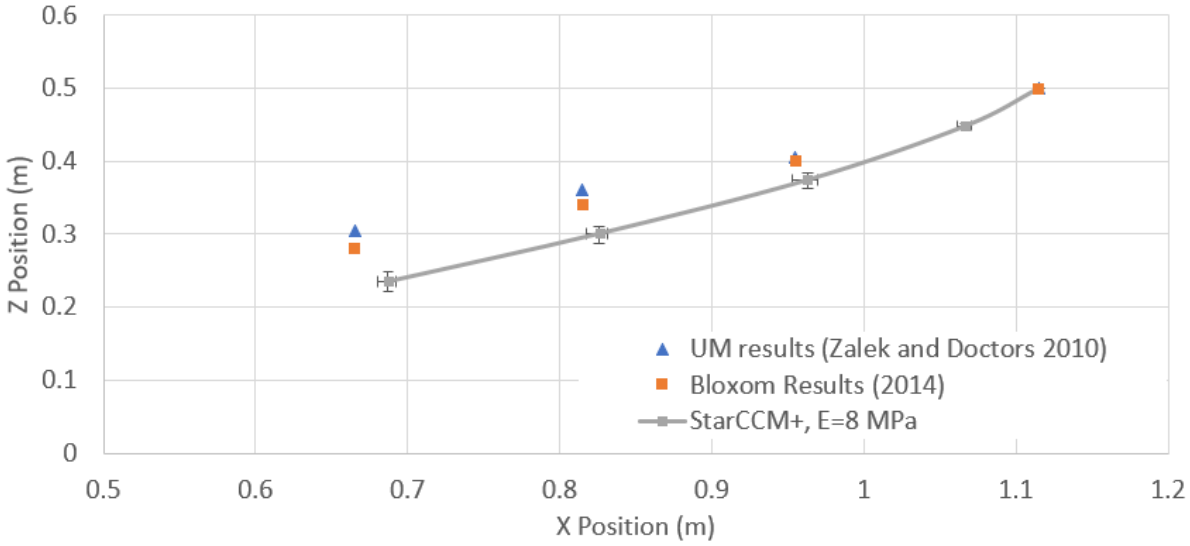

Figure 45. Seal deflection comparison, run 1121, P_c = 997 Pa

Comprehensive deflection results for all cases are provided in Table 16. "Range (+)" indicates the range above the mean, whereas "Range (-)" indicates the range below the mean. The small standard deviations reveal the seal oscillations are small for all cases, except at the lowest pressure of P_c = 252 Pa. At this condition, the range of the X and Z positions show it is very lively upon the free surface, flattening as it is pulled by shear forces.

Table 16. Planer seal deflection comprehensive results

			Position				
Pressure (*Pa*)	**Coordinate**		**Attachment**	**Pt 1**	**Pt 2**	**Pt 3**	**Tip**
252	X	*Avg*	1.115	1.087	0.941	0.815	0.665
		Range (+)	0.000	0.0184	0.0209	0.0173	0.0172
		Range (-)	0.000	0.0171	0.0266	0.0260	0.0255
		Std. Dev.	0.000	0.00843	0.0120	0.0116	0.0115
	Z	*Avg*	0.500	0.435	0.399	0.394	0.374
		Range (+)	0.000	0.00984	0.0249	0.0178	0.0124
		Range (-)	0.000	0.00413	0.0282	0.0235	0.0189
		Std. Dev.	0.000	0.00311	0.0103	0.00904	0.00754
475	X	*Avg*	1.115	1.069	0.917	0.792	0.644
		Range (+)	0.000	0.00786	0.00720	0.00653	0.00679
		Range (-)	0.000	0.00865	0.00939	0.00865	0.00923
		Std. Dev.	0.000	0.00325	0.00350	0.00296	0.00309
	Z	*Avg*	0.500	0.445	0.419	0.401	0.365
		Range (+)	0.000	0.00782	0.01338	0.01143	0.00820
		Range (-)	0.000	0.00628	0.01540	0.01645	0.01371
		Std. Dev.	0.000	0.00275	0.00651	0.00582	0.00444
953	X	*Avg*	1.115	1.066	0.962	0.823	0.683
		Range (+)	0.000	0.00353	0.00704	0.00509	0.00368
		Range (-)	0.000	0.00383	0.00566	0.00482	0.00358
		Std. Dev.	0.000	0.00171	0.00316	0.00244	0.00193
	Z	*Avg*	0.500	0.449	0.375	0.305	0.243
		Range (+)	0.000	0.00333	0.00889	0.00898	0.00800
		Range (-)	0.000	0.00321	0.00733	0.00704	0.00810
		Std. Dev.	0.000	0.00154	0.00396	0.00403	0.00397
997	X	*Avg*	1.115	1.067	0.963	0.826	0.687
		Range (+)	0.000	0.00405	0.00697	0.00545	0.00529
		Range (-)	0.000	0.00505	0.0100	0.00821	0.00685
		Std. Dev.	0.000	0.00193	0.00359	0.00287	0.00259
	Z	*Avg*	0.500	0.448	0.375	0.301	0.235
		Range (+)	0.000	0.00383	0.00942	0.00941	0.0136
		Range (-)	0.000	0.00406	0.0112	0.0129	0.0147
		Std. Dev.	0.000	0.00167	0.00438	0.00485	0.00577

Seal Resistance

The total force on the seal front surface results from hydrodynamic pressure and shear loads due to the passing fluid. The total force on the seal inner surface results from air pressure within the cushion acting normal to the seal. Toward the end of the simulation, the seal dynamics have largely subsided and the body inertial forces are generally low. The seal attachment force is then calculated to satisfy the force balance in Eq. 72. The seal resistance in the x-direction, R_s, is the summation of the hydrodynamic pressure R_{hydro} and shear forces R_τ acting on the seal front

surface in the *x*-direction. The cushion pressure force acting on the seal inner surface in the *x*-direction is R_{cush}. The reaction force due to the attachment in the *x*-direction is R_x .

$$\Sigma F_x = 0 = R_s + R_{cush} + R_x$$

$$\text{where: } R_s = R_{hydro} + R_\tau \tag{72}$$

In a similar fashion to results presented by both Bloxom (2014) and Zalek and Doctors (2010), the resistance results are nondimensionalized for the Froude number F_δ of 1.6. Again, the characteristic length chosen for calculation of the Froude number (Eq. 73) is the seal static immersion depth, δ_s. R_s is nondimensionalized according to the form shown in Eq. 74, where B_c is the cushion beam. This matches the form provided in *Dimensional Analysis* when U^2 is exchanged for $g\delta_s$. The cushion pressure P_c is collected from the cushion pressure monitor located within the cushion region, slightly above and behind the seal. It is nondimensionalized according to Eq. 75.

$$F_\delta = {U}/{\sqrt{g\delta_s}} \tag{73}$$

$${R_s}/{\rho g B_c {\delta_s}^2} \tag{74}$$

$${P_c}/{\rho g \delta_s} \tag{75}$$

Figure 46 plots non-dimensional resistance vs non-dimensional cushion pressure using the mean of the final five seconds of the transient simulation. As the simulation width consists of a single cell of width 0.01 m, all forces are scaled by 152.4 to compare with the experimental seal width of 1.524 m. The current approach overpredicts resistance at all cushion pressures when compared to

both the Bloxom results and the UM results (32%, 59%, 16%, 19% for Run 1051, 1058, 1114, and 1121, respectively). The most probable explanation for the overprediction in the higher-pressure cases is that the linear elastic seal modulus of 8 MPa is overly stiff, especially near the attachment. A hyperelastic material model could perhaps improve the results, as the stiffness would decrease with increased stress. This does not explain the resistance delta at the lower pressures however, as the average deflections are a near match for these cases.

Table 17 provides the resistance component breakdown for each cushion pressure. As the results for R_s are mean values over the final 5 s of the simulation, the standard error of the mean is shown as $\sigma_{\bar{x}}$. The standard deviations for R_s are shown as σ. Interestingly, the values for σ are generally very similar despite the large difference in cushion pressures. This may indicate the sources of unsteadiness such as numerical noise or upstream free surface spillage have equal influence across a broad range of conditions. Also, the largest value for σ (Run 1058) correlates precisely to the greatest percent error for resistance.

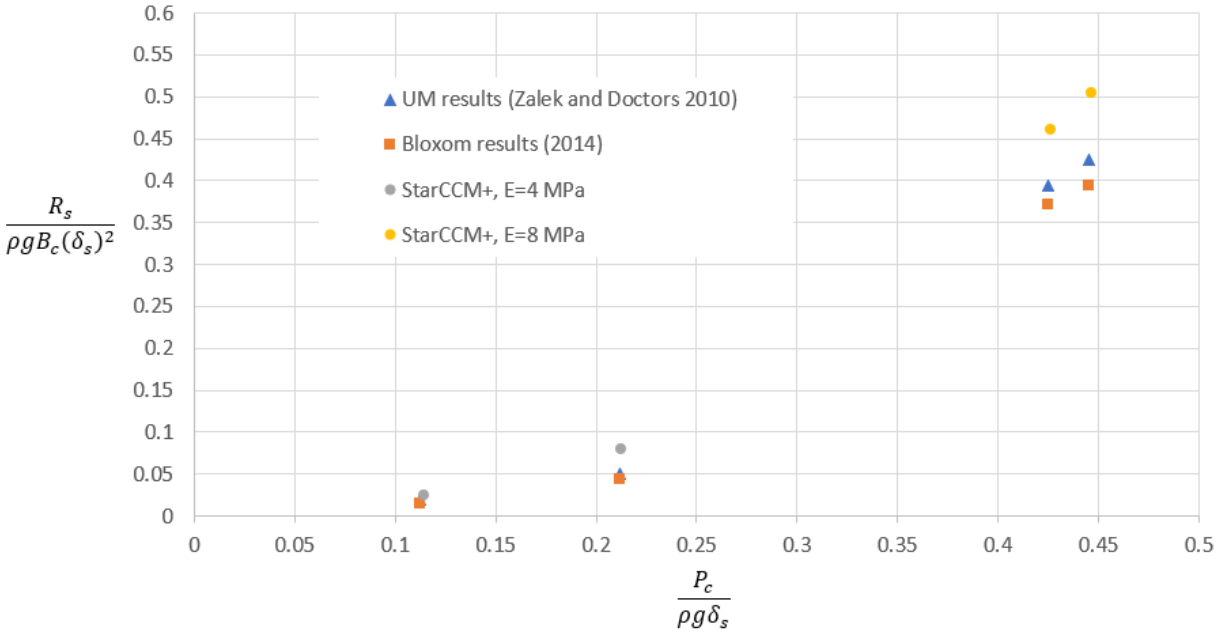

Figure 46. Non-dimensional resistance versus non-dimensional cushion pressure, F_δ = 1.6

Table 17. Resistance results at various P_c for F_δ = 1.6

Run	F_δ	P_C (Pa)	R_τ (N)	R_{hydro} (N)	R_{cush} (N)	R_x (N)	R_s (N)	$\frac{P_c}{\rho g \delta_s}$	$\frac{R_s}{\rho g B_c (\delta_s)^2}$	$\sigma_{\bar{x}}$	σ
1051 (E = 4 MPa)	1.6	256.0	1.953	17.629	-40.740	18.790	19.582	0.114	0.025	0.00133	0.0293
1058 (E = 4 MPa)	1.6	477.0	1.997	60.135	-88.065	25.196	62.132	0.213	0.080	0.00163	0.0359
1114 (E = 8 MPa)	1.6	955.0	3.207	356.110	-363.385	-4.068	359.317	0.426	0.460	0.00107	0.0239
1121 (E = 8 MPa)	1.6	1001.0	3.604	390.760	-393.379	0.985	394.364	0.447	0.505	0.00120	0.0269

Figure 47 plots the results for seal resistance versus cushion pressure using an alternative non-dimensional form found by the dimensionless group derivation in section 2.2. The left axis makes resistance dimensionless by $\rho g B_c \delta_s^2$, whereas the right axis makes resistance dimensionless by $\rho U^2 B_c^2$. An interesting result is that both data sets show similar exponents when the relationship is reflected as a power law; revealing either form is equally useful for scaling. The current STAR-CCM+ results show resistance as a factor of $P_c^{2.24}$. Analysis using Bloxom's results show resistance as a factor of $P_c^{2.49}$.

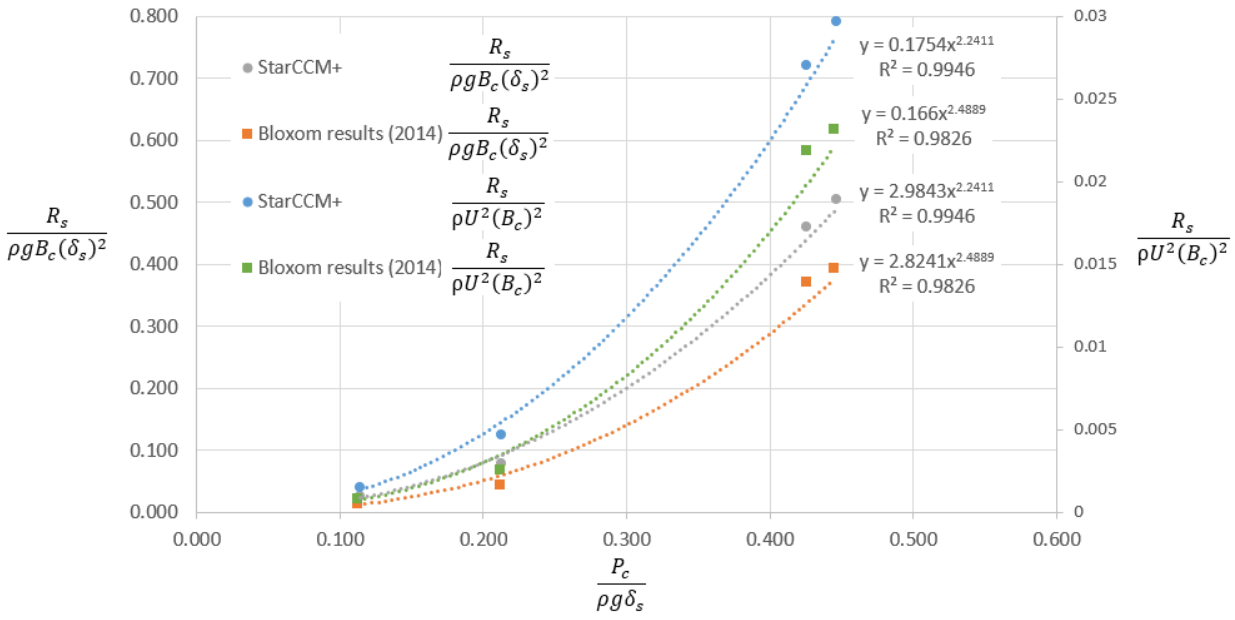

Figure 47. Non-dimensional resistance versus non-dimensional cushion pressure (2), F_δ = 1.6

Uncertainty analysis

Recall both errors and uncertainty are present in CFD analyses. Examples of numerical errors for the planer bow seal problem include: iteration error, convergence error, and spatial discretization error. Iteration error and convergence error are mitigated by requiring low residuals in the computations and by time averaging the resistance values for the unsteady analysis.

While a formal spatial discretization convergence study is not conducted for all cushion pressure cases, resistance data is obtained on three mesh levels using P_c = 953 Pa. A coarse mesh is developed by reducing the element base size by 50%, and a fine mesh is developed by increasing the element base size by 50%. Thus, the baseline case is the medium mesh. The free surface volumetric refinements are altered similarly, whereas the seal prism layer is maintained constant. Results for seal resistance provide 352, 359, and 370 N for the coarse,

medium, and fine meshes, respectively. The percent change is 3% and less. As additional evidence of grid-independence, the aerodynamic influence study discussed below shows a mean seal resistance difference of only 1.25% between two separate medium-sized grids.

Recall aleatory uncertainties are probabilistic distributions in the specified physical parameters. Examples of these for the planer bow seal problem may include: inflow velocity, seal thickness, seal modulus, static seal immersion, turbulent viscosity, among others. As an all-encompassing analysis of these factors requires significant time and resources, the Probabilistic Collocation method is used here to demonstrate how the uncertainty of inflow velocity may propagate into the seal resistance result for the case of F_δ = 1.6, P_c = 475 Pa, and δ_s = 0.2286 m.

The mean inflow velocity is $\overline{U} = 2.43$ m/s. The uncertainty of $\overline{U}$ is assumed to be a normal distribution with equal probability of a higher or lower value. The coefficient of variation ($CV = {}^{\sigma}/_{\overline{U}}$) is assumed to be 3%, providing a standard deviation of $\sigma = 0.0729$ m/s and a variance about the mean of $\sigma^2 = 5.314 \cdot 10^{-3}$ m^2/s^2. The uncertain inflow speeds for a 3% *CV* are *U* = 2.357 m/s and *U* = 2.503 m/s.

The simulation is computed at these speeds and the deterministic results for seal resistance are shown in Table 18. Assuming the polynomial orders of 0 and 1 are sufficient estimates of the error, Eq. 65 and Eq. 66 are used to compute the mean seal resistance as $\overline{R_s} = 64.270$ N, and the standard deviation as $\sigma_{R_s} = 26.119$ N. The relatively large value for σ_{R_s} demonstrates why this exercise in valuable. It shows that a relatively small variance for inflow velocity (± 3%) for the case of F_δ = 1.6 and P_c = 475 Pa can have a large effect on resistance. Figure 48

plots this data with error bars representing σ_{R_S} about the mean. Observe the lower bound for uncertainty in inflow may certainly account for the difference between the various results.

Table 18. Seal resistance results for +/- 3% uncertainty in *U*, P_c = *475* Pa, F_δ = 1.6

Polynomial order	Collocation point	Quadrature weight, ω	Inflow velocity U (m/s)	R_s (N)	$\frac{R_s}{\rho g B_c (\delta_s)^2}$
0	1	1.0	2.430	62.132	0.0796
1	1	0.5	2.357	90.378	0.116
	2	0.5	2.503	38.160	0.0489

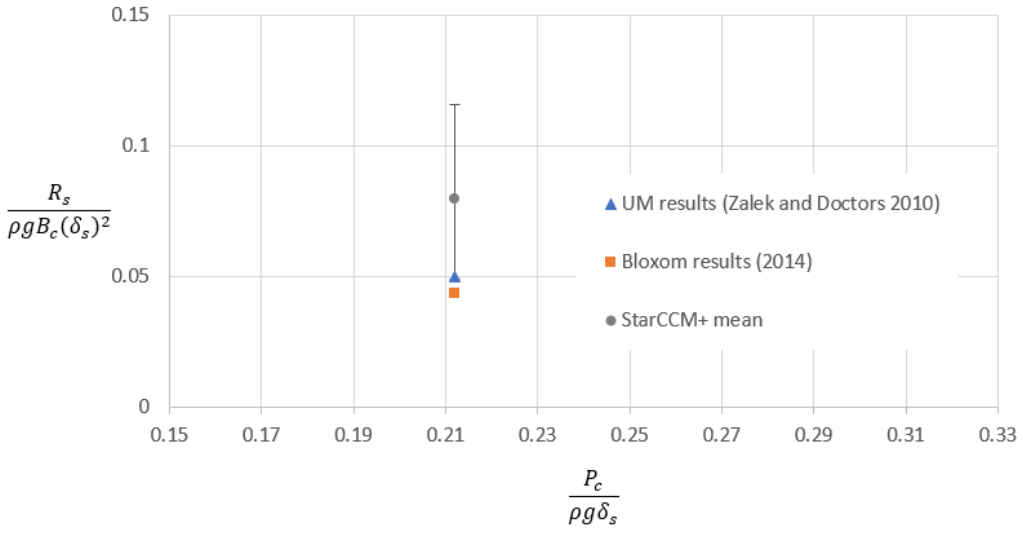

Figure 48. Non-dimensional resistance versus non-dimensional cushion pressure, F_δ = 1.6

Figure 49 plots two forms of non-dimensional seal resistance at three values of F_δ for the cushion pressure providing δ_c/δ_s = 0.213. Each trendline shows decreasing resistance with increased speed for the same cushion pressure. While this would not make sense for a fixed hull geometry ($R \propto U^2$), the seal deflects in response to the additional speed at these low-to-moderate cushion pressures. The change in form presented to the flow is significant enough to reduce, rather than increase, the force on the front of the seal.

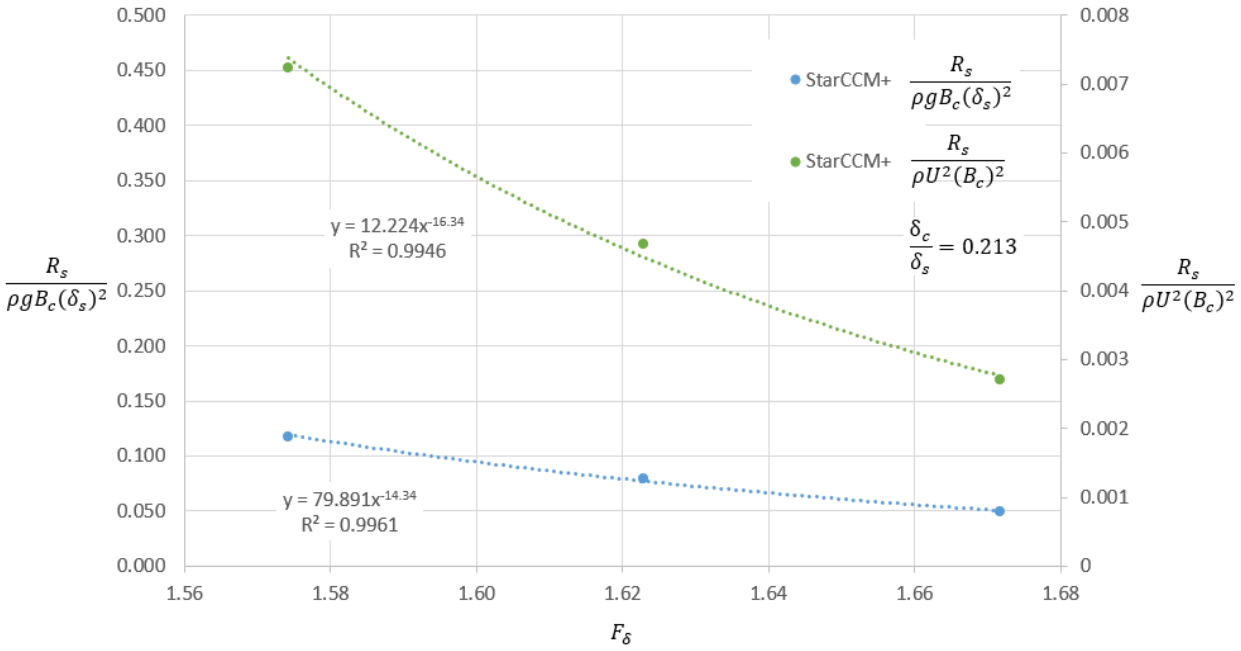

Figure 49. Non-dimensional resistance versus F_δ, $\delta_c/\delta_s = 0.213$

Aerodynamic influence

With comparisons shown above for both deflection and resistance, a question remains regarding the influence of aerodynamic forces on the unwetted upper portion of the seal. This is especially interesting for the low cushion pressure conditions where the free surface rise is insignificant and hydrodynamic forces are low. In the above simulations, air inflow velocity (U_{air}) is assumed negligible and the inlet boundary condition does not impose a velocity upon the air component of the VOF wave model implementation. However, as the UM experiment by Zalek and Doctors (2010) required the carriage to be towed through the tank, an aerodynamic force was generated and thus it was deducted from the overall force summation to reveal the seal hydrodynamic resistance. They estimated the aerodynamic force by assuming a drag coefficient for the platform and by measuring the unwetted area supported

by the load cells. It was generally found that the aerodynamic resistance is 20% or less of the imposed cushion force. While this ratio is a significant factor in the force balance, it is particular to the specific geometry of their experimental rig and the height of the seal above the free surface.

In order to investigate the influence of aerodynamic force upon both the seal front surface and free surface rise, the current STAR-CCM+ simulation is expanded to more closely replicate that used in the UM experiment (Figure 50). The domain is extended vertically and a complete SES platform geometry is added to allow air to envelope the platform and exit at the outlet boundary. The same mesh controls are used to generate a new mesh, which results in similar spatial discretization but slightly different nodal locations.

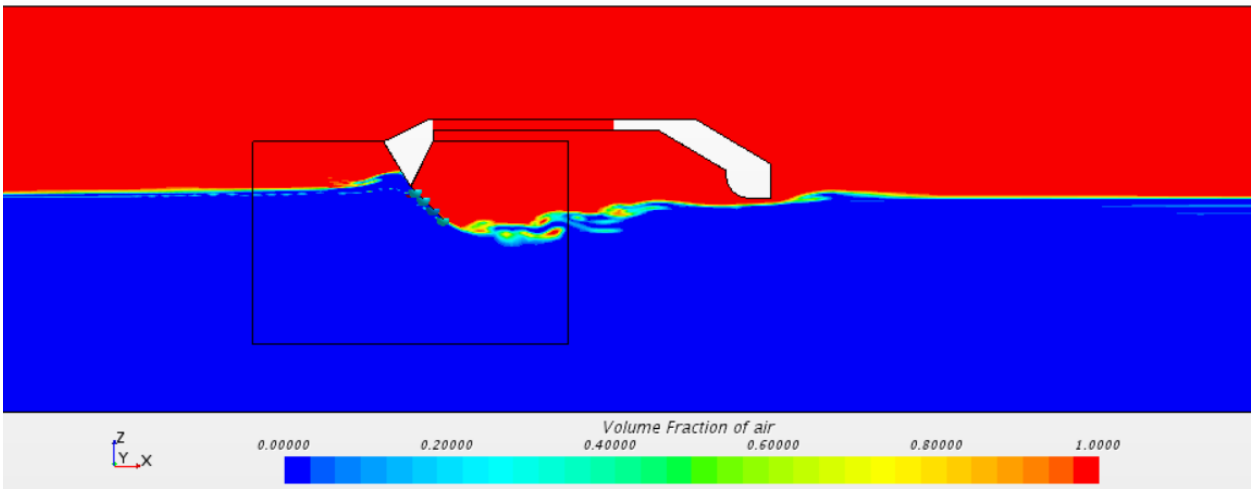

Figure 50. Planer bow seal expanded domain, t = 10 s, F_δ = 1.6, P_c =475 Pa

First, a comparative run is conducted at $U_{air} = 0$, F_δ = 1.6, and P_c = 475 Pa to ensure the result from the expanded domain is similar to the baseline model described above. The non-dimensional seal resistance $\frac{R_s}{\rho g B_c {\delta_s}^2}$ obtained from the expanded domain is 0.81 and the relative

error from the baseline resistance previously obtained is 1.25%. Thus, the expanded domain can be used to investigate the aerodynamic influence. With the "wind" component of the inlet wave model now activated for $U_{air} = 2.43$ m/s, the seal resistance increased by 12.8% to 0.104 (Figure 51). The conclusion is that the wind load upon the seal at these speeds is significant, and accurate accounting of the resistance components should be considered when performing a scaled model test. For this reason, the decision is made to hold $U_{air} = 0$ m/s in all simulations.

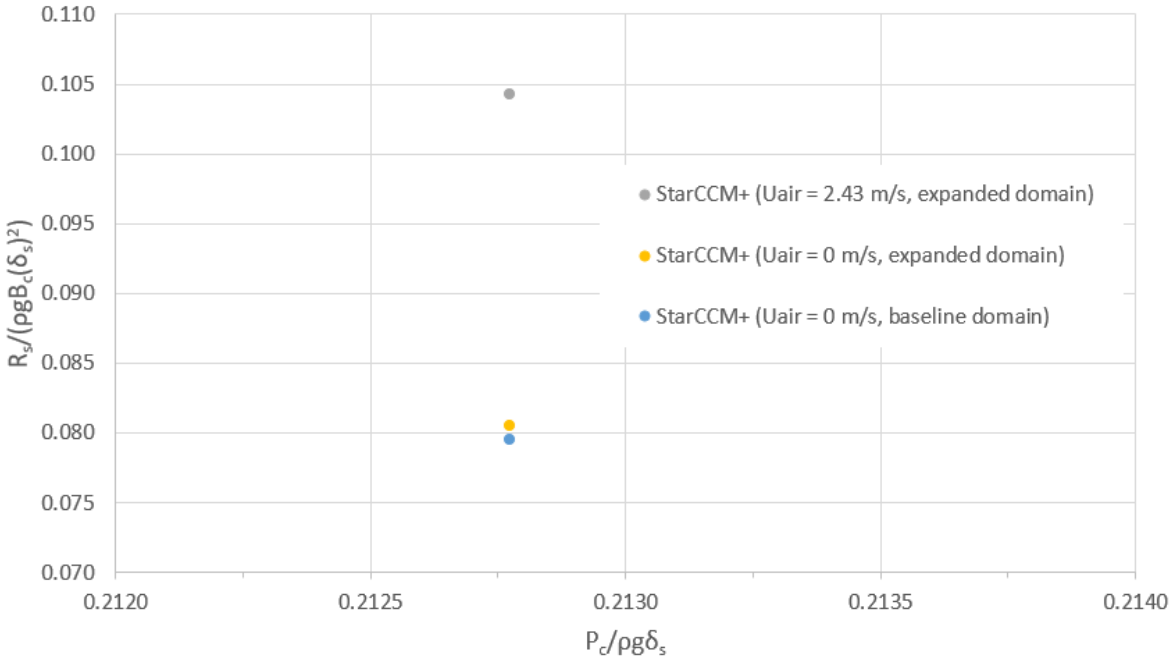

Figure 51. Non-dimensional resistance for baseline and expanded domain, F_δ = 1.6, P_c = 475 Pa

Chapter 5

Abaqus/Explicit - Coupled Eulerian Lagrangian method

The Coupled Eulerian-Lagrangian (CEL) method within Abaqus/Explicit is a technique that enables interaction between Lagrangian elements and Eulerian material within an Eulerian domain. By modeling an ACV seal in the Lagrangian domain and the fluid in an Eulerian domain, this coupled CEL capability offers the potential for a FSI solution while taking advantage of each separate domain characterization. In Abaqus/Explicit the CEL method is implemented by simply placing Lagrangian elements and Eulerian elements in the same computational space and using the General Contact feature. The simplification of the contact and interaction without the need to re-mesh or utilize mesh morphing makes this especially appealing. This chapter describes the Abaqus/Explicit approach in its entirety, including descriptions of the computational methods, fluid and structural models, verification and validation efforts, and results. While the merits of this approach are demonstrated, the method is unable to provide data of sufficient quality for a parametric planer bow seal study.

5.1 Abaqus/Explicit CEL computational approach

Aspects of the computational approach using Abaqus/Explicit CEL are enumerated as follows based upon the documentation (Dassault Systemes, 2013). While complete numerical details are not provided here, the goal is to orient the reader who may find this method foreign.

1) The CEL algorithm uses a partitioned, loosely coupled algorithm to facilitate fluid-structure interactions. It is partitioned in that the fluid solver and structure solver operate independently and do not require simultaneous solution. Also, since there is no iterative solution process between the fluid solution and the structural solution, they are considered loosely coupled. Solutions for the fluid at a given time increment result in a force imbalance upon the structure. Deflections of the structure are updated to establish dynamic equilibrium, which are then passed back to the fluid to begin the next increment. Although not an iterative process, the interaction is "two-way" in that forces from the fluid are applied to the structure and the resulting deflection results from a balance between the external and internal forces. Without subsequent iterations to establish strong coupling, the time step utilized by Abaqus/Explicit to maintain accuracy with this approach is very small and is discussed below.

2) An explicit central-difference integration scheme is used to advance time in the absence of a set of simultaneous equations. Dynamic equilibrium is established at a given time increment *i* and the acceleration of a rotation or displacement (u^N) is solved using Eq. 76. *M* is the mass matrix, *P* is the load matrix, *I* is the internal force vector, and *N/J* denote the degrees of freedom.

$$\ddot{u}_{(i)}^{N} = (M^{NJ})^{-1}\left(P_{(i)}^{J} - I_{(i)}^{J}\right) \tag{76}$$

Next, solutions for the acceleration at increment *i* advance the velocity according to Eq. 77. The new velocity is then used to advance the displacement or rotation according to Eq. 78. The explicit nature of the calculation stems from the use of the previous known values of both velocity (at increment = *i-1/2*) and acceleration (at increment *i =1*). In order to start the process when *i* = 0 and *t* = 0, initial velocity and acceleration are assumed zero unless otherwise specified.

$$\dot{u}^N_{(i+\frac{1}{2})} = \dot{u}^N_{(i-\frac{1}{2})} + \frac{\Delta t_{(i+1)}+\Delta t_{(i)}}{2}\ddot{u}^N_{(i)} \tag{77}$$

$$u^N_{(i+1)} = u^N_{(i)} + \Delta t_{(i+1)}\dot{u}^N_{(i+\frac{1}{2})} \tag{78}$$

3) The Volume of Fluid (VOF) method is used to track material movement through the Eulerian mesh, which is calculated for each element as the Eulerian volume fraction (EVF). Each element is comprised of either one or more physical materials or is assigned a "void" material. Thus, it is never truly empty. When the element is full of one or more materials, the EVF is 1; and when it is full of void material the EVF is 0. Void material is not assigned mass or strength but provides algorithmic continuity for the space. It is assigned to elements automatically and non-void material must be introduced into the model during the initialization or as a result of the simulation. The material interfaces within elements of EVF less than one are represented by simple planar facets. The location and arrangement of the facet is determined by an interface reconstruction algorithm but is discontinuous between adjacent elements. This can be misleading and unrealistic when visualizing the results. A fine grid resolution can help define the material boundary and would be especially important in modeling free surface interactions.

4) The stable time increment is described by Eq. (79), where L_e is element length and c_d is the dilatational wave speed. This is equivalent to satsfying the Courant-Friedrichs-Lewy (CFL)

condition established for the first order or second order wave equation (Anderson, 1995). Derivation of this criterion is shown in section 3.5.2 The *min* qualifier reflects the fact that the domain may be constructed of various grid sizes or material properties. All elements must be surveyed at each increment to determine the maximum time step allowed throughout the domain.

$$\Delta t = min\left(\frac{L_e}{c_d}\right) \tag{79}$$

When various materials are specified within the computational domain the dilatational wave properties will also vary. For example, the wave speed for a fluid such as water may be 1500 m/s, whereas the wave speed for an elastic solid is based on its Lamè constants and density according to Eq. 81. The derivation of this relation is provided by Graff (1975). For an isotropic rubber solid with an elastic modulus of E = 16.9 MPa, Poisson ratio of ν = 0.4, and density of ρ = 1100 kg/m^3, the Lamè constants are calculated according to the relations of Eq. 80 as $\mu = 6.0E6,\ \lambda = 2.4E7$. The wave speed calculated in Eq. 81 is shown to be much lower than that for the fluid. Therefore, given equal mesh sizes of 0.001 m, the explicit time step will be limited by the fluid elements, as shown in Eq. 82 and Eq. 83.

$$E = 2\mu(1+\nu);\ \ E = \frac{\lambda(1+\nu)(1-2\nu)}{\nu} \tag{80}$$

$$c_d = \sqrt{{(\lambda + 2\mu)}/{\rho}} = \sqrt{{\left(2.4E7 + 2(6.0E6)\right)}/{1100\,\frac{kg}{m^3}}} = 181\,{m}/{s}\,; \tag{81}$$

$$Solid\ \ \Delta t = min\left(\frac{L_e}{c_d}\right) = \ \frac{0.001\,m}{181\,m/s} = 5.5 \cdot 10^{-6}\,s \tag{82}$$

$$Fluid\ \ \Delta t = min\left(\frac{L_e}{c_d}\right) = \ \frac{0.001\,m}{1500\,m/s} = 6.7 \cdot 10^{-7}\,s \tag{83}$$

5) Abaqus/Explicit uses a "Lagrange-plus-remap" formulation for Eulerian time integration, which consists of a Lagrangian phase and then an Eulerian phase. During the Lagrangian phase, the nodes are considered fixed in the material and the elements are allowed to deform according to the governing equations. Then, in the Eulerian phase, a deformation tolerance test identifies which elements are highly distorted. These elements are then re-meshed and the material flow between elements is calculated. In this way, the algorithm solves for displacement of the fluid material, rather than the traditional velocity.

6) Second-order advection is the default scheme for Eulerian material elements. The distribution slope at the element integration point is found by differentiating a quadratic interpolation of the values from adjacent elements. The values are then integrated over the new element size (volume or mass). The element's new variable value is found by dividing the integral by the size (volume or mass).

8) Contact within Abaqus/Explicit CEL is allowed using the "general contact formulation." It utilizes a penalty-based enforcement method defined by a pressure-overclosure relationship. The weighting of the penalty force is determined using a balanced master-slave surface approach. The first contacting surface is identified as the master and the second is identified as the slave. The nodes of a master surface are allowed to penetrate a slave surface, but the nodes of a slave surface are not permitted to penetrate a master surface. The surface roles are then swapped and the algorithm repeated to determine an average weighting of the penetration distances. Reaction forces are then developed and applied to each node as a function of the penetration distance and weighting. As the topic of contact within FEM is complex and techniques are plentiful, the reader

is referred to the Abaqus documentation for a more thorough explanation of its general contact numerical formulation (Dassault Systemes, 2013).

5.1.1 Abaqus/Explicit effective fluid equations

Abaqus/Explicit is an explicit, compressible finite element code having a foundation in computational structural mechanics. As such, there has been some confusion in the literature and within the Abaqus documentation regarding how the Navier-Stokes equations are solved using the Abaqus/Explicit CEL method. Some insight is provided by Abaqus in a knowledge base article (Dassault Systemes, 2009), which is summarized here.

Abaqus/Explicit solves the governing conservation equations, which are continuity, momentum, and energy. A constitutive assumption is then applied to these equations based upon whether the material is a solid or fluid. For a "Newtonian Fluid", Abaqus applies the Newton-Poisson law of viscosity, (Eq. 84) (Papanastasiou, 1999) to a general equation of motion (Eq. 85), where $\boldsymbol{\sigma}$ is the stress tensor and $\dot{\boldsymbol{\varepsilon}}$ is the strain rate tensor defined by $\frac{1}{2}[\nabla \boldsymbol{V} + (\nabla \boldsymbol{V})^T]$. This results in the Navier-Poisson equation for fluid (Eq. 86).

$$\boldsymbol{\sigma} = -p\mathbf{1} + \lambda(\nabla \cdot \boldsymbol{V})\boldsymbol{I} + 2\mu\dot{\boldsymbol{\varepsilon}} \tag{84}$$

$$\rho \frac{D\mathbf{V}}{Dt} = \nabla \cdot \boldsymbol{\sigma} + \rho\mathbf{f} \tag{85}$$

$$\rho \frac{D\boldsymbol{V}}{Dt} = -\nabla p + (\lambda + \mu)\nabla(\nabla \cdot \boldsymbol{V}) + \mu\nabla^2\boldsymbol{V} + \rho\mathbf{f} \tag{86}$$

Applying the Stokes condition of zero bulk viscosity $\left(\lambda + \frac{2}{3}\mu = 0\right)$ results in Eq. 87. This is a commonly recognized form of the fluid equations (Anderson 1995), indicating that Abaqus does indeed solve the Navier-Stokes equations.

$$\rho \frac{D\boldsymbol{V}}{Dt} = -\nabla p + \frac{\mu}{3}\nabla(\nabla \cdot \boldsymbol{V}) + \mu\nabla^2 \boldsymbol{V} + \rho\mathbf{f} \tag{87}$$

However, while the form is recognizable, Abaqus's solution procedure is a compressible scheme. An equation of state (EOS) is introduced to directly relate the fluid variables of pressure, density, and energy. The algorithm does not appear to incorporate low-Mach preconditioning or other methods to maintain numerical stability when modeling low speed flows having high sound speeds. Significant prior work has been conducted on identifying the need and solution for conditioning compressible low-speed flow solvers (Wong et al., 2001, Puoti, 2003, Turkel et al., 1996). Results presented in section 5.2.5 demonstrate this problem.

To artificially introduce a form of preconditioning into Abaqus/Explicit, the fluid sound speed can be explicitly adjusted within the equation of state to allow increased compressibility, raising the freestream Mach number. This is acceptable because the steady state result is the primary importance. However, density variations must be checked in the final solution within the region of interest to estimate the impact. An additional benefit to lowering the fluid sound speed is the relaxation of the explicit time step restriction. As discussed in section 3.5.2, the CFL condition must be met to maintain stability. Therefore, lowering the dilatational wave speed for a given cell size increases the minimum stable time increment. For example, Challa (2015) used a sound speed for water of 100 m/s (0.07% of nominal) in his research using the explicit code LS-Dyna. Tippman

et al. (2009) artificially lowered the fluid sound speed to satisfactorily solve a sloshing tank problem using Abaqus/Explicit.

5.1.2 Abaqus/Explicit equations of state

Abaqus/Explicit offers numerous forms of an EOS depending on the problem at hand. For fluid simulations, a linear Hugoniot form of the Mie-Grüneisen relation has been shown to perform well in several benchmark problems within the Abaqus documentation (Dassault Systemes, 2013). Originally applied to solids, Mie-Grüneisen has successfully been used to model the pressure-volume-energy behavior of water, especially in the case of high speed/pressure/temperature applications where compressibility and shock formation is of interest (Liu and Liu, 2003, Krehl, 2009, Wu, 2013).

The Gruneisen model relating volume to pressure by means of internal energy is given by Eq. (88). Γ is the Gruneisen ratio, V is specific volume, p is pressure, and e is specific internal energy. Integrating gives Eq. (89) where ρ is density and p_0 and e_0 are integration constants representing the reference pressure and reference internal energy, respectively. The definition of Gruneisen ratio Γ relates the material density to a reference density with a material constant Γ_0 in Eq. (90).

$$\Gamma = V\left(\frac{dp}{de}\right)_V \tag{88}$$

$$p - p_0 = \frac{\Gamma}{V}(e - e_0) = \Gamma\rho(e - e_0) \tag{89}$$

$$\Gamma = \Gamma_0 \frac{\rho_0}{\rho} \tag{90}$$

A Hugoniot curve is commonly used to relate pressure and density (or specific volume) for a material and is based upon empirical data. A Hugoniot energy term can be written based upon the

nominal volumetric strain of the material (η) in Eq. (91), where $\eta = 1 - {\rho_0}/{\rho}$ and the "H" subscripts denote state variables solved using the Hugoniot relations. Combining Eq. (89) with Eq. (90) and using the Hugoniot pressure and Hugoniot energy in Eq. (91) as the reference values gives Eq. (92). Abaqus uses the Hugoniot curve fit in Eq. (93) to provide the reference pressure, which assumes a linear relationship between shock velocity (U_s) and particle velocity (U_p) in Eq. (94). Here, c_0 is the speed of sound and s is the slope coefficient.

$$E_H = \frac{p_H \eta}{2\rho_0} \tag{91}$$

$$p = p_H \left(1 - \frac{\Gamma_0 \eta}{2}\right) + \Gamma_0 \rho_0 e \tag{92}$$

$$p_H = \frac{\rho_0 c_0^2 \eta}{(1 - s\eta)^2} \tag{93}$$

$$U_s = c_0 + sU_p \tag{94}$$

The linear Hugoniot form of the Mie-Gruniesen equation can then be written as Eq. (95). With this form, only the initial conditions and material constants Γ_0, c_0, and s are required to fully define the equation of state. In low speed regimes, the particle velocity's influence upon the shock velocity can be neglected by assigning $s = 0$ in Eq. (94). The shock velocity then equals the speed of sound.

Based upon empirical data for water, the Gruniesen parameter Γ_0 is typically 0.5 (Liu and Liu, 2003). But in the case where heat conduction is not important, further simplifications can be made by assuming $\Gamma_0 = 0$, reducing the EOS to Eq. (96). This relation shows why slight compressibility is required to solve for pressure using the bulk modulus $\rho_0 c_0^2$. Incompressibility leads to a trivial

result. Also, with pressure varying as a square of the speed of sound c_0, it is evident how changing this value artificially increases or decreases compressibility effects.

$$p = \frac{\rho_0 c_0^2 \eta}{(1-s\eta)^2}\left(1 - \frac{\Gamma_0 \eta}{2}\right) + \Gamma_0 \rho_0 e \tag{95}$$

$$p = \rho_0 c_0^2 \left(1 - \frac{\rho_0}{\rho}\right) \tag{96}$$

5.2 Abaqus/Explicit CEL verification and validation

This section presents the numerous verification and validation problems conducted to explore the capability of the Abaqus/Explicit CEL approach. First, structural verification is conducted via analysis of linear elastic beam deflection. Fluid verification follows using simulations of Couette flow, circular-Couette flow, cylinder flow, and NACA0012 flow. Finally, FSI verification and validation is conducted for a gate deflection simulation using both experimental and numerical datasets.

Results of structural verification show a successful implementation of the analytic case and demonstrate the Abaqus solver is well suited to investigate flexible seals. Results for the fluid verifications show generally acceptable behavior, however some weakness are revealed as the complexity is increased. Simulations of NACA0012 flow reveal a fundamental flaw of the compressible scheme at low Mach numbers, and a means to rectify the problem is demonstrated. Results for the gate deflection validation problem demonstrate Abaqus' FSI coupling algorithm and the importance of a hyperelastic material model for rubber seal materials.

5.2.1 Linear elastic beam deflection verification problem

Abaqus/Explicit requires a fine mesh of linear elements for large deformation problems and mesh distortions (Dassault Systemes, 2013). The only continuum elements offered by Abaqus/Explicit are the linear hexahedral forms with or without reduced integration (C3D8R) and the modified quadratic tetrahedral (C3D10M). This study is conducted to verify the performance of these elements and identify the most appropriate choice for modeling extreme deformation. As mentioned above, linear elements can be overly stiff under extreme bending when fully integrated. Therefore, a fine mesh of reduced integration continuum elements C3D8R are a good choice for a thin flexible structure. To confirm this choice and to understand what level of mesh is required to obtain acceptable results, a comparison between the linear C3D8R element and the quadratic C3D20 is made using Abaqus/Standard. It is an implicit solver that offers both geometric orders for the C3D element.

To verify the model solutions, a comparison with analytical results for beam deflection can be made using Euler-Bernoulli beam theory. The governing equation relating deflection to applied load is given in Eq. (97), where E is the elastic modulus, I is second moment of area, w is deflection, and P is a distributed load (Rao, 1995). If EI is a constant and the load is not distributed, such as for a tip load, it is simplified to Eq. (98). For a cantilevered beam of length L, the boundary conditions of Eq. set (99) assign a zero slope at the clamped end, zero deflection at the clamped end, and zero deflection at the tip. The final boundary condition applies a tip load P as a shear force acting at $x = L$.

$$\frac{d^2}{dx^2}\left(EI\frac{d^2w}{dx^2}\right) = P(x) \tag{97}$$

$$EI\frac{d^4w}{dx^4} = 0 \tag{98}$$

$$w|_{x=0} = 0; \quad \left.\frac{dw}{dx}\right|_{x=0} = 0; \quad \left.\frac{d^2w}{dx^2}\right|_{x=L} = 0; \quad -EI\left.\frac{d^3w}{dx^3}\right|_{x=L} = P \tag{99}$$

Successive integration of Eq. (98) leads to:

$$\frac{d^3w}{dx^3} = C_1; \;\; \frac{d^2w}{dx^2} = C_1x + C_2; \;\; \frac{dw}{dx} = \frac{C_1}{2}x^2 + C_2x + C_3; \;\; w(x) = \frac{C_1}{6}x^3 + \frac{C_2}{2}x^2 + C_3x + C_4 \tag{100}$$

Applying boundary conditions provides the integration constants $C_1 = \frac{P}{-EI}, C_2 = \frac{PL}{EI}, C_3 = 0,$ $C_4 = 0$. An expression for the beam's tip displacement, δ_{tip}, can then be written as Eq. (101).

$$w(L) = \delta_{tip} = \frac{-P}{6EI}L^3 + \frac{PL}{2EI}L^2 = \frac{PL^3}{3EI} \tag{101}$$

For a comparison with the above analytical solution, a linear elastic beam is modeled in Abaqus with geometry similar to that used for the elastic gate problem below. It is 0.005 m thick, 0.090 m long and 0.030 m wide (Figure 52). It is assigned a linear elastic material modulus = 12 *MPa* and $\nu = 0$ in order to compare with analytical results. To simulate a clamped, cantilevered condition, one end of the beam is fixed in all degrees of freedom using the encastre boundary condition.

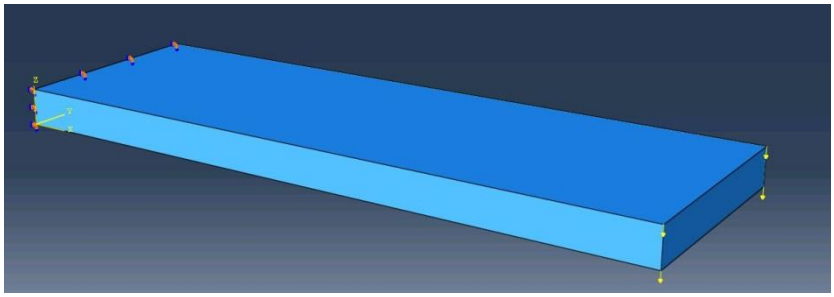

Figure 52. Linear elastic cantilevered beam

A total load of 1 *N* is distributed equally across the four corner nodes at the tip and the displacement is measured from the unloaded center top node to prevent the influence of local strain effects. In reality, this load would result in extreme nonlinear bending with the deflection order of magnitude approaching the beam's length. However, for this analysis where a comparison is made to linear beam theory, nonlinear geometry effects are not considered. Thus, the stiffness matrix is calculated initially and is not updated as a function of tip displacement or loading angle. The exact solution for tip displacement using Eq. (44) and the parameters above is 0.0648 m.

Table 19 displays the various grids and results for the beam meshed with C3D20 elements. Beginning with a single element, five mesh levels were achieved by uniformly refining the grid in all directions by a factor of 2. The observed order of accuracy (OOA) and grid convergence index (GCI) were calculated using the formulations above. Values for GCI approaching zero indicate solutions approaching asymptotic convergence. This data establishes a baseline for comparison with the linear C3D8R element.

Table 19. Grid study for C3D20 elements

C3D20	Total Elements	Element size	Spacing, h	Displacement (m)	Exact error (m)	r	OOA, p	GCI (Fs = 1.25)
Mesh 1	4096	.005625 x .001875 x .0003125 m	1	-6.48259E-02	2.59E-05	----	----	----
Mesh 2	512	.01125 x .00375 x .000625 m	2	-6.47553E-02	4.47E-05	2	3.03	0.0002
Mesh 3	64	.0225 x .0075 x .00125 m	4	-6.41781E-02	6.22E-04	2	2.25	0.0030
Mesh 4	8	.045 x .015 x .0025 m	8	-6.14260E-02	3.37E-03	2	2.16	0.0155
Mesh 5	1	.090 x .030 x .005 m	16	-4.91603E-02	1.56E-02	2	----	----

Table 20 displays the various grids and results for the beam meshed with C3D8R elements. The same spacing and refinement was used. The GCI is approaching zero, and the OOA is approximately the formal order of 2 on the more refined grids. The large value of OOA and the associated GCI for mesh 4 should be disregarded, as this is due to the large jump in accuracy from mesh 5 to mesh 4. Because the C3D8R element has only one integration point per element

direction, mesh 5 uses only one integration point for the entire beam (located on the neutral axis) and is thus meaningless. As the C3D8R element has only two nodes and one integration point per element direction, it is suspected the mesh density should be doubled (a single refinement with *r* = 2) to replicate accuracy similar to a C3D20 mesh having three nodes and three integration points. The results confirm this, as the accuracy achieved by the C3D20 beam using mesh 4 was approximately that of the C3D8R beam using mesh 3.

Table 20. Grid study for C3D8R elements

C3D8R	Total Elements	Element Size	Spacing, h	Displacement (m)	Exact error (m)	r	OOA, p	GCI (Fs = 1.25)
Mesh 1	4096	.005625 x .001875 x .0003125 m	1	-6.50390E-02	2.39000E-04	----	----	----
Mesh 2	512	.01125 x .00375 x .000625 m	2	-6.56335E-02	8.33500E-04	2	2.04	0.0037
Mesh 3	64	.0225 x .0075 x .00125 m	4	-6.80742E-02	3.27420E-03	2	2.37	0.0111
Mesh 4	8	.045 x .015 x .0025 m	8	-8.06926E-02	1.58926E-02	2	8.06	0.0009
Mesh 5	1	.090 x .030 x .005 m	16	-3.43667E+00	3.37187E+00	2	----	----

Finally, the tetrahedral element C3D10M is examined as another option available in Abaqus/Explicit. The "M" represents a modified formulation for use within explicit contact simulations. As it is quadratic, it uses three nodes and three integration points per side (10 total) and offers more computational efficiency than the linear element. Table 21 displays the various grids and results for the beam meshed with C3D10M elements. The GCI is approaching zero, and the OOA is just below the formal order of 2. Although the same spacing and refinement was used, a direct comparison to the hexahedral elements cannot be made because of the way the tetrahedral grid is structured. It is able to achieve similar accuracy as the C3D20 element, but at the expense of many more elements and nodes for the same mesh level.

Table 21. Grid study for C3D10M elements

C3D10M	Total Elements	Element Size	Spacing, h	Displacement (m)	Exact error (m)	r	OOA, p	GCI (Fs = 1.25)
Mesh 1	6812	.005625 x .001875 x .0003125 m	1	-6.56227E-02	8.22700E-04	----	----	----
Mesh 2	1563	.01125 x .00375 x .000625 m	2	-6.52868E-02	4.86800E-04	2	1.70	0.0028
Mesh 3	342	.0225 x .0075 x .00125 m	4	-6.41962E-02	6.03800E-04	2	1.78	0.0086
Mesh 4	76	.045 x .015 x .0025 m	8	-6.04541E-02	4.34590E-03	2	2.21	0.0200
Mesh 5	12	.090 x .030 x .005 m	16	-4.30907E-02	2.17093E-02	2	----	----

Results for the discretization error are shown in Figure 53 for various grid spacing and element types. This shows both the C3D20 and C3D10M elements perform similarly when the grid is under-refined, but non-monotonic convergence behavior is exhibited by the C3D10M mesh on finer grids. The slopes of this data and the plot in Figure 54 show convergence near second order, as expected. Figure 55 shows deflection of the beam versus nodes used for various meshes. The C3D20 element is overly stiff and approaches the solution from below, whereas the C3D8R element is overly flexible and approaches the solution from above. The C3D10M element shows non-monotonic convergence by over-shooting the exact solution at first.

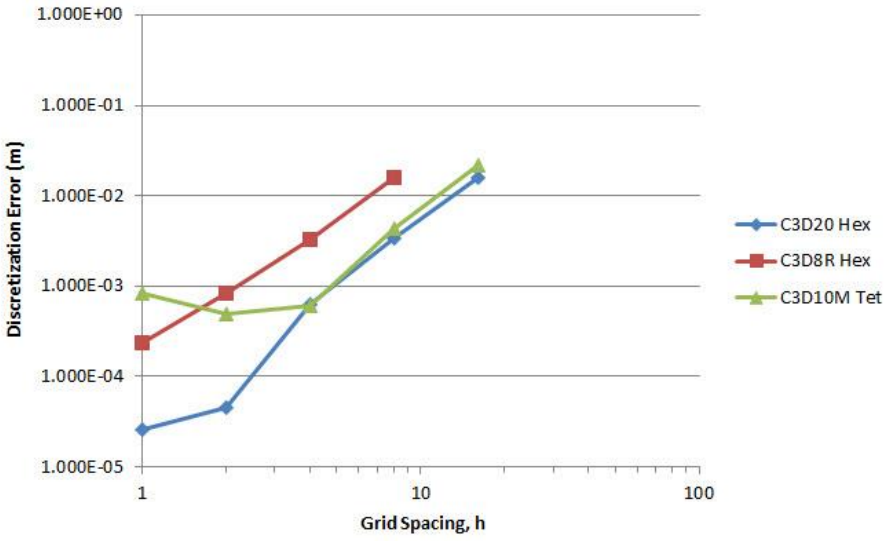

Figure 53. Discretization error for linear elastic beam deflection

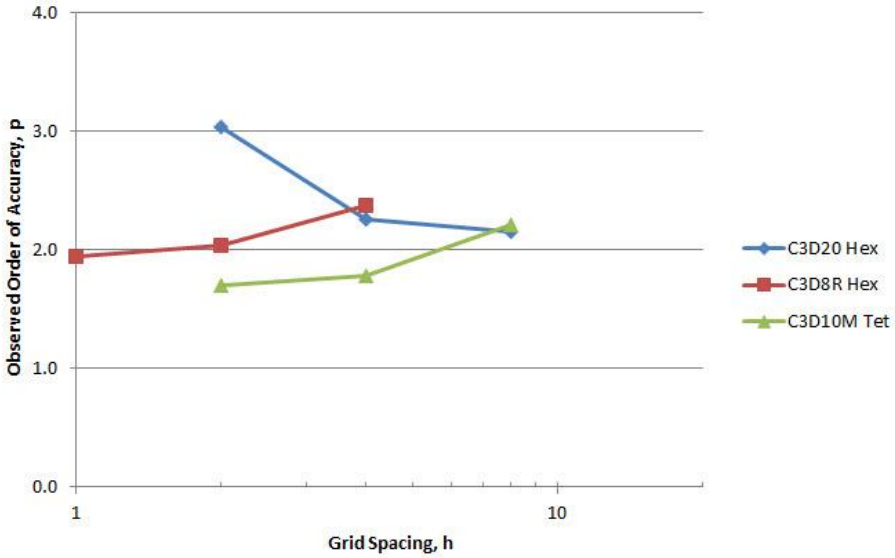

Figure 54. Observed order of accuracy for linear beam deflection

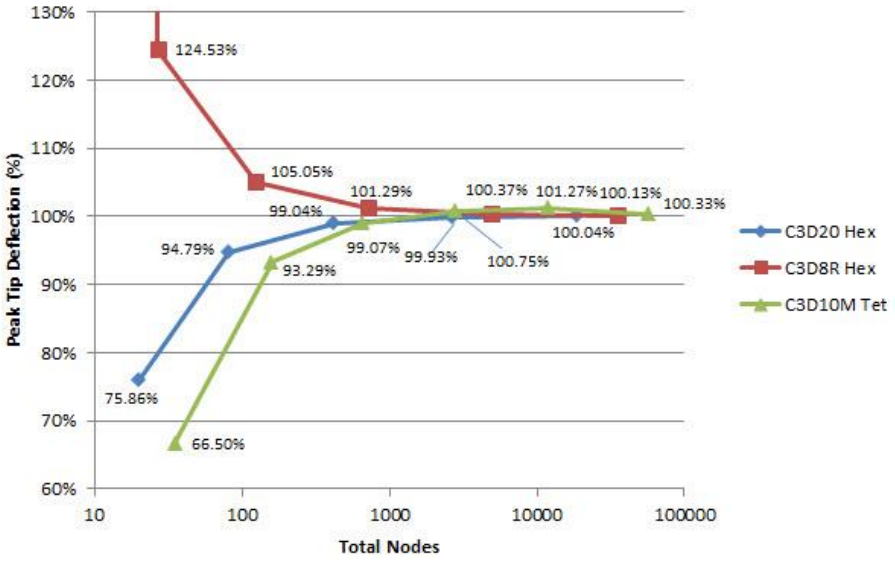

Figure 55. Deflection (% of theory) versus nodes with uniform refinement

While the above study does speak to the observed order of accuracy for various element formulations, it does not properly reflect the relative computational costs. The results in Figure 55 are based on uniform grid refinement without considerations for grid optimization. Because

the loading for the linear beam deflection problem is one-dimensional, refinement in the width or thickness directions does not contribute to increases in accuracy when the C3D20 element is used. This is proven in Table 22 where only axial refinement is applied to subsequent meshes. The errors achieved, observed orders of accuracy, and convergence nearly match the previous C3D20 grid refinement study results in Table 19, but the number of elements (and nodes) are drastically smaller.

Table 22. Length refinement using C3D20

C3D20	Total Elements	Element size	Nodes	Spacing, h	Displacement (m)	Discretization error (m)	r	OOA, p	GCI (Fs = 1.25)
Mesh 1	16	.005625 x .030 x .005 m	200	1	-6.48220E-02	2.20E-05	2	----	----
Mesh 2	8	.01125 x .030 x .005 m	104	2	-6.47488E-02	5.12E-05	2	3.00	0.00020
Mesh 3	4	.0225 x .030 x .005 m	56	4	-6.41647E-02	6.35E-04	2	2.32	0.00283
Mesh 4	2	.045 x .030 x .005 m	32	8	-6.12518E-02	3.55E-03	2	2.05	0.01801
Mesh 5	1	.090 x .030 x .005 m	20	16	-4.91603E-02	1.56E-02	----	----	----

For the linear element C3D8R however, refinements in both the length and thickness are important. This is because the reduced integration results in only 1 integration point within the element. Table 23 provides results for variations in length and thickness refinements, indicating that despite subsequent refinements in one dimension, reductions in error may never be achieved. When the mesh is refined in the length direction only, the results appear to converge according to the GCI, but the discretization error remains large. When the mesh is refined in the length and thickness direction, the discretization error continues to decrease along with GCI.

Table 23. Length and thickness refinement using C3D8R

Refinements in length only

C3D8R	Total Elements	Element Size (m)	Nodes	Spacing, h	Displacement (m)	Discretization error (m)	r	OOA, p	GCI (Fs = 1.25)
Mesh 1	16	.005625 x .030 x .005 m	68	1	-4.57540E+00	4.51060E+00	2	----	----
Mesh 2	8	.01125 x .030 x .005 m	36	2	-4.56320E+00	4.49840E+00	2	2.12	0.0010
Mesh 3	4	.0225 x .030 x .005 m	20	4	-4.51019E+00	4.44539E+00	2	2.02	0.0048
Mesh 4	2	.045 x .030 x .005 m	12	8	-4.29569E+00	4.23089E+00	2	2.00	0.0198
Mesh 5	1	.090 x .030 x .005 m	8	16	-3.43664E+00	3.37184E+00	----	----	----

Refinements in length and thickness

C3D8R	Total Elements	Element Size (m)	Nodes	Spacing, h	Displacement (m)	Discretization error (m)	r	OOA, p	GCI (Fs = 1.25)
Mesh 1	256	.005625 x .030 x .0003125 m	578	1	-6.50635E-02	2.63500E-04	2	----	----
Mesh 2	64	.01125 x .030 x .000625 m	162	2	-6.56374E-02	8.37400E-04	2	2.08	0.0034
Mesh 3	16	.0225 x .030 x .00125 m	50	4	-6.80584E-02	3.25840E-03	2	2.38	0.0109
Mesh 4	4	.045 x .030 x .0025 m	18	8	-8.06926E-02	1.58926E-02	2	8.05	0.0009
Mesh 5	1	.090 x .030 x .005 m	8	16	-3.43664E+00	3.37184E+00	----	----	----

The non-uniform refinement study results are used in Figure 56 to compare the increase in accuracy with increased computational cost. It shows that similar results for each element type can be achieved when the mesh is very coarse, but accuracy is increased more quickly with the C3D20 formulation. It should be mentioned that these results are applicable only to this particular problem and combinations of mesh refinement chosen. Variations in geometry and mesh densities may result in different magnitudes of the relationship and error extrapolation techniques, such as Richardson extrapolation, may not apply.

It is understood from the above study that the use of the C3D8R element in an Abaqus/Explicit analysis will require sufficient refinement to reproduce the expected bending behavior of ACV seals. Selective mesh refinement may be needed where extreme deformation is present and a grid refinement study is a necessity for confidence in convergence of the structure.

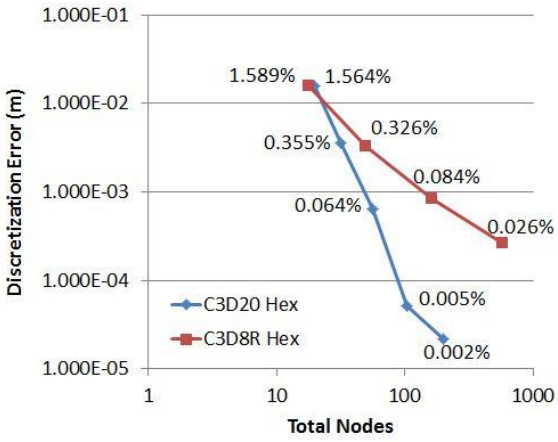

Figure 56. Discretization error versus nodes for C3D20 and C3D8R

5.2.2 Couette flow verification problem

Couette flow is a well-known canonical viscous fluid flow. It consists of viscous fluid captured between two infinitely long plates. One plate is stationary while the other moves with a defined constant velocity. Viscous drag forces resulting from the moving plate result in shear stresses throughout the fluid, forming a velocity gradient transverse to the plate motion (Figure 57). U and V are the velocities in the X and Y directions, respectively, and U_o represents the constant plate velocity. Certain other simplifying assumptions for the problem provide for a purely analytical solution to the Navier-Stokes equations. Thus, this problem is well suited to verify the accuracy of Eulerian fluid formulation within Abaqus/Explicit.

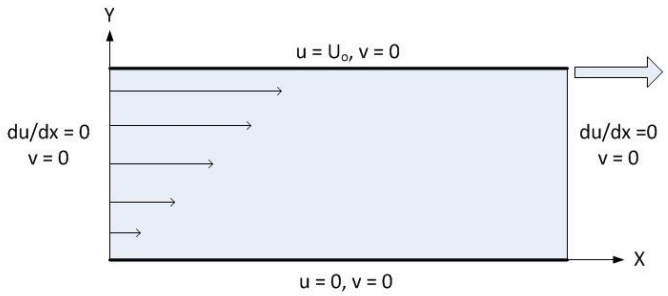

Figure 57. Couette flow

The flow can be solved using the conservation equations in the *X* and *Y* directions.

Continuity: $$\frac{\partial \rho}{\partial t} + \nabla \cdot \rho \boldsymbol{V} = \frac{\partial \rho}{\partial t} + \frac{\partial \rho u}{\partial x} + \frac{\partial \rho v}{dy} = 0 \quad (102)$$

X-Momentum: $$\rho \frac{Du}{Dt} = \left[-\frac{\partial p}{\partial x} + \frac{\partial \tau_{xx}}{\partial x} + \frac{\partial \tau_{yx}}{\partial y} + \frac{\partial \tau_{zx}}{\partial z} \right] + \rho f_x \quad (103)$$

Y-Momentum: $$\rho \frac{Dv}{Dt} = \left[-\frac{\partial p}{\partial y} + \frac{\partial \tau_{xy}}{\partial x} + \frac{\partial \tau_{yy}}{\partial y} + \frac{\partial \tau_{zy}}{\partial z} \right] + \rho f_y \quad (104)$$

Eq. (105) through Eq. (107) is obtained by applying the following Couette flow assumptions:

- Neglecting gravity and all body forces: $f = 0$
- Infinitely long plates: no *d/dx* terms
- Steady state: no *d/dt* terms
- Incompressible flow: $d\rho/dt = 0$ and ρ is constant
- Newtonian fluid with μ as the fluid viscosity
- Uni-directional flow with no pressure gradient

Continuity: $$\frac{\partial v}{\partial y} = 0 \quad (105)$$

X-Momentum: $$0 = \left[\frac{\partial \tau_{yx}}{\partial y} \right] \quad (106)$$

Y-Momentum: $$0 = \left[\frac{\partial \tau_{yy}}{\partial y} \right] \Rightarrow \tau_{yy} = 0 \ \ (no\ x\ dependency) \quad (107)$$

Referring to Newman (1977), the exact solution for Couette flow with pressure gradient becomes:

$$u(y) = \frac{\partial p}{\partial x}\left(\frac{y^2 - hy}{2\mu}\right) + \frac{U_0 y}{h} \tag{108}$$

The velocities along the height of the flow can now be solved for any given pressure gradient, dP/dx, which is accomplished in Table 24. The physical parameters chosen are μ = 50 Ns/m^2, h = 0.5 m, and U_0 = 10 m/s. It is noted that a realistic dynamic viscosity for water is μ = 0.001 Ns/m^2. Using this value however would result in a long computational time, as the viscous forces are small relative to the inertial forces (Re = 5E6). In order to minimize the stabilization time and establish a laminar flow with a low Re, the viscosity has been artificially increased to μ = 50 Ns/m^2 (Re = 100). The pressure gradients chosen range from -1E4 to 1E4 (Pa/m). Concerning pressure gradients, it should be noted that they are positive when the flow moves into a region of higher pressure, or $dP/dx > 0$. As such, a driving pressure for Couette flow moving left to right (as in this example) is a negative gradient, or $dP/dx < 0$.

Table 24. Couette flow velocity profiles (μ = 50 Ns/m^2, h = 0.5 m, and U_0 = 10 m/s)

dP/dx (Pa/m) =	-1.00E+04	-5.00E+03	-2.00E+03	0.00E+00	2.00E+03	5.00E+03	1.00E+04
y (m)	u (m/s)	u (m/s)	u (m/s)	u (m/s)	u (m/s)	u (m/s)	u (m/s)
0	0	0	0	0	0	0	0
0.05	3.25	2.125	1.45	1	0.55	-0.125	-1.25
0.1	6	4	2.8	2	1.2	0	-2
0.15	8.25	5.625	4.05	3	1.95	0.375	-2.25
0.2	10	7	5.2	4	2.8	1	-2
0.25	11.25	8.125	6.25	5	3.75	1.875	-1.25
0.3	12	9	7.2	6	4.8	3	0
0.35	12.25	9.625	8.05	7	5.95	4.375	1.75
0.4	12	10	8.8	8	7.2	6	4
0.45	11.25	10.125	9.45	9	8.55	7.875	6.75
0.5	10	10	10	10	10	10	10

It is convenient to present the information in non-dimensional forms for use with other geometries and speeds. The non-dimensional pressure gradient P is given in Eq. (109) according to the definition by Newman (1977). Height and velocity are nondimensionalized by dividing by the plate separation distance and top plate speed, respectively. The results are shown in Table 25 and Figure 58.

$$P = -\frac{dP}{dx}\frac{h^2}{2\mu u} \tag{109}$$

Table 25. Non-dimensional Couette flow velocity profiles

P =	2.50	1.25	0.50	0.00	-0.50	-1.25	-2.50
y/h	u/Uo	u/Uo	u/Uo	u/Uo	u/Uo	u/Uo	u/Uo
0	0	0	0	0	0	0	0
0.1	0.325	0.2125	0.145	0.1	0.055	-0.0125	-0.125
0.2	0.6	0.4	0.28	0.2	0.12	0	-0.2
0.3	0.825	0.5625	0.405	0.3	0.195	0.0375	-0.225
0.4	1	0.7	0.52	0.4	0.28	0.1	-0.2
0.5	1.125	0.8125	0.625	0.5	0.375	0.1875	-0.125
0.6	1.2	0.9	0.72	0.6	0.48	0.3	0
0.7	1.225	0.9625	0.805	0.7	0.595	0.4375	0.175
0.8	1.2	1	0.88	0.8	0.72	0.6	0.4
0.9	1.125	1.0125	0.945	0.9	0.855	0.7875	0.675
1	1	1	1	1	1	1	1

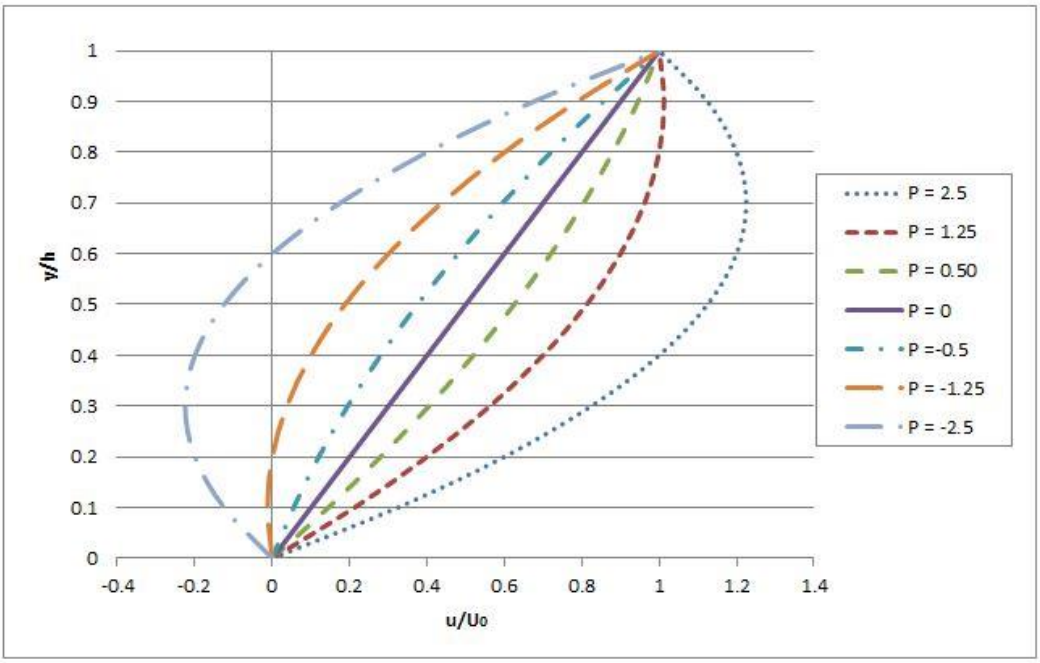

Figure 58. Non-dimensional Couette flow velocities at various pressure gradients

With the exact solution for Couette flow given above, a comparison with Abaqus/Explicit's Eulerian fluid formulation can now be made. First, a 0.5 m x 5 m domain of Eulerian fluid is created using a predefined field with a void fraction of 1. Water assigned to the domain by using the linear Hugoniot fit of the Mie-Grüneisen equation of state with the parameters c_0 = 1500 m/s, s = 0, and Γ_0 = 0. Other assigned properties are dynamic viscosity μ = 50 Ns/m^2 and density ρ = 1000 Kg/m^3. Again, an artificially high value for dynamic viscosity is used to reduce the simulation time.

As the bottom and top surfaces represent the plates, they are assigned zero-velocity boundary conditions in the *y*-direction to prevent outflow normal to these surfaces. The bottom surface is given a no-slip boundary condition by setting its *x*-direction velocity to zero. The top surface is given an *x*-velocity boundary condition equal to U_0 = 10 m/s to simulate a no-slip condition on a

moving plate. A 2D representation is constructed by setting the *z*-velocity to zero on both *x*-*y* faces to prevent flow in the third dimension. The inflow face is given a "free inflow" Eulerian boundary condition and the outflow face is given a "free outflow" Eulerian boundary condition. No pressure gradients are assigned so that the linear velocity profile is developed. The domain is discretized with EC3D8R elements and a global mesh size of 0.05 m (1000 total elements) in Figure 59. Following 5 s of simulation, the viscous fluid forces fully develop the flow, as shown in Figure 60.

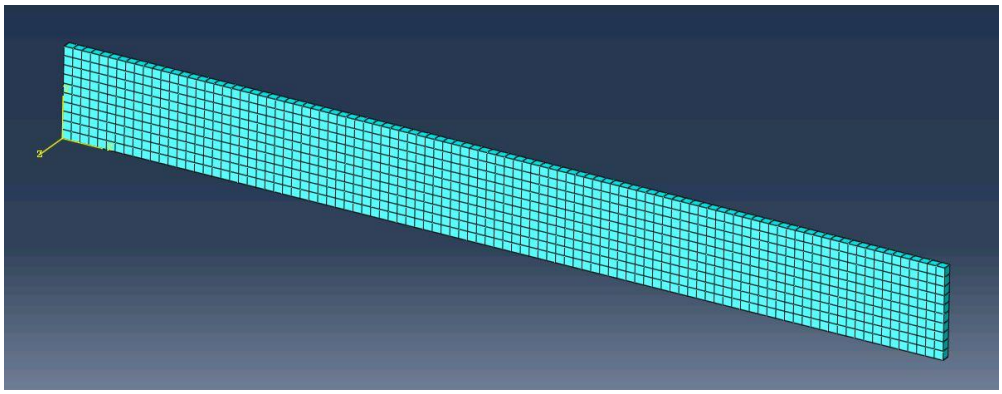

Figure 59. Couette flow domain, 0.5 x 5 m, 0.05 m grid

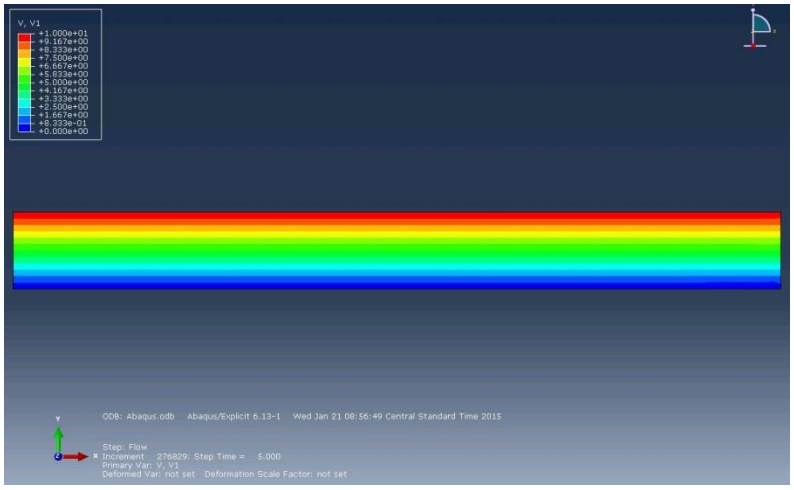

Figure 60. Velocity profile in Couette flow (*t* = 5 s)

Figure 61 displays the values for the nodal *x*-velocity through a cut at x = 2.5 m, the domain center. The asymptotic range is achieved at around 3 s with a linear velocity profile. For this mesh size of 0.05 m, the value of the node (x, y, t, = 2.5, 0.25, 5) is 5.005 m/s using single precision. As the exact solution for this position is 5 m/s, the spatial percent error is ||5 – 5.005||/5.005 = 0.1%.

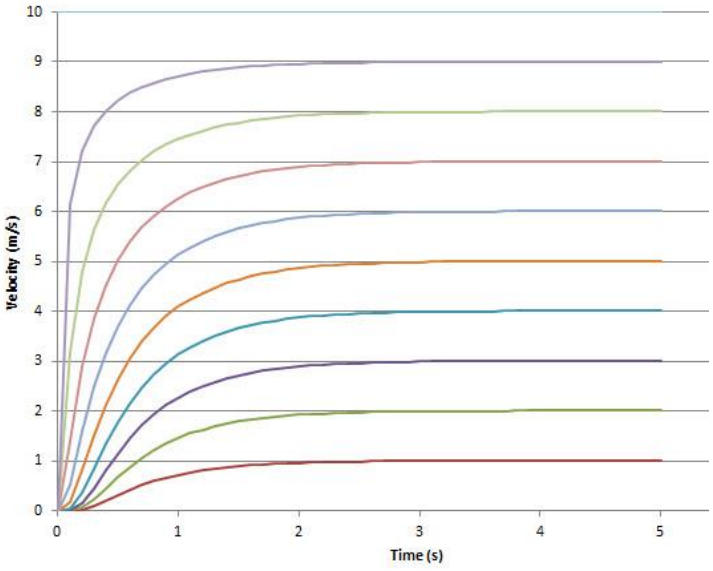

Figure 61. Couette outflow velocities, *U* = 10 m/s, *dp/dx* = 0

To further examine spatial errors using the EC3D8R element, a grid refinement study can be performed for Couette flow having a large pressure gradient within the domain. The pressure gradient will provide a nonlinear velocity profile so that large errors exist when using a coarse mesh of linear elements. To establish a pressure gradient of P = 2.5 over the 5 m length ($\frac{dP}{dx} = -10000\ Pa/m$), pressure loads of 50.001 KPa and 1 Pa are applied at both the *y*-*z* inflow and outflow faces, respectively. To ensure steady state is reached, the simulation time is extended to 8 s for all cases, and *y*-velocities are checked to ensure they are near zero (*O*E-9 using double precision).

The domain is initially discretized with a global mesh of δx = 0.25 m (40 total elements) and then uniformly refined by a factor of 2 to obtain six grid spacings of h = 1 to 32. The results for the grid refinement study are shown in Table 26. L_{inf} and L_2 error norms are calculated for each mesh using the velocities at the selected nodes. The average spatial error is calculated as the difference between the exact solution and the Abaqus solution. The OOA (p) is then calculated using both L_{inf} and L_2 error norms. The variations of OOA as the mesh is refined results from oscillations of the solution. Finally, the GCI (absolute relative) is determined using the error for at midpoint node (y/h = 0.5) and shows near identical results when refining from mesh 2 to mesh 1. This indicates further refinement will not significantly reduce error. Although the spatial errors are small relative to the exact solution (<0.2%), the inconsistent reduction in them as the mesh is refined indicates other, larger error sources exist when solving this problem using the explicit Eulerian material code. From an engineering perspective, it can be argued that a fluid solution within 0.2% of the exact answer is adequate, and further effort or code complexity to reduce the residual error beyond this point may not be warranted.

Table 26. Grid study for Couette flow with pressure gradient, P = 2.5 (Abaqus/Explicit)

INPUTS:	P = 2.5	dp/dx = -10000 (Pa/m)	Inflow Pressure (Pa) =	50001								
	Domain size (m) =	0.5 x 5	Outflow Pressure (Pa) =	1								
Mesh Level	**Total Elements**	**Element Size (m)**	**Nodes**	**Spacing, h**	**Linf_Norm**	**L2_Norm**	**Avg. Error (%)**	**r**	**p (Linf)**	**p (L2)**	**Fs**	**GCI (%)**
1	40960	.007812 x .007812 x .007812	83330	1	2.4200E-02	1.8890E-02	0.20%	2	0.000	0.001	3	0.0000
2	10240	.015625 x .015625 x .015625	21186	2	2.4200E-02	1.8904E-02	0.20%	2	-1.273	-1.502	3	0.1410
3	2560	.03125 x .03125 x .03127	5474	4	1.0015E-02	6.6759E-03	0.07%	2	1.279	1.539	3	0.1421
4	640	.0625 x .0625 x .0625	1458	8	2.4300E-02	1.9405E-02	0.20%	2	1.222	1.123	3	0.2235
5	160	.125 x .125 x .125	410	16	5.6700E-02	4.2252E-02	0.37%	2	-2.790	-2.365	3	0.0649
6	40	.25 x .25 x .25	126	32	8.2000E-03	8.2000E-03	0.08%	----	----	----	----	----

For comparison, the same model, boundary conditions, and mesh spacings have been implemented using Abaqus/CFD. This code uses an incompressible, implicit finite volume solver and a FC3D8 element, where "F" designates the CFD implementation of the 8-node linear element. Observe in

Table 27 that this code provides lower spatial errors and an OOA approaching the formal order of 2 as $h \rightarrow 0$. Grid convergence via the GCI parameter is also more consistent. This shows that the model setup is correct, but differences in the specific numerical techniques used by the Abaqus/Explicit Eulerian code and Abaqus/CFD codes result in subtly different solutions and convergence characterisitics.

Table 27. Grid study for Couette flow with pressure gradient, *P* = 2.5 (Abaqus/CFD)

INPUTS:	P = 2.5	dp/dx = -10000 (Pa/m)	Inflow Pressure (Pa) =	50001								
	Domain size (m) =	0.5 x 5	Outflow Pressure (Pa) =	1								
Mesh Level	**Total Elements**	**Element size (m)**	**Nodes**	**Spacing, h**	**Linf_Norm**	**L2_Norm**	**Avg. Error (%)**	**r**	**p (Linf)**	**p (L2)**	**Fs**	**GCI (%)**
1	40960	.007812 x .007812 x .007812	83330	1	4.0000E-04	3.0806E-04	0.03%	2	1.907	1.895	3	0.0098
2	10240	.015625 x .015625 x .015625	21186	2	1.5000E-03	1.1460E-03	0.11%	2	1.874	1.912	3	0.0356
3	2560	.03125 x .03125 x .03127	5474	4	5.5000E-03	4.3130E-03	0.41%	2	2.124	1.979	3	0.1316
4	640	.0625 x .0625 x .0625	1458	8	2.3975E-02	1.7001E-02	1.58%	2	2.157	2.164	3	0.7712
5	160	.125 x .125 x .125	410	16	1.0690E-01	7.6204E-02	6.61%	2	2.282	2.770	3	3.7063
6	40	.25 x .25 x .25	126	32	5.1990E-01	5.1990E-01	51.99%	----	----	----	----	----

5.2.3 Circular Couette flow verification problem

In order to further investigate the numerical error shown above in the Couette flow problem, a second fluid problem is simulated using Abaqus/Explicit. Circular Couette flow is similar to the above, but the plates are now arranged as two concentric cylinders as shown in Figure 62. The outer cylinder wall remains stationary while the inner wall rotates at a prescribed angular velocity. Incompressible, viscous fluid captured between the two infinitely long cylinders transfers shear stress throughout the flow domain resulting in velocity gradients normal to the cylindrical surfaces in both *x* and *y* directions.

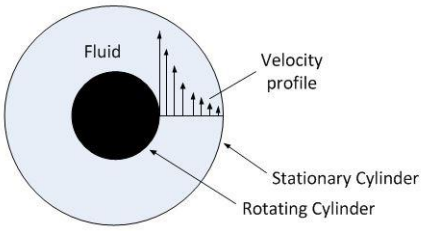

Figure 62. Circular Couette flow

A steady, analytical solution to the problem using cylindrical coordinates is provided in early work by Taylor (1923) as Eq. (110), where V is the velocity at any radius r, from the rotational axis. A and B are constants relating the angular velocity to the cylinder geometries. They can be obtained using the definition of angular velocity, $V = \Omega r$, where Ω_i and Ω_o are the inner and outer cylinder speeds respectively, and R_i and R_o are the cylinder radii, respectively. At the inner radius where $r = R_i$, Eq. (110) can be written as Eq. (111) and then simplified to give Eq. (112). A similar approach at the outer radius gives Eq. (113).

$$V = Ar + {}^{B}/_{r} \tag{110}$$

$$V = \Omega_i R_i = AR_i + {}^{B}/_{R_i} \tag{111}$$

$$\Omega_i = A + {}^{B}/_{{R_i}^2} \tag{112}$$

$$\Omega_o = A + {}^{B}/_{{R_o}^2} \tag{113}$$

If the outer cylinder is stationary so that $\Omega_o = 0$, Eq. (112) and Eq. (113) can be combined to solve explicitly for the constants A and B, shown by Eq. (114) and Eq. (115). Finally, Table 28 provides

inputs and analytical results for circular Couette flow using Eqs. (110), (114), and (115); where $\eta = {R_i}/{R_o}$.

$$A = -\Omega_i \frac{\eta^2}{(1-\eta^2)} \tag{114}$$

$$B = \Omega_i \frac{{R_i}^2}{(1-\eta^2)} \tag{115}$$

Table 28. Circular Couette flow analytical results

INPUTS					
Ri (m)	Ro (m)	Ω_i (rad/s)	Ω_o(rad/s)		
1	2	6.2832	0		
r (m)	**η**	**A**	**B**	**V (m/s)**	**dP/dr**
2	0.5	-2.094	8.378	0.00	0.00
1.875	0.5	-2.094	8.378	0.54	156.13
1.75	0.5	-2.094	8.378	1.12	719.36
1.625	0.5	-2.094	8.378	1.75	1889.02
1.5	0.5	-2.094	8.378	2.44	3980.33
1.375	0.5	-2.094	8.378	3.21	7507.87
1.25	0.5	-2.094	8.378	4.08	13343.71
1.125	0.5	-2.094	8.378	5.09	23034.34
1	0.5	-2.094	8.378	6.28	39478.42

The problem setup in Abaqus/Explicit consists of a circular Eulerian fluid domain having a 2 m radius. All *z*-direction velocities are set to zero to represent a two-dimensional problem. To represent no-slip boundaries of an outer cylinder wall, all velocities at the fluid domain outer diameter are set to zero. A rigid body cylinder of 1 *m* radius is then placed concentric to the Eulerian domain and an angular velocity of 2π rad/s is applied about its *z*-axis. A "rough" general contact interaction is prescribed on its surface to enforce a no-slip boundary.

The linear Hugoniot fit of the Mie-Grüneisen equation of state is again used to define the fluid. The properties are: c_0 = 1500 m/s, s = 0, Γ_0 = 0, μ = 50 Ns/m^2 and density ρ = 1000 Kg/m^3. Again,

an artificially high value for dynamic viscosity is used to reduce the simulation time. No properties are required for the rigid body inner cylinder.

The simulation is conducted on four mesh levels using a refinement factor of 2, maintaining one element in the *z*-direction for all meshes. The rigid body cylinder is refined equally with the fluid domain in order to facilitate consistent contact interactions (Dassault Systemes, 2013). Data for the velocities through the domain are collected at each of the indicated positions in Figure 63. The positions remain the same for each grid. Figure 64 shows the resultant velocity vectors throughout the domain at steady state, revealing development of the velocity gradient normal to the inner cylinder surface.

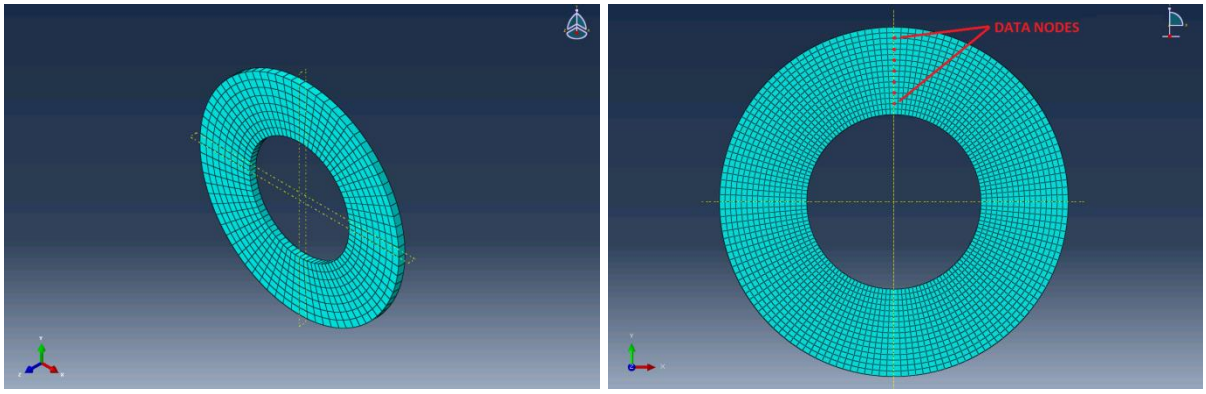

Figure 63. Circular Couette flow fluid grids (δx = 0.125 m and 0.0625 m)

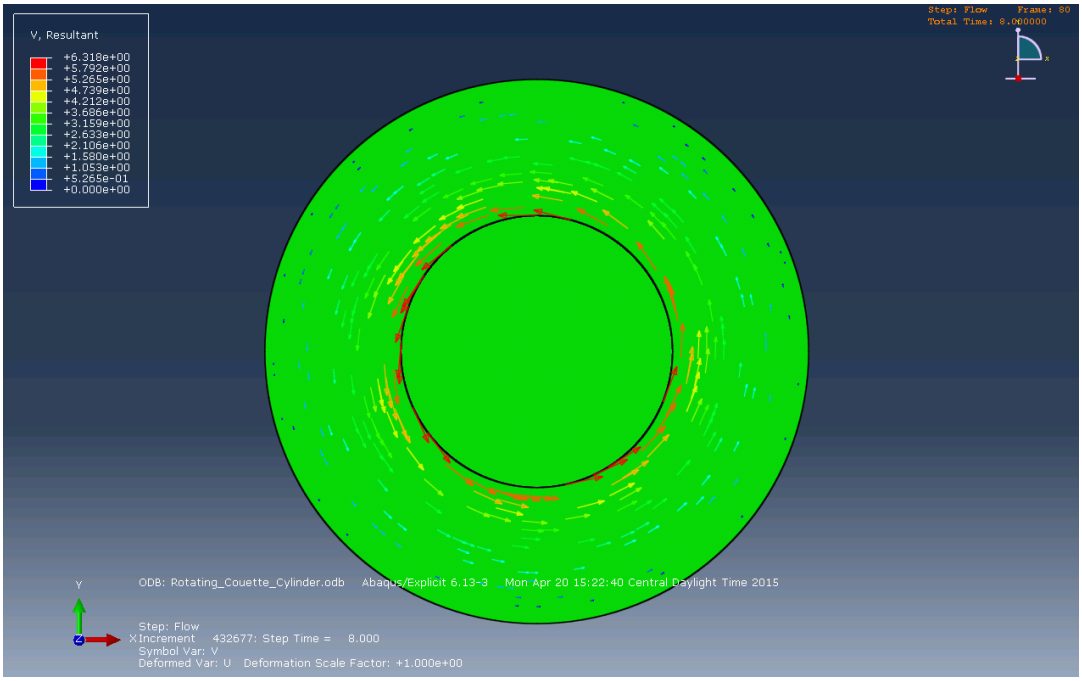

Figure 64. Circular Couette flow, resultant velocity (δx = 0.0625 m)

Calculations from the numerical results collected at the nodal locations identified above are shown in Table 29. Reducing the grid spacing reduces the average error, which is defined as the average of all the relative differences between the Abaqus/Explicit solution and the analytical solution. The GCI also reduces with spacing; however, further refinements would be necessary to show grid convergence for this problem. The observed orders of accuracy (p) all fall below the formal order, but a curiously low result for this factor is found on the finest mesh. In general, the results for this problem echo the curious performance exhibited above. Error reductions are not consistent between all mesh levels and a Richardson Extrapolation technique may not be applicable for the results shown here. One theory is that error introduced by the contact algorithm required to enforce a non-slip condition along the inner cylinder surface is not perfectly correct. Despite this, the argument can again be made that a fluid solution within 0.7% of the exact answer is adequate from

an engineering perspective, especially if it reduces the complexity and expense typical for strongly-coupled, implicit solutions.

Table 29. Grid study for circular Couette flow

INPUTS:	Outer DIA (m) =	2	Outer Velocity (m/s) =	0
	Inner DIA (m) =	1	Inner Velocity (rad/s) =	6.283185
	Element type =	EC3D8R		

Mesh Level	Fluid Elements	Element Size (m)	Nodes	Spacing, h	L2_Norm	Avg_Error (%)	r	p (L2_Norm)	Fs	GCI (%)
1	9632	.03125 x .03125 x .03125	19866	1	3.4229E-02	0.67%	2	0.34626	3	2.4818
2	2368	.0625 x .0625 x .0625	5032	2	4.3514E-02	2.19%	2	1.60101	3	8.1508
3	608	.125 x .125 x .125	1368	4	1.3200E-01	5.23%	2	1.50395	3	16.6224
4	144	.25 x .25 x .25	360	8	3.7438E-01	20.28%	----	----	----	----

5.2.4 Cylinder in flow verification problem

The following work is conducted to verify the computational domain and imposed boundary conditions are correct for simulating an open channel flow with a free surface. First, a rectangular Eulerian domain is constructed and a vertical cylinder is placed equidistant from the sides (Figure 65). The domain is meshed with EC3D8R elements having an approximate edge length of 0.04 m. Fluid material is predefined in the bottom half of the domain in order to establish a free surface, as indicated by the void fraction in Figure 65. Dirichlet boundary conditions are imposed to prevent penetrations through the sides (*Y* velocity = 0) and bottom (*Z* velocity = 0). Slip is permitted; there is no *X/Z* velocity restriction on the sides and no *X/Y* velocity restriction on the bottom. At $t = 0$, the bottom half of the domain is initialized with water at the inlet velocity. At $t = 0.01$ s, only the inlet plane remains at the prescribed velocity, and the remainder of the flow field is solved subject to the boundary conditions.

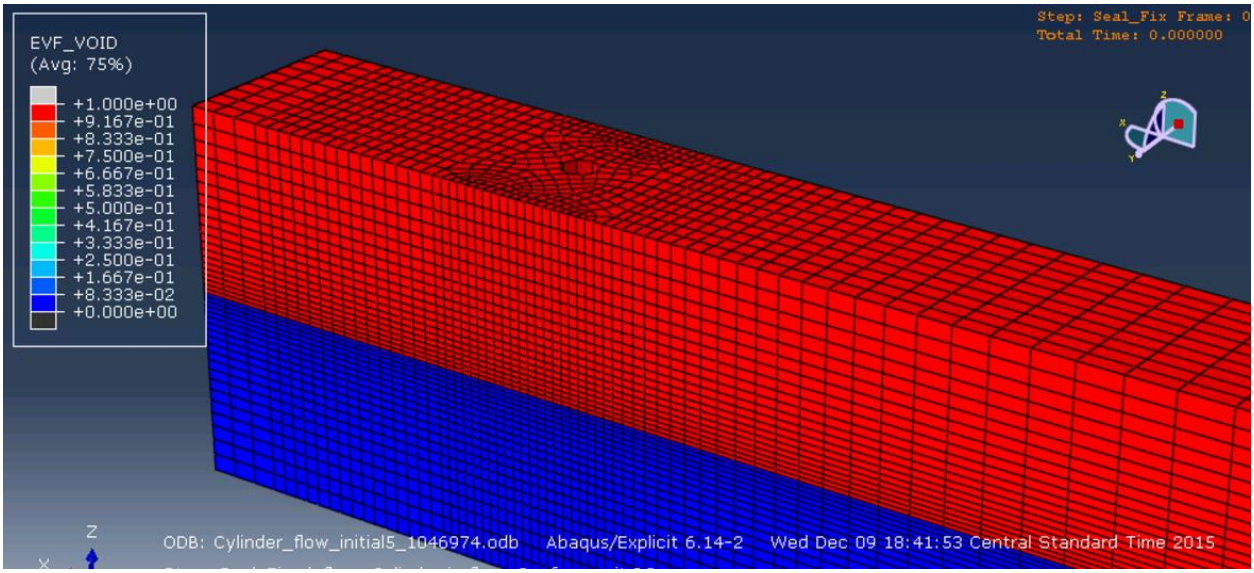

Figure 65. Cylinder in flow domain, void fraction

At the exit boundary, hydrostatic pressure is required in order to generate a stable free surface. Because Abaqus does not explicitly offer this specialized boundary condition common in many modern CFD codes, some creativity is required. Hydrostatic pressure is simulated by applying a pressure load upon the flow exit region. It is set to zero at the anticipated free surface elevation and is linearly increased with depth according to Eq. 116. To minimize the influence of the open Eulerian boundary above the anticipated free surface elevation at the exit, a no-penetration condition is imposed on that surface (X velocity = 0).

$$P = \rho g h \tag{116}$$

These exit conditions effectively require all flow to leave the domain through a prescribed space and against a prescribed back pressure regardless of the domain length and what may be occurring upstream. For these simulations, the exit free surface elevation is chosen to be equal to the inlet free surface elevation, as required by continuity. However, because the model is finite, errors

arrive when the fluid free surface falls below or rises above the explicitly prescribed fixed pressure boundary. Thus, a domain length study is conducted to assess how the finite length may affect the results.

As the immediate focus of this study is the effect of the exit boundary location and not the accuracy of the cylinder drag result, the mesh density used in the investigation is coarse and is held constant. The region around the cylinder is partitioned and meshed separately to minimize variations in the element length as the domain length is changed. The mesh aft of the partition is biased larger toward the exit and biased smaller toward the initial free surface. Each simulation is allowed to run for 20 s to dissipate any start-up transients. The total cylinder reaction force is determined as the summation of each nodal force on the cylinder surface. A one second running average of the force and the standard deviation over one second are calculated to discern when a quasi-steady state is reached.

A summary of parameters used for the investigation is given in Table 30. The domain dimensions provide boundaries that exceed the recommended minimum of 5 diameters upstream, and 15 diameters downstream, (Zdravkovich 1997). The flow parameters are chosen to obtain a laminar case with Re = 50 based on the cylinder diameter in order to minimize unsteady behavior. The length-based Froude number (F_n) is approximately 1, whereas a depth-based Froude number (F_δ) is 0.45, indicating subcritical flow.

Table 30. Cylinder in flow parameters, Re = 50, Ma = 6.66E-4

Cylinder in flow						
Inlet velocity	1	(m/s)		Cylinder diameter	0.1	(m)
fluid density ρ	1000	(kg/m^3)		Domain width	0.5	(m)
μ	2	(kg/(m-s)		Cylinder center to inlet	0.8	(m)
gravity	9.8	(m/s^2)		Cylinder center to outlet	4, 6, 8	(m)
Re	50			Initial free surface height	0.5	(m)
Fr (length based)	1.01					
Fr (depth based)	0.45					

Figure 66 plots the *X*-component of the total cylinder reaction force for exit boundary distances of 4 m, 6 m, and 8 m. From these plots, it is clear that numerical noise in the simulation results in oscillations with a standard deviation of 1.7% to 5% of the magnitude. Characteristic changes in the slope of the results stem from rebounding and oscillation of the free surface, which is most prevalent in the longer length domains.

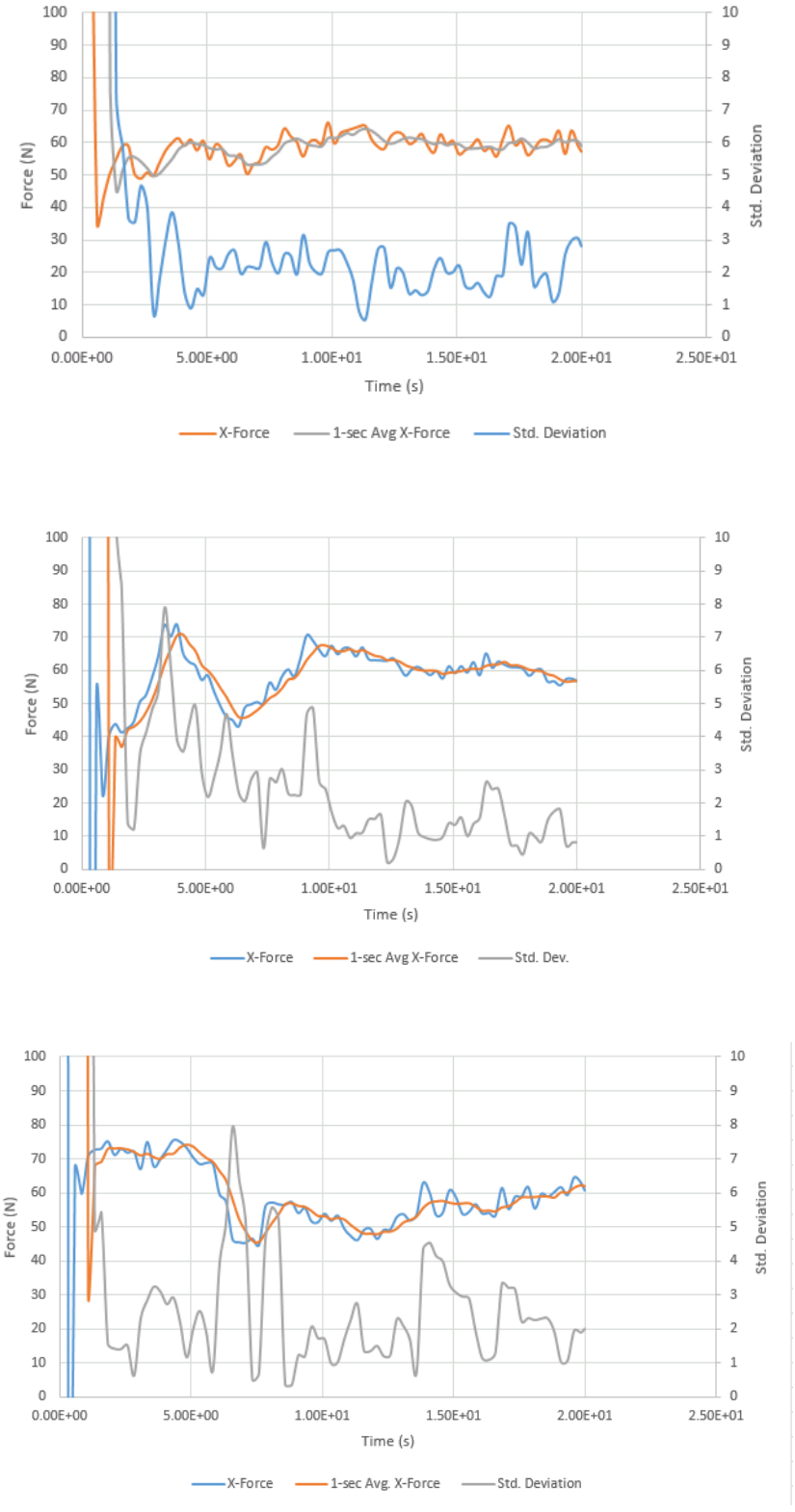

Figure 66. *X*-force on cylinder; pressure exit boundary; 4 m, 6 m, 8 m, respectively

As an alternate exit boundary condition, a constant prescribed exit velocity is also investigated in lieu of the hydrostatic back pressure load. In this modeling approach, mass continuity in the domain is enforced by setting the exit area size and velocity equal to the inlet area size and velocity. Hydrostatic pressure in the fluid column is established due to the gravity body force acting on the fluid. Using the parameters of Table 30 once again, Figure 67 plots the *X*-component of the total cylinder reaction force when this exit boundary is used. These plots show similar oscillation of the force magnitude, but with slightly smaller standard deviations of 1.7% to 4.2%. Characteristic changes in the slope of the results remain due to rebounding of the free surface; again, most prevalent in the longer length domains.

To investigate whether the oscillations will eventually damp out in longer simulations, the 4 m exit boundary model was re-run for a total simulated time of 35 s. Figure 68 shows the results for the final 15 s of the run. The oscillations continue to persist with no indication of diminishing with time. Variations in the standard deviations over 1 s also are consistent with no additional convergence. This reveals the best resolution obtainable for the given parameters and boundary conditions.

Since the pressure is not explicitly prescribed anywhere in the model boundary conditions, the exit boundary is also investigated to verify proper hydrostatic pressure is established in the fluid column. Figure 69 shows the pressure as a function of depth through the column on the centerline of the exit boundary. Also plotted is an "ideal pressure" curve based on the calculation of Eq. 116. Running averages of static pressure over 1, 2, and 3 s all correlate well with the ideal pressure, indicating proper development of the hydrostatics within the domain.

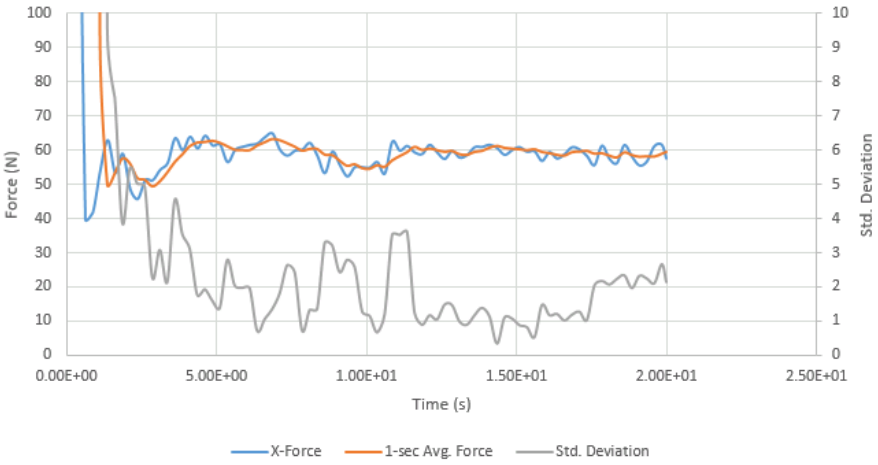

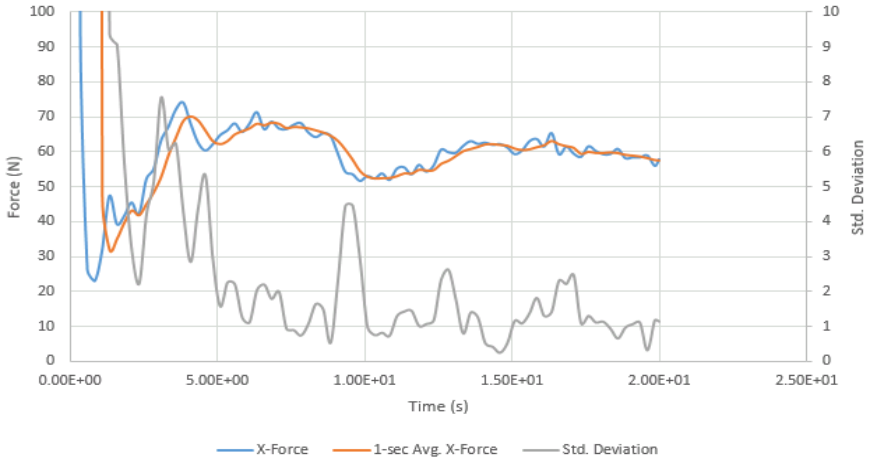

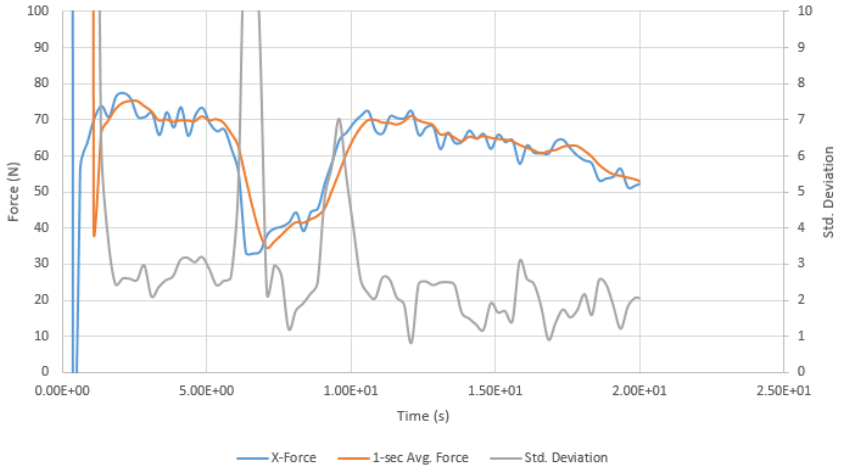

Figure 67. *X*-force on cylinder; velocity exit boundary; 4 m, 6 m, 8 m, respectively

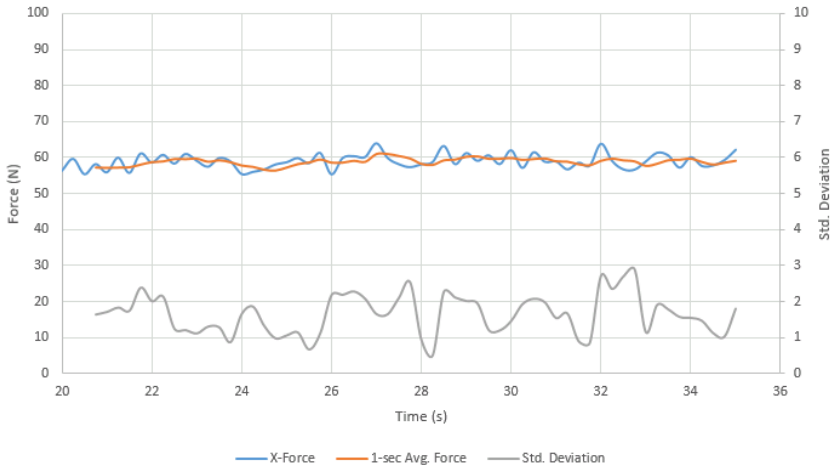

Figure 68. *X*-force on cylinder; velocity exit boundary at 4 m

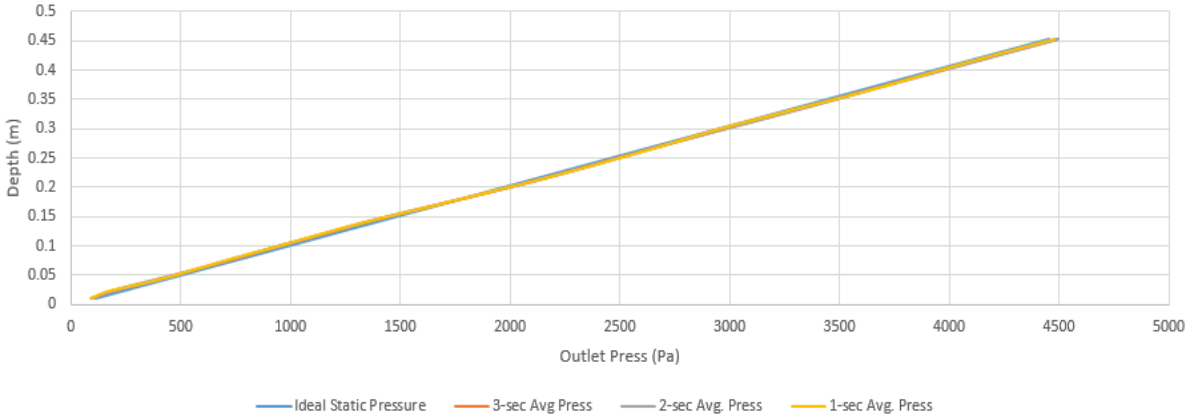

Figure 69. Static pressure through outlet centerline; velocity exit boundary at 4 m

A side-by-side comparison can be made between the hydrostatic exit boundary condition (BC) and velocity exit BC using the *X*-force results for the 4 m exit boundary distance. While Figure 70 shows a general qualitative agreement between the two in terms of magnitude, the standard deviation for the velocity exit boundary appears slightly more consistent over the final 8 s of simulated time.

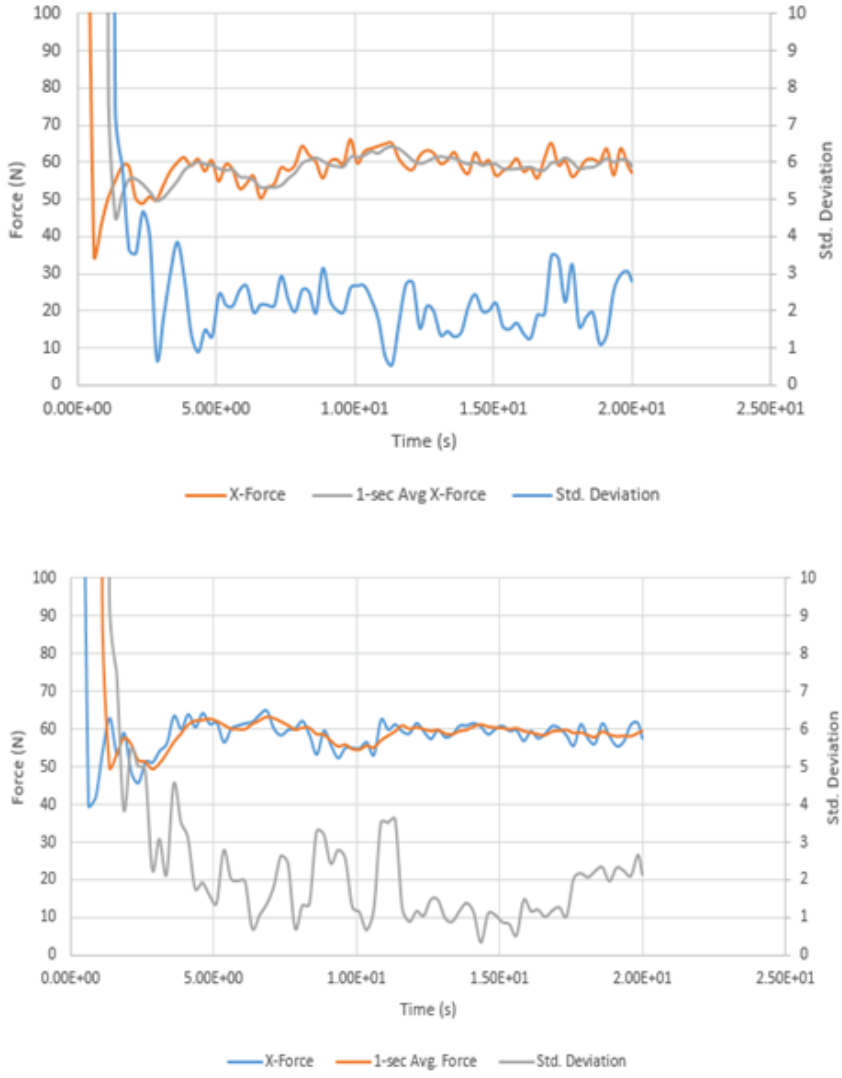

Figure 70. *X*-force for 4 m exit boundary; pressure exit BC (top), velocity exit BC (bottom)

Close examination of the results for the above runs reveals upstream pressure oscillations which appear to significantly contribute to the standard deviation. To determine if these effects are the result of the prescribed inlet velocity, the inlet and exit BCs are switched. Here hydrostatic pressure is prescribed only on the inlet and velocity is prescribed only on the exit. The results are shown in Figure 71. While it appears a slight reduction in the standard deviation is seen when hydrostatic pressure is applied to the inlet, it is valuable to learn that either approach could be used

should future problems warrant one over the other. A curious observation is that the force upon the cylinder does not seem to find a pure steady-state, even at the low Re = 50. Noise in the signal remains prevalent and the standard deviation does not diminish for all cases investigated.

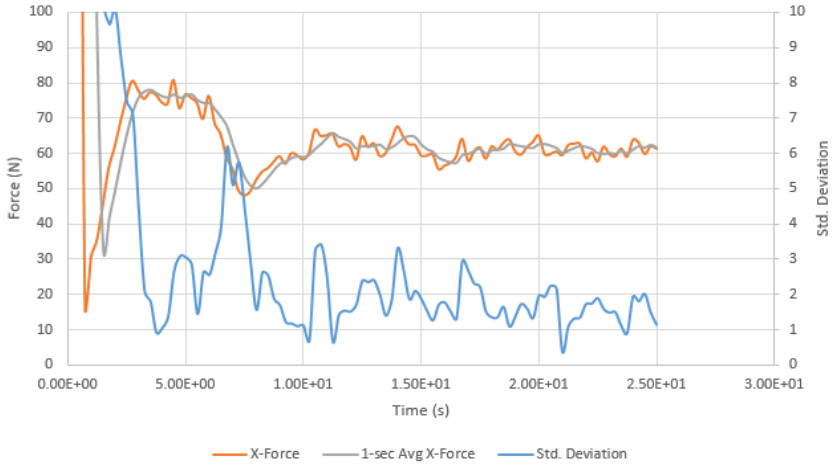

Figure 71. *X*-force on cylinder; pressure inlet boundary, velocity exit BC

A final investigation is conducted to assess the influence of viscosity using a higher Re = 2E4. A new cylinder model having a much finer mesh and no free surface is developed and shown in Figure 72. The cylinder diameter is 0.1 m, the domain length, width, and depth are 8 m, 4 m, and 1.5 m, respectively. The simulation is conducted for 30 s and the shedding vortex developed is clearly shown in the x-velocity plot provided in Figure 73. Despite this realistic appearance, correctly computing the viscous component of the drag force is difficult for Abaqus/Explicit because a turbulence model is not available, and the required mesh size needed to resolve the boundary layer would be computationally prohibitive. The shedding seen here is believed to largely result from numerical unsteadiness, and thus the accuracy of the shedding frequency as compared to expected values is low.

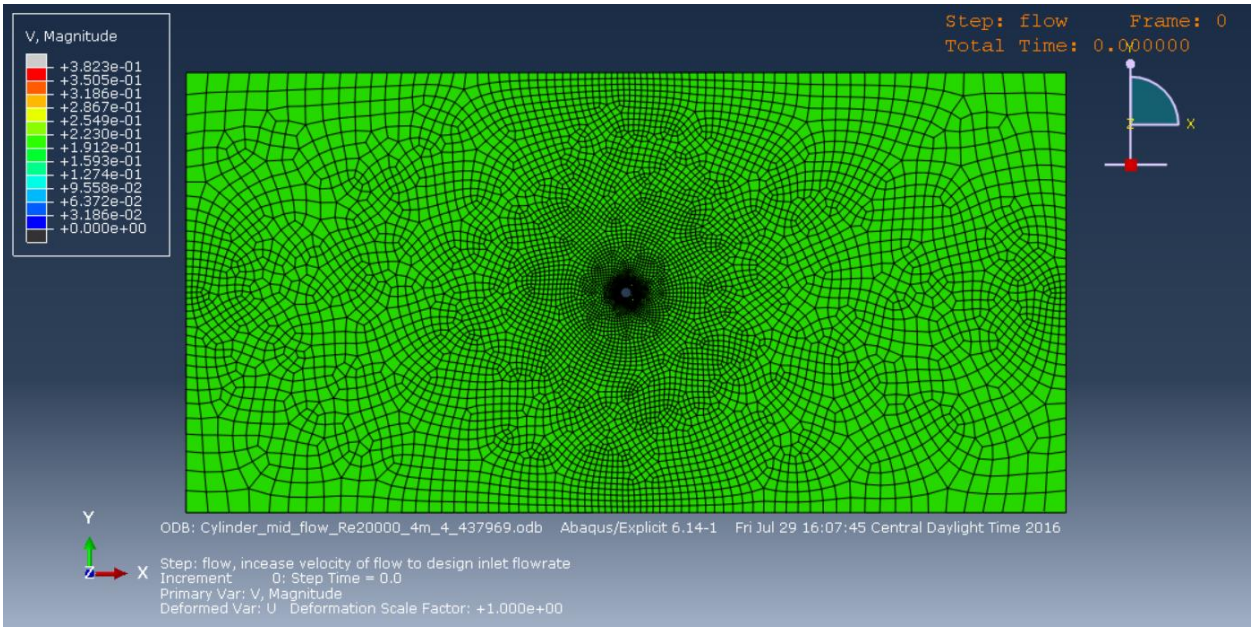

Figure 72. Cylinder in flow, Re = 2E4, U = 0.2 m/s

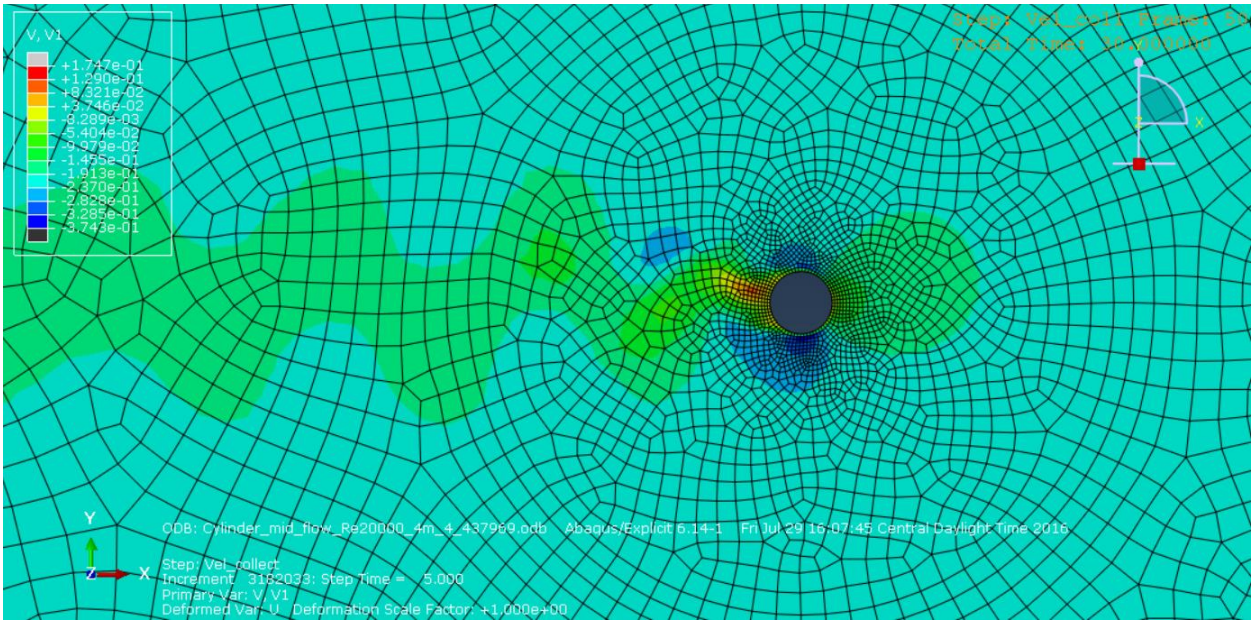

Figure 73. Cylinder flow x-velocities (t = 30 s)

To assess if the dominating shedding physics are represented, a Strouhal frequency analysis is conducted. The Strouhal number, St, is a non-dimensional ratio of the shedding speed to flow

speed, as defined in Eq. 117, where f is the vortex shedding frequency, L is the characteristic length, and U is the freestream velocity. For the parameters in this simulation, it is calculated as St = 0.198.

$$St = {}^{fL}/_{U} \tag{117}$$

Vortex shedding from the cylinder can be visualized by plotting the velocity of a centerline node (#25595) located approximately 0.1 m aft of the cylinder. Figure 74 then compares this transient velocity to an ideal sinusoidal curve having a frequency equal to the Strouhal value of 0.198 (f = 0.396 Hz). One can observe the model's shedding frequency is approximately 0.5 Hz, or 125% of the expected frequency.

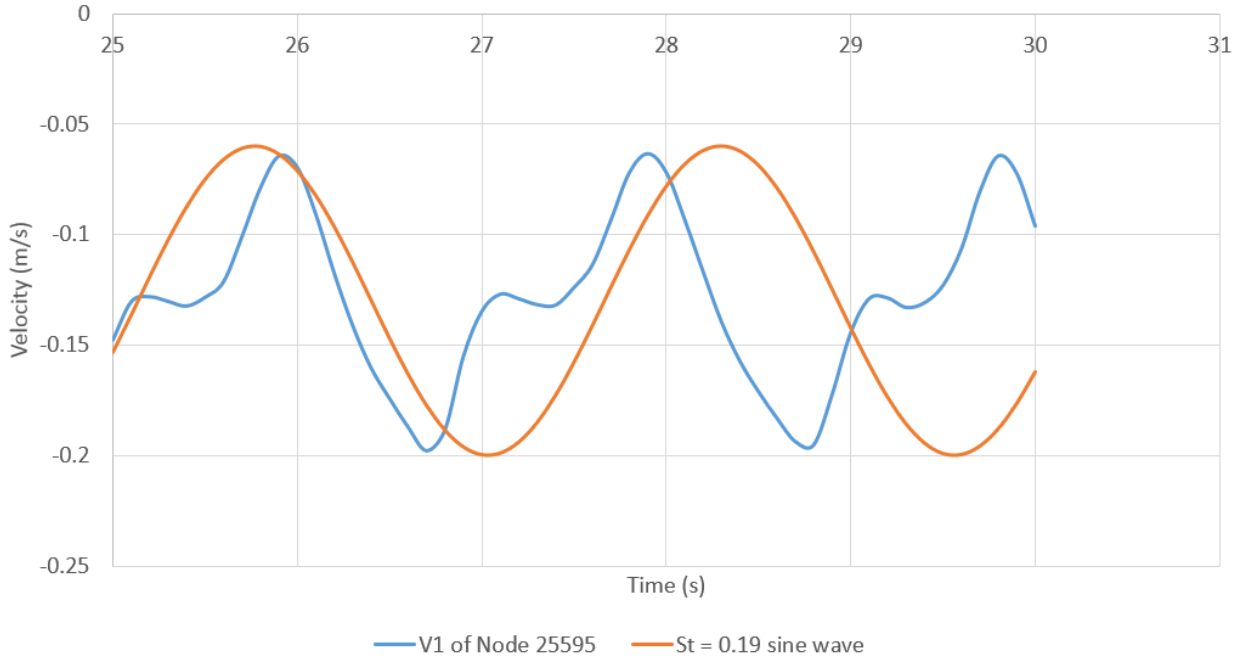

Figure 74. Cylinder shedding comparison

The drag obtained for this simulation is captured at 10 Hz and is plotted in Figure 75, along with experimental results provided by Zhou (2015). It is apparent from the large oscillations in the data

that the algorithm has trouble resolving the quasi-steady behavior. For a 3 s running average over the period of 20-30 s, the mean drag is calculated as 2.72 N with a standard deviation (σ) of 1.03 *N*. Zhou's average drag coefficient for this condition gives *3.3* N, thus the Abaqus model is 82% of the empirical value. More concerning is that σ is the same order of magnitude as the base result. It is significantly worse for the raw data taken at 10 Hz (σ = 15.9!). What is understood from this excursion is that models of viscous-dominated flows and largely unsteady flows may not yield accurate results. Further, even quasi-steady oscillations in the structure may make parametric resistance studies impossible if the magnitude of the effects are within the standard deviations.

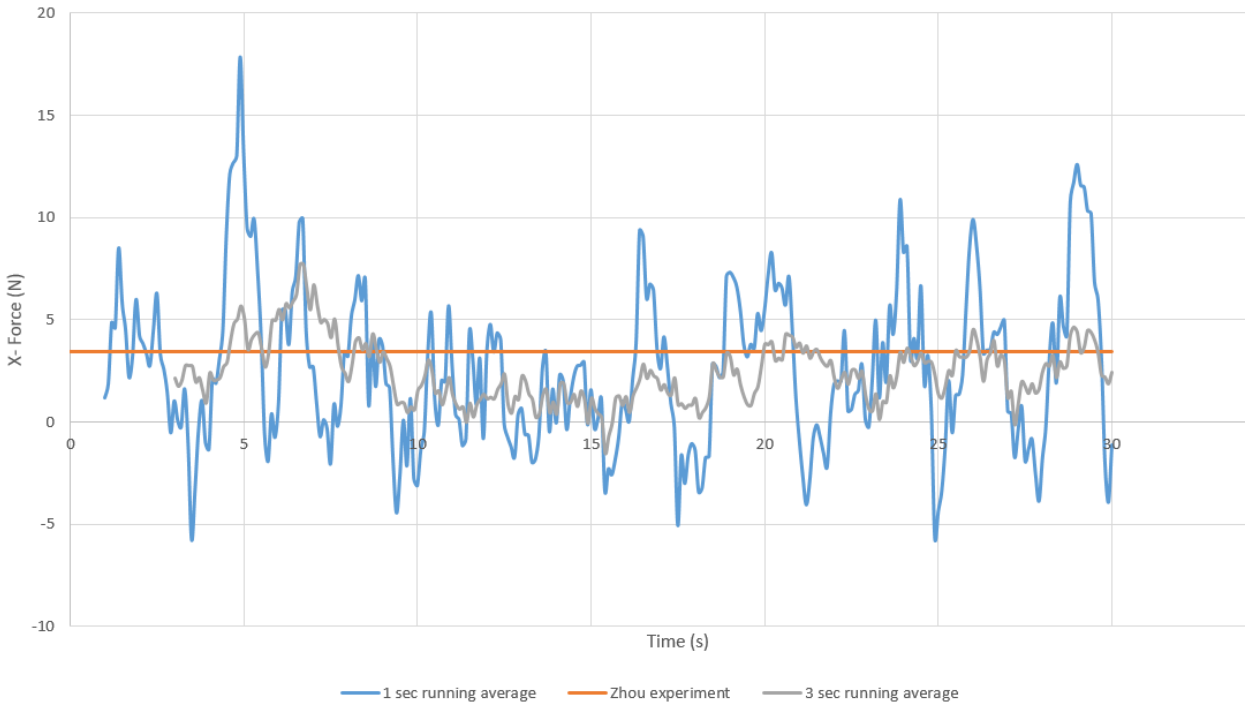

Figure 75. Cylinder drag, *D* = 0.1 m, *L* = 1.5 m, Re = 2E4

5.2.5 NACA0012 foil verification problem

The cylinder examples above revealed significant unsteadiness of the velocity and uncertainty in the drag data. Therefore, a more streamlined shape, the NACA0012 foil, is investigated here. As the drag calculation for this flow problem is generally viscous dominated, it is particularly interesting and challenging for Abaqus/Explicit's CEL technique for two reasons. First, the mesh size required to resolve a meaningful boundary layer is computationally prohibitive because of its influence on the global explicit time step. Second, there is no turbulence model available to estimate the vorticity influence within the boundary layer. This means a drag calculation will not be correct for Re numbers where viscosity dominates the drag.

There is an abundance of experimental and computational drag data for the NACAC0012 foil. Abbot and von Doenhoff (1959) provides a zero-lift drag coefficient (C_d) of 0.0058 for an "untripped" foil throughout a range of 3E6 < Re < 9E6. Abbot and von Doenhoff's "tripped" experimental data at Re = 6E6 provides C_d = 0.009, and Ladson's (1988) and McCroskey's (1988) "tripped" experimental data at Re = 6E6 each provides C_d = 0.0082. Computational evaluations with rigorous approaches to turbulence and boundary modeling have confirmed a zero-lift drag C_d = 0.008 (Langley 2014). Smith (2016) achieved a C_d = 0.0079 at this same Re using the implicit finite volume code Unified Navier Stokes (UNS) with a SST turbulence model. Even at a lower Re = 3E6, Eleni (2012) found C_d = 0.008 using a variety of turbulence models.

The dimensions of the NACA0012 foil and flow parameters used in this example are shown in Table 31. The 0012 designation indicates a symmetric foil with a thickness to chord ratio of 12%. The chord length is chosen to result in a thickness equal to the cylinder diameter above. In order to properly resolve the boundary layer at Re ~= 1E6, flat-plate boundary theory (White, 2011) is

used to estimate the non-dimensional wall distance $y+$. Using Eqs. 118 to 121, an estimated wall mesh size (y) of 1.2E-5 m is required to achieve $y+ = 1$. In these equations, c_f is the friction coefficient, u_* is the friction velocity, and τ_w is the wall shear stress. While perfectly suitable in an implicit CFD code, using this extremely small grid in an explicit analysis would drive the time step down to an impractical value.

Table 31. NACA0012 dimensions and flow parameters

NACA 0012 chord	0.8331	*m*
span	1	*m*
max thickness	0.1	*m*
Reference area (A)	0.8331	*m^2*
ρ	1000	*kg/m^3*
u	2	*m/s*
μ	0.001	*Ns/m^2*
Re	1666200	

$$c_f = \frac{0.027}{Re_x^{1/7}} \tag{118}$$

$$\tau_w = \rho u^2 \frac{c_f}{2} \tag{119}$$

$$u_* = \sqrt{\frac{\tau_w}{\rho}} \tag{120}$$

$$y = \frac{y^+ \mu}{\rho u_*} \tag{121}$$

This simulation is for the zero-lift drag case where the angle of attack (α) is zero. With the advantage of symmetry, a half-foil is modeled in an Eulerian domain using Abaqus/Explicit (Figure 76). The half-domain is 2 m wide and 8 m long and the foil is centrally located. While other studies point to the sensitivity of the far-field boundary location (Langley, 2014), extreme

values would be cost prohibitive unless a drastically stretched mesh was used. Influence of the far-field boundary location is especially important for large values of α (Langley, 2014). The rectilinear structured mesh of EC3DR elements becomes unstructured approximately one-half chord length upstream and downstream from the foil. The finest mesh around the wall of the foil is 0.005 m (Figure 77).

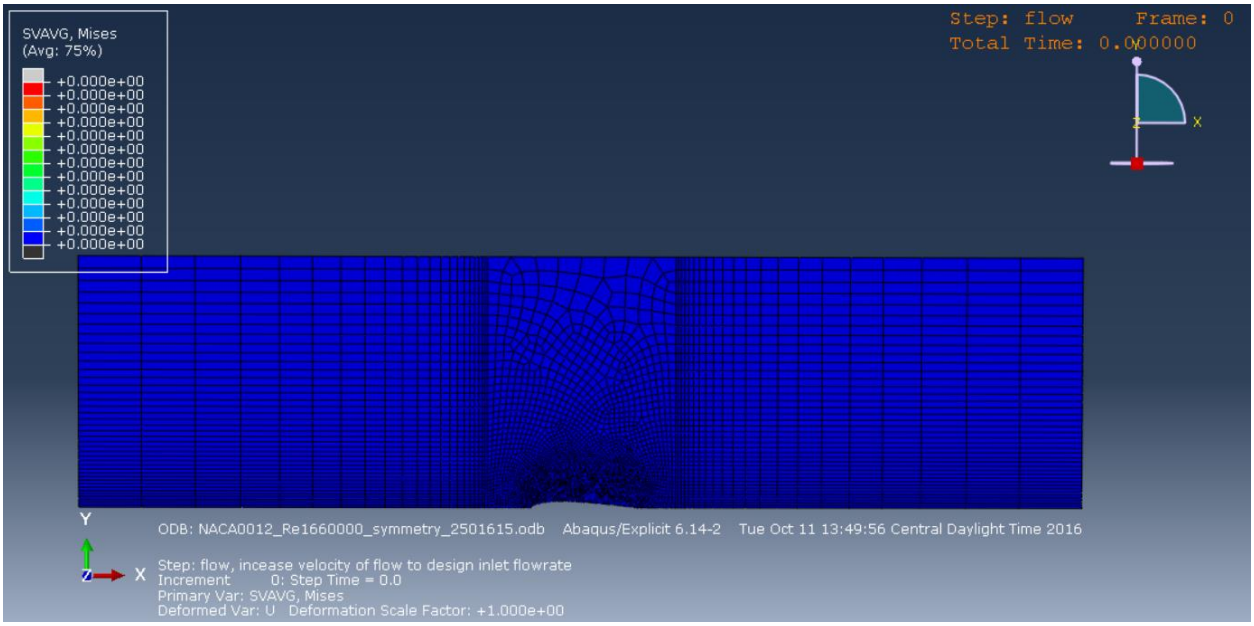

Figure 76. NACA0012 half-foil domain (1)

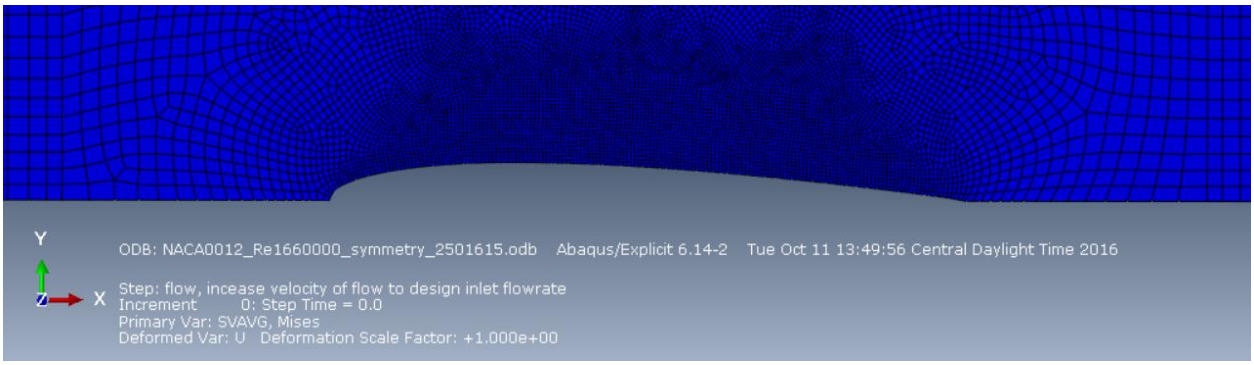

Figure 77. NACA0012 half-foil domain (2)

Upon startup, the fluid is initialized at the nominal velocity and the BCs are held consistent with the previous examples. The simulation is allowed to progress until the startup transients dissipate and a quasi-steady result is reached. Figure 78 through Figure 80 plots the velocity magnitude and *x* and *y* velocities at the final frame.

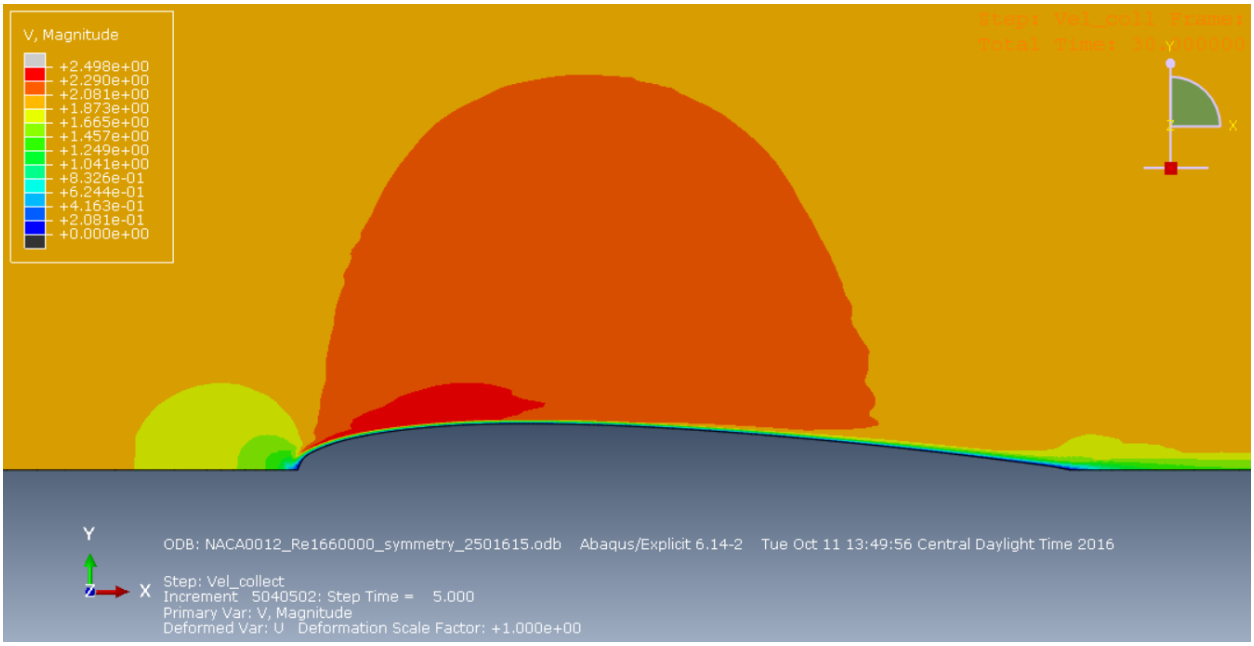

Figure 78. NACA0012 velocity magnitude

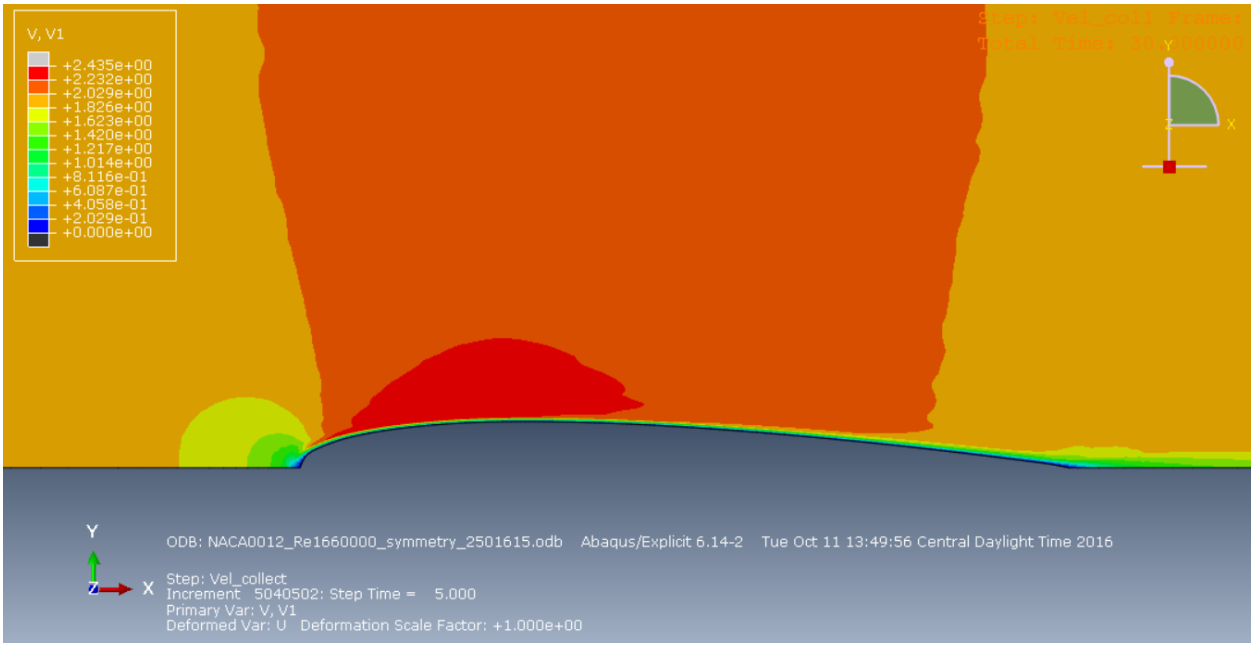

Figure 79. NACA0012 *x*-velocity

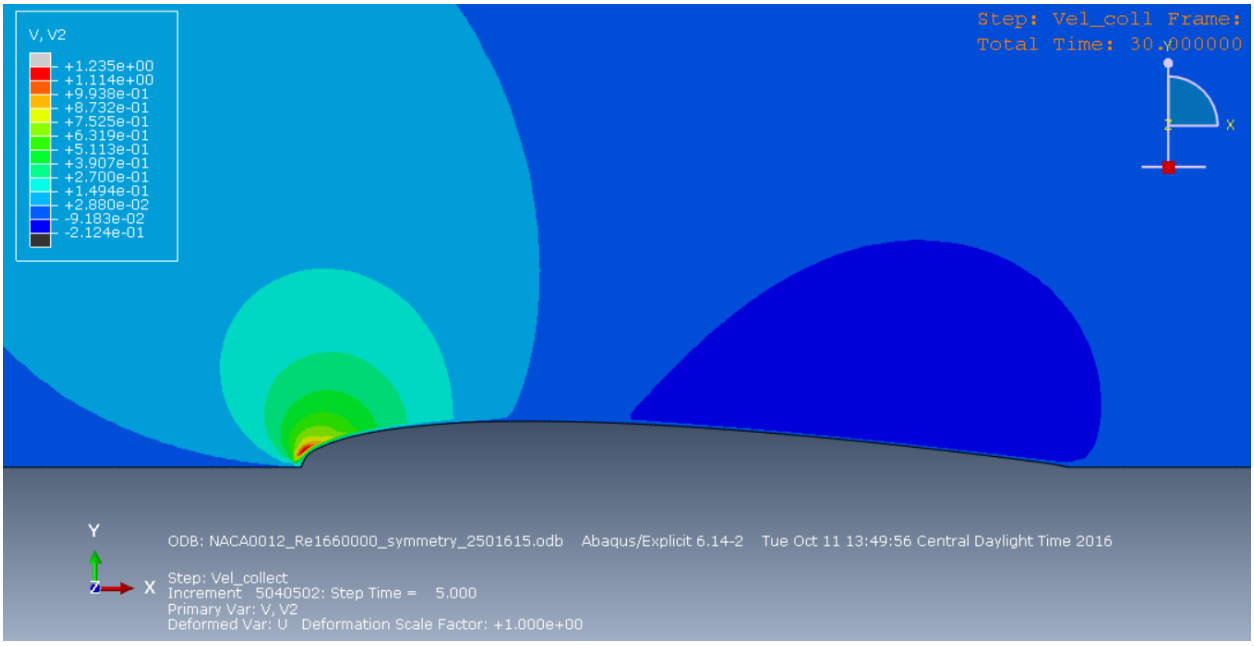

Figure 80. NACA0012 *y*-velocity

The reaction forces at each node along the foil surface are collected at 100 Hz. Figure 81 displays the drag results versus time for the last 5 s of a 30 s simulation. As the raw data exhibits large oscillations, a 1 *s* running average and a Butterworth-filtered set using a 10 Hz cut-off are also plotted. For comparison, a theoretical drag coefficient is provided by the program XFOIL (Drela, 1989, XFOIL, 2013). Using the recommended turbulence factor for an "average wind tunnel" of *Ncrit* = 9, the reported drag coefficient is C_d = 0.0054. Dimensionalizing this coefficient results in a drag of -4.49 N, which is plotted in Figure 81.

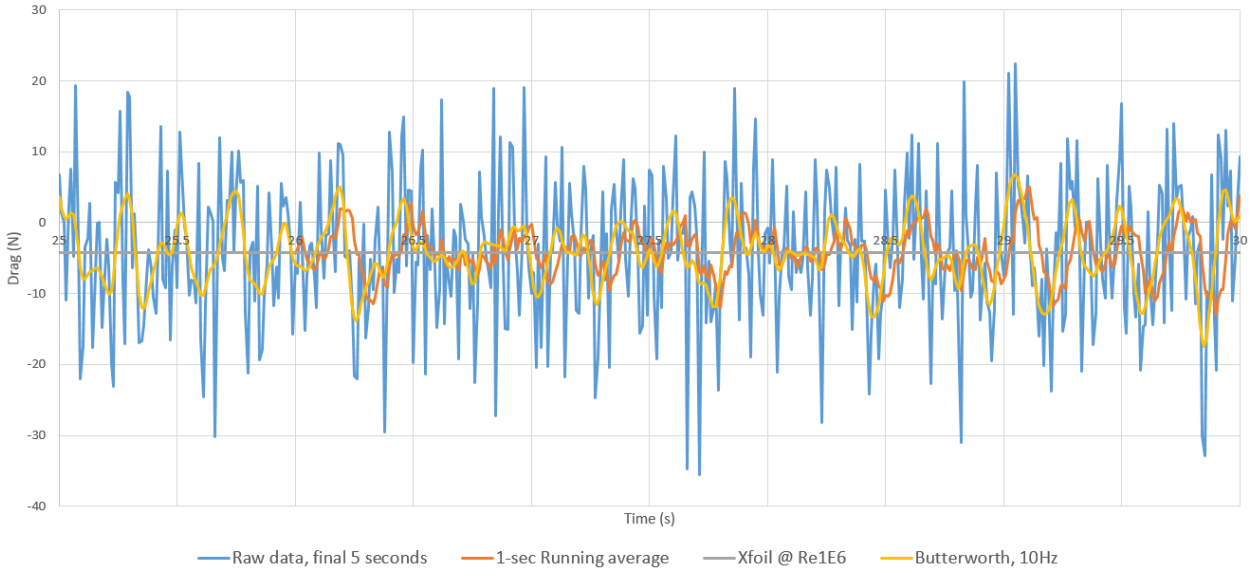

Figure 81. NACA0012 half-foil drag results, Re =1.66E6

Other studies have shown it is beneficial to filter Abaqus/Explicit data in order to reduce the unsteadiness caused by impulsive startups and numerical "ringing" of the materials within the domain (Dassault Systemes, 2013, Diehl, 2010). To that end, the raw data has been passed through a digital Butterworth filter using 1, 2, 5, and 10 Hz cut off frequencies. The filtered data sets are plotted in Figure 82 and statistical analysis is shown in Table 32. Interestingly, both the raw data and 10 Hz data have a similar mean of -4.13 N, indicating that the influence of numerical

oscillations above this frequency is small. This mean value varies from the XFOIL result by 8%. This relative agreement between XFOIL and Abaqus is curious because Abaqus is known to not be calculating the viscous component of drag correctly for the two reasons discussed above (boundary layer mesh size and turbulence model).

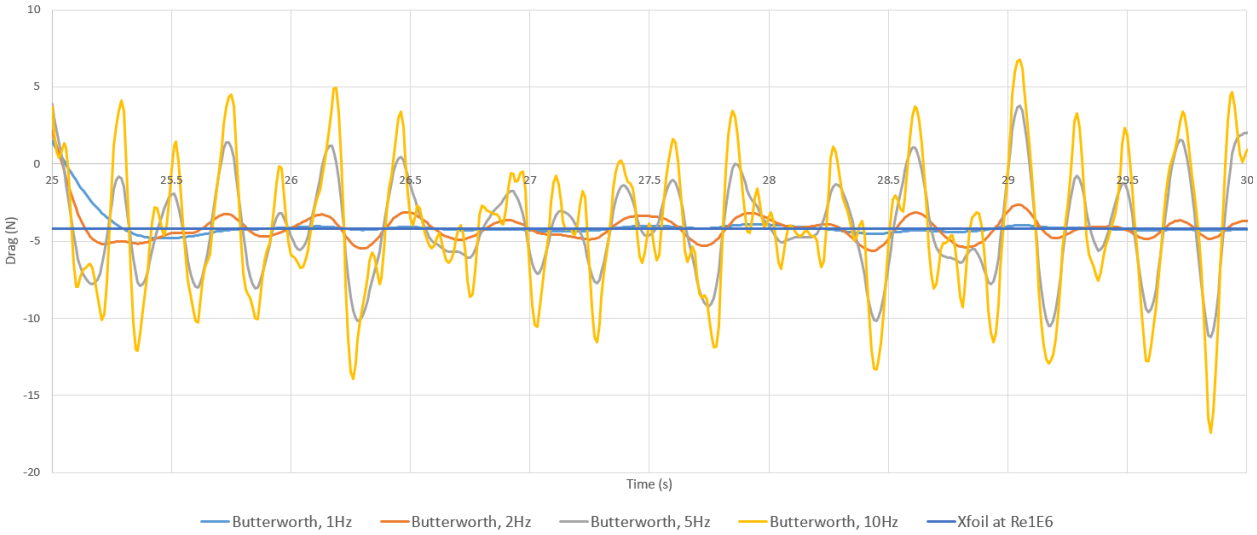

Figure 82. NACA0012 half-foil drag results (filtered), Re =1.66E6

Table 32. NACA0012 half-foil drag statistics using various filters

		Cutoff frequencies			
	No filter	10 Hz	5 Hz	2 Hz	1 Hz
Mean Force (N)	-4.13777	-4.13196	-4.12739	-4.15634	-4.0949
Standard Error	0.443822	0.194693	0.135243	0.039591	0.033259
Median	-4.17469	-4.27634	-4.37462	-4.21673	-4.22984
Standard Deviation	9.934071	4.362172	3.030175	0.88705	0.745182
Sample Variance	98.68577	19.02855	9.181958	0.786857	0.555296
Kurtosis	0.157548	-0.20882	-0.34985	13.35492	28.32985
Skewness	-0.11807	-0.04492	0.132276	2.502377	5.061708
Range	57.90442	24.23415	15.10168	7.80138	6.31888
Minimum	-35.4896	-17.4428	-11.233	-5.61669	-4.82342
Maximum	22.41478	6.79135	3.86868	2.18469	1.49546

Given the difficulty in obtaining an accurate, converged flow solution as indicated above, it is clear that the Abaqus/Explicit algorithm is having problems resolving the pressure field for the conditions currently prescribed. Research into other similar flows using this technique for FSI has revealed similar problems (Constantinescu, 2011), which emphasizes the importance of low-Mach preconditioning for compressible schemes.

To artificially introduce a form of preconditioning into Abaqus/Explicit, compressibility of the flow is increased by reducing the fluid sound speed in three subsequent simulations to C = 0.012, 0.008, and 0.006 m/s. At U = 1.2E-3 m/s, this provides Ma = 0.1, 0.15, and 0.2 respectively. This change greatly affects the temporal accuracy of the simulation, which is only acceptable because the steady state result is of primary importance. Figure 83 compares the resistance for the half-foil using C = 0.006 m/s with a result provided by UNS (Smith, 2016). With increased compressibility the explicit timestep is greatly increased, allowing the simulation to efficiently complete 4E3 s. Convergence of the resistance is greatly improved and it compares well to the implicit, incompressible UNS result. However, the large timescales required to converge the fluid solution may prove problematic for a constantly evolving fluid boundary, as in the case of a flexible ACV seal.

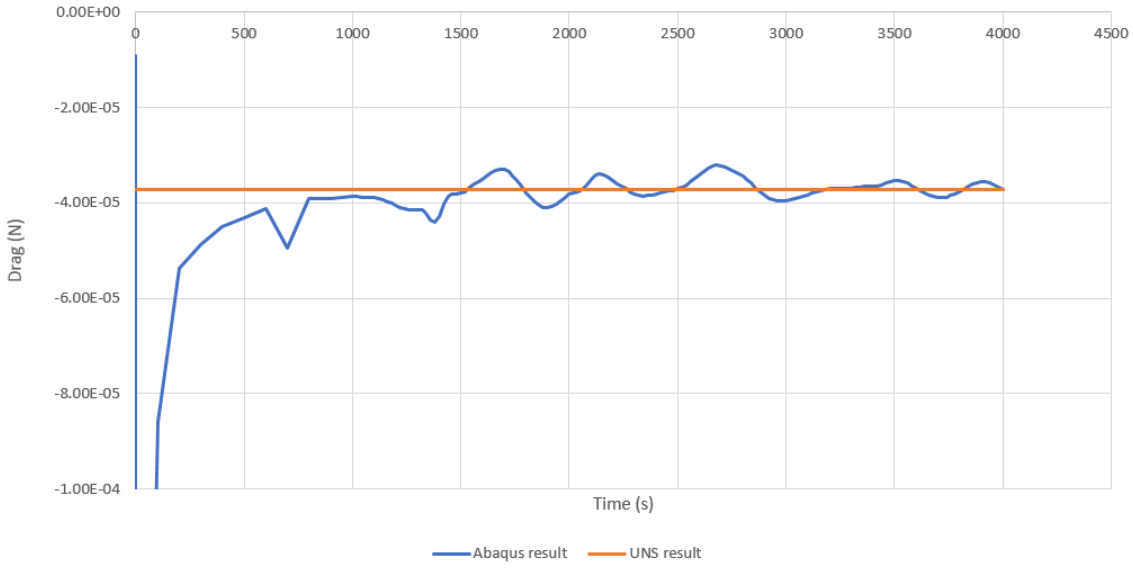

Figure 83. NACA0012 half-foil drag, 0.1 m thick, α = 0, Re = 1000, Ma = 0.2

Figure 84 compares the resistance obtained by Abaqus at Ma = 0.1, 0.15, and 0.2 with the UNS result. While increased oscillations are observed as Ma is reduced toward the incompressible limit, the mean values generally agree with the UNS result. This is in stark contrast to the results obtained at the nearly-incompressible case shown in Figure 81. It is therefore demonstrated that for a steady-state case, reducing the fluid sound speed is an acceptable means to improve convergence of the fluid solution using Abaqus/Explicit.

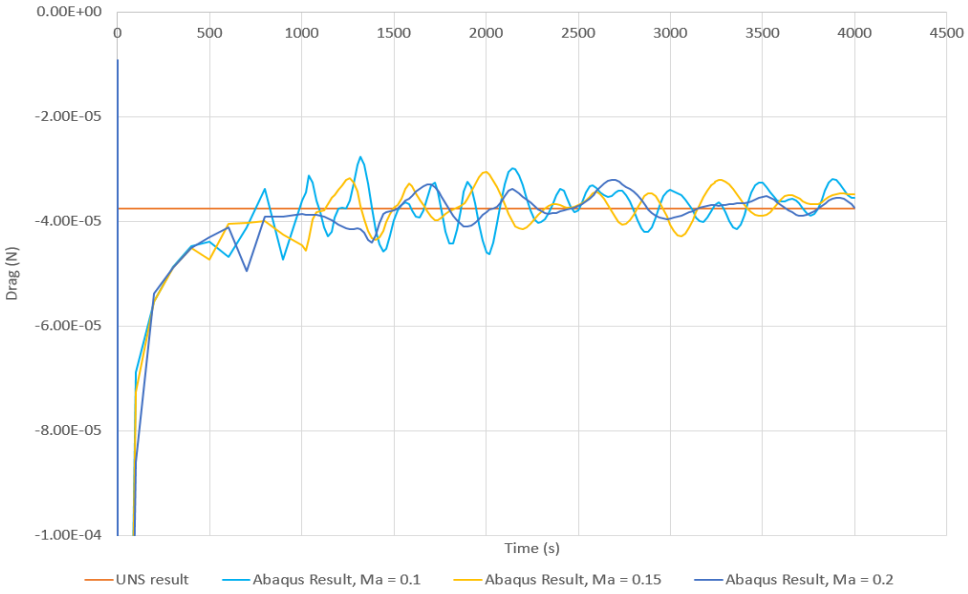

Figure 84. NACA0012 half-foil drag, 0.1 m thick, α = 0, Re = 1000, Ma = 0.1, 0.15, 0.2

To gain insight into the origin of differences between the Abaqus results and UNS, the pressure coefficient C_p versus non-dimensional chord *x/c* is plotted in Figure 85. C_p is defined in Eq. 122, where *p* is obtained along the foil surface as an average pressure over the final 1000 s of the simulation. From this plot, the peak stagnation pressure at the leading edge is predicted well at all Ma values, but slight deviations are prevalent in the high velocity regions (negative pressures) and at the trailing edge.

$$C_p = \frac{p - p_\infty}{\frac{1}{2}\rho_\infty U_\infty^2} \qquad \text{(Eq. 122)}$$

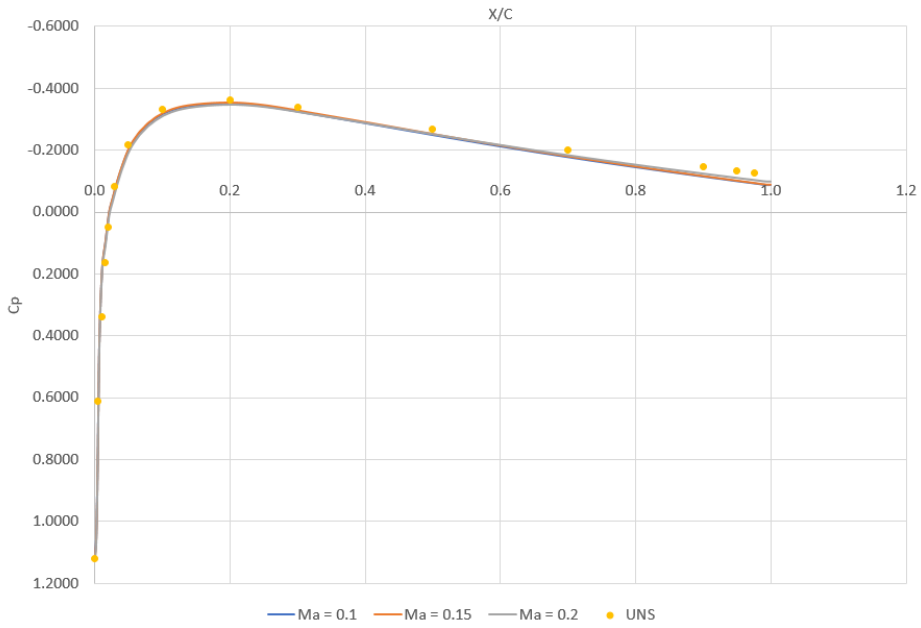

Figure 85. NACA0012 half-foil C_p versus *x/c*, α = 0, Re = 1000, Ma = 0.1, 0.15, 0.2

5.2.6 Elastic gate validation problem

To explore the FSI capability of the Abaqus/Explicit CEL method, a benchmark problem is composed similar to that in the software documentation (Dassault Systemes, 2013). This problem simulates deflection of an elastic gate due to hydrostatic pressure from a water column contained within a tank. It is based upon geometry and experimental data published by Antoci et al., (2007). According to Figure 86, the tank is rectangular with an initial fill height, *H*, of 0.14 m. The gate length, *L*, is 0.079 m, the tank width, *A*, is 0.1 m, and the tank depth is 0.1 m. The floor, left, and right walls are rigid. At time t = 0 s, the gate is allowed to break free at the bottom and the fluid column flows beneath it. As no structure exists after the gate, the evacuated flow is free to leave the domain in the -*x*-direction. Time history of the gate tip deflection in both the vertical and horizontal directions is captured in the experiment and can be compared with a numerical simulation.

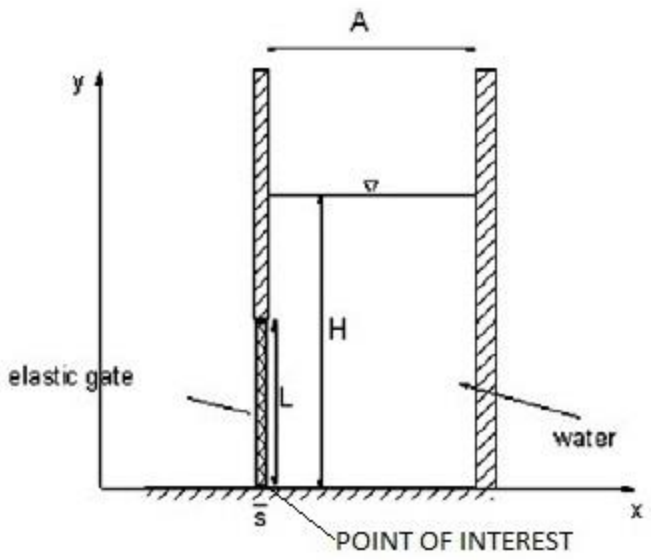

Figure 86. Profile of gate break (Antoci, 2007)

To model the problem using Abaqus, first an Eulerian domain is specified according to the tank size, with additional accommodation to allow for gate deflection and outflow. A Lagrangian structure of 0.160 m long and 0.005 m thick is then added to represent the left wall and gate. Its top portion is constrained whereas the bottom 0.079 m is free to move. The floor, right side, front, and back of the tank are assigned zero-penetration boundary conditions to prevent any outflow from these surfaces. There are no boundary conditions assigned for the anticipated outflow region. With the assumption that effects of the tank width do not influence the deflection (as justified by Antoci) a 2D-representation is constructed by retaining only one element in the *z*-direction.

To simulate water within the tank, the Eulerian domain requires that the initial filled region and void region are identified. To do this, the domain is partitioned according to the size and location of the initial water column. Then, a predefined field of water is specified with a volume fraction of 1. A gravity body force is added to the entire model. With the global body force applied, fluid

advection into a void region will still see a gravitational load. In addition, an initial stress field is added to represent the hydrostatic pressure at t = 0 s. To enable Abaqus' CEL capability, a frictionless general contact definition is selected to allow water and gate interaction.

The Eulerian domain is meshed using a uniform distribution of EC3D8R elements, having dimensions of 0.005 m in all directions. According to the Abaqus documentation (Dassault Systemes, 2013), using rectilinear elements in an Eulerian analysis helps maintain accuracy. In the Lagrangian domain, C3D8R elements are used for the gate; 75 elements in the length, 4 elements through the thickness, and 3 elements in the depth. The EC3D8R element is an Eulerian formulation of the standard C3D8R element; an 8-node linear brick with reduced integration and hourglass control. Thus, the total problem size with the above discretization is 1706 elements, 3258 nodes, and 9774 variables.

Initially, the gate is assumed linear elastic and assigned material parameters specified by Antoci (2007): Young's modulus = 12 MPa, Poisson's ratio = 0.4, and density of 1100 kg/m^3. The water properties are ρ = 1000 kg/m^3 and μ = 0.001 Ns/m^2. The Mie-Grüneisen equation of state is used for the fluid with the parameters c_0 = 1500 m/s, s = 0, and Γ_0 = 0.

The tip displacement results are shown in Figure 87. The data represents the motion of the tip's lower right corner ("point of interest" in Figure 86), with Z as the vertical coordinate in lieu of Y. While the initial slopes of the deflection and peak displacements compare well with the experiment, there is a significant discrepancy in the post-peak behavior of the gate tip. Close inspection of the displacement reveals a gentle rise in the tip around 0.3 s which is not completely evident in the experiment. From Antoci et al. (2007), the gate material was initially estimated as ~10 MPa, but then curiously altered to 12 MPa to best fit the simulation results. Therefore, the

Abaqus simulation was re-run using a linear elastic modulus of 10 MPa. Not much improvement is seen with this change, and the characteristic spring-back behavior remains. This supports the notion that the material is not linear elastic with a constant modulus and may be better represented with a hyperelastic model. Figure 88 compares the uniaxial strain data with results for linear elastic models having moduli of 10 and 12 MPa. This plot reveals that nonlinear behavior is present beyond even the smallest strains and a linear approximation based upon the stress/strain slope at the onset of deformation is not applicable for additional strain.

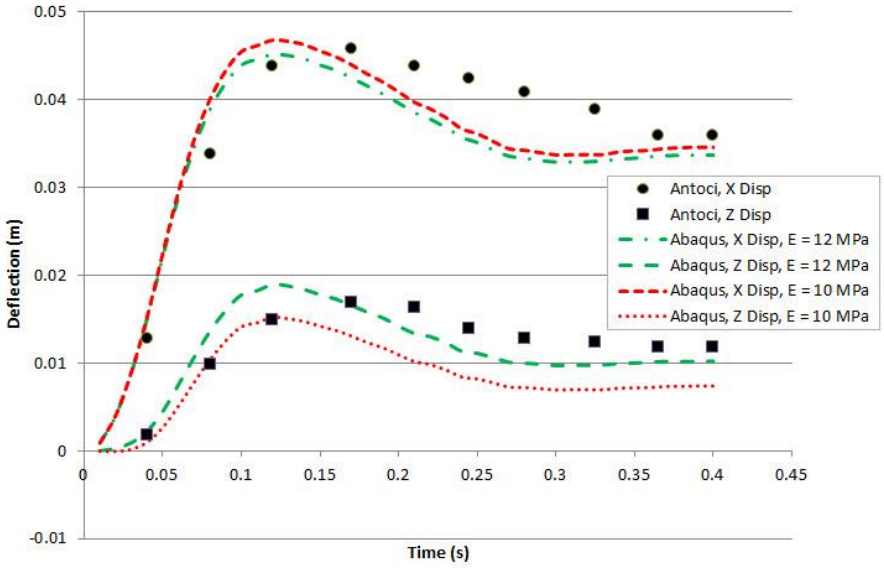

Figure 87. Abaqus linear elastic gate break tip motion

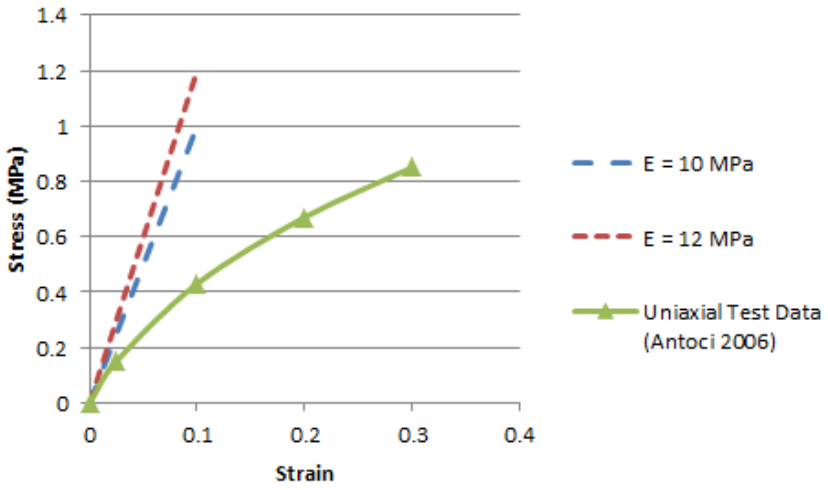

Figure 88. Gate elasticity model comparison

In work by Yang (2011), the Mooney-Rivlin (MR) strain-energy potential model was confirmed to be a better fit for simulating the material. In Figure 89, his linear elastic results under-predicted the peak displacements in both *X* (horizontal) and *Z* (vertical) directions, whereas the MR model more nearly matched the peak and post-peak behavior. Notice the MR model does not exhibit the characteristic spring-back and tip-rise behavior seen in the linear elastic models.

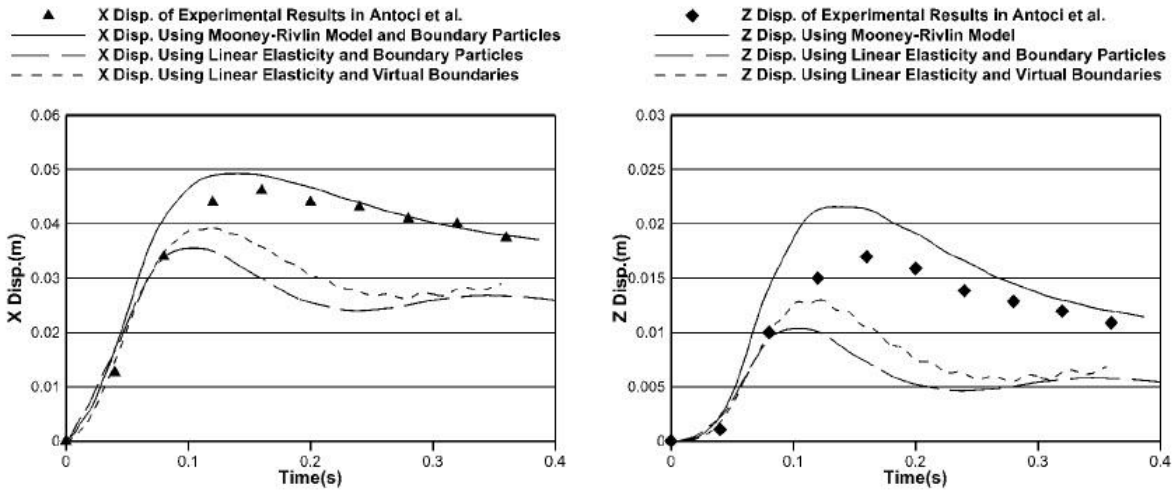

Figure 89. Yang's results of Antoci's gate deflection (Yang, 2011)

Based upon this insight, a hyperelastic isotropic material model using MR strain energy potential is invoked in Abaqus. To determine the appropriate MR coefficients, Abaqus' embedded material evaluation tool (described in Appendix A) is used to analyze the uniaxial strain data acquired by Antoci for the gate material. Figure 90 displays deflection of the tip using the MR material model for the gate on three mesh levels. Although the peak displacements are slightly over-predicted, the post-peak behavior is a much better fit to the experiment. The rate of change of the gate's spring-back is a near match, and there is no indication of tip-rise at t = 0.3 s. These results also complement Yang's work (2011), as they repeat the peak over-predictions for both X and Z displacements.

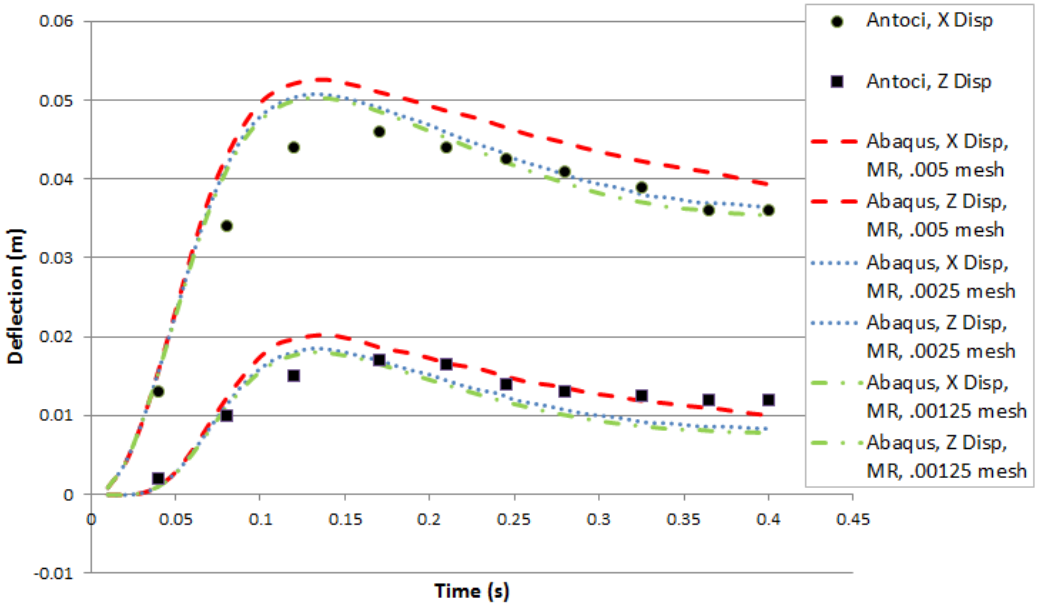

Figure 90. Abaqus hyperelastic gate tip deflection

A grid refinement factor of 2 was then applied to the model for two subsequent simulations, also shown in Figure 90. Each refinement resulted in a better match to the peak displacement and X displacement, but greater deviation for the Z displacement. Yet, the small difference between the

0.0025 m mesh and the 0.00125 m shows the results are approaching convergence. Figure 91 provides screen captures of the simulation as the Eulerian material flows from beneath the breeched gate. The fifth frame (t = 0.3 s) reveals how the gate's spring-back causes the free surface to rise slightly at the contact point.

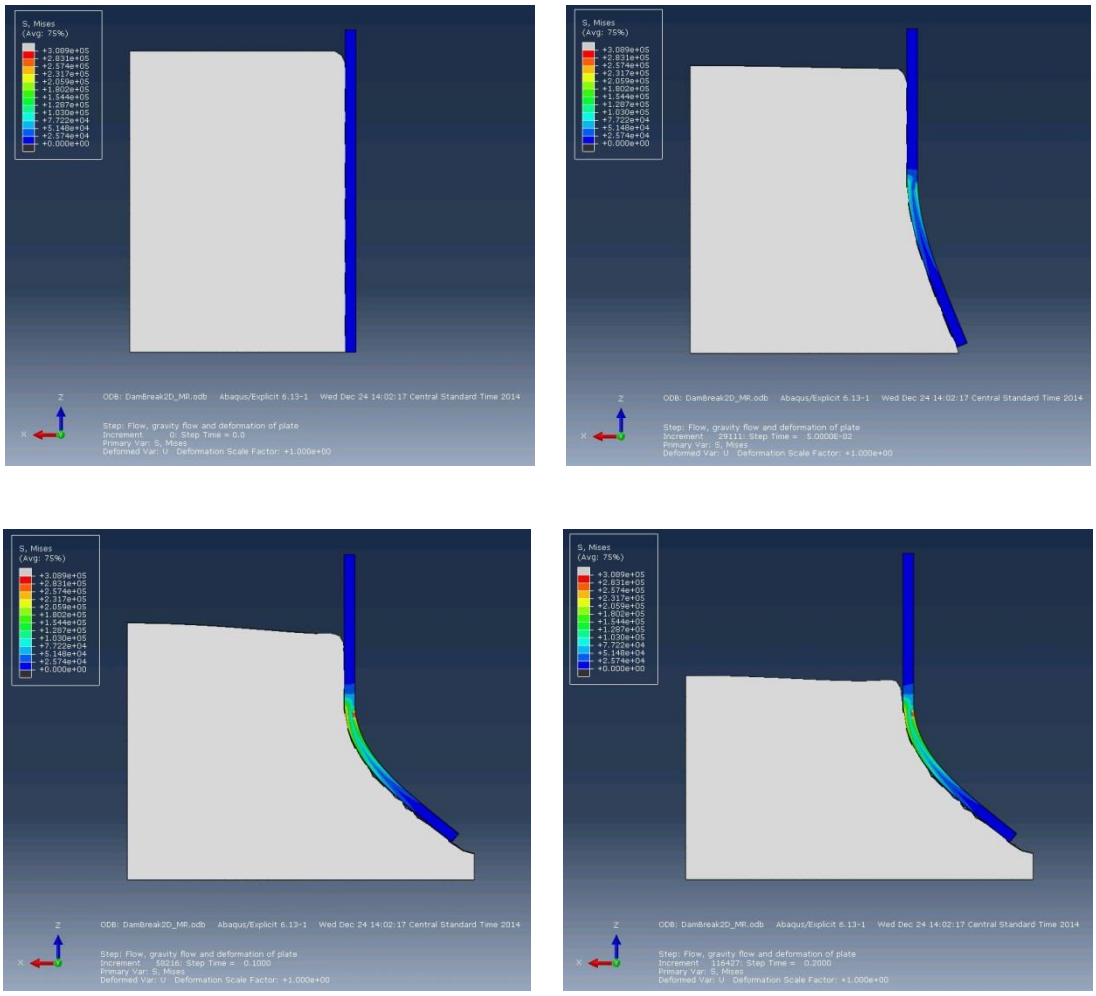

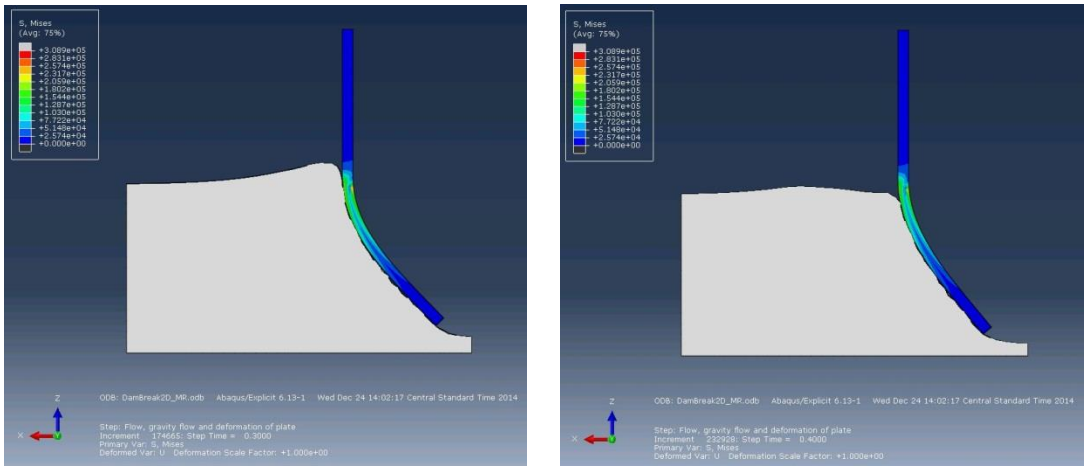

Figure 91. Gate deflection simulation (*t* = 0, 0.05, 0.1, 0.2, 0.3, 0.4 s)

While it is tempting at this point to include additional material stiffness and damping to reduce peak displacements and spring-back in the *Z* direction, this would be merely an attempt to match experimental results and any error they might contain. Considering the material model was purposely limited to the known characteristics made available through the literature, such as the uniaxial test data and Mooney-Rivlin theory, the results provided by the Abaqus/Explicit simulation are impressive. What can be reiterated here is the importance of properly reporting and identifying the material key characteristics through testing, especially for hyperelastic rubber materials. This point is also made by other researchers (Bloxom, 2014, Wiggins, 2014, Brieu, 2007, Escarpita et al., 2012). It is shown above that simply indicating a linear modulus without a strain energy potential does not provide a complete material characterization. Specific uniaxial test data is required to achieve the best fit.

5.3 Abaqus/Explicit CEL planer seal results

As introduced above, the University of Michigan seal experiments (Zalek and Doctors, 2010) provide a validation dataset for a flexible planer bow seal in a free surface flow. To understand the appropriate boundary conditions and how they might be applied using the aforementioned Abaqus/Explicit CEL approach, two similar planer seal models are developed. The first model uses a prescribed pressure upon a membrane to impose the free surface boundary, and the second model introduces a second fluid species to facilitate the free surface.

The simulation conditions for each model are in accordance with UM run 1026, shown in Table 33. The seal depth is the static immersion of the seal prior to deflection and *X* and *Z* are the coordinates of measured deflections at three locations (low, med, and high). The seal is 0.507 m long and is attached to a test platform at *X* and *Z* locations of 1.117 m and 0.502 m, respectively, from the global origin. The seal is 3.175 mm thick with a density of 1096 kg/m^3. A linear elastic modulus for the seal material is reported as 16.9 MPa. Bloxom (2014) also used this dataset for his FSI numerical investigation, yet he developed a hyperelastic material model for the seal using the Mooney-Rivlin coefficients C10 = 1.3E6, C01 = 0, and D1 = 2E-8.

Table 33. Planer bow seal results (Zalek and Doctors, 2010)

Run	Inflow Speed (m/s)	Fn	Fd	Static Seal Depth, δs (m)	X low (m)	Z low (m)	X med (m)	Z med (m)	X high (m)	Z high (m)	X top (m)	Z top (m)	Cushion Press. (Pa)
1026	1.828	0.160	1.221	0.2286	0.7005	0.2591	0.8372	0.315	0.9812	0.3711	1.117	0.502	567.15

5.3.1 Planer bow seal having prescribed cushion pressure

The first model used for this study is shown in Figure 92. The domain is 20 m long and 3 m tall with the seal and test platform centrally located. First, a stable flow with a free surface must be established based on lessons learned from the above cylinder study. It revealed the chosen boundary conditions are critical to correctly prescribe an incoming flow and establish steady state. The domain is initially filled up to the specified free surface level of 2.5 m with fluid moving at the inflow speed (Figure 93). An initial geostatic stress field is applied to the fluid to replicate hydrostatic pressure.

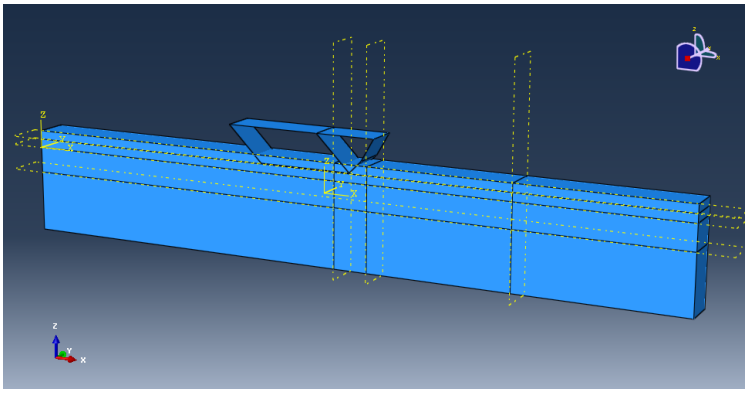

Figure 92. Planer seal model domain

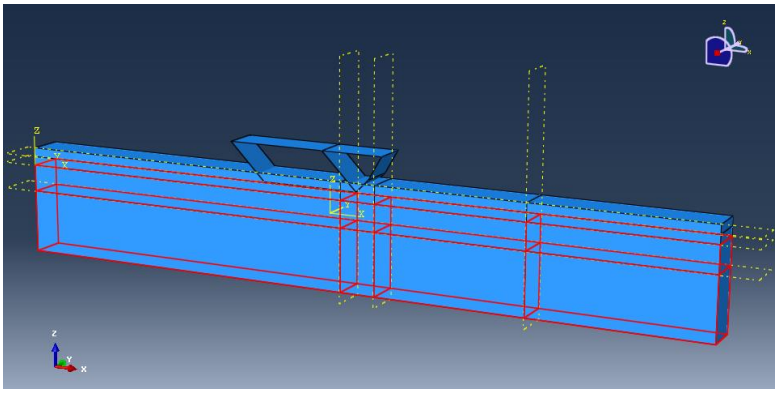

Figure 93. Predefined fluid in planer seal model

At the domain outlet, a constant flow velocity is prescribed in order to maintain the flow speed throughout the simulation. Accuracy with this approach requires an exit well aft of the region of interest to minimize influence upon velocity gradients in the fluid column. At the sides, symmetry is prescribed to represent a wide planer seal. At the bottom and top of the domain, non-penetration is enforced by setting the normal velocities to zero.

The inlet boundary specification is important and can dramatically affect the steady state condition. As velocity is a Dirichlet boundary prescribed at the outlet, pressure is required at the inflow for a well-posed problem. The pressure normal to the inlet boundary is the hydrostatic pressure, $P = \rho g h_z$, where h_z is the depth from the free surface. If the exit boundary is established near a wave-generating disturbance that alters the free surface height, the hydrostatic pressure must also vary accordingly. If the inlet boundary is established well away from the disturbance in the far-field, the hydrostatic pressure can be approximated as a constant linear pressure distribution based upon a specified free surface height. Ideally, establishing the inlet boundary as close to the seal as possible would minimize the problem size as long as the upstream surface profile is not of interest. However, it would also require a user sub-routine to identify the free surface height and adjust the hydrostatic backpressure for each increment. For this reason, the far-field approach is taken to establish the upstream inlet boundary.

The domain depth is chosen as 2.5 m below the static free surface, consistent with that used in the experiment. With the prescribed inflow velocity shown in Table 33, a depth-based Froude number of 0.369 indicates subcritical flow characteristics according to Eq. 123. This means an upstream soliton will propagate forward of the disturbance with a velocity (U_d) equal to the difference in the

wave celerity, *c*, and the inflow velocity, *U*, according to Eq. 124. The inlet boundary must be able to accommodate this upstream disturbance.

$$F_\delta = \frac{U}{\sqrt{gD}} = \frac{1.828}{\sqrt{g \cdot 2.5}} = 0.369 \tag{123}$$

$$U_d = c - U = \sqrt{gD} - U = \sqrt{g \cdot 2.5} - 1.828 = 3.12 \ {}^{m}/_{s} \tag{124}$$

The seal is attached to a rigid body platform fixed at the upper attachment (Figure 94 and Figure 95). It is initially meshed with four C3D8R continuum elements through the thickness in order to obtain accurate flexural response. However, with the seal being only 0.003175 m thick, the resulting maximum element length is 0.00079 m. As the CEL contact algorithm prefers equal node spacing between the Lagrangian and Eulerian materials, the maximum explicit time step is restricted based on the smallest of either the fluid wave speed or solid wave speed according to Eq. 125 and Eq. 126. Therefore, it is shown that using continuum elements for the seal and matching the mesh size reduces the explicit time step by approximately an order of magnitude, which is considerable for a 20 s simulation.

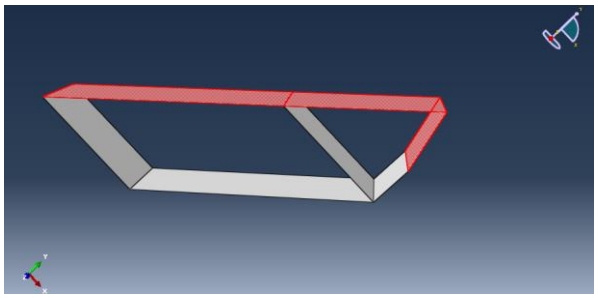

Figure 94. Bow seal platform (rigid elements highlighted)

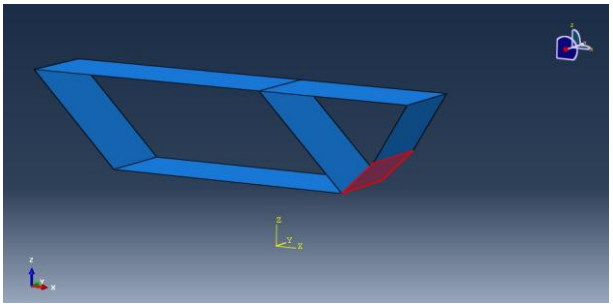

Figure 95. Bow seal platform (seal elements highlighted)

$$Fluid\ \Delta t = min\left(\frac{L_e}{c_d}\right) = \frac{.00079\,m}{1500\,m/s} = 5.3 \cdot 10^{-7}\ s \tag{125}$$

$$Solid\ \Delta t = min\left(\frac{L_e}{c_d}\right) = \frac{.00079\,m}{181\,m/s} = 4.4 \cdot 10^{-6}\ s \tag{126}$$

To ease this time step restriction, the seal is subsequently meshed with SR4 shell elements. Five integration points are specified through the thickness to replicate the bending accuracy of four reduced-integration continuum elements. The shell elements thus provide the bending rigidity without reducing the time step, as demonstrated in Figure 96. This plots the deformation of the seal model under gravity when equally meshed with either SR4 (shell) or C3D8R (continuum) elements. The seal is fixed at an *x/y* position of (0.34, 0.34). The deformation is identical.

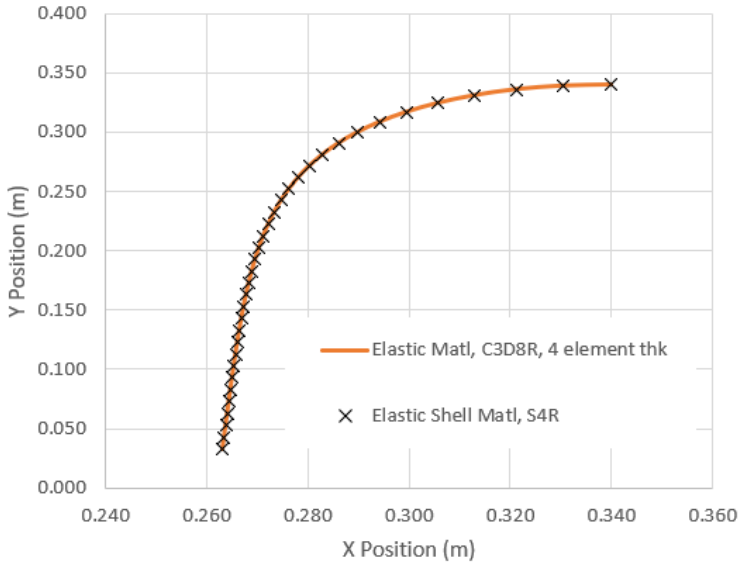

Figure 96. Seal with elastic shell SR4 versus continuum elements C3D8R

In initial simulations, the seal pressure would drive it up, over, and out of the flow in an unrealistic fashion. In order to prevent this occurrence, a near-massless membrane is attached from the seal trailing edge to the platform to provide a forward restraint, similar to the restraint wires used in the UM seal experiments (Figure 97). In order to replicate inflation pressure acting downward on the free surface in the cushion, another membrane is stretched from the seal trailing edge aft and attached to the platform. The prescribed inflation pressure is imposed on this near-massless membrane normal to the surface which contacts the fluid. This is seen as an improvement to modeling the free surface/seal interaction when compared to Challa (2015), who modeled the air inside the cushion only in combination with a rigid bow seal.

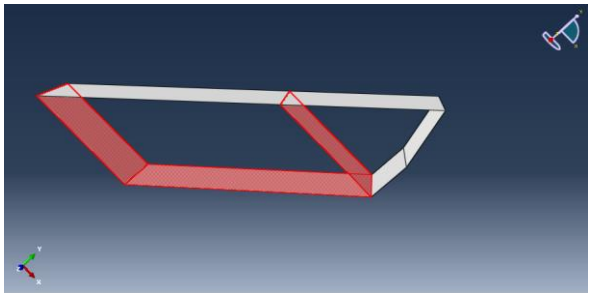

Figure 97. Bow seal platform (membrane highlighted)

While the skin friction force on the seal was shown to be small relative to the overall pressure force (Bloxom, 2014), it is modeled using two approaches. The first approach applies a downstream surface traction of 2 Pa to the seal surface. The magnitude of the traction force is based upon the average magnitude seen in the numerical results for shear stress reported by Bloxom (2014). He used a Spalart-Allmaras turbulence model within a Reynolds-Averaged Navier-Stokes (RANS) fluid solver in STAR-CCM+ to determine the skin friction. The traction acts tangential to the seal surface and follows the nodal rotation. Accuracy with this approach suffers when a significant portion of the seal is not immersed in fluid, or when deformation of the seal varies the orientation of the traction force from the fluid motion.

The second approach applies nodal forces on the seal trailing edge approximately equal to the average friction force calculated from the shear stresses reported by Bloxom (2014). Viewed as more accurate than the first, its weakness is that the friction magnitude is specified a-priori and may not be applicable to subsequent simulations with varying flow velocities. This was the approach chosen to carry forward in future modeling. For clarification, friction was only applied to the seal and not the trailing membrane.

Meshing the fluid domain is straightforward using a double-biased rectilinear grid (Figure 98). In the *x*-direction, the node spacing is biased from 1.0 m at the ends to 0.02 m toward the center. The center partition provides more accuracy in the region of interest and is meshed using a constant 0.020 m node spacing in the *x*-direction. The domain is also biased in the (+) *z*-direction from 0.25 m to 0.02 m. A free surface partition is employed throughout the domain length, which enables additional fidelity for the free surface and FSI interaction. The node spacing in the *z*-direction within this partition is 0.02 m. The width of the domain is 1.0 m.

The simulation is conducted as follows. First, a cushion inflation pressure of 567.15 Pa is specified for the seal inner surface using the prescribed pressure approach (Figure 99). At t = 0 s (Figure 98), the platform is lowered into the flow over a period of 5 s until the prescribed seal immersion of 0.2286 m is reached. Simultaneously, the cushion pressure is smoothly ramped up over 2 s to prevent a sudden pressure discontinuity on the seal. Once the platform is in position, the simulation is allowed to progress for an additional 15 s (20 s total sim time). Figure 100 provides shows the platform in a quasi-steady configuration at t = 12 s, and Figure 101 provides a close-up of the interaction of the seal with the free surface at t = 18 s. Observe how the cushion membrane attached at the bow seal trailing edge rides the free surface and applies the explicitly applied cushion pressure.

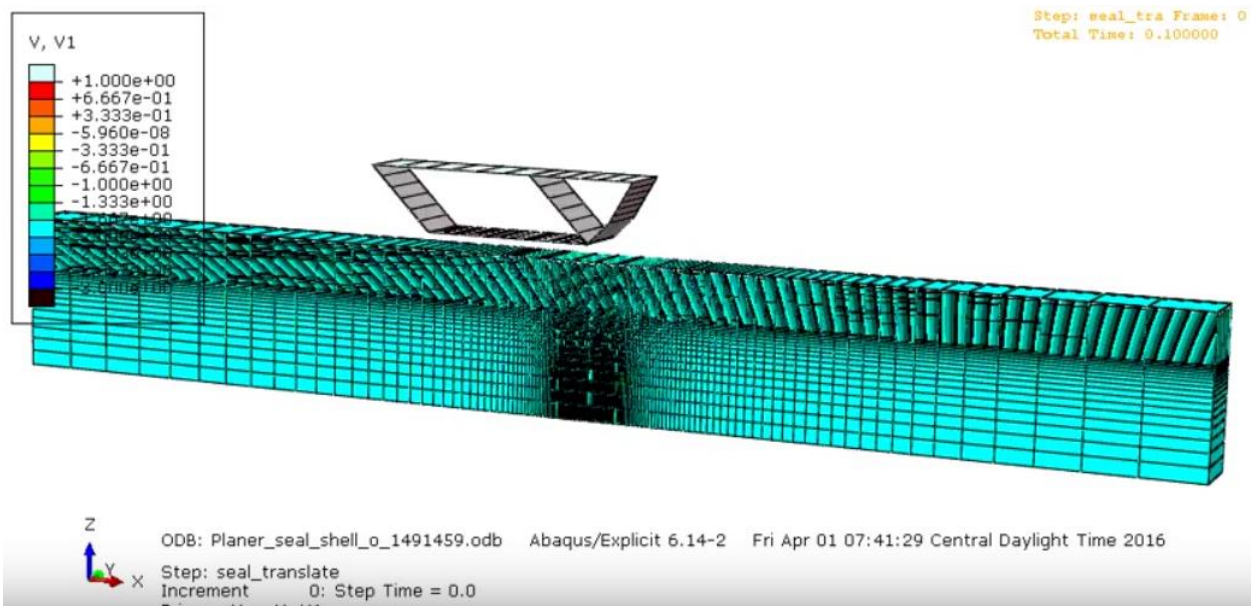

Figure 98. Planer bow seal, *V1* at *t* = 0.1 s

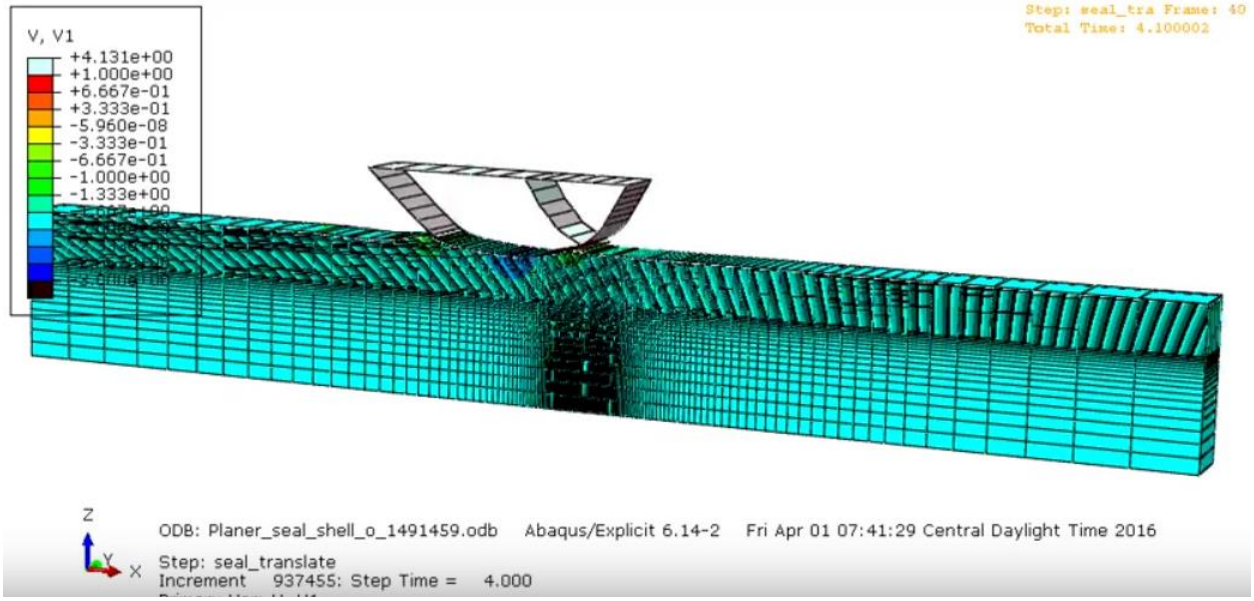

Figure 99. Planer bow seal, *V1* at *t* = 4.1 s

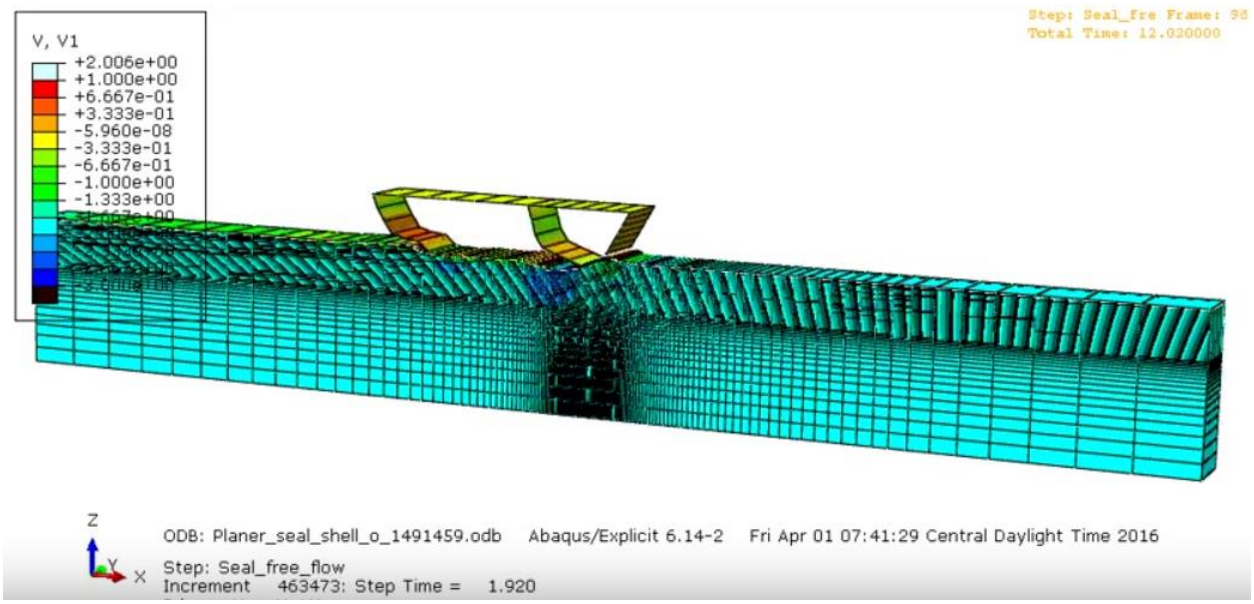

Figure 100. Planer bow seal, *V1* at *t* = 12 s

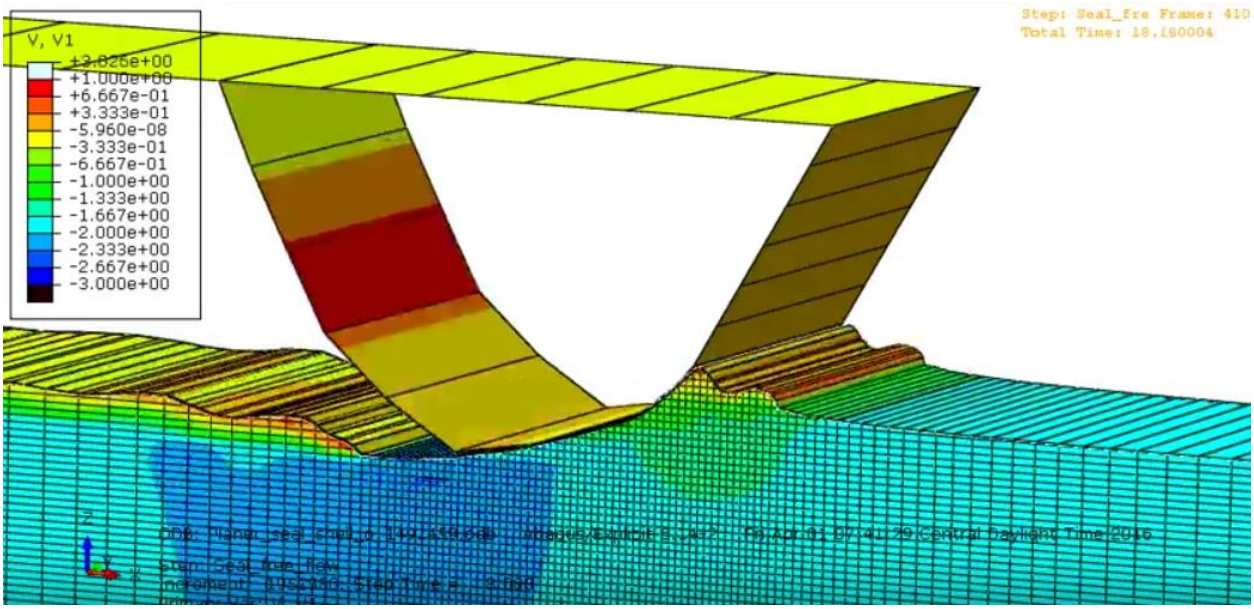

Figure 101. Planer bow seal, *V1* at *t* = 18 s

Prescribed Pressure Results

The approach described above for model development and loading yields the following results. Figure 102 shows the average cross-section profile of the seal once a quasi-static state is reached, as determined by the slope of the standard deviation of tip position. This is further confirmed by comparing the profiles averaged over the final 5 s and 10 s periods; they are a near match. Also, plotted for comparison are results from Bloxom (2014) and Zalek and Doctors (2010). The Abaqus results match Zalek and Doctors very well except for a slight deviation at the tip. They appear to compare slightly more favorably to the UM experiment than the Bloxom results.

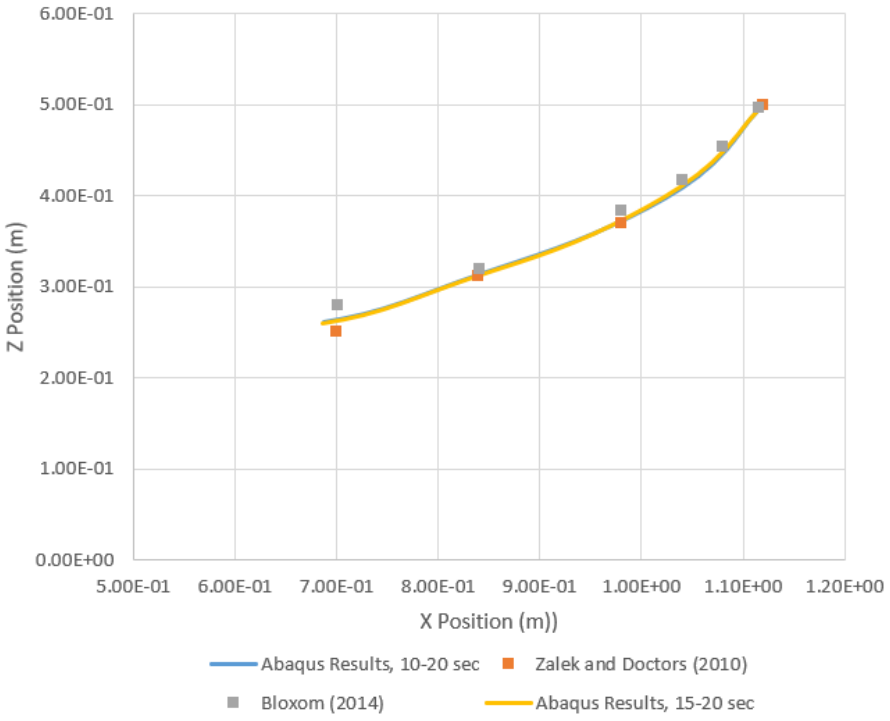

Figure 102. Average membrane seal position, UM run 1026, F_δ = 1.22, P_c= 567 Pa

As an indication of the dynamics of the seal, the displacement versus time for the tip and midpoint are shown in Figure 103. During the initial five seconds, oscillations for each are about 10% of

the mean. However, the effects of sloshing within the domain can be seen beginning at 15 s where the incoming free surface drops slightly, allowing the seal to drop approximately 0.02 m. While it slowly rises over the next five seconds, these flow dynamics repeatedly plague the seal simulations and compromise the data.

The seal attachment reaction force for the same period is plotted in Figure 104. A five-second running average of the data reveals a similar influence of the free surface drop upon resistance. The effect is a reaction force reduction of over twice the mean. More startling is the magnitude of the standard deviations, which are almost an order of magnitude higher than the mean. This effect is demonstrated in the previous NACA0012 results, where nonconvergence of the pressure field makes force assessments difficult. For these reasons, the prescribed pressure-membrane approach is developed further to incorporate a two-fluid cushion model, as detailed below.

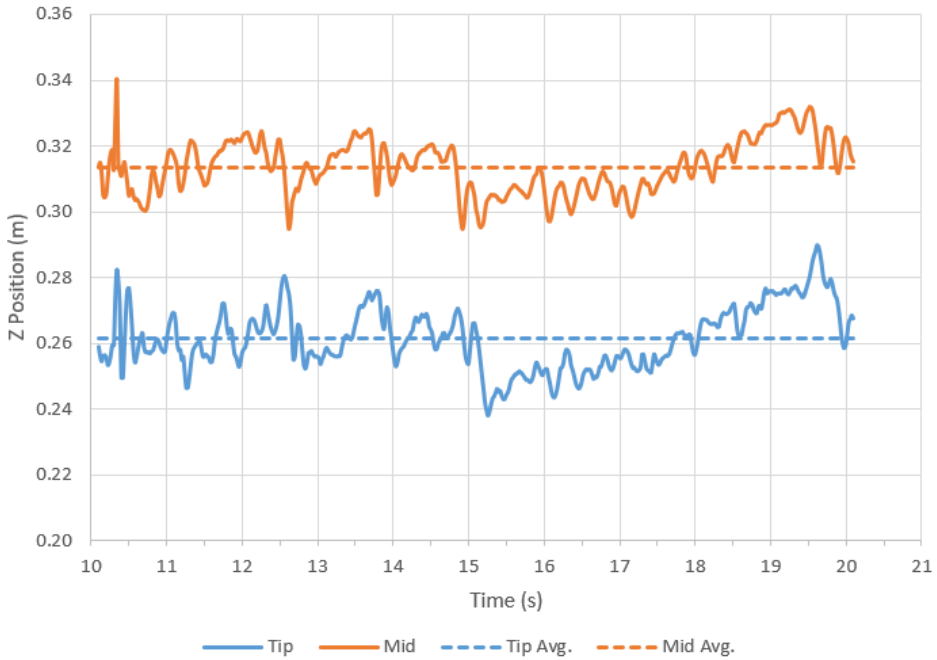

Figure 103. Seal mid-point and tip displacement versus time

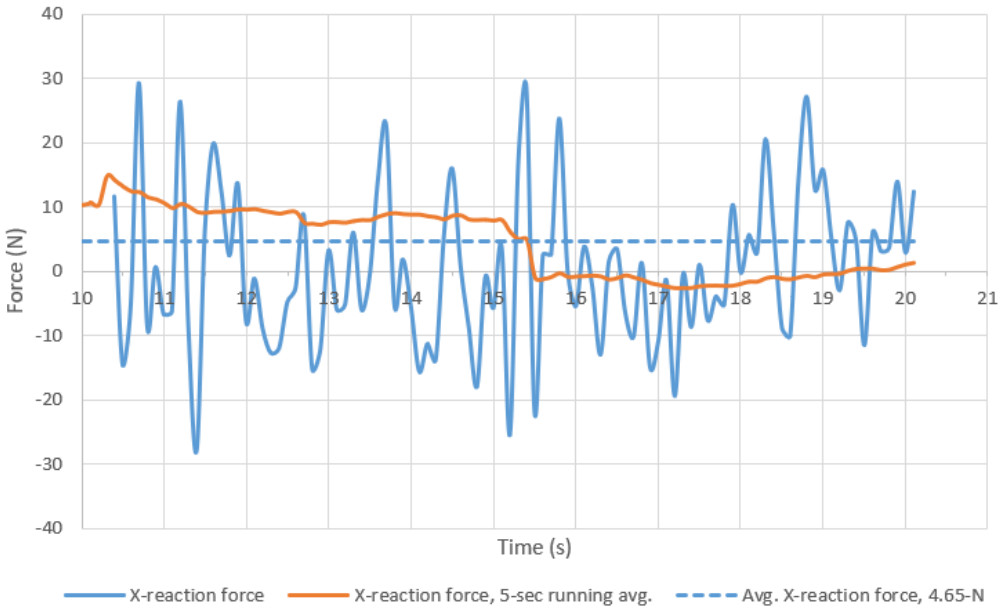

Figure 104. Seal attachment reaction force, *x*-direction

5.3.2 Planer bow seal with cushion model

With the above modeling approach an explicitly prescribed cushion pressure is applied to a near massless membrane in order to balance the pressure at the trailing edge of the seal and free surface within the cushion. It was idealized as two dimensional and variations through the beam were not important. As one may have perceived, this is a considerable weakness moving forward in the cases of practical geometry, as three-dimensional effects become important. Further, large standard deviations in the attachment reaction force prevented a parametric seal resistance study.

For this reason, the planning bow seal model is developed further to include a dynamic cushion model. This is achieved by introducing a second fluid species into the computational domain having the properties of air. The material is defined using the ideal gas equation of state and the following properties: ρ = 1.23 kg/m^3, μ = 0.001 Ns/m^2, gas constant R = 287 J/kg-K, ambient

pressure p_a = 101 KPa, and specific heat capacity, c = 1000 J/kg-K. It should be noted that the viscosity used for the cushion is artificially high in order to match that of the fluid. It was found through significant troubleshooting that the increased viscosity dramatically helps dissipate numerical noise and reduce the instability of the structure at the air-water interface. As the dynamics of the seal are not the primary concern in a steady state analysis, the cost of this compromise is not significant.

Figure 105 shows the new model constructed with the planer bow seal centrally located. The fluid domain is 20 m long, 3 m high, and 1 m wide. The domain initial free surface elevation is 2.12 m. Side, top, bottom, inlet, and outlet boundary conditions are prescribed similar to the previous modeling approach. Portions of the model that predefine the air and water material at t = 0 s are shown in Figure 106 and Figure 107, respectively.

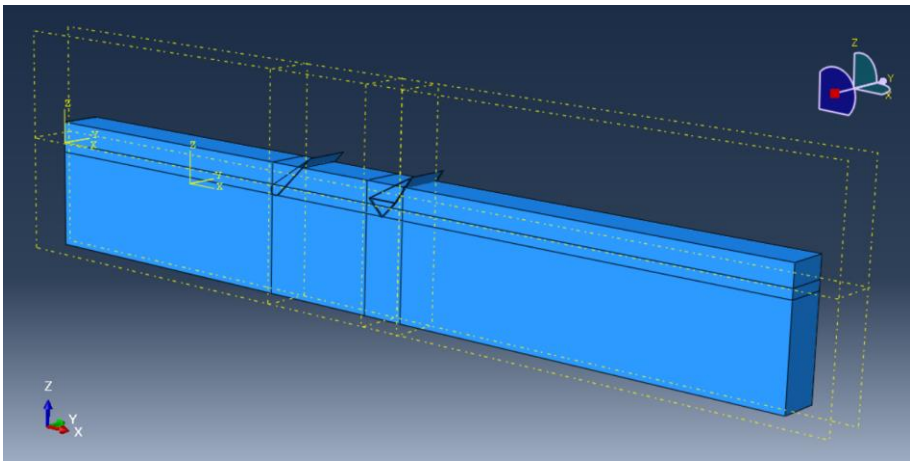

Figure 105. Planer bow seal with cushion domain

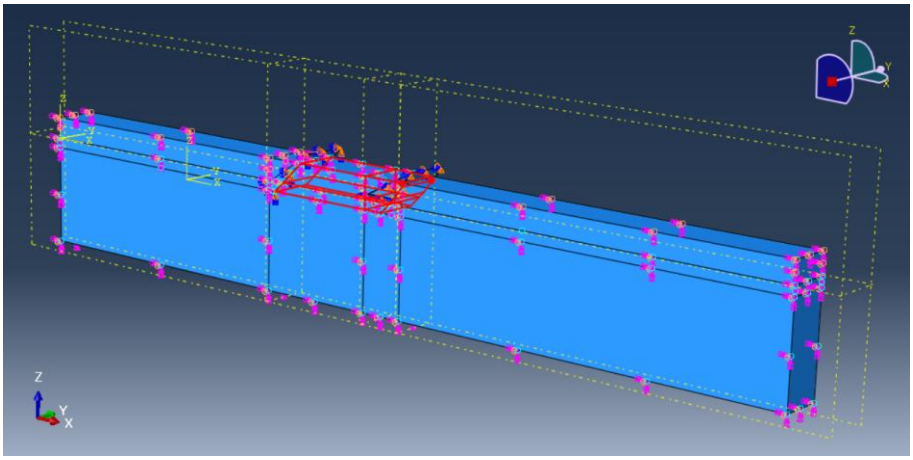

Figure 106. Planer bow seal domain (initialized air material highlighted)

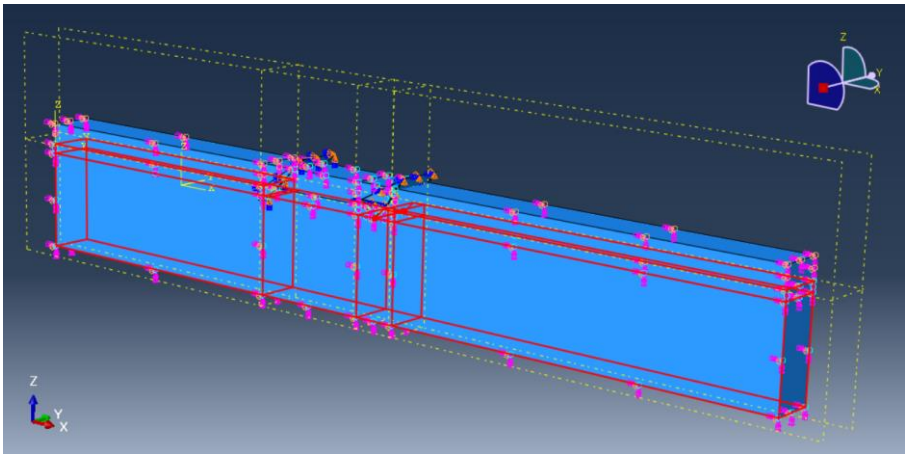

Figure 107. Planer bow seal domain (initialized water material highlighted)

The bow seal platform is shown in Figure 108 through Figure 110 and consists of three primary components. The bow seal (Figure 108) is assigned SR4 shell elements having the properties of rubber used in the UM experiment (Zalek and Doctors, 2010). It is attached to a supporting structure which is fixed in space throughout the simulation. In order to prevent the bow seal from riding up and over the free surface upon startup, two massless membrane straps attach the platform to the trailing edges of the bow seal (Figure 109). These straps resist forward motion of the seal

tip. Model definitions are in place to ensure they do not impose any unwanted moments in the seal, and they are positioned outside of the flow domain. The aft seal (Figure 110) is a rigid element structure oriented 45° to the flow, located approximately 3 m aft of the bow seal. It seals the cushion volume and mimics the experimental configuration. A 0.125 m radius minimizes free surface disturbances. In this model, the bow seal platform and aft seal are initialized at the specified static seal immersion δ_0 and remain fixed throughout the simulation. Through extensive troubleshooting, this was determined as the best way to achieve a steady seal immersion.

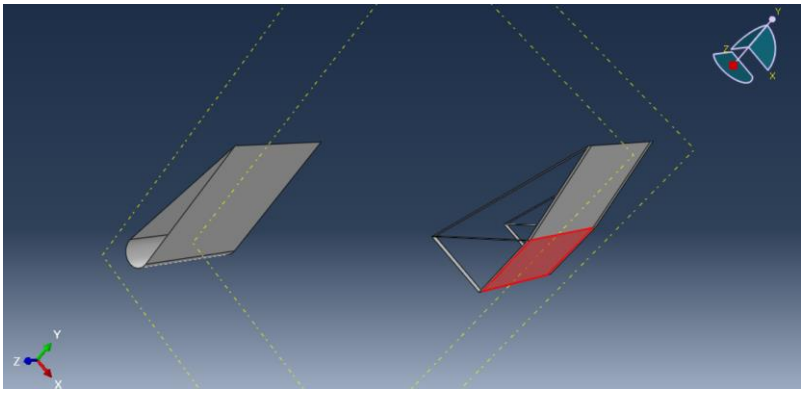

Figure 108. Planer bow seal platform; bow seal highlighted

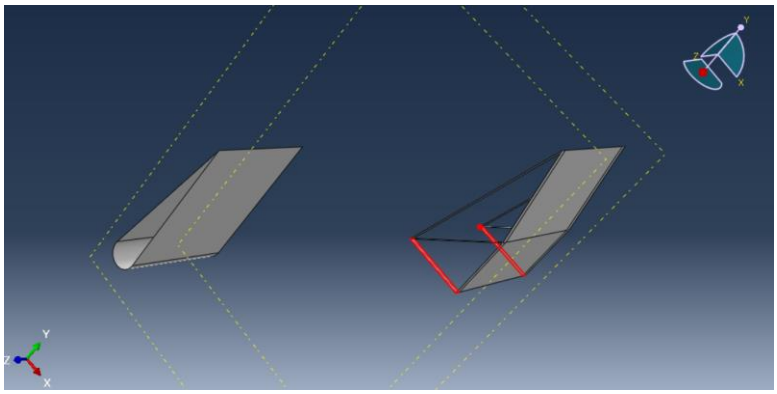

Figure 109. Planer bow seal platform; membrane straps highlighted

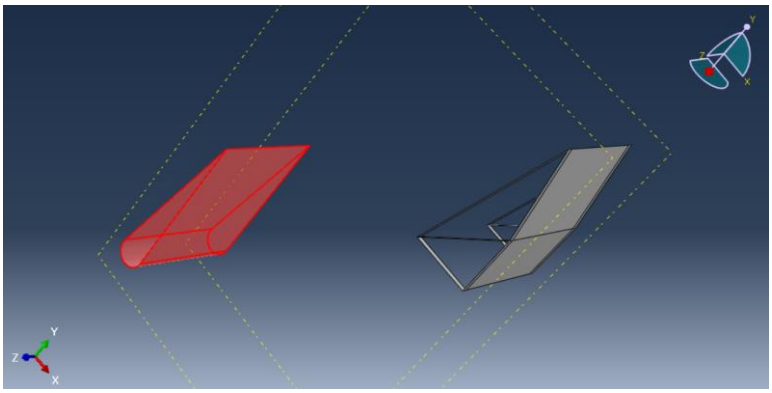

Figure 110. Planer bow seal platform; aft seal highlighted

Air cushion model

Modeling the air cushion in Abaqus/Explicit is not a straightforward process as in other purpose-built codes. For instance, it is not possible to explicitly specify a momentum or mass flux into the domain having particular properties. Instead, to maintain the cushion inflation pressure, the surface between the bow and aft seal is specified to apply a pressure load throughout the simulation (Figure 111). At this Eulerian boundary, material is allowed either to flow out if the cell pressure is greater than the prescribed load, or flow in if the cell pressure is lower than the prescribed load. As the species of the flux material depends on the species currently present in the cell, care must be taken to maintain a stable cushion with densities near that prescribed for air at all times. To properly establish a balanced pressure at the free surface within the cushion, the cushion pressure is set to the hydrostatic pressure of the seal displacement at initialization. Figure 112 and Figure 113 show the fluid density and fluid pressure developed through the domain at initialization.

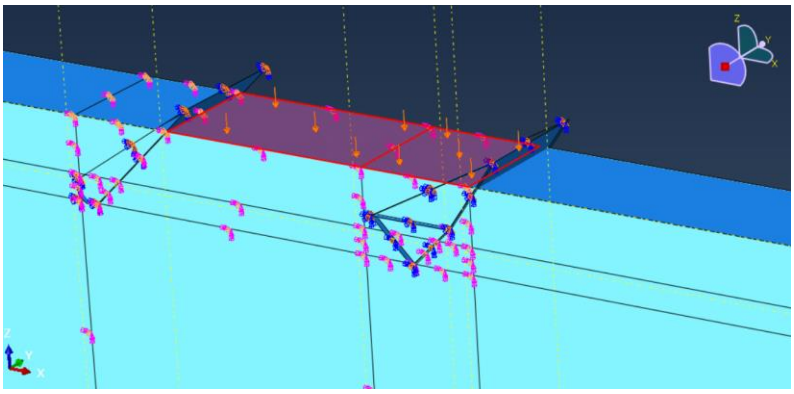

Figure 111. Planer bow seal with cushion; cushion pressure loading

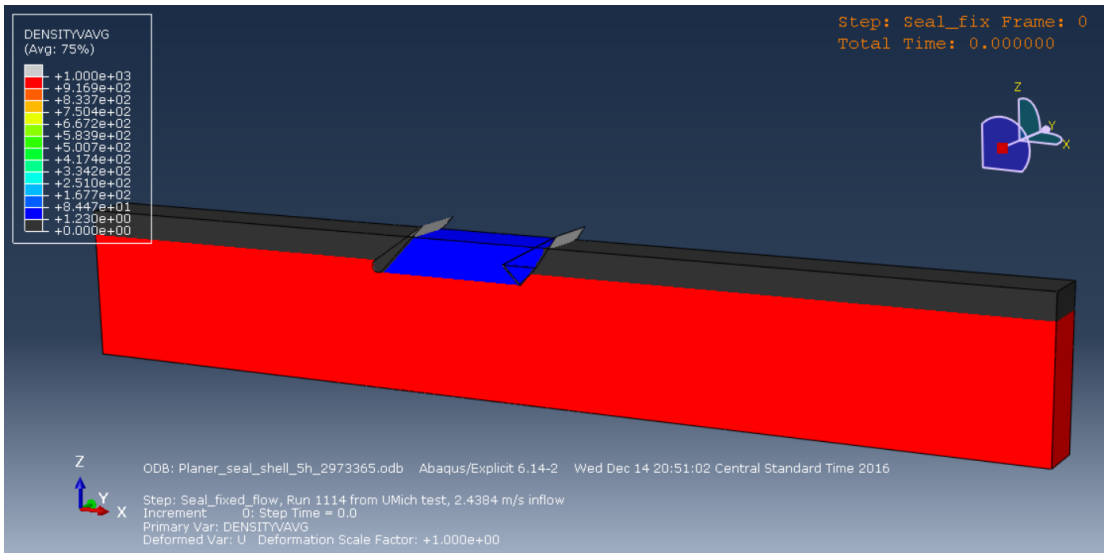

Figure 112. Fluid density at t = 0 s using the two-fluid cushion model

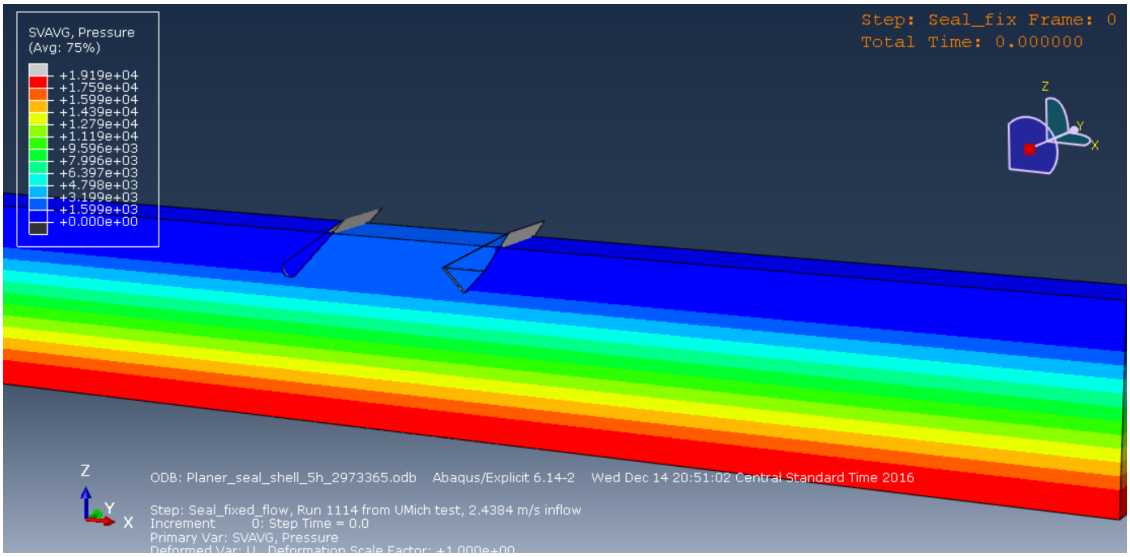

Figure 113. Fluid pressure at t = 0 s using the two-fluid cushion model

Initialization and startup

The simulation is conducted as follows. At t = 0 s, the fluids are initialized with predefined stress fields according to their depth in the domain. Gravity is specified throughout at -9.8067 m/s^2. The water region is initialized with an X velocity of -0.01828 m/s, which is one percent of the nominal far field flow velocity. From t = 0 to t = 3 s, the aft seal is translated up 0.15 m to minimize its influence on the upstream flow. Simultaneously the cushion pressure is reduced to the nominal pressure of P_c = 567 Pa as the flow velocity is increased in a smooth ramp to achieve -1.828 m/s. The inlet and outlet flow boundaries mimic this acceleration. From t = 3 to t = 23 s the model is allowed to freely evolve. Captures of the fluid densities in the X-Z plane are shown in Figure 114 through Figure 120. Tension in the membrane straps shown in Figure 116 reveal they are providing some seal stability early on, while the large catenary in Figure 119 shows they are of little influence when the fluid domain is quasi-steady.

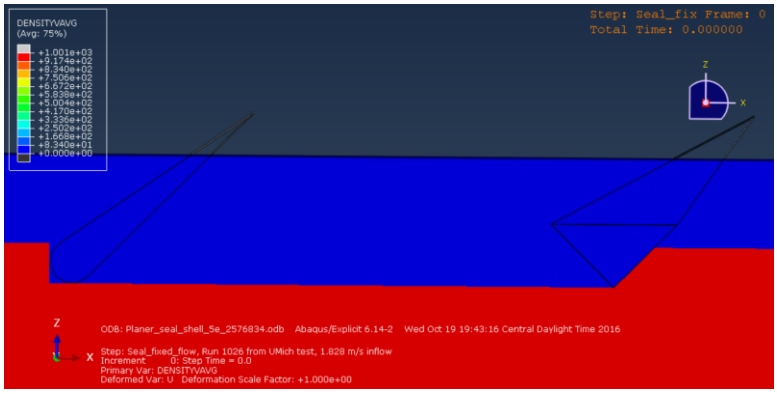

Figure 114. Planer bow seal with cushion results; t = 0 s

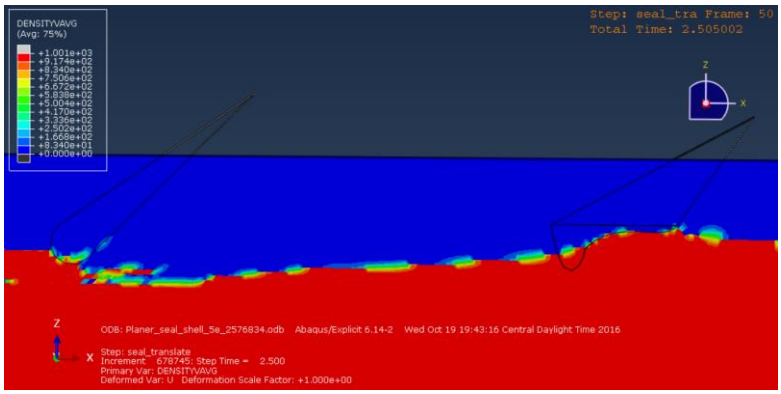

Figure 115. Planer bow seal with cushion results; t = 2.5 s

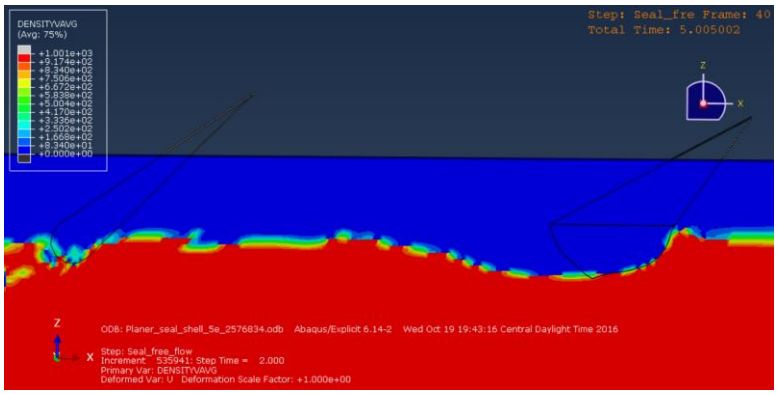

Figure 116. Planer bow seal with cushion results; t = 5 s

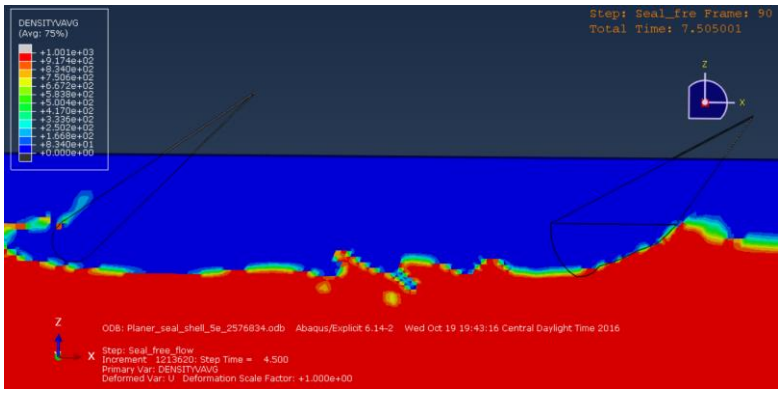

Figure 117. Planer bow seal with cushion results; t = 7.5 s

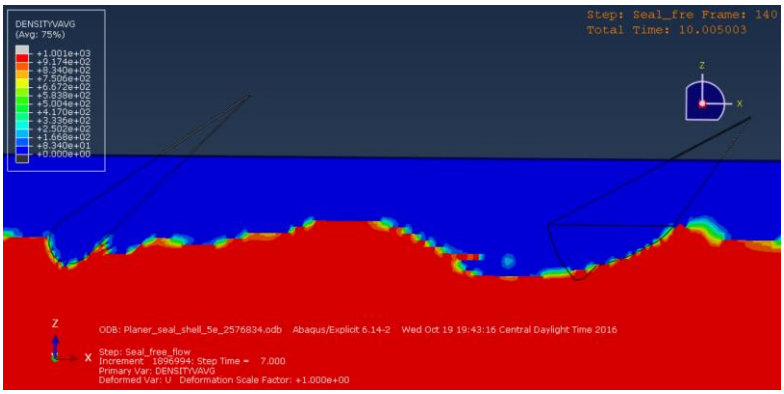

Figure 118. Planer bow seal with cushion results; t = 10 s

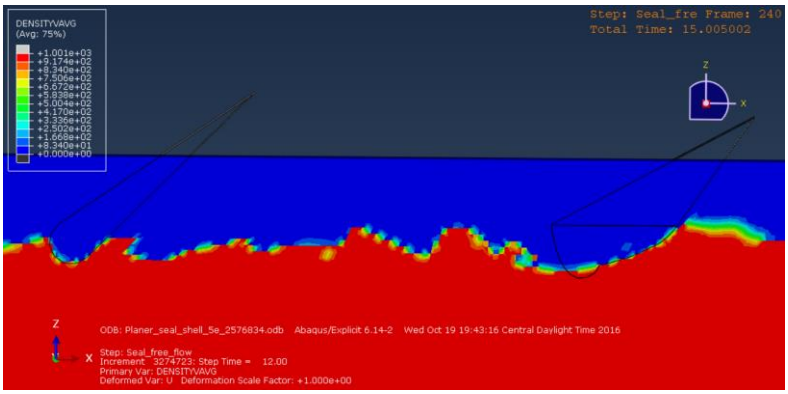

Figure 119. Planer bow seal with cushion results; t = 15 s

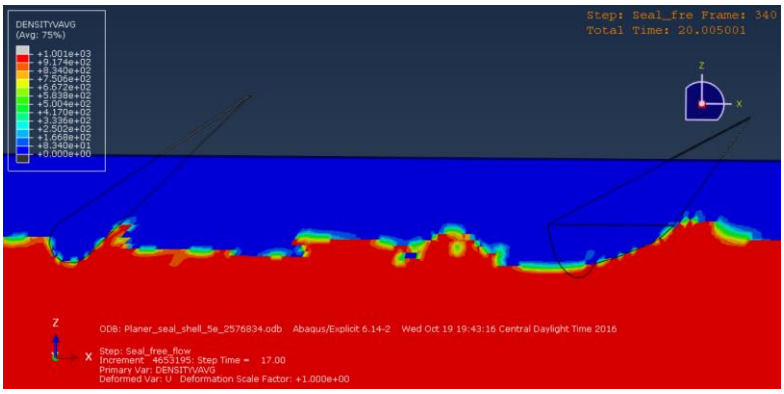

Figure 120. Planer bow seal with cushion results; t = 20 s

Cushion Model Results

Figure 121 shows the average cross-section profile of the seal once a quasi-static state is reached for the two-fluid Abaqus model (job# 2576834 Results). Plotted for comparison is the profile for the previous Abaqus results using the free surface-following membrane (job# 1491459 Results). Bloxom (2014) and Zalek and Doctors (2010) profiles are plotted as well. The two-fluid Abaqus model appears to compare more favorably to Bloxom's results. However, the seal motions remain high and it is difficult to pinpoint exactly what is the root cause of the improvement due to the numerous differences in the physics modeling.

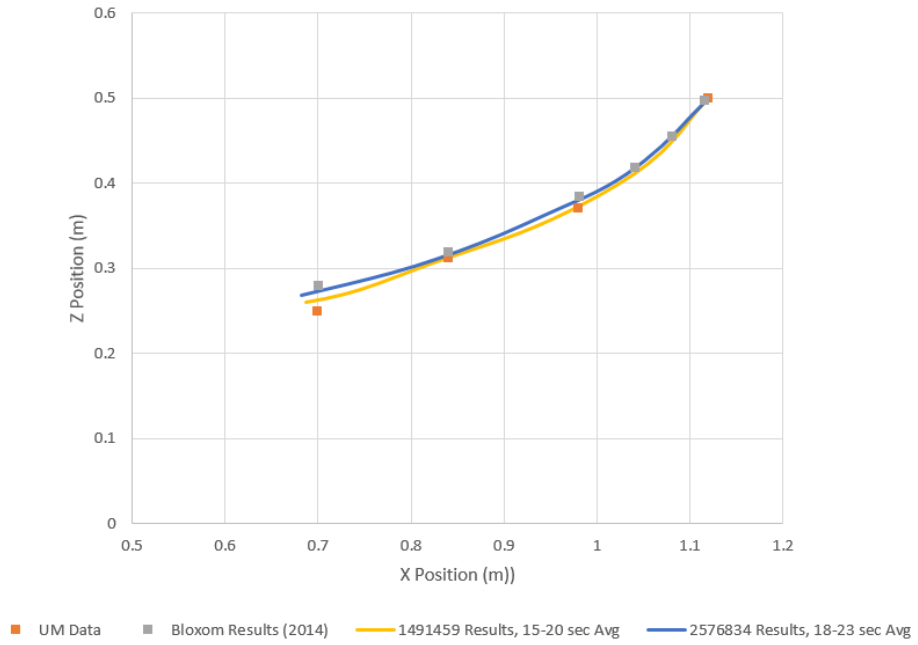

Figure 121. Average seal position, run 1026, F_δ = 1.22, P_c= 567 Pa

To test the robustness of the two-fluid cushion model, a second set of flow and pressure conditions (U = 2.43 m/s, P_c = 953 Pa) are specified to simulate UM run 1114 (job# 2973365). Again, mean displacements of the seal using the two-fluid cushion model compare well to previous results (Figure 122). The inlet cushion pressure monitor for the run shows the pressure ramp down to the nominal running cushion pressure (Figure 123). Figure 124 reveals the inlet cushion pressure is a near match to the prescribed nominal cushion pressure load, while oscillations of the pressure monitor adjacent to the seal reveal the influence of the seal dynamics.

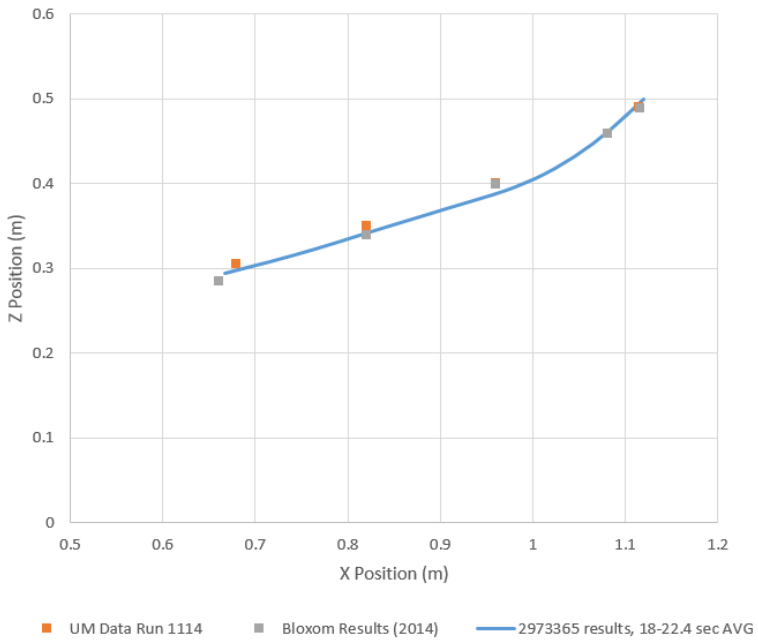

Figure 122. Average seal position, run 1114, F_δ = 1.6, P_c= 953 Pa

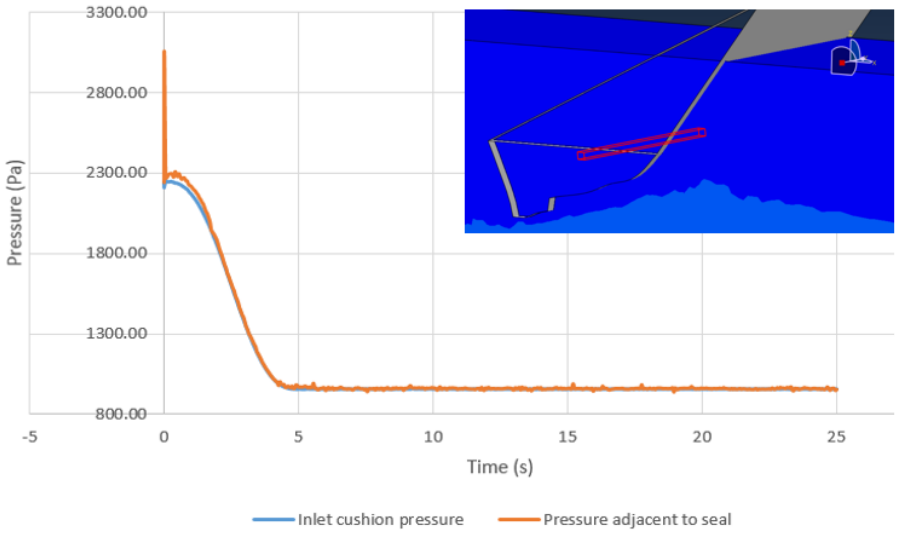

Figure 123. Inlet cushion pressure monitor, P_c = 953 Pa. (monitor location highlighted)

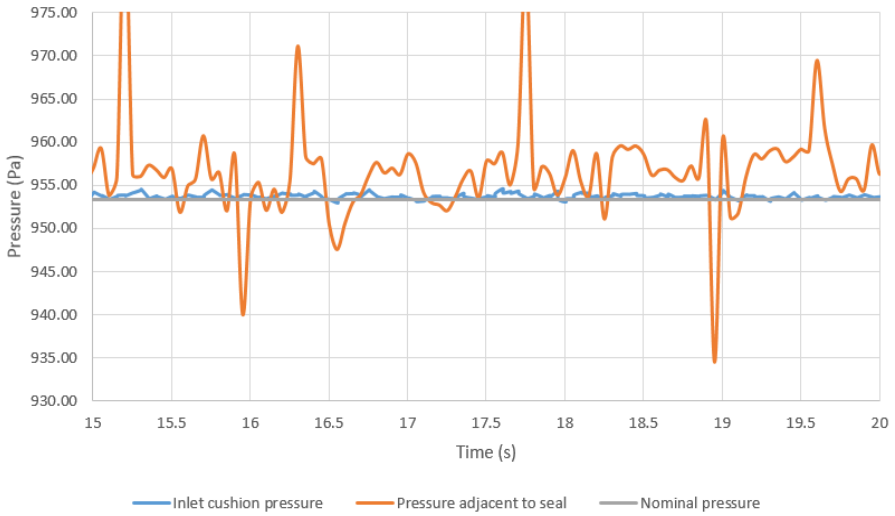

Figure 124. Cushion pressure monitors, t = 15 to 20 s, P_c = 953 Pa

Despite good predictions for average seal positions at two different inflow and pressure conditions, the two-fluid cushion model fails to provide improvements in standard deviations of the drag data. Oscillations of the free surface due to sloshing, in combination with the CEL loose coupling technique does not provide the computational foundation for a precise parametric study of seal resistance. While the simulations above are conducted using the nominal fluid sound speed of 1500 m/s, little improvement is seen by reducing the sound speed as demonstrated in the NACA0012 problem. Attempts to reach steady state were unsuccessful. Further, with explicit time integration, the time scale required to reach convergence (*O*E3) using increased compressibility cannot be accommodated due to the time step restriction of the structural elements (*O*E-6).

Mass Scaling

On the verge of abandoning the explicit CEL approach, Mass Scaling (MS) (Olovsson, 2005) is a final technique explored to reduce oscillation of the seal and improve convergence.

Commonplace in explicit dynamic simulations, the idea behind MS is to selectively increase the numerical density, and thus reduce the dilatational properties of the solid to enable vast increases in the explicit time step. Recall the stability criterion in explicit schemes limits the size of the time step based upon edge length, L_e and dilatational constant, c_d as: $\Delta t = min\left(\frac{L_e}{c_d}\right)$. According to $c_d = \sqrt{(\lambda + 2\mu)/\rho}$, increases in ρ reduces c_d, increasing Δt. When preservation of the dynamics is important, MS must be used sparingly, and only to the most critical elements in areas that do not largely affect the results. For a quasi-steady interaction, such as the case of the flexible seal, dynamics can be disregarded and MS can be applied in large portions to all structural elements. An important distinction is that MS modifies the numerical density only and affects the inertial properties of the structure. The physical density that dictates equation of state properties or external body forces such as gravity remain unscaled. In Abaqus/Explicit CEL, MS can be applied by setting a goal time step or by explicitly setting a MS density scaling factor (Dassault Systemes, 2013). For the planer seal problem, various MS factors up to 10,000 are applied to the flexible seal structure. Although reductions in oscillations are observed, the large oscillations in pressure develop an enormous amount of seal momentum. This results in a lack of free surface compliance and subsequent cushion venting in many cases. For this reason, the large-scale application of MS for this problem is deemed unsuccessful.

Chapter 6

Conclusion

This work documents an effort to verify, validate, and apply a commercial multi-physics tool toward the difficult problem of ACV seal resistance. *Introduction* (Chapter 1) provided a review of the ACV mission, discussed the importance of modeling and simulation, and stated the relevance for improving the resistance predictions for these craft. The chapter concluded with a review of recent numerical and experimental ACV seal studies.

Dimensional analysis (Chapter 2) identified key physical variables and derived numerous dimensionless parameters that should be considered when exploring the problem of ACV seal resistance. Two of the forms were used in Chapter 4 to demonstrate a power law relationship between seal resistance and cushion pressure.

Computational approach (Chapter 3) reviewed the numerical methods employed, including the finite element method, finite volume method, and those pertaining to FSI. A discussion of verification, validation, and uncertainty made the case that formal V&V is a necessity for numerical investigations. Lastly, the Probabilistic Collocation method was introduced as one means for efficiently estimating aleatory uncertainty in parameters that can be statistically characterized.

Results (Chapter 4) detailed the model development and V&V effort for both the elastic beam FSI benchmark simulations and planer bow seal simulations. The elastic beam FSI benchmark 1

results for the fluid domain showed timestep size played an important role in obtaining accuracy for the highly transient unsteady problem. Estimating the exact value for mean drag using Richardson Extrapolation gave a result that differed from the benchmark by only 0.034%, validating the fluid model. The elastic beam FSI benchmark 2 results for the structural domain used a grid refinement study for both quadratic and linear elements to demonstrate an observed order of accuracy slightly less than the formal order. The estimate of the exact solution using Richardson Extrapolation gave a tip deflection that differed from the benchmark by only 0.8%, validating the structural model. The elastic beam FSI benchmark 3 results for the coupled FSI problem explored the effects of spatial discretization at two timesteps, the effects of FSI under-relaxation factor, and the effects of inner iteration count. In the FSI under-relaxation study, the tradeoff between stability and speed was demonstrated, identifying $0.5 < UR < 0.9$ as an acceptable range. In the FSI inner-iteration study, improvements in percent error where seen as iterations increased and significant inner iterations were required to achieve results comparable to the reference solution. This reinforced the importance of convergence within the fluid equations when time accuracy is needed. Finally, FSI benchmark 3 revealed the increasing presence of added-mass instability with high inner iterations.

In the second half of *Results* (Chapter 4), STAR-CCM+ was used to simulate the UM planer bow seal experiment. With a two-fluid VOF solver implemented, the simulation was able to achieve deflection and resistance results in good agreement with previous work. The importance of choosing and tuning a material model to replicate the seal was demonstrated, as the absence of a hyperelastic model required the substitution of a linear-elastic model. The cushion pressure model was shown to perform perfectly using the fan momentum interface option and user-defined fan

curves. The seal resistance results were then used to predict power law relationships between non-dimensional seal resistance and cushion pressure. An uncertainty analysis for inflow velocity was performed, which revealed large deviations in seal resistance when all other parameters remain constant. Lastly, the results for a full-hull SES with and without wind were used to show the importance of the aerodynamic load upon the seal.

Abaqus/Explicit (Chapter 5) covered extensive V&V of an explicit approach to large deformation fluid-structure interaction modeling. Significant effort was needed to develop and verify the boundary conditions required to achieve stable, free-surface flow using the explicit CEL technique. Problems studied included elastic beam deflection, Couette flow, circular Couette flow, free surface cylinder flow, NACA0012 flow, and elastic gate deflection FSI. A final set of problems using Abaqus/Explicit were conducted for the planer bow seal problem. Unfortunately, due to large deviations and noise in the pressure results, the approach was ultimately abandoned as a technique to study seal resistance.

6.1 Contributions

The primary contribution of this work is the verification and validation of the commercial multi-physics tool STAR-CCM+ for FSI problems with or without a free surface. The program is successfully used to replicate benchmark results for the unsteady elastic beam FSI problem proposed by Turek and Hron (2006). Previously, separate partitioned solvers were required to simulate the various physics needed to achieve these results. With this work, verification of STAR-CCM+ as a stand-alone partitioned FSI solver drastically speeds up the setup, runtime, and complexity of previous approaches. Through extensive trial and error, the program is also used to replicate planer bow seal resistance results (Zalek and Doctors, 2010, Bloxom, 2014) for various

cushion pressures and inflow speeds. As another primary contribution of this work, validation of STAR-CCM+ as a seal resistance exploratory tool opens the door to designers who may have been computationally limited previously.

A secondary contribution of this work is the application of Abaqus/Explicit for both fluid dynamic and FSI simulations. Using the two-way, loose coupling explicit approach, techniques for achieving stable free surfaces for channel flow are successfully developed, and methods are demonstrated for reducing the instability of the compressible flow equations at low sound speeds. Ultimately, the approach failed to develop a converged pressure solution for the planer seal simulation.

6.2 Future work

From the work above, a great many aspects of ACV seal modeling and behavior remain unexplored, and the prospects for future work are plentiful. For a direct continuation of this research, the planer seal parameters should be altered to develop results that more-fully explore the parametric relationships identified in section 2.2. Variations in seal face angle, width, and height should be explored to build confidence for designers of larger SES, such as the T-Craft. Variations in flow speed, pressures, and static immersion should be explored further and compared through the numerous non-dimensional forms presented. Previously, this was computationally difficult to achieve. Now, with a verified and validated commercial tool that computes all physics within the same framework, this is immediately achievable.

A current restriction in the present results is the absence of a hyperelastic material model for the seal. While other specialized explicit structural solvers offer these (Abaqus/Explicit, LS-Dyna,

etc.), the coupling between these tools and STAR-CCM+ adds significant complexity to the communications and problem specifications. Continued attention should be paid to the availability of tools that offer hyperelastic models and implicit solvers to accommodate behavior of nonlinear materials.

The current STAR-CCM+ model could be expanded into three dimensions to enable the study of more realistic seal geometries, such as fingers. While planer seals are simple and idealized geometries for experimentalists and numerical modelers, they have generally been abandoned for practical applications. Instead, finger geometries are commonly used for their inherent stability and ease of conformity to a varying supporting surface. At present, simulation of finger seal geometry is a much more difficult and expensive computation. First, spatial discretization required in regions near the seal tip must be consistent with the seal thickness, leading to large cell counts for realistic 3D geometry. A further consequence of the small elements is the impact to timestep. Courant numbers below 1 (ideally < 0.5 for HRIC scheme) are needed to maintain refinement of the interface with the VOF solver; typically leading to $\Delta t \approx$ 1E-4 s or smaller. This, in combination with the unsteady approach toward a steady solution, makes a 20 to 30 s simulation a very expensive computation.

Finger seal geometries exhibit complex deformation and chaotic motions at some conditions (Wiggins, 2014). For this reason, much thought should be given in future work to an efficient means for modeling fingers seals without compromising interactions with the free surface or their neighbors. The boundaries, assumptions, and any simplifications must minimize reductions in the physics complexity. One such geometry proposed by the author is that of Figure 125 and Figure 126. By modeling two adjacent half-fingers in contact, the cushion region is isolated from the

ambient region upstream and leakage through the seals is minimized. A contact interface is required between the fingers, while symmetry boundaries in the structure and fluid at each finger centerline provide sidewall closure.

Another challenge for future researchers modeling finger seal geometries is the need for repetitive remeshing of the fluid region. Current mesh motion solvers deform elements up to the point of cell inversion, or where the fluid solver fails to converge. While particular limits for skewness or cell quality can be specified to stop the simulation before failure occurs, the rapid diminishing of cell size in the region of finger-to-finger contact makes automatic remeshing a necessity. For example, the author found the cell quality reduced to the minimum criterion in as little as 40 timesteps using the geometry in Figure 125. Currently in STAR-CCM+, automatic remeshing can be implemented at great expense using a java macro, however the author has had limited success to date in its employ for the finger geometry. A suggested solution could be the application of Immersed Boundary methods. While smaller mesh refinements may be required over a larger area to accommodate motion of the seal, it would reduce the periodicity for remeshing significantly.

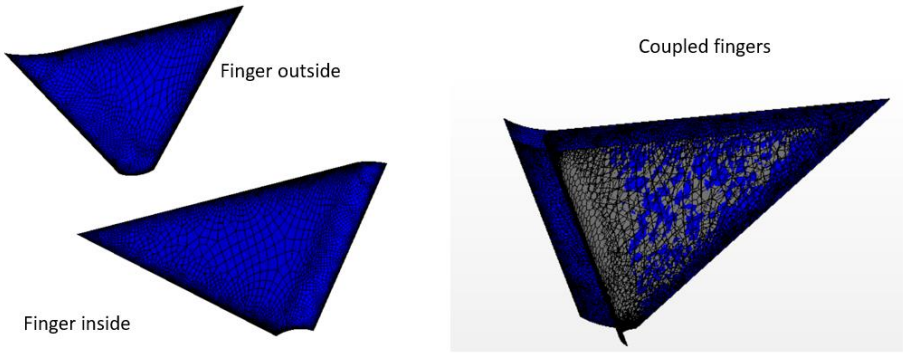

Figure 125. ACV finger half-models in STAR-CCM+

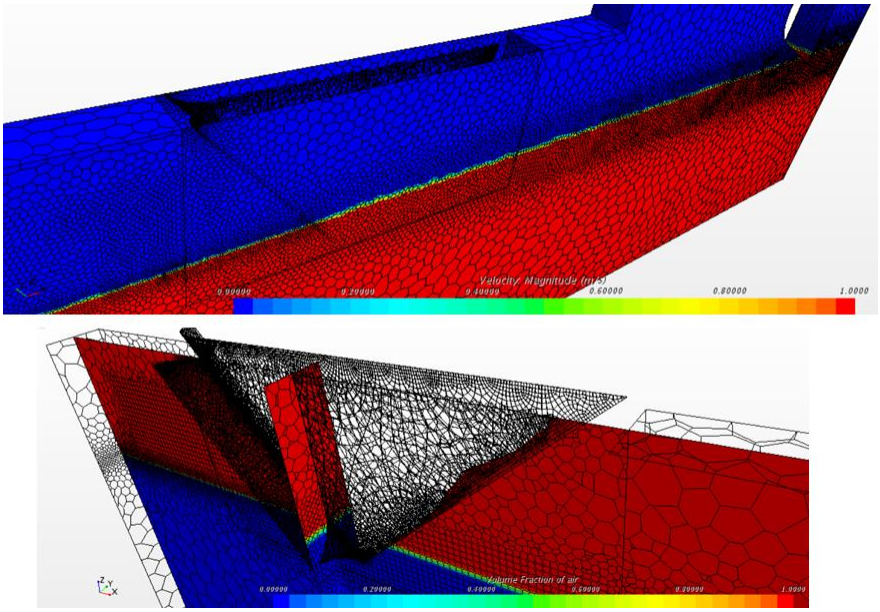

Figure 126. ACV finger simulations in-development using STAR-CCM+

A final opportunity for future work is the integration of high-fidelity flexible seal models with 6-degrees-of-freedom craft models. Based upon the computational expense experienced in this work, it is believed highly difficult to simultaneously model a realistic three-dimensional craft geometry in turbulent flow along with a physically realistic and properly discretized flexible seal. Approaches that bridge the gap between the various physical scales at play and capitalize upon the next generation of high-performance computing resources may offer promising pathways to a fully integrated, numerical SES and ACV performance prediction tool.

The work above was conducted primarily on high performance computing systems at both Virginia Tech (Blueridge) and the US Army Research Laboratory (Excalibur). As core-hours and other metrics for computational costs are unreported in the above work, the following metrics are provided. Generally, a thirty second run for the planer seal model at the problem size described required 2000 core-hours to compute on a single node of 32 cores (2.3 GHz). This runtime is

largely affected by discretization and speed of the flow, as a Courant number limitation is needed resolve the fluid/air interface. For the 2D planer seal problem, the costs to remesh the grid are insignificant. However, it is observed that for the 3D finger geometry, greater than 50% of the computational time is spent moving the mesh. This could prove a substantial cost impact.

Another limitation that should be considered is the scalability of the coupled solvers. It was found that requesting additional cores beyond those contained on a single HPC node would not provide any significant reduction in runtime. In some circumstances, the runtime increased. From this observation, there seems to be opportunities for better data packaging and/or communication protocols between nodes. Alternatively, HPCs with greater quantities of cores per node would provide an immediate benefit.

If one were to scope fulltime work to develop the finger model and perform a corresponding parametric study, an estimate would be 3 months of full time model development and validation, followed by an additional 3 months for production runs. With core-hours approaching 8000 hours per run, a reasonable allocation request could be 160,000 hours.

Appendix A – Abaqus/Explicit material models

A primary advantage of Abaqus over STAR-CCM+ is the ability to specify nonlinear material models for solids based upon definition of the strain energy potential. This appendix reviews the testing techniques required to obtain characteristic data for the various material models that describe the energy potential. This section concludes with an analysis and characterization of the material used in the elastic gate deflection simulation in section 5.2.6.

A.1 Hyperelastic material models

In Abaqus, the constants required to define the appropriate material model can either be provided directly or obtained using data from the following four laboratory tests: Uniaxial Tension, Biaxial Tension, Planar Tension, and Volumetric. Figure 127 shows the deformations performed for each test and how the resulting principal deformations are obtained. In the Uniaxial Tension test, a dog-bone sample is pulled and both tension and strain are recorded. In the Biaxial Tension test, two perpendicular directions are pulled. The biaxial device must ensure the directions of pull are completely orthogonal to each other and do not create transverse shear within the specimen, which typically leads to complex devices (Escarpita, 2012). In the Planar Tension test, a wider specimen is tested in tension such that the reduction in width (the "2" direction) is negligible. The principle deformation in the "2" direction can then be approximated as 1. In the Volumetric test, pressures applied to all faces of a specimen identify the volumetric strain. Figure 127 also conveys that a compressive variation of the tests can be used which may assist in the physical implementation, especially for the Volumetric test where tri-axial tension is difficult to achieve.

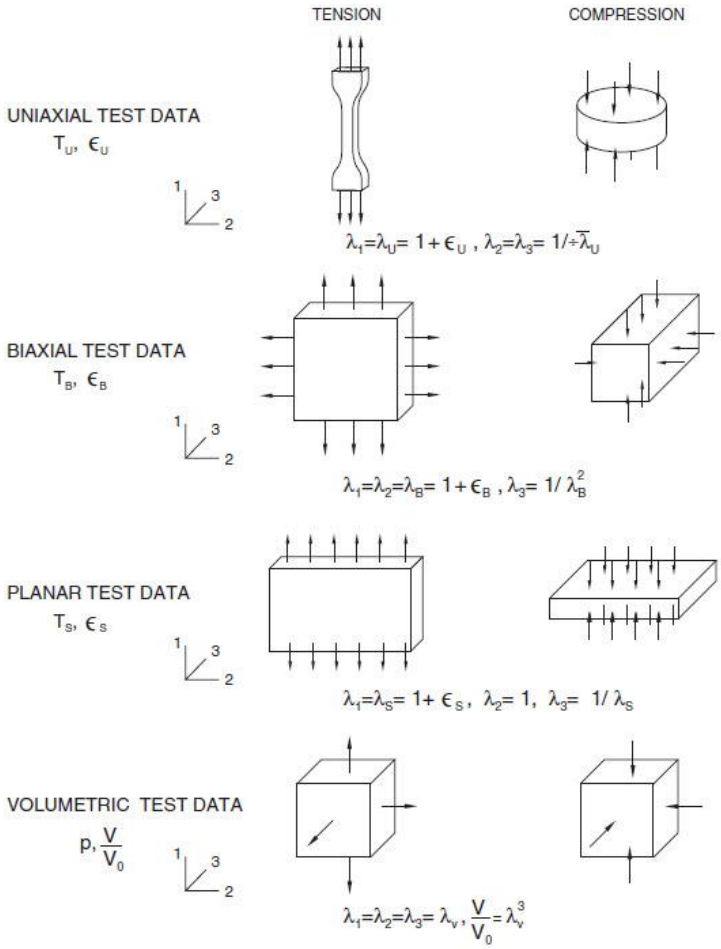

Figure 127. Hyperelastic material strain-energy tests (Dassault Systemes, 2013)

It is noted that in the absence of a dedicated material testing program, it is rare to have the full complement of test data available for a material. Most mechanical labs are outfitted with uniaxial tension machines, but only a small number can also perform a biaxial test (Brieu, 2007). Further, many suggest isotropic rubber materials cannot be adequately classified using only uniaxial data (Treolar, 1944, Rivlin, 1951). For this reason, some researchers in this field have developed novel mechanisms which convert uniaxial motion into pure orthogonal biaxial motion (Brieu, 2007 and Escarpita, 2012). This enables a biaxial test to be conducted using a more common and less expensive uniaxial tension machine. Abaqus suggests however, that when only data from a single

test is available, the Marlow form of strain potential energy performs well and is a good starting point (Dassault Systemes, 2013). This form requires only information on the first deviatoric strain invariant to determine the deviatoric component and makes assumptions regarding compressibility for the volume component if not provided.

The various strain energy potential models available in Abaqus are: Arruda-Boyce, Marlow, Mooney-Rivlin, neo-Hookean, Ogden, Polynomial, Reduced Polynomial, Van der Waals and Yeoh. They are briefly reviewed here to reveal how they are interrelated and offer distinct advantages based upon the material characterization data available.

The Arruda-Boyce strain energy potential is provided in Eq. A1, where U is the strain energy per unit volume, and μ and D are temperature dependent material constants obtained from test data. λ_m is the "locking stretch"; the maximum stretch obtained when the hyperelastic material becomes rigid and stress rises towards infinity.

$$U = \mu\left\{\frac{1}{2}(\bar{I}_1^1 - 3) + \frac{1}{20\lambda_m^2}(\bar{I}_1^2 - 9) + \frac{11}{1050\lambda_m^4}(\bar{I}_1^3 - 27) + \frac{19}{7000\lambda_m^6}(\bar{I}_1^4 - 81) + \frac{519}{673750\lambda_m^8}(\bar{I}_1^5 - 243)\right\} + \frac{1}{D}\left(\frac{J_{el}^2-1}{2} - \ln J_{el}\right) \quad \text{(A1)}$$

In the above equation, $\bar{I}_1$ is the first deviatoric strain invariant and J_{el} is the elastic volume ratio. Their definitions are given in Eq. A2 and Eq. A3, respectively. The deviatoric stretches ($\bar{\lambda}_i$) are based upon each "principal stretch" and the total volume ratio J according to Eq. A4. If the material is incompressible, the total volume ratio reduces to one. The further assumption that the case is isothermal reduces the thermal strain (ϵ^{th}) to zero. The elastic volume ratio then becomes 1 in this case.

$$\bar{I}_1 = \bar{\lambda}_1^2 + \bar{\lambda}_2^2 + \bar{\lambda}_3^2 \quad \text{(A2)}$$

$$J_{el} = \frac{J}{(1+\epsilon^{th})^3} \tag{A3}$$

$$\bar{\lambda}_i = \frac{\lambda_i}{(J)^{1/3}} \tag{A4}$$

The Marlow strain energy potential is provided in Eq. A5. In addition to the definitions above, the deviatoric and volumetric components of the potential are determined from test data supplied to Abaqus.

$$U = U_{dev}(\bar{I}_1) + U_{vol}(J_{el}) \tag{A5}$$

The Mooney-Rivlin strain energy potential is provided in Eq. A6. In addition to the definitions above, C_{10}, C_{01} and D_1 are temperature dependent material constants, and $\bar{I}_2$ is the second deviatoric strain invariant per Eq. A7.

$$U = C_{10}(\bar{I}_1 - 3) + C_{01}(\bar{I}_2 - 3) + \frac{1}{D_1}(J_{el} - 1)^2 \tag{A6}$$

$$\bar{I}_2 = \bar{\lambda}_1^{-2} + \bar{\lambda}_2^{-2} + \bar{\lambda}_3^{-2} \tag{A7}$$

The neo-Hookean strain energy potential is provided in Eq. A8. The form of which was a prime contributor to the Mooney-Rivlin model above.

$$U = C_{10}(\bar{I}_1 - 3) + \frac{1}{D_1}(J_{el} - 1)^2 \tag{A8}$$

The Ogden strain energy potential is provided in Eq. A9. In addition to the definitions above, μ_i, α_i, and D_i are temperature dependent material constants. *N* is a specified material parameter.

$$U = \sum_{i=1}^{N} \frac{2\mu_i}{\alpha_i^2}\left(\bar{\lambda}_1^{\alpha_i} + \bar{\lambda}_2^{\alpha_i} + \bar{\lambda}_3^{\alpha_i} - 3\right) + \sum_{i=1}^{N} \frac{1}{D_i}(J_{el} - 1)^{2i} \tag{A9}$$

The Polynomial strain energy potential is provided in Eq. A10, where C_{ij} is a specified material constant. Particular selections for C_{ij} lead to the Mooney-Rivlin, neo-Hookean, and Yeoh forms for the strain energy potential. A simplified form of this equation is the Reduced Polynomial strain energy potential (Eq. A11).

$$U = \sum_{i+j=1}^{N} C_{ij}(\bar{I}_1 - 3)^i(\bar{I}_2 - 3)^j + \sum_{i=1}^{N} \frac{1}{D_i}(J_{el} - 1)^{2i} \tag{A10}$$

$$U = \sum_{i=1}^{N} C_{i0}(\bar{I}_1 - 3)^i + \sum_{i=1}^{N} \frac{1}{D_i}(J_{el} - 1)^{2i} \tag{A11}$$

The Van der Waals strain energy potential is provided by Eq. A12. In addition to the definitions above, η is a parameter that relates the deviatoric strain invariant to the locking stretch according to Eq. A1. β is a parameter that relates the deviatoric strain invariants using Eq. A14. a is the global interaction parameter.

$$U = \mu\left\{-\left(\bar{\lambda}_m^2 - 3\right)[\ln(1-\eta) + \eta] - \frac{2}{3}a\left(\frac{\bar{I}-3}{2}\right)^{\frac{3}{2}}\right\} + \frac{1}{D}\left(\frac{J_{el}^2-1}{2} - \ln J_{el}\right) \tag{A12}$$

$$\eta = \sqrt{\frac{\bar{I}-3}{\lambda_m^2-3}} \tag{A13}$$

$$\bar{I} = (1-\beta)\bar{I}_1 + \beta\bar{I}_2 \tag{A14}$$

The Yeoh strain energy potential is provided in Eq. A15.

$$U = C_{10}(\bar{I}_1 - 3) + C_{20}(\bar{I}_1 - 3)^2 + C_{30}(\bar{I}_1 - 3)^3 + \frac{1}{D_1}(J_{el} - 1)^2 + \frac{1}{D_2}(J_{el} - 1)^4 + \frac{1}{D_3}(J_{el} - 1)^6 \tag{A15}$$

A.2 Hyperelastic material evaluation for elastic gate

A uniaxial strain data set is provided by Antoci (2006) for the rubber material used in the gate deflection experiment in section 5.2.6. In order to determine which strain energy potential model is most appropriate to represent the material behavior, Abaqus' material evaluation tool analyzes the available test data to develop coefficients for each strain energy model. A comparison can be made between the test data and a simulated pull test using model data to find the best fit.

Figure 128 provides the results for four strain energy models: Marlow, Mooney-Rivlin (Poly_N1), Arruda-Boyce, and Van DerWaals. The best fit to the test data is provided by the Marlow model, as it is a near match through the full range of strain. Abaqus does suggest this model as the first choice when only uniaxial data is available. The Mooney-Rivlin (Poly_N1) model seems to provide the next best fit, followed closely by the Van Der Waals. The Arruda-Boyce model provides the worst results by under-predicting the stress at low strains and over-predicting the stress at high strains.

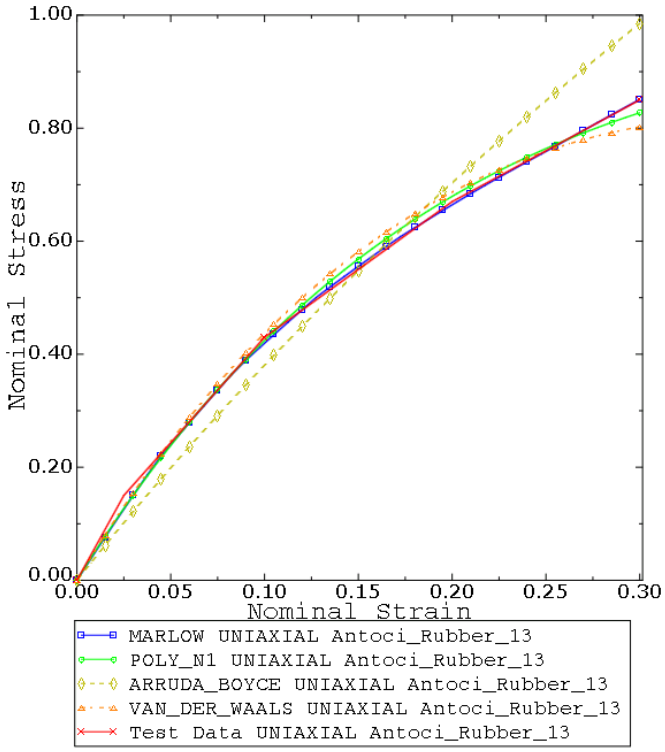

Figure 128. Uniaxial results for various strain energy potential models

In the absence of material test data for any of the other hyperelastic strain-energy tests shown in Figure 127 above, the strain energy models can be used to create plots as a surrogate for test data. As Antoci did not report biaxial strain test data for the material used for the elastic gate problem, the Abaqus material evaluation tool provides stress and strain for biaxial loading in Figure 129. The curves for each strain energy model are created using the coefficients developed from the available uniaxial test data. They present a wide variation of stress response for a given strain, which reinforces the importance of proper material testing and characterization.

For example, based solely upon the uniaxial data above, one could choose either Marlow or Mooney-Rivlin (Poly_N1) models as good representative fits. However, these models for the material under uniform biaxial loading dramatically deviate in Figure 129. There is a 100%

variation between them beginning at a strain as low as 0.12. The variation between the Mooney-Rivlin and the Van DerWaals curves is even more pronounced for large strains. This reinforces how important it is to have a complete test data set or validated structural model for a particular hyperelastic material.

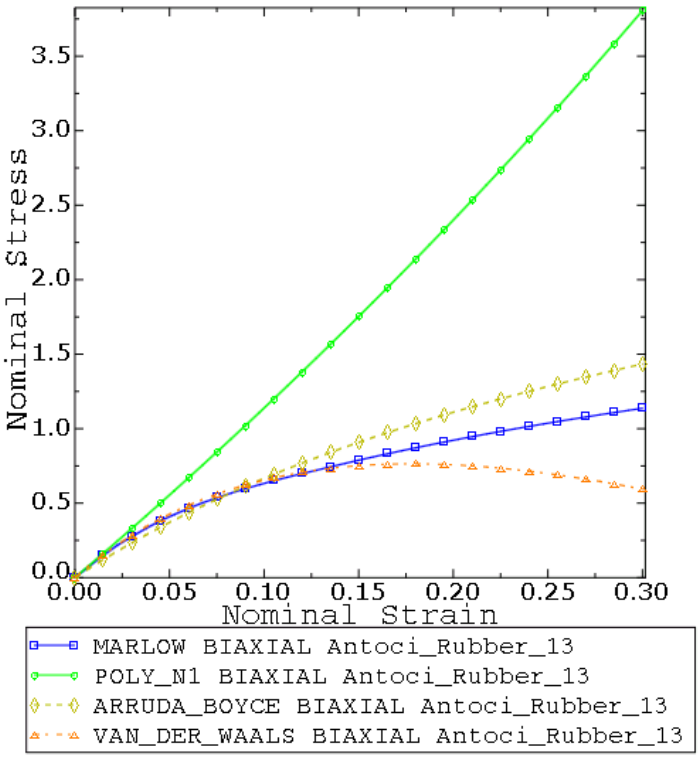

Figure 129. Biaxial results for various strain energy potential models

Even in the absence of test data, these plots are beneficial in that they identify key levels of strain that should not be exceeded without validation through test data. If biaxial stress is imposed resulting in a strain below 0.025 in the above example, the choice of model is not as important. But, any biaxial strain beyond that could result in deviation from the true material behavior. Similarly, if the loading presents disproportionate strains in one direction versus another, it may

be assumed the material load is largely uniaxial, and the choice of strain energy model may not be as critical.

References

1. Abbott, I. H., von Doenhoff, A. E. (1959). *Theory of wing sections: Including a summary of airfoil data*. Dover Publications, Inc. New York.

2. AIAA G-077 (2002). *Guide for the Verification and Validation of Computational Fluid Dynamics Simulations*. Computational Fluid Dynamics Committee, eISBN: 9781-56347-285-5 (https://doi.org/10.2514/4.472855).

3. Anderson, Jr., J. (1995). *Computational Fluid Dynamics*. McGraw Hill, New York.

4. Antoci, C. (2006). *Simulazione numerica dell' interazione fluido-struttura con la tecnica SPH.* PhD thesis, Universita di Pavia.

5. Antoci, C., Gallati, M. and Sibilla, S. (2007). Numerical simulation of fluid–structure interaction by SPH. *Computers and Structures*, 85:879–890.

6. Beatson, R. K., Powell, M. J. D. and Tan, A. M. (2006). Fast evaluation of polyharmonic splines in three dimensions. *DAMTP* 2006/NA03.

7. Breuer, M. et al. (2012). Fluid Structure Interaction using partitioned semi-implicit predictor-corrector coupling scheme for the application of large-eddy simulation. *Journal of Fluids and Structures,* 29:107–130.

8. Brieu, M. et al. (2007). A new biaxial tension test fixture for uniaxial testing machine - A validation for hyperelastic behavior of rubber-like materials. *Journal of Testing and Evaluation,* 35(4), JTE100688.

9. Birkhoff, G. (1955). *Hydrodynamics – a study in logic, fact, and similitude*. Dover Publishing, New York.

10. Bloxom, A. L. (2014). *Numerical Simulation of the Fluid-Structure Interaction of a Surface Effect Ship Bow Seal*. PhD dissertation. s.l.: Virginia Polytechnic Institute and State University, Aerospace and Ocean Engineering Department, Blacksburg, Virginia.

11. Bungartz, H. and Schäfer, M. (Eds.) (2006). *Fluid Structure Interaction*, Springer, New York, ISBN-13 978-3-540-34595-4.

12. Burman, E. and M. Fernandez, M. (2009). Stabilization of explicit coupling in fluid–structure interaction involving fluid incompressibility. *Comput. Methods Appl. Mech. Engrg.,* 198:766–784.

13. Causin, P. et al. (2005). Added-mass effect in the design of partitioned algorithms for fluid–structure problems. *Comput. Methods Appl. Mech. Engrg.*, 194:4506–4527.

14. Challa, R. (2015). *Hydrodynamic Contact/Impact Modeling and Application to Ocean Engineering Problems*. PhD thesis, Oregon State University.

15. Chorin, A. J. (1967). A numerical method for solving incompressible viscous flow problems. *Journal of Computational Physics*, 2:12-26.

16. Colagrossi, A. and Landrini, M. (2003). Numerical simulation of interfacial flows by smoothed particle hydrodynamics. *Journal of Computational Physics*, 191:448–475.

17. Cole, R. (2010). NSWC-PCD skirt and fan tests. *On Cushion Magazine - Oct2010*. Department of the Navy, Program Executive Office Ships, Washington Navy Yard, DC.

18. Collette, M. and Sielski, R. (2016). *Fluid Structure Interaction: A Community View*. Univ. of Michigan Marine Structures Design Lab, report 2016-003, 13 March.

19. Comstock, J. (Ed.). (1983). *Principles of Naval Architecture*. The Society of Naval Architects and Marine Engineers, New York.

20. Constantinescu A., et al. (2011). Numerical and experimental investigations of simple geometries in slamming. *International Journal of Offshore and Polar Engineering*, IJOPE 21(3):216-224.

21. Dalrymple, R. A. and Knio, O. (2001). SPH modeling of water waves. *Proceedings of Coastal Dynamics*, Lund, Sweden, pp. 779–787.

22. Dassault Systemes (2013). *SIMULIA Abaqus 6.13 Documentation*.

23. Dassault Systemes (2009). Effective fluid equations. *SIMULIA Abaqus Knowledge Base*. (https://www.3ds.com/support/knowledge-base/).

24. Diehl, T. (2012). *Getting more from Abaqus by tackling noisy and challenging data*. (http://www.bodietech.com/pdfs/Tackling_noisy_data_Web.pdf).

25. DoD Directive No. 5000.1 (1994). *The Defense Acquisition System*. (www.msco.mil).

26. DoD Directive No. 5000.59 (1994). *DoD Modeling and Simulation (M&S) Management*. (www.msco.mil).

27. Doctors, L. J. and Sharma, S. D. (1972). The wave resistance of an air cushion vehicle in steady and accelerated motion. *Journal of Ship Research*, 16-4.

28. Doctors, L. J., and McKesson, C. B. (2006). The resistance components of a surface-effect ship. *Proc. Twenty-Sixth Symposium on Naval Hydrodynamics*, Rome, Italy, 14 September.

29. Doctors, L. J. (2012). *Design tools for the sea-base-connector transformable craft (T-Craft) prototype demonstrator*. Fort Lauderdale, Florida, 10-13 January.

30. Doctors, L. J. et al. (2014). Experiments on the resistance and lift of a surface-effect-ship bow seal. *Thirtieth Symposium on Naval Hydrodynamics*, Hobart, Tasmania, 2-7 November.

31. Drela, M. (1989). XFOIL: An analysis and design system for low reynolds number airfoils. *Conference on Low Reynolds Number Airfoil Aerodynamics*, University of Notre Dame.

32. Eleni, D. C., et. al. (2012). Evaluation of the turbulence models for the simulation of the flow over a National Advisory Committee for Aeronautics (NACA) 0012 airfoil. *Journal of Mechanical Engineering Research*, 4(3):100-111.

33. Engels, T. et al. (2015). Numerical simulation of fluid–structure interaction with the volume penalization method. *Journal of Computational Physics*, 281:96–115.

34. Escárpita D. A. A. et al. (2012). Biaxial Tensile Strength Characterization of Textile Composite Materials. *Composites and Their Properties*. ISBN 978-953-51-0711-8.

35. *Expeditionary Force 21* (2014). Department of the Navy, Headquarters, United States Marine Corp., 4 March.

36. Faltinsen, O. M. (2005). *Hydrodynamics of High-Speed Marine Vehicles*. Cambridge University Press, New York.

37. Farhat, C., et al. (2010). Robust and provably second-order explicit-explicit and implicit-explicit staggered time-integrators for highly non-linear compressible fluid-structure interaction problems. Int'l J. Num. Methods Eng.84:73-137.

38. Faul, A. C., Goodsell, G. and Powell, M. J. D. (2005). A Krylov subspace algorithm for multiquadric interpolation in many dimensions. *IMA Journal of Numerical Analysis*, 25:1-24.

39. Forster, C. et al. (2007). Artificial added-mass instabilities in sequential staggered coupling of nonlinear structures and incompressible viscous flows. *Comput. Methods Appl. Mech. Engrg.*,196(7):1278–1293.

40. Gautschi, W. (2005). Orthogonal polynomials (in Matlab). *Journal of Computational and Applied Mathematics*, 178:215-234.

41. Gianellis, N. and Vio, G. (2015). Computational benchmark of commercial fluid-structure interaction software for aeroelastic applications," *International Forum on Aeroelasticity and Structural Dynamics,* St. Petersburg, Russia.

42. Gilbert, J. (2015). *Accelerating an SPH-FEM solver using heterogeneous computing for use in fluid-structure interaction problems*. PhD dissertation. s.l.: Virginia Polytechnic Institute and State University, Aerospace Engineering Department, Blacksburg, Virginia.

43. Graff, K. F. (1975). *Wave Motion in Elastic Solids*. Ohio State University Press.

44. Grüneisen, E. (1912). Theorie des festen zustandes einatomiger elemente. *Ann. Phys.*, 344:257–306.

45. Gumerov, N. A. and Duraiswami, R. (2007). Fast radial basis function interpolation via preconditioned Krylov iteration. *SIAM Journal on Scientific Computing*, 29:1876-1899.

46. Hardy, R. L. (1990). Theory and applications of the multiquadric-biharmonic method. *Comput. Math. Applic*., 19:163-208.

47. Hillegas, A. et al. (2001). *The use of modeling and simulation tools in acquisition program offices: results of a survey*. Hicks and Associates, Inc., McLean, VA.

48. Hird, C. W. and Nichols, B. D. (1981). Volume of fluid (VOF) method for dynamics of free boundaries. *Journal of Comp. Phy*., 39:201-225.

49. Hou, G. et al. (2012). Numerical methods for fluid-structure interaction. *Commun. Comput. Physics*, 12(2):337-377.

50. Hubner, B., Walhorn, E., and Dinkler, D. (2004). A monolithic approach to fluid-structure interaction using space-time finite elements. *Comput. Methods Appl. Engrg*., 193:2087-2104.

51. Jameson, A., Schmitt, W. and Turkel, E. (1981). Numerical solutions of the Euler equations by finite volume methods with Runge-Kutta time stepping schemes. *AIAA* 81:1259.

52. Kiara, A. (2010). *Analysis of the smoothed particle hydrodynamics method for free-surface flows.* PhD dissertation. s.l.: Massachusetts Institute of Technology Dept. of Mechanical Engineering.

53. Kramer, M. R. (2013). *Numerical investigation of the steady-state interaction between surface effect ship seals, air cushion, free-surface waves, and vessel motion*. PhD dissertation. s.l.: University of Michigan, Naval Architecture and Marine Engineering.

54. Krehl, P. O. K. (2009). *History of shockwaves, explosions and impact*. Springer, Berlin.

55. Kwasniewski, L. (2013). Application of grid convergence index in FE computation. *Bulletin of the Polish Academy of Technical Sciences*, 61-1.

56. Ladson, C. L. (1988). Effects of independent variation of Mach and Reynolds numbers on the low-speed aerodynamic characteristics of the NACA 0012 airfoil section. *NASA TM 4074*.

57. Langley Research Center Turbulence Modeling Resource. (2014). *2D NACA 0012 airfoil validation case*. (https://turbmodels.larc.nasa.gov/naca0012_val_ffeffect.html).

58. Lavis, D., Bartholomew, R. and Jones, J. (1974). Response of air cushion vehicles to random seaways and the inherent distortion in scale models. *Journal of Hydronautics*, 8(3):83-94.

59. Lavis, D. R. (2011). *Fifty years and more of hovercraft development*. Brief given at International Hydrofoil Society dinner meeting, 8 February.

60. Le Tallec, P. and Mouro, J. (2001). Fluid structure interaction with large structural displacements. *Comput. Methods Appl. Mech. Engrg*., 190:30396-3067.

61. Liu, G. and Liu, M. (2003). *Smoothed Particle Hydrodynamics: a meshfree particle method*. World Scientific Publishing Co., ISBN 981-238-456-1.

62. Loeven, G. (2010). *Efficient uncertainty quantification in computational fluid dynamics*. PhD dissertation, Delft University of Technology.

63. Lohner, R. et al. (2006). Extending the range and applicability of the loose coupling approach for FSI simulations. *Lecture Notes in Computational Science and Engineering: Fluid-Structure Interaction Modelling, Simulation, Optimisation*. Springer, New York, ISBN-10 3-540-34595-7.

64. Malakhoff, A. and Davis, S. (1981). Dynamics of SES bow seal fingers. *AIAA*, 81:2087.

65. Mantle, P. J. (1980). *Air cushion craft development*. U.S., David W. Taylor Naval Ship Research and Development Center, Bethesda, Maryland.

66. Marine Corp Operations MCDP 1-0. (2011). United States Marine Corp. Policy Control Number 142-000014-00.

67. McCroskey, W. J. (1988). A critical assessment of wind tunnel results for the NACA0012 airfoil. *Advisory Group for Aerospace Research and Development CP-*429.

68. Monaghan, J. J. (2005). Smoothed particle hydrodynamics. *Reports on Progress in Physics*, 68:1703-1759.

69. Muzaferija, S. et al. (1999). A two-fluid Navier-Stokes solver to simulate water entry. *Symposium on Naval Hydrodynamics*, pp. 638-651, Washington D.C.

70. *Naval Amphibious Capability in the 21st Century - Strategic Opportunity and a Vision for Change*, (2012). Amphibious Capabilities Working Group, 27 April.

71. Newman, J. N. (1977). *Marine Hydrodynamics*. MIT Press, Cambridge, ISBN 978-0-262-14026-3.

72. Nichols, B. D. and Hird. C. W. (1971). Improved free surface boundary conditions for numerical incompressible-flow calculations. *Journal of Comp. Phy*., 8:434-448.

73. Oberkampf, W. L. and Roy, C. J. (2010). *Verification and Validation in Scientific Computing*. Cambridge University Press, ISBN: 0-521-11360-1.

74. Olovsson, L. et al. (2005). Selective mass scaling for explicit finite element analyses. *International Journal for Numerical Methods in Engineering*, 63(10):1436-1445.

75. Osher, S. and Sethian, J. A. (1988). Fronts propagating with curvature dependent speed: algorithms based on Hamilton-Jacobi formulation. *J. Comp. Phys*., 79:12-49.

76. Palanikolau, A. (2001). Review of advanced marine vehicle concepts. *Norwegian Maritime Technology Forum*, 22-23 November.

77. Patankar, S. V. and Spalding, D. B. (1972). A calculation procedure for heat, mass and momentum transfer in three-dimensional parabolic flows. *Int. J. Heat and Mass Transf*., 15:1787-1806.

78. Patankar, S. V. (1980). *Numerical Heat Transfer and Fluid Flow*. Hemisphere Publishing Corp., Washington D.C.

79. Popovac, A. and Hanjalic, K. (2007) Compound wall treatment for RANS computation of complex turbulent flows and heat transfer. *Flow Turbulence Combust*., 78:177-202.

80. Przemieniecki, J. S. (1985). *Theory of matrix structural analysis*. Dover Publications, New York.

81. Puoti, V. (2003). Preconditioning method for low-speed flows. *AIAA*, 41(5).

82. Rao, S. S. (1995). *Mechanical Vibrations.* 3rd Ed., Addison-Wesley, Reading, Mass.

83. Richardson, L. F. (1910). The approximate arithmetical solution by finite differences of physical problems involving differential equations with an application to the stresses of a masonry dam. *Philos. Trans. R. Soc. London*, Ser. A 210:307-357.

84. Rivlin, R. S. and Saunders, D. W. (1951). Large elastic deformations of isotropic materials: experiments on the deformation of rubber. *Philos. Trans. R. Soc. London*, Ser. A 243:251-288.

85. Roache, P. J. (1994). Perspective: a method for uniform reporting of grid refinement studies. *Journal of Fluids Engineering*,116:405.

86. Roy, C. J. (2003). Grid convergence error analysis for mixed-order numerical schemes *AIAA*, 41-4.

87. Rugonyi, S. and Bathe, K. J. (2001). On finite element analysis of fluid flows fully coupled with structural interactions. *CMES*, 2-2:195-212.

88. Sethian, J. A. (1994). Curvature flow and entropy conditions applied to grid generation. *J. Comp. Phys.*, 115:440-454.

89. Sheldon, J. P. et al. (2014). Methodology for comparing coupling algorithms for fluid-structure interaction problems. *World Journal of Mechanics*, 4:54-70.

90. Shyy, W. et al. (1996). *Computational Fluid Dynamics with Moving Boundaries*. Dover Publications, New York.

91. Siemens (2018). STAR-CCM+ Documentation. (https://thesteveportal.plm.automation.siemens.com).

92. Skolnick, A. and Wilson, R. A. (2011). T-Craft- what, why & how? *11th Int. Conf. on Fast Sea Transport*, Honolulu, Hawaii.

93. Smith, R. W. (2016). personal email correspondence, 30 November.

94. Spalart, P. R. and Allmaras, S. R. (1992). A one-equation turbulence model for aerodynamic flows. *AIAA*, 92:439.

95. Stokes, G. G. (1845). On the theories of the internal friction of fluids in motion, and of the equilibrium and motion of elastic solids. *Trans. Camb. Philos. Soc*., 8:287-319.

96. Tatang, M. A. et al. (1997). An efficient method for parametric uncertainty analysis of numerical geophysical models. *J. of Geophysical Research*, 102:21925-21932.

97. Taylor, G. I. (1923). Stability of a viscous liquid contained between two rotating cylinders. *Philos. Trans. R. Soc. London*, Ser. A 223:289.

98. T-Craft Tool Development (2012). Annual technical review meeting, FAU Sea Tech Campus, Dania Beach, Florida: 10-13 January.

99. Tippman, J. et al. (2009). 2-D tank sloshing using the coupled Eulerian-Lagrangian (CEL) capability of Abaqus/Explicit. *Simulia Customer Conference*, 18-21 May, London, England.

100. Treoloar, L. R. G. (1944). Stress-strain data for vulcanized rubber under various types of deformation," *Trans. Faraday Soc*., 40:59-70.

101. Turek S. and Hron J. (2006). Proposal for numerical benchmarking of fluid-structure interaction between an elastic object and laminar incompressible flow. *Fluid-Structure Interaction: Lecture notes in computational science and engineering Vol. 53*, Springer, Berlin.

102. Turek, S. et al. (2011). Numerical benchmarking of fluid-structure interaction: A comparison of different discretization and solution approaches. *Fluid-Structure Interaction: Lecture notes in computational science and engineering Vol. 73*, Springer, Berlin.

103. Turkel, E. et al. (1996). Preconditioning methods for low speed flows. *Institute for Computer Applications in Science and Engineering,* NASA Langley Research Center, Hampton, Virginia.

104. Venkatakrishnan, V. (1994). On the convergence of limiters and convergence to steady state solutions. *AIAA*, 93:0880.

105. Vierendeels, J. (2006). Implicit coupling of partitioned fluid-structure interaction solvers using reduced-order models. *Lecture Notes in Computational Science and Engineering: Fluid-Structure Interaction Modelling, Simulation, Optimisation*, Springer, Berlin, ISBN-10 3-540-34595-7.

106. White, F. M. (2011) *Fluid Mechanics,* 7th Ed., McGraw Hill.

107. Wiener, N. (1938) The homogenous chaos. *Amer. J. Math,* 60:897-936.

108. Wiggins, A. D. (2014). *Hydroelastic response of surface-effect ship bow seals: large-scale experiments and post-buckling analysis*, PhD dissertation. s.l.: University of Michigan, Naval Architecture and Marine Engineering, Ann Arbor, Michigan.

109. Wong, J. S. et. al. (2001). The solution of the compressible Euler equations at low Mach numbers using a stabilized finite element algorithm. *Comput. Methods Appl. Mech. Engrg.*, 190:5719-5737.

110. Wu, Z. D. et al. (2013). Computational investigation of the mitigation of an underwater explosion. *Acta Mechanica*, 224:3159–3175.

111. XFOIL (2013). Subsonic airfoil development system. (http://web.mit.edu/drela/Public/web/xfoil)

112. Yang, Q. (2011). *SPH simulation of fluid-structure interaction problems with application to hovercraft*. PhD dissertation. s.l.: Virginia Polytechnic Institute and State University, Aerospace Engineering Department, Blacksburg, Virginia.

113. Yun, L. and Bliault, A. (2000). *Theory and Design of Air Cushion Craft*. John Wiley and Sons, New York.

114. Zalek, S. F. and Doctors, L. J. (2010). Experimental study of the resistance of surface-effect-ship seals. *Proc. of the Twenty-Eighth Symposium on Naval Hydrodynamics*, Pasadena, California.

115. Zdravkovich, M. M. (1997). *Flow Around Circular Cylinders: Volume I: Fundamentals*, Oxford Science Publications.

116. Zienkiewicz, O. C. and Taylor, R. L. (1991). *The Finite Element Method*, 4th Ed., McGraw-Hill, London, ISBN 0-07-084175-6.

117. Zhou, B. et. al. (2015). Experimental study of flow past a circular cylinder with rough surface. *Ocean Engineering*, 109:7-13.